Dynamics of dispersed heavy particles in swirling flow

R.H.A. IJzermans

Dynamics of dispersed heavy particles in swirling flow
R.H.A. IJzermans

Cover: W.H.T. IJzermans

Thesis University of Twente, Enschede - With summary in Dutch.
ISBN 978-90-365-2525-1

DYNAMICS OF DISPERSED HEAVY PARTICLES IN SWIRLING FLOW

PROEFSCHRIFT

ter verkrijging van
de graad van doctor aan de Universiteit Twente,
op gezag van de rector magnificus,
prof. dr. W.H.M. Zijm,
volgens besluit van het College voor Promoties
in het openbaar te verdedigen
op donderdag 5 juli 2007 om 16.45 uur

door

Rutgerus Henricus Anthonius IJzermans

geboren op 31 mei 1980
te Zevenaar

Dit proefschrift is goedgekeurd door de promotor:
prof. dr. ir. H.W.M. Hoeijmakers

en de assistent-promotor:
dr. ir. R. Hagmeijer

TABLE OF CONTENTS

INTRODUCTION

1 CHAPTER

This chapter gives a brief introduction to the motion of heavy particles and droplets in gas flows. Each one of the next chapters is provided with an additional introduction dedicated to the particular aspects of the subject treated in that chapter.

1.1 Etymological aspects of dispersed two-phase flow

The present thesis is devoted to the study of droplets and particles in gas flows. In order to determine relevant characteristics of droplet- and particle-laden flows, it is instructive to look at the etymology of the words 'droplet', 'particle' and 'gas'.

The word 'droplet' is derived from the onomatopoeia 'drop' [71], 'let' being a diminutive conjugation which has become rather obsolete in english.* Thus, we see a droplet is traditionally regarded as a relatively small amount of liquid.

The english word 'particle' is related to the latin word 'particula', which itself is the diminutive form of 'partis', in english 'part' [71]. So, 'particle' means something like 'small part'.† Etymology apparently suggests that particles are relatively small; in addition, since a 'part' denotes a fraction of a larger quantity, we may conclude that particles can be found in large groups.

Finally, the word 'gas' is an originally dutch derivation from the Greek word 'chaos', made by the flemish scientist Jan Baptista Van Helmont (1580-1644) [71]. He used it in order to describe the large number of degrees of freedom in the motion the gas molecules. The word 'gas' was first used in a scientific treatise in 1779, in the context of turbomachinery. Since the word 'gas' obtained its own meaning, in the beginning of the 20th century the word 'chaos' could be used to denote something different, namely an extreme sensitivity to initial conditions in dynamical systems.

*Other examples of the diminutive '-let' are leaflet, piglet, starlet and wavelet. The dutch counterpart '-el' (druppel) is used in words like 'trommel' (trom), 'stengel' (stang), 'eikel' (eik) and 'ijzel' (ijs).

†The meaning of 'particle' as 'small part' is not restricted to english and Romance languages like french (particule), italian (particella) and spanish (partícula); remarkably enough, even the dutch and german translations of 'particle', 'deeltje' and 'Teilchen', respectively, share the literal meaning of 'small part'.

From these findings, we can deduce the following:

- Droplets and particles are small;
- Particles can be found in large groups;
- Gas is a collection of chaotically moving molecules.

These preliminary remarks can be seen as a prelude to the present thesis, in which we study the motion of groups of particles and droplets due to their interactions with gas flows. In this thesis, the emphasis is on the motion of heavy particles, i.e. particles with a much higher mass density than the surrounding fluid.

1.2 Particle-laden flows in Nature and industry

Flows which contain large groups of relatively small particles and/or droplets are frequently observed in Nature and in industry. One can think of the transport of ash and stones during the eruption of a vulcano, soot in exhaust pipes of cars, dispersed fuel droplets in combustion chambers, and the ubiquity of particles in the process industry. Since the introduction in 1924 of the first spin dryer, produced by the Savage Arms Corporation in America[‡], more and more people have acquired their own droplet-laden flow at home.

In order to describe some characteristic properties of dispersed multiphase flows, below we treat three examples in some more detail.

1.2.1 Formation of rain droplets in turbulent clouds

Despite the familiarity of the phenomenon, the development of rain showers is not yet completely understood and therefore subject to many studies (see e.g. the review article by Shaw [89] for references). In general terms, three stages can be distinguished in the process of rain drop formation. Initially, tiny droplets form by condensation of water vapor on preexisting aerosol particles that serve as condensation nuclei; the typical diameter of these droplets is of the order of microns. If the conditions allow, the droplets grow on to a diameter of millimeters in a subsequent stage. Finally, the droplets are large enough to fall, under the influence of gravity, through the cloud and reach the ground.

Observations and experimental results show that the entire process from the formation of tiny droplets to the actual precipitation can take place in approximately half an hour. Such a small time scale could never be possible if the droplets grew only due to condensation (see e.g. [89] for a first estimate). Hence, droplets must collide

[‡]See `http://thefusebox.ce-electricuk.com`.

and coalesce in order to achieve the explosive growth necessary to produce particles large enough to fall from a cloud.

It was long thought [80] that gravitational coalescence, during which a large droplet falls through a quiescent fluid overtaking smaller droplets, is the most effective mechanism of coalescence. In the past decade, however, an alternative explanation has been proposed [24], [89]: the influence of turbulence on the distribution of droplets, generally phrased 'preferential concentration'.

Preferential concentration refers to the non-uniform distribution of particles or droplets as a consequence of small-scale turbulent motions. Due to the density difference between the particles and the carrier flow, particles are expelled from regions of high vorticity and accumulate in regions of high strain. Preferential concentration has been widely observed both in experiments [23] and in numerical simulations [59],[91]. The degree of particle aggregation has a strong dependence on the value of the Stokes number, i.e. the particle relaxation time τ_p made dimensionless by the Kolmogorov time scale τ_η of the turbulent motion; qualitatively, for very small Stokes numbers particles tend to follow fluid streamlines, and for very large Stokes numbers particles do not respond to the fluid motion significantly during the lifetime of an eddy. Although preferential concentration can be observed for a wide range of Stokes numbers, the effect is most important when the Stokes number is of order unity. Indeed, in a recent publication, Bec *et al.* [9] report, after having done extensive direct numerical simulations in stationary homogeneous turbulence, that the maximum clustering takes place when the Stokes number is approximately 0.6.

The relation between preferential concentration and the formation of cloud droplets has been explained by Balkovsky *et al.* [5], and by Falkovich *et al.* [24]: due to their inertia, droplets concentrate in strain regions on the smallest scales of the turbulent flow in the cloud. Since the collision rate (i.e. the number of collisions per unit of volume per unit of time) is to good approximation proportional to the particle number density squared [89], [93], it is expected that preferential concentration has a major effect on the probability of collisions and coalescence.

The example of droplet formation in clouds illustrates that (i) in turbulent flows, droplets and particles are likely to distribute non-uniformly, (ii) inter-particle collisions can have an important influence, both qualitatively and quantitatively, on the properties of droplet-laden flows.

1.2.2 Formation of protoplanets in stellar systems

Stars condense from interstellar dust [50], an interstellar medium consisting mostly of gas containing a mixture of solid particles. Both observational and numerical studies suggest that, as the central star contracts, around it material remains that contains a part of the initial angular momentum of the whole system. In this so-called nebula, the centrifugal force balances the stellar gravity in the radial direction and a disk is formed.

As the dust settles towards the midplane of this disk, it is somehow accumulated into protoplanetary objects of the size of approximately 10 km, which later grow on to become planets and moons. Barge & Sommeria [6] explained the transition from a primarily gaseous protoplanetary disk to a limited number of large objects by emphasizing the inherent property of inertial particles to distribute non-uniformly in a gas flow. This explanation was further elaborated by Bracco *et al.* [15], who assumed that the nebular disk sustains turbulence. Since the turbulence is approximately two-dimensional, large vortices are formed in the process of the inverse cascade of kinetic energy from small to large scales.

Bracco *et al.* found that in the two-dimensional turbulent flow heavy particles are quickly ejected from cyclonic vortices, i.e. regions where the vorticity is high and has the same sign as the main rotation of the flow. First, the dust particles in the solar nebula are concentrated in the high-strain regions between vortices. Subsequently, remarkably enough, the particles concentrate inside anticyclonic vortices, i.e. regions where the vorticity is high and has a sense opposite with respect to the main rotation of the flow. The reason for this particle accumulation lies in the Coriolis force, as Provenzale explains [79]. The particles remain trapped in the anticyclonic vortices for a very long time, and have thus the opportunity to collide and to agglomerate. Later, Chavanis [16] studied the formation of the Solar System, showing a strong correlation between the regions where particles have the highest probability to accumulate and the positions of the largest planets, i.e. Jupiter and Saturn.

The example from planet formation shows that the motion of heavy particles in gas flows is not only influenced by the local properties of the gas at the position of the particle, but also by the presence of a rotation of the whole system. Due to this rotation, particles may accumulate in vortices instead of in high-strain regions.

1.2.3 Particle separation processes

When natural gas is extracted from the earth, it contains several unwanted components such as water vapor and dust. Since these components are undesired, they need to be separated as quickly as possible after the production from the wells.

Traditionally, the separation of water vapor and impurities from natural gas is achieved by cooling the mixture in order to condense the vapor. In a subsequent stage, the vapor is filtered from the gas. This process has the drawback that it requires an apparatus of considerable size, which makes it impractical to use on off-shore platforms.

Recently, the company Twister B.V.[§] has developed a new type of gas-liquid separators. Inside these separators, the natural gas is expanded to low pressures. In this expansion the gas cools to low temperatures while the flow reaches supersonic speeds. In this expansion process, high values of the cooling speed are achieved resulting in

[§]See `www.twisterbv.com`.

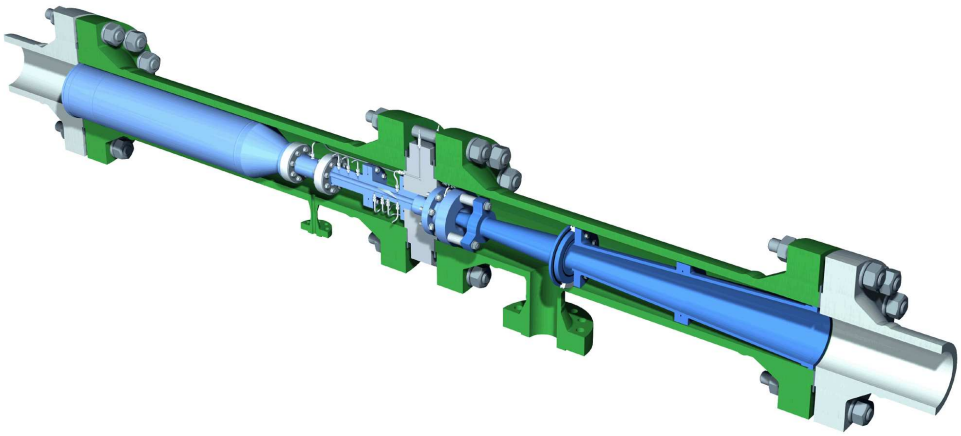

FIGURE 1.1: *Configuration sketch of a gas-liquid separator with a helical vortex filament in the deposition section. The contaminated gas is accelerated through the converging-diverging nozzle (left part). Droplets are expelled in the separation section (right part); the swirl is induced by a delta-wing attached to the wall. (This picture has been provided by Twister B.V..)*

a highly supersaturated state of the gas. As a consequence, homogeneous condensation occurs with vapor components such as water condensing to droplets, which can be separated from the flow by applying a swirl; due to the density difference, the droplets are expelled from the flow in a similar way as happens in a spin dryer.

Two different concepts have been developed by Twister B.V.. The first concept, which is depicted schematically in Fig. 1.1, consists of a converging-diverging nozzle, followed by a deposition section in which a swirling flow is established. The swirl is introduced by means of a delta-wing type of vortex generator. The flow field is characterized by a region with concentrated vorticity of helical (i.e. spiralling) shape, which is supposed to force the droplets from the flow to the pipe wall.

In the second concept, sketched in Fig. 1.2, the processes of condensation and separation are combined in one section. Upon entering the apparatus, the gas is accelerated in both axial and azimuthal direction. The flow expands to low pressure and temperature and reaches a supersonic speed. This causes the vapor components of the gas to homogeneously condense to droplets. Due to the swirl, the droplets are forced towards the wall, where they deposit.

The flow through both configurations of the gas-liquid separator is highly complex. The flow Reynolds numbers $\mathrm{Re} = UD/\nu = O(10^6)$, where U denotes the magnitude of the mean velocity and D is the diameter of the pipe in the gas-liquid separator; ν denotes the kinematic viscosity of the gas. The following effects play an important role: a high cooling speed in the flow expanding to supersonic speed, the

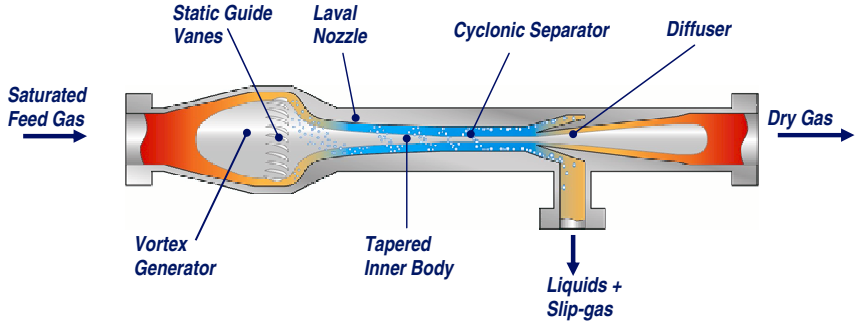

FIGURE 1.2: *Configuration sketch of a gas-liquid separator with axisymmetric flow. The contaminated gas is brought into rotation, and then accelerated. (This picture has been provided by Twister B.V..)*

release of latent heat during the condensation of vapor, a non-uniform deposition of droplets, and the interaction between the turbulent flow and the motion of droplets. An understanding of these processes is fundamental in order to enable optimizations of the performance of the separator.

1.3 Objectives of the present study

In the present thesis, we study the motion of heavy particles in the presence of regions with concentrated vorticity, and the motion of heavy particles and droplets in a turbulent boundary layer of a swirling flow in a pipe. These research topics are related to the industrial gas-liquid separators discussed in section 1.2.3. The results of the present research provide some fundamental knowledge about the dynamics of heavy particles in gas flows.

The following research questions are addressed in the present thesis:

- Is it possible to derive some general criterion for the accumulation of heavy particles in gas flows?

- How do heavy particles and droplets move in the presence of regions with concentrated vorticity inside a circular pipe?

- On which parameters does the particle deposition on the pipe wall in high-speed swirling flows depend?

- What is the influence of inter-particle collisions and coalescence on the deposition rates in turbulent boundary layers?

Generally spoken, two different approaches can be taken in the study of the motion of particles. Firstly, the so-called Eulerian approach refers to the study and the modelling of the motion of particles in a fixed frame of reference. In contrast, in the Lagrangian approach each individual particle is followed along its trajectory.[¶] A fundamental problem in modelling any dispersed two-phase flow arises from the fact that the equations describing the carrier flow are formulated in an Eulerian fashion, whereas the equation of motion of particles is formulated in a Lagrangian fashion.

In the present research, we choose to employ a Lagrangian formulation. The advantage of this formulation is that no approximations have to be made to the particle equations of motion. In addition, it is physically more insightful since each particle can be traced individually. As a result, both trajectories of individual particles and distribution patterns of a group of particles are readily obtained from Lagrangian simulations.

1.4 Thesis outline

The present thesis is devoted to the motion of heavy particles and droplets near regions of concentrated vorticity and the motion of heavy particles and droplets in turbulent boundary layers. The thesis is organized as follows.

In Chapter 2, we present the equation of motion for heavy particles and droplets in a gas flow. We show that the Stokes drag and gravity are the dominant forces when the particles have a small size and a high density compared to the density of the carrier fluid. In addition, we relate the accumulation of small heavy particles to the local properties of the carrier flow field.

Part I is devoted to the motion of heavy particles in flows generated by strong vortices. In Chapter 3, results are presented for heavy particles in a closed circular domain containing one point vortex. The motion of heavy particles in a closed circular domain containing two point vortices is studied in Chapter 4. Finally, Chapter 5 is dedicated to the motion of heavy particles in the three-dimensional flow field induced by a helical vortex filament in an infinite straight tube of circular cross-section.

In Part II, we discuss the motion of heavy particles and droplets in turbulent boundary layers. The flow field along the particle trajectory is modelled using a stochastic method. In Chapter 6, the most important properties of stochastic differential equations are presented. In Chapter 7, we study the dynamics of heavy particles and droplets in the turbulent boundary layer over a flat plate. Results for the motion of heavy particles and droplets in the turbulent boundary layer in a swirling flow in a pipe are presented in Chapter 8.

Finally, conclusions and recommendations for future research are formulated in Chapter 9.

[¶]It is noted that both the Eulerian and Lagrangian frame were first derived by Euler [45].

Flows laden with dispersed heavy particles

Chapter 2

In this chapter, the equation of motion is presented for a solid, rigid particle in a non-uniform flow. It is assumed that the particle does not influence the flow field (one-way coupling). It will be shown that the Stokes drag and gravity are the dominant forces in the case of small heavy particles and droplets in gas flows, so that the equation of motion can be simplified considerably. The simplified equation of motion can be solved analytically for linear velocity fields, as is shown in section 2.2. In section 2.3, we use the simplified equation of motion in order to derive some general properties of particle accumulation in any smooth flow. We show that the dissipative nature of the equation of motion causes a continuous decrease of the phase space volume occupied by a group of particles. However, this does never result in an accumulation of particles to one point from all directions in phase space simultaneously. In addition, we show that in physical space small heavy particles are expelled from high-vorticity regions and concentrate in high-strain regions.

2.1 Equation of motion of rigid spherical particles

We consider a rigid spherical particle with radius a_p and density ρ_p in a non-uniform velocity field $\tilde{\boldsymbol{u}}(\tilde{\boldsymbol{x}},\tilde{t})$ of a fluid with kinematic viscosity ν and density ρ. The acceleration of the particle is described by the equation of motion, here given in the form presented by Maxey & Riley [58]:

$$
\begin{aligned}
\frac{\mathrm{d}\tilde{\boldsymbol{x}}_p}{\mathrm{d}\tilde{t}} &= \tilde{\boldsymbol{u}}_p, \\
m_p\frac{\mathrm{d}\tilde{\boldsymbol{u}}_p}{\mathrm{d}\tilde{t}} &= (m_p-m_f)\boldsymbol{g} + m_f\Big(\frac{\mathrm{D}\tilde{\boldsymbol{u}}}{\mathrm{D}\tilde{t}}\Big)_{\tilde{\boldsymbol{x}}=\tilde{\boldsymbol{x}}_p(\tilde{t})} - \frac{1}{2}m_f\frac{\mathrm{d}}{\mathrm{d}\tilde{t}}\Big[\tilde{\boldsymbol{u}}_p - \Big(\tilde{\boldsymbol{u}}+\frac{a_p^2}{10}\nabla^2\tilde{\boldsymbol{u}}\Big)_{\tilde{\boldsymbol{x}}=\tilde{\boldsymbol{x}}_p(\tilde{t})}\Big] + \\
&\quad -6\pi a_p\rho\nu\Big[\tilde{\boldsymbol{u}}_p - \Big(\tilde{\boldsymbol{u}}+\frac{a_p^2}{6}\nabla^2\tilde{\boldsymbol{u}}\Big)_{\tilde{\boldsymbol{x}}=\tilde{\boldsymbol{x}}_p(\tilde{t})}\Big] + \\
&\quad -6\pi a_p^2\rho\nu\int_0^{\tilde{t}}\frac{1}{\sqrt{\pi\nu(\tilde{t}-\tilde{\tau})}}\Big(\frac{\mathrm{d}}{\mathrm{d}\tilde{\tau}}\Big[\tilde{\boldsymbol{u}}_p - \Big(\tilde{\boldsymbol{u}}+\frac{a_p^2}{6}\nabla^2\tilde{\boldsymbol{u}}\Big)_{\tilde{\boldsymbol{x}}=\tilde{\boldsymbol{x}}_p(\tilde{\tau})}\Big]\Big)\mathrm{d}\tilde{\tau}, \qquad (2.1)
\end{aligned}
$$

where $\tilde{\boldsymbol{x}}_p$ is the position of the particle, $\tilde{\boldsymbol{u}}_p$ is the velocity of the particle, $\boldsymbol{g}$ is the acceleration of gravity vector, $m_p = 4\pi\rho_p a_p^3/3$ is the mass of the particle, $m_f = 4\pi\rho a_p^3/3$ is the mass of the fluid displaced by the particle. Finally, the terms $(\tilde{\boldsymbol{u}} + (a_p^2/10)\nabla^2\tilde{\boldsymbol{u}})_{\tilde{\boldsymbol{x}}=\tilde{\boldsymbol{x}}_p(\tilde{t})}$ and $(\tilde{\boldsymbol{u}} + (a_p^2/6)\nabla^2\tilde{\boldsymbol{u}})_{\tilde{\boldsymbol{x}}=\tilde{\boldsymbol{x}}_p(\tilde{t})}$ denote the average velocity of the carrier fluid over the particle volume, and the average velocity of the carrier fluid over the particle surface, respectively. Although these velocities are seemingly not meaningful (there is no fluid in the region occupied by the particle, so it does not have any velocity either), they can be regarded as some measure for the velocity of the carrier fluid in the vicinity of the supposedly very small particle.

The terms on the RHS of Eq. (2.1) denote buoyancy, a force due to the acceleration of the undisturbed fluid, an inertia force of added mass, a viscous drag force, and finally a viscous force due to unsteady relative acceleration (also known as the Basset history force), respectively. Eq. (2.1) is valid for situations in which the particle Reynolds number $\mathrm{Re}_p \equiv 2|\tilde{\boldsymbol{u}}_p - \tilde{\boldsymbol{u}}|a_p/\nu = O(1)$, i.e. Stokes flow is assumed around the particle [58].

Upon dividing the second equation of Eq. (2.1) by m_p, the following equation is obtained:

$$
\begin{aligned}
\frac{\mathrm{d}\tilde{\boldsymbol{x}}_p}{\mathrm{d}\tilde{t}} &= \tilde{\boldsymbol{u}}_p, \\
\frac{\mathrm{d}\tilde{\boldsymbol{u}}_p}{\mathrm{d}\tilde{t}} &= (1-\frac{\rho}{\rho_p})\boldsymbol{g} + \frac{\rho}{\rho_p}\Big(\frac{\mathrm{D}\tilde{\boldsymbol{u}}}{\mathrm{D}\tilde{t}}\Big)_{\tilde{\boldsymbol{x}}=\tilde{\boldsymbol{x}}_p(\tilde{t})} - \frac{1}{2}\frac{\rho}{\rho_p}\frac{\mathrm{d}}{\mathrm{d}\tilde{t}}\Big[\tilde{\boldsymbol{u}}_p - \Big(\tilde{\boldsymbol{u}} + \frac{a_p^2}{10}\nabla^2\tilde{\boldsymbol{u}}\Big)_{\tilde{\boldsymbol{x}}=\tilde{\boldsymbol{x}}_p(\tilde{t})}\Big] + \\
&\quad -\frac{1}{\tau_p}\Big[\tilde{\boldsymbol{u}}_p - \Big(\tilde{\boldsymbol{u}} + \frac{a_p^2}{6}\nabla^2\tilde{\boldsymbol{u}}\Big)_{\tilde{\boldsymbol{x}}=\tilde{\boldsymbol{x}}_p(\tilde{t})}\Big] + \\
&\quad -\frac{a_p}{\tau_p}\int_0^{\tilde{t}} \frac{1}{\sqrt{\pi\nu(\tilde{t}-\tilde{\tau})}}\Bigg(\frac{\mathrm{d}}{\mathrm{d}\tilde{\tau}}\Big[\tilde{\boldsymbol{u}}_p - \Big(\tilde{\boldsymbol{u}} + \frac{a_p^2}{6}\nabla^2\tilde{\boldsymbol{u}}\Big)_{\tilde{\boldsymbol{x}}=\tilde{\boldsymbol{x}}_p(\tilde{\tau})}\Big]\Bigg)\mathrm{d}\tilde{\tau},
\end{aligned}
\tag{2.2}
$$

where τ_p is defined as the particle response time, equal to:

$$
\tau_p \equiv \frac{2}{9}\frac{\rho_p}{\rho}\frac{a_p^2}{\nu}. \tag{2.3}
$$

If the density and the viscosity of the surrounding fluid are uniform, the particle response time τ_p is a constant.

In the present thesis, we consider particles and droplets which have a much higher density than the surrounding fluid: $\rho_p \gg \rho$. In addition, we assume the particle radius to be so small that $a_p^2|\nabla^2\tilde{\boldsymbol{u}}| \ll |\tilde{\boldsymbol{u}}|$. The Basset history term is neglected under the assumption that the accelerations of the carrier flow field are sufficiently small, e.g. shocks are not present [95]. Using these assumptions, which are relevant for

many applications in Nature and industry, Eq. (2.2) can be approximated by:

$$\frac{\mathrm{d}\tilde{\boldsymbol{x}}_p}{\mathrm{d}\tilde{t}} = \tilde{\boldsymbol{u}}_p, \qquad \frac{\mathrm{d}\tilde{\boldsymbol{u}}_p}{\mathrm{d}\tilde{t}} = \frac{1}{\tau_p}(\tilde{\boldsymbol{u}} - \tilde{\boldsymbol{u}}_p) + \boldsymbol{g}, \tag{2.4}$$

where $\tilde{\boldsymbol{u}} = \tilde{\boldsymbol{u}}(\tilde{\boldsymbol{x}}_p(\tilde{t}), \tilde{t})$ is written for the sake of brevity. Apparently, the Stokes drag and gravity are the dominant forces.

The equation of motion Eq. (2.4) can be made dimensionless by means of a typical length scale $\mathcal{L}$ and a typical time scale $\mathcal{T}$. The result is:

$$\frac{\mathrm{d}\boldsymbol{x}_p}{\mathrm{d}t} = \boldsymbol{u}_p, \qquad \frac{\mathrm{d}\boldsymbol{u}_p}{\mathrm{d}t} = \frac{1}{\mathrm{St}}(\boldsymbol{u} - \boldsymbol{u}_p) + \frac{1}{\mathrm{Fr}^2}\frac{\boldsymbol{g}}{|\boldsymbol{g}|}, \tag{2.5}$$

where St denotes the Stokes number defined by $\mathrm{St} \equiv \tau_p/\mathcal{T}$, and Fr is the Froude number defined by $\mathrm{Fr} \equiv \mathcal{T}^{-1}\sqrt{\mathcal{L}/|\boldsymbol{g}|}$.

2.2 Analytical solutions of particle equation of motion

For some simple flows, the equations of motion Eq. (2.5) can be solved analytically. In the present section, first a general solution is provided. Subsequently, the general solution is applied to two archetypical two-dimensional flow fields.

Mathematically, Eq. (2.5) is a system of first-order ordinary differential equations of the form:

$$\frac{\mathrm{d}\boldsymbol{\chi}}{\mathrm{d}t} = \boldsymbol{F}(\boldsymbol{\chi}, t), \tag{2.6}$$

where $\boldsymbol{\chi}$ is a column vector containing both the position and the velocity of the particle: $\boldsymbol{\chi} \equiv (\boldsymbol{x}_p, \boldsymbol{u}_p)^T$.

If the Froude number $\mathrm{Fr} \gg 1$ so that the effect of gravity can be neglected, and if the carrier flow velocity $\boldsymbol{u}$ is a time-independent linear function of the spatial coordinates, then $\boldsymbol{F}(\boldsymbol{\chi}, t) = \boldsymbol{F}(\boldsymbol{\chi})$, with $\boldsymbol{F}$ linear in $\boldsymbol{\chi}$, and Eq. (2.5) can be solved analytically. Under these assumptions, the equation of motion of heavy particles becomes:

$$\frac{\mathrm{d}\boldsymbol{x}_p}{\mathrm{d}t} = \boldsymbol{u}_p, \qquad \frac{\mathrm{d}\boldsymbol{u}_p}{\mathrm{d}t} = \frac{1}{\mathrm{St}}([\sigma]_d\boldsymbol{x}_p - \boldsymbol{u}_p), \tag{2.7}$$

where the matrix $[\sigma]_d$ is the rate-of-deformation tensor which contains the spatial derivatives of the velocity field: its elements are $\sigma_{ij} \equiv \partial u_i/\partial x_j$. Eq. (2.7) has the form:

$$\frac{\mathrm{d}\boldsymbol{\chi}}{\mathrm{d}t} = M\boldsymbol{\chi}, \tag{2.8}$$

where M is the following matrix:

$$M = \begin{pmatrix} [0]_d & [I]_d \\ \frac{1}{\mathrm{St}}[\sigma]_d & \frac{-1}{\mathrm{St}}[I]_d \end{pmatrix}. \tag{2.9}$$

Here, $[0]_d$ and $[I]_d$ denote a $d \times d$-dimensional null matrix and identity matrix, respectively. Since the matrix M is time-independent, the solution of this system has the following general form:

$$\boldsymbol{\chi}(t) = \sum_{k=1}^{2d} a_k \boldsymbol{r}_k \exp(\lambda_k t), \tag{2.10}$$

where λ_k denotes the k-th eigenvalue of the matrix M, and d denotes the dimension of the physical space, i.e. $d = 2$ for a two-dimensional flow, and $d = 3$ for a three-dimensional flow. The vector $\boldsymbol{r}_k$ is the right eigenvector corresponding to λ_k, and the coefficients a_k can be determined from the initial condition $\boldsymbol{\chi}(t = 0) = \boldsymbol{\chi}_0$.

The eigenvalues λ can be determined from $\det(M - \lambda I) = 0$:

$$0 = \det\begin{pmatrix} -\lambda[I]_d & [I]_d \\ \frac{1}{\mathrm{St}}[\sigma]_d & -(\frac{1}{\mathrm{St}} + \lambda)[I]_d \end{pmatrix}. \tag{2.11}$$

With help of a Gauss-Jordan transformation, we obtain:

$$0 = \det\begin{pmatrix} -\lambda[I]_d & [I]_d \\ [0]_d & -(\frac{1}{\mathrm{St}} + \lambda)[I]_d + \frac{1}{\lambda \mathrm{St}}[\sigma]_d \end{pmatrix}. \tag{2.12}$$

This is equivalent to:

$$0 = \det\left(\frac{1}{\mathrm{St}}[\sigma]_d - (\frac{\lambda}{\mathrm{St}} + \lambda^2)[I]_d\right). \tag{2.13}$$

It is clear that the d eigenvalues of the matrix $[\sigma]_d$, α say, are related to λ as follows:

$$\lambda^2 + \frac{\lambda}{\mathrm{St}} = \frac{\alpha}{\mathrm{St}}. \tag{2.14}$$

The solution for λ is:

$$\lambda_i = \frac{-1 + \sqrt{1 + 4\mathrm{St}\alpha_i}}{2\mathrm{St}}, \qquad \lambda_{i+d} = \frac{-1 - \sqrt{1 + 4\mathrm{St}\alpha_i}}{2\mathrm{St}}, \tag{2.15}$$

for $i = 1, \ldots, d$.

If the d right eigenvectors of $[\sigma]_d$ are denoted by $\boldsymbol{s}_i$, associated to the eigenvalues α_i, then the right eigenvectors of M, $\boldsymbol{r}_k$, associated to the eigenvalues λ_k, are:

$$\boldsymbol{r}_i = [\boldsymbol{s}_i, \lambda_i \boldsymbol{s}_i]^T, \qquad \boldsymbol{r}_{i+d} = [\boldsymbol{s}_i, \lambda_{i+d} \boldsymbol{s}_i]^T, \qquad \text{for } i = 1, \ldots, d. \tag{2.16}$$

It is noted that the eigenvectors $\boldsymbol{r}_k$ are not orthogonal; in particular, the product $\boldsymbol{r}_i \cdot \boldsymbol{r}_{i+d} \neq 0$ in general.

2.2.1 Linear flow fields in two dimensions

For a two-dimensional flow, M in Eq. (2.8) is:

$$M_{2D} = \begin{pmatrix} 0 & 0 & 1 & 0 \\ 0 & 0 & 0 & 1 \\ \frac{1}{\mathrm{St}}\frac{\partial u}{\partial x} & \frac{1}{\mathrm{St}}\frac{\partial u}{\partial y} & -\frac{1}{\mathrm{St}} & 0 \\ \frac{1}{\mathrm{St}}\frac{\partial v}{\partial x} & \frac{1}{\mathrm{St}}\frac{\partial v}{\partial y} & 0 & -\frac{1}{\mathrm{St}} \end{pmatrix}. \tag{2.17}$$

The characteristic polynomial for the eigenvalues of M_{2D} is:

$$\lambda^2\Big(\lambda + \frac{1}{\mathrm{St}}\Big)^2 - \frac{\lambda}{\mathrm{St}}\Big(\lambda + \frac{1}{\mathrm{St}}\Big)\Big(\frac{\partial u}{\partial x} + \frac{\partial v}{\partial y}\Big) + \frac{\mathcal{H}}{\mathrm{St}^2} = 0, \tag{2.18}$$

where $\mathcal{H}$ is defined as:

$$\mathcal{H} \equiv \Big(\frac{\partial u}{\partial x}\Big)\Big(\frac{\partial v}{\partial y}\Big) - \Big(\frac{\partial u}{\partial y}\Big)\Big(\frac{\partial v}{\partial x}\Big). \tag{2.19}$$

If the carrier flow is incompressible ($\nabla \cdot \boldsymbol{u} = 0$), the four eigenvalues of M_{2D} are:

$$\lambda_i = \frac{-1 \pm \sqrt{1 \pm 4\mathrm{St}\sqrt{-\mathcal{H}}}}{2\mathrm{St}}. \tag{2.20}$$

Example I: separation point type of flow

The incompressible flow near a separation point can be modelled by a linear strain field. The flow field is linear in the coordinates x and y. At the position of the particle (x_p, y_p), the velocities in horizontal and vertical direction are given by:

$$u = -Kx_p, \qquad v = Ky_p, \tag{2.21}$$

with $K \in \mathbb{R}^+$.

The eigenvalues can be obtained from Eq. (2.20), where $\mathcal{H} = -K^2$. If $\mathrm{St} \leq \{4K\}^{-1}$, then all eigenvalues are real:

$$\begin{aligned} \lambda_1 &= \frac{-1 + \sqrt{1 - 4\mathrm{St}K}}{2\mathrm{St}}, \\ \lambda_2 &= \frac{-1 + \sqrt{1 + 4\mathrm{St}K}}{2\mathrm{St}}, \\ \lambda_3 &= \frac{-1 - \sqrt{1 - 4\mathrm{St}K}}{2\mathrm{St}}, \\ \lambda_4 &= \frac{-1 - \sqrt{1 + 4\mathrm{St}K}}{2\mathrm{St}}. \end{aligned} \tag{2.22}$$

The corresponding right eigenvectors are:

$$\begin{aligned}
\boldsymbol{r}_1 &= [1, 0, \frac{-1 + \sqrt{1 - 4\mathrm{St}K}}{2\mathrm{St}}, 0]^T, \\
\boldsymbol{r}_2 &= [0, 1, 0, \frac{-1 + \sqrt{1 + 4\mathrm{St}K}}{2\mathrm{St}}]^T, \\
\boldsymbol{r}_3 &= [1, 0, \frac{-1 - \sqrt{1 - 4\mathrm{St}K}}{2\mathrm{St}}, 0]^T, \\
\boldsymbol{r}_4 &= [0, 1, 0, \frac{-1 - \sqrt{1 + 4\mathrm{St}K}}{2\mathrm{St}}]^T.
\end{aligned} \tag{2.23}$$

Finally, the constants a_i are found from imposing the initial conditions $x_p(0) = x_0$, $y_p(0) = y_0$, $u_p(0) = u_0$ and $v_p(0) = v_0$:

$$\begin{aligned}
a_1 &= \frac{x_o\lambda_3 - u_0}{\lambda_3 - \lambda_1}, \\
a_2 &= \frac{y_o\lambda_4 - v_0}{\lambda_4 - \lambda_2}, \\
a_3 &= \frac{x_o\lambda_1 - u_0}{\lambda_1 - \lambda_3}, \\
a_4 &= \frac{y_o\lambda_2 - v_0}{\lambda_2 - \lambda_3},
\end{aligned} \tag{2.24}$$

Insertion of Eq. (2.22), Eq. (2.23) and Eq. (2.24) in Eq. (2.10) yields the solution for $x_p(t)$, $y_p(t)$, $u_p(t)$ and $v_p(t)$.

Because only λ_2 is positive and all the other eigenvalues are negative, the particle motion at large times is dominated by a motion away from the origin, in the y-direction, for all initial conditions except $y_0 = 0$ and $v_0 = 0$.

If $\mathrm{St} > \{4K\}^{-1}$, then the following eigenvalues are obtained:

$$\begin{aligned}
\lambda_1 &= \frac{-1 + i\sqrt{4\mathrm{St}K - 1}}{2\mathrm{St}}, \\
\lambda_2 &= \frac{-1 + \sqrt{4\mathrm{St}K + 1}}{2\mathrm{St}}, \\
\lambda_3 &= \frac{-1 - i\sqrt{4\mathrm{St}K - 1}}{2\mathrm{St}}, \\
\lambda_4 &= \frac{-1 - \sqrt{4\mathrm{St}K + 1}}{2\mathrm{St}},
\end{aligned} \tag{2.25}$$

with corresponding right eigenvectors:

$$\begin{aligned}
\boldsymbol{r}_1 &= [1, 0, \frac{-1 + i\sqrt{4\mathrm{St}K - 1}}{2\mathrm{St}}, 0]^T, \\
\boldsymbol{r}_2 &= [0, 1, 0, \frac{-1 + \sqrt{4\mathrm{St}K + 1}}{2\mathrm{St}}]^T, \\
\boldsymbol{r}_3 &= [1, 0, \frac{-1 - i\sqrt{4\mathrm{St}K - 1}}{2\mathrm{St}}, 0]^T, \\
\boldsymbol{r}_4 &= [0, 1, 0, \frac{-1 - \sqrt{4\mathrm{St}K + 1}}{2\mathrm{St}}]^T.
\end{aligned} \tag{2.26}$$

The coefficients a_i are again given by Eq. (2.24).

The results for λ_2 and λ_4 have not changed compared to Eq. (2.22); this means that the particle trajectory will converge towards a motion in y-direction for large times also if $\mathrm{St} > \{4K\}^{-1}$. The eigenvalues λ_1 and λ_3, however, form a pair of complex conjugates with real part smaller than zero, and their corresponding eigenvectors point in the x-direction only. The physical significance of this result is, that a particle with $\mathrm{St} > \{4K\}^{-1}$ describes an oscillatory motion around the y-axis while converging to it [57].

In Fig. 2.1, we present the resulting particle trajectories for $\mathrm{St}K = 1$ and for $\mathrm{St}K = 1/10$. Indeed, we see that for the case $\mathrm{St}K = 1$, the particles cross the y-axis. The strict distinction between small particles with $\mathrm{St} \leq \{4K\}^{-1}$ and large particles with $\mathrm{St} > \{4K\}^{-1}$ may result in different behaviour in real flows in which the dominant eddy frequency is K. Small particles will follow fluid trajectories closely and stay with the eddy. In contrast, large particles move from one eddy to another.

Example II: solid body rotation

A solid-body rotation flow is characterized by a uniform, non-zero vorticity over the whole domain. The linear flow field at the position of the particle is given by:

$$u = -\Omega y_p, \qquad v = \Omega x_p. \tag{2.27}$$

The eigenvalues, obtained from Eq. (2.20) with $\mathcal{H} = \Omega^2$, are:

$$\begin{aligned}
\lambda_1 &= \frac{-1 + \sqrt{1 + 4i\mathrm{St}\Omega}}{2\mathrm{St}}, \\
\lambda_2 &= \frac{-1 + \sqrt{1 - 4i\mathrm{St}\Omega}}{2\mathrm{St}}, \\
\lambda_3 &= \frac{-1 - \sqrt{1 + 4i\mathrm{St}\Omega}}{2\mathrm{St}}, \\
\lambda_4 &= \frac{-1 - \sqrt{1 - 4i\mathrm{St}\Omega}}{2\mathrm{St}}.
\end{aligned} \tag{2.28}$$

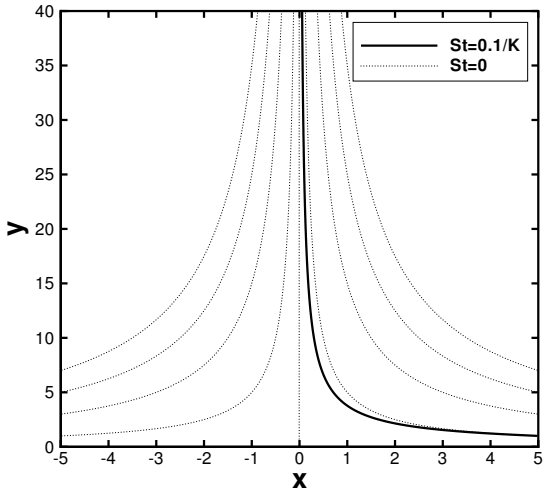

a)

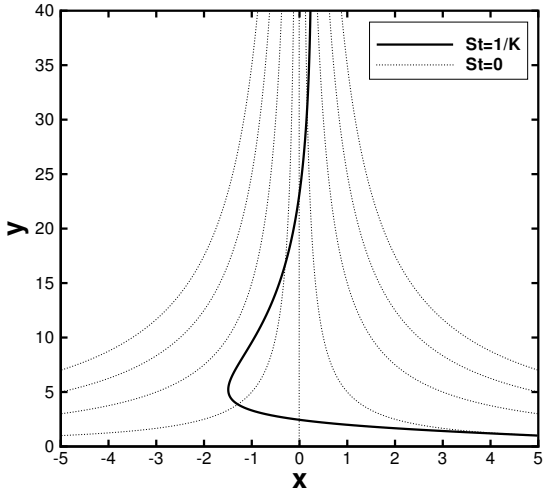

b)

FIGURE 2.1: *Trajectory of a heavy particle in a linear strain field, released at* $(x, y) = (5, 1)$. *Their initial velocity is equal to the local carrier flow velocity. The lines* $St = 0$ *correspond to trajectories of passive tracers (streamlines). a)* $St = 0.1/K$*; b)* $St = 1/K$.

Separation of the real and imaginary parts yields:

$$\begin{aligned}
\lambda_1 &= \frac{1}{2\mathrm{St}}(-1 + C_r + iC_i),\\
\lambda_2 &= \frac{1}{2\mathrm{St}}(-1 + C_r - iC_i),\\
\lambda_3 &= \frac{1}{2\mathrm{St}}(-1 - C_r - iC_i),\\
\lambda_4 &= \frac{1}{2\mathrm{St}}(-1 - C_r + iC_i),
\end{aligned} \tag{2.29}$$

where the variables C_r and C_i are defined as:

$$\begin{aligned}
C_r &\equiv \sqrt{\frac{1}{2} + \frac{1}{2}\sqrt{1 + 16\mathrm{St}^2\Omega^2}},\\
C_i &\equiv \sqrt{-\frac{1}{2} + \frac{1}{2}\sqrt{1 + 16\mathrm{St}^2\Omega^2}}.
\end{aligned}$$

The corresponding right eigenvectors are:

$$\begin{aligned}
\boldsymbol{r}_1 &= [i, 1, i\lambda_1, \lambda_1]^T,\\
\boldsymbol{r}_2 &= [1, i, \lambda_2, i\lambda_2]^T,\\
\boldsymbol{r}_3 &= [i, 1, i\lambda_3, \lambda_3]^T,\\
\boldsymbol{r}_4 &= [1, i, \lambda_4, i\lambda_4]^T.
\end{aligned} \tag{2.30}$$

The solution for the position and the velocity of a particle follow from Eq. (2.10), with the eigenvalues λ_k given by Eq. (2.29), the right eigenvectors $\boldsymbol{r}_k$ given by Eq. (2.30) and the coefficients a_k given by:

$$a_1 = \mathcal{A}_1 - i\mathcal{A}_2, \quad a_2 = \mathcal{A}_2 - i\mathcal{A}_1, \quad a_3 = \mathcal{A}_3 - i\mathcal{A}_4, \quad a_4 = \mathcal{A}_4 - i\mathcal{A}_3, \tag{2.31}$$

with:

$$\begin{aligned}
\mathcal{A}_1 &= \frac{1}{4(C_r^2 + C_i^2)}\Big(-C_i x_0 + \Big[C_r^2 + C_i^2 + C_r\Big]y_0 - 2\mathrm{St}C_i u_0 + 2\mathrm{St}C_r v_0\Big),\\
\mathcal{A}_2 &= \frac{1}{4(C_r^2 + C_i^2)}\Big(\Big[C_r^2 + C_i^2 + C_r\Big]x_0 + C_i y_0 + 2\mathrm{St}C_r u_0 + 2\mathrm{St}C_i v_0\Big),\\
\mathcal{A}_3 &= \frac{1}{4(C_r^2 + C_i^2)}\Big(C_i x_0 + \Big[C_r^2 + C_i^2 - C_r\Big]y_0 + 2\mathrm{St}C_i u_0 - 2\mathrm{St}C_r v_0\Big),\\
\mathcal{A}_4 &= \frac{1}{4(C_r^2 + C_i^2)}\Big(\Big[C_r^2 + C_i^2 - C_r\Big]x_0 - C_i y_0 - 2\mathrm{St}C_r u_0 - 2\mathrm{St}C_i v_0\Big),
\end{aligned} \tag{2.32}$$

where $x_0 = x_p(0)$, $y_0 = y_p(0)$, $u_0 = u_p(0)$ and $v_0 = v_p(0)$ denote again the initial condition. Since λ_1 and λ_2 have a positive real part, it is clear that a particle, regardless

of its initial condition, is eventually moving away from the center of rotation. (An exception should be made for a particle released in the origin with zero velocity; in this model there is no force to bring it into motion.)

The trajectories of two different heavy particles in a solid-body rotation flow field are presented in Fig. 2.2. As expected, the particles are expelled from the core region, and this effect becomes more important as the Stokes number increases.

2.3 Particle accumulation in any smooth flow

In this section, we investigate the motion of heavy particles in the $2d$-dimensional phase space of position and velocity, with d the dimension of physical space. Criteria are derived for the non-uniform concentration of heavy particles in physical space.

2.3.1 Phase space volume occupied by a group of particles

Following the example of Ottino [73], we consider a $2d$-dimensional 'volume' in phase space χ, occupied by a group of particles. This 'volume' in phase space can be denoted by $\mathcal{V}$:

$$\mathcal{V}(t) = \int_{\mathcal{V}(t)} \mathrm{d}\mathcal{V}. \tag{2.33}$$

The time development of $\mathcal{V}$ is:

$$\frac{\mathrm{d}\mathcal{V}}{\mathrm{d}t} = \frac{\mathrm{d}}{\mathrm{d}t} \int_{\mathcal{V}(t)} \mathrm{d}\mathcal{V}. \tag{2.34}$$

This can be expressed as:

$$\frac{\mathrm{d}\mathcal{V}}{\mathrm{d}t} = \int_{\mathcal{S}(t)} \frac{\mathrm{d}\chi_j}{\mathrm{d}t} n_j \mathrm{d}\mathcal{S}, \tag{2.35}$$

where $\mathcal{S}$ is the closed 'surface' of the 'volume' $\mathcal{V}$, with unit vector $\boldsymbol{n}$ the external normal to the surface. Using the theorem of Gauss, the following relation is obtained:

$$\frac{\mathrm{d}\mathcal{V}}{\mathrm{d}t} = \int_{\mathcal{V}(t)} \left(\frac{\partial}{\partial \chi_j} \frac{\mathrm{d}\chi_j}{\mathrm{d}t} \right) \mathrm{d}\mathcal{V}. \tag{2.36}$$

Inserting Eq. (2.6) yields:

$$\frac{\mathrm{d}\mathcal{V}}{\mathrm{d}t} = \int_{\mathcal{V}(t)} \left(\frac{\partial}{\partial \chi_j} F_j(\chi, t) \right) \mathrm{d}\mathcal{V}. \tag{2.37}$$

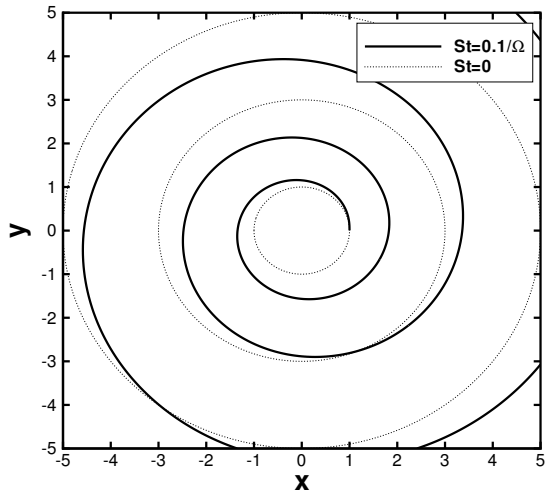

a)

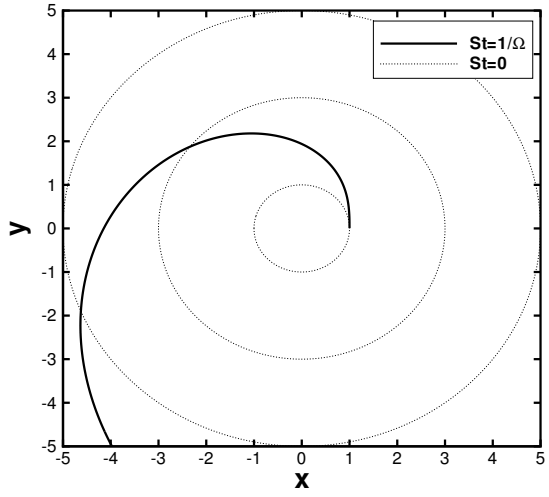

b)

FIGURE 2.2: *Trajectories of heavy particles in a solid body rotation flow, released at* $(x, y) = (1, 0)$*. Their initial velocity is equal to the local carrier flow velocity. The lines* $St = 0$ *correspond to trajectories of passive tracers (streamlines). a)* $St = 0.1/\Omega$*; b)* $St = 1/\Omega$*.*

From Eq. (2.5) it follows that $\partial F_j/\partial \chi_j = -d/\mathrm{St}$, regardless of the carrier flow field or gravity. Therefore, we obtain the following relation for $\mathcal{V}$:

$$\frac{\mathrm{d}\mathcal{V}}{\mathrm{d}t} = \frac{-d}{\mathrm{St}}\mathcal{V}. \tag{2.38}$$

with solution:

$$\mathcal{V}(t) = \mathcal{V}(0)\exp(\frac{-d}{\mathrm{St}}t). \tag{2.39}$$

It is clear that this system is dissipative, i.e. the $2d$-dimensional 'volume' occupied by a group of particles in phase space tends to zero exponentially [73].

The 'volume' $\mathcal{V}$ tends to zero faster for particles with smaller St. This can be explained by the observation that the effect of the initial conditions for the motion of smaller particles is not felt very long. Very large particles, on the other hand, continue their route through space almost independently of the flow.

Particle accumulation from all directions in phase space

Now that we know that the volume in phase space occupied by heavy particles decreases continuously, it is interesting to see how this volume contraction is established. In particular, we investigate whether it is possible that the volume in phase space contracts in all directions simultaneously. If this is possible, it means that in phase space a point can exist to which all particles in its vicinity are attracted.

First, we consider two particles that are very close to each other in phase space, i.e. both their positions and their velocities are almost the same. Their positions in phase space can be denoted by $\boldsymbol{\chi}_1$ and $\boldsymbol{\chi}_2$, respectively, so that their separation can be denoted by $\boldsymbol{R} \equiv \boldsymbol{\chi}_2 - \boldsymbol{\chi}_1$.

Using the equations of motion, Eq. (2.5), and assuming that the carrier flow field is smooth, i.e. $\partial u_i/\partial x_j$ exists, the time change of $\boldsymbol{R}$ can be determined to be (up to first order in $|\boldsymbol{R}|$):

$$\frac{\mathrm{d}}{\mathrm{d}t}\boldsymbol{R} = M\boldsymbol{R}, \tag{2.40}$$

where M has the same form as in Eq. (2.9). Due to the possible non-uniformity and unsteadiness of the carrier flow, the matrix M may be time-dependent. On the basis of Eq. (2.40) and Eq. (2.9), we can determine some general properties of particle accumulation in smooth flow fields.

If the separation between particles becomes smaller in all directions in phase space, the following equation must hold:

$$\frac{\mathrm{d}}{\mathrm{d}t}|\boldsymbol{R}|^2 < 0, \qquad \forall \boldsymbol{R}. \tag{2.41}$$

With Eq. (2.40) this can be rewritten to:

$$\frac{\mathrm{d}}{\mathrm{d}t}|\boldsymbol{R}|^2 = \frac{\mathrm{d}}{\mathrm{d}t}(\boldsymbol{R}\cdot\boldsymbol{R}) = 2\boldsymbol{R}\cdot\frac{\mathrm{d}\boldsymbol{R}}{\mathrm{d}t} = 2\boldsymbol{R}\cdot(M\boldsymbol{R}) < 0, \qquad \forall \boldsymbol{R}, \tag{2.42}$$

i.e., the matrix M is negative definite.

The matrix M is negative definite if and only if the symmetric matrix M_S, defined as:

$$M_S \equiv \frac{1}{2}(M + M^T) = \begin{pmatrix} [0]_d & \frac{1}{2}(\frac{1}{\mathrm{St}}[\sigma]_d + [I]_d) \\ \frac{1}{2}(\frac{1}{\mathrm{St}}[\sigma]_d + [I]_d) & -\frac{1}{\mathrm{St}}[I]_d \end{pmatrix}, \tag{2.43}$$

is negative definite, i.e. if all of its eigenvalues are negative. Due to the symmetry of M_S, all eigenvalues λ_S are real, and the corresponding eigenvectors are orthogonal [48]. The eigenvalues follow from:

$$0 = \det\begin{pmatrix} -\lambda_S[I]_d & \frac{1}{2}(\frac{1}{\mathrm{St}}[\sigma]_d + [I]_d) \\ \frac{1}{2}(\frac{1}{\mathrm{St}}[\sigma]_d + [I]_d) & -(\frac{1}{\mathrm{St}} + \lambda_S)[I]_d \end{pmatrix}. \tag{2.44}$$

This equation can be simplified by Gauss-Jordan transformations, so that the following matrix is obtained:

$$0 = \det\begin{pmatrix} -\lambda_S[I]_d & \frac{1}{2}(\frac{1}{\mathrm{St}}[\sigma]_d + [I]_d) \\ [0]_d & \frac{1}{\lambda_S}\Big(-(\frac{\lambda_S}{\mathrm{St}} + \lambda_S^2)[I]_d + [\bar{\Sigma}]_d\Big) \end{pmatrix}, \tag{2.45}$$

where $[\bar{\Sigma}]_d$ is a matrix defined by:

$$[\bar{\Sigma}]_d \equiv \frac{1}{4\mathrm{St}^2}[\sigma + \mathrm{St}I]_d[\sigma + \mathrm{St}I]_d^T. \tag{2.46}$$

By definition, $[\bar{\Sigma}]$ is a symmetric, positive definite matrix, so its eigenvalues are strictly positive and real. Eq. (2.45) shows that the d eigenvalues of $\bar{\Sigma}$, β say, are related to the eigenvalues λ_S of the matrix M_S by:

$$\lambda_S^2 + \frac{\lambda_S}{\mathrm{St}} = \beta. \tag{2.47}$$

Clearly, each eigenvalue β is associated to two eigenvalues λ_S of the matrix M_S:

$$\lambda_{S,i} = \frac{-1 + \sqrt{1 + 4\beta_i\mathrm{St}^2}}{2\mathrm{St}}, \qquad \lambda_{S,i+d} = \frac{-1 - \sqrt{1 + 4\beta_i\mathrm{St}^2}}{2\mathrm{St}}. \tag{2.48}$$

Since all β_i are real and larger than zero, half of the $2d$ eigenvalues λ_S are larger than 0. Hence, matrix M_S is not negative definite and thus a uniform accumulation of heavy particles (in all directions of the phase space) is not possible in any flow field. In summary, there is no possible flow field in which a group of heavy particles, distributed uniformly in a small volume of phase space, converges simultaneously to a single point in phase space; there is always at least one direction in which the separation between particles grows.

2.3.2 Accumulation of heavy particles in physical space

In many practical applications, it is more important to obtain information on the distribution of heavy particles in physical space rather than in phase space. Therefore, we determine a relationship between the concentration of particles in physical space and the properties of the flow field.

The separation vector $\boldsymbol{R}$, introduced in Eq. (2.40), can be expressed in terms of the eigenvectors $\boldsymbol{r}_k$ as follows:

$$\boldsymbol{R} = \sum_{k=1}^{2d} a_k \boldsymbol{r}_k, \tag{2.49}$$

where a_k are, possibly complex, coefficients. Then, the instantaneous change of the separation vector $\boldsymbol{R}$ is, according to Eq. (2.40):

$$\frac{\mathrm{d}}{\mathrm{d}t}\boldsymbol{R} = M\boldsymbol{R} = \sum_{k=1}^{2d} a_k \boldsymbol{r}_k \lambda_k, \tag{2.50}$$

where λ_k denote the eigenvalues of the separation matrix M, which are given by Eq. (2.15).

We now consider particles for which the Stokes number is small. The eigenvalues λ_k can then be approximated by:

$$\lambda_i = \alpha_i - \mathrm{St}\alpha_i^2 + O(\mathrm{St}^2), \qquad \lambda_{i+d} = -\frac{1}{\mathrm{St}} - \alpha_i + \mathrm{St}\alpha_i^2 + O(\mathrm{St}^2), \tag{2.51}$$

where the term $\sqrt{1 + 4\mathrm{St}\alpha_i}$ in Eq. (2.15) has been expanded in a Taylor series around $\mathrm{St} = 0$. It is noted that Eq. (2.51) is valid for any value of α_i, either real or complex.

If the Stokes number is sufficiently small so that $\mathrm{St}\alpha_i \ll 1$, then disturbances in the $\boldsymbol{r}_{i+d}$-direction are quickly damped out compared to disturbances in the $\boldsymbol{r}_i$-direction. Therefore, only disturbances in the $\boldsymbol{r}_i$-direction, with $1 \le i \le d$, can exist for a sufficiently long time:

$$\frac{\mathrm{d}}{\mathrm{d}t}\boldsymbol{R} = M\boldsymbol{R} \simeq \sum_{i=1}^{d} a_i \lambda_i \boldsymbol{r}_i. \tag{2.52}$$

Concentration of particles in two dimensions

We first study the particle accumulation in two dimensions, i.e. $d = 2$. A group of particles is supposed to occupy a relatively small area A, spanned by the two basis vectors $\boldsymbol{\delta}_1 = a_1\boldsymbol{s}_1$ and $\boldsymbol{\delta}_2 = a_2\boldsymbol{s}_2$, where $\boldsymbol{s}_i$ is related to $\boldsymbol{r}_i$ according to Eq. (2.16). The size of the area is $A = |\det(\boldsymbol{\delta}_1, \boldsymbol{\delta}_2)|$. In the course of time, the separation of the particles in A increases or decreases according to Eq. (2.52); in the two directions we have:

$$\frac{\mathrm{d}}{\mathrm{d}t}\boldsymbol{\delta}_1 = \lambda_1\boldsymbol{\delta}_1, \qquad \frac{\mathrm{d}}{\mathrm{d}t}\boldsymbol{\delta}_2 = \lambda_2\boldsymbol{\delta}_2. \tag{2.53}$$

As a consequence, the area A changes according to:

$$\frac{\mathrm{d}A}{\mathrm{d}t} = \frac{\mathrm{d}}{\mathrm{d}t}\Big|\det(\boldsymbol{\delta}_1, \boldsymbol{\delta}_2)\Big| = A(\lambda_1 + \lambda_2). \tag{2.54}$$

The area occupied by a number of particles is inversely proportional to the concentration of particles c: $c \sim 1/A$. Therefore, the time change of the concentration is:

$$\frac{\mathrm{d}c}{\mathrm{d}t} = -c(\lambda_1 + \lambda_2). \tag{2.55}$$

Inserting the expressions for λ_i from Eq. (2.51) yields:

$$\frac{\mathrm{d}c}{\mathrm{d}t} = -c\Big[\alpha_1 + \alpha_2 - \mathrm{St}(\alpha_1^2 + \alpha_2^2)\Big]. \tag{2.56}$$

This equation relates the change in concentration of particles in the case of small Stokes numbers explicitly to the eigenvalues of the rate-of-deformation tensor $[\sigma]_d$.

In an incompressible flow, $\alpha_1 + \alpha_2 = 0$, so that $\alpha_1 = -\alpha_2$; due to the fact that the elements of $[\sigma]_d$ are real, the value of α_1 is either purely real, or purely imaginary. Eq. (2.56) shows that the concentration of heavy particles increases in regions where α_1 is purely real (strain regions) and decreases in regions where α_1 is purely imaginary (vortex regions).

Concentration of particles in three dimensions

We now study the particle accumulation in three dimensions, i.e. $d = 3$. We consider an infinitesimally small volume V which encompasses a large number of particles. Suppose that V has the shape of a parallelepiped, spanned by the three basis vectors $\boldsymbol{\delta}_1 = a_1\boldsymbol{s}_1$, $\boldsymbol{\delta}_2 = a_2\boldsymbol{s}_2$ and $\boldsymbol{\delta}_3 = a_3\boldsymbol{s}_3$; again, $\boldsymbol{s}_i$ is related to $\boldsymbol{r}_i$ according to Eq. (2.16). The size of the volume is $V = |\boldsymbol{\delta}_1 \cdot (\boldsymbol{\delta}_2 \times \boldsymbol{\delta}_3)|$. In the course of time, the separation of the particles in V increases or decreases according to Eq. (2.52); in the three directions we have:

$$\frac{\mathrm{d}}{\mathrm{d}t}\boldsymbol{\delta}_1 = \lambda_1\boldsymbol{\delta}_1, \quad \frac{\mathrm{d}}{\mathrm{d}t}\boldsymbol{\delta}_2 = \lambda_2\boldsymbol{\delta}_2, \quad \frac{\mathrm{d}}{\mathrm{d}t}\boldsymbol{\delta}_3 = \lambda_3\boldsymbol{\delta}_3. \tag{2.57}$$

As a consequence, the volume of V, occupied by the particles, changes according to:

$$\frac{\mathrm{d}V}{\mathrm{d}t} = \frac{\mathrm{d}}{\mathrm{d}t}\Big|\det(\boldsymbol{\delta}_1, \boldsymbol{\delta}_2, \boldsymbol{\delta}_3)\Big| = \frac{\mathrm{d}}{\mathrm{d}t}\Big|\boldsymbol{\delta}_1 \cdot (\boldsymbol{\delta}_2 \times \boldsymbol{\delta}_3)\Big| = V(\lambda_1 + \lambda_2 + \lambda_3). \tag{2.58}$$

Because the volume occupied by a number of particles is inversely proportional to the concentration of particles c, the time change of the concentration then becomes:

$$\frac{\mathrm{d}c}{\mathrm{d}t} = -c(\lambda_1 + \lambda_2 + \lambda_3). \tag{2.59}$$

Inserting the expressions for λ_i from Eq. (2.51) yields:

$$\frac{\mathrm{d}c}{\mathrm{d}t} = -c\Big[\alpha_1 + \alpha_2 + \alpha_3 - \mathrm{St}(\alpha_1^2 + \alpha_2^2 + \alpha_3^2)\Big]. \tag{2.60}$$

In an incompressible flow, Eq. (2.60) reduces to:

$$\frac{\mathrm{d}c}{\mathrm{d}t} = c\mathrm{St}(\alpha_1^2 + \alpha_2^2 + \alpha_3^2). \tag{2.61}$$

In a three-dimensional incompressible flow, either all eigenvalues of the rate-of-deformation tensor are purely real with $\alpha_1 + \alpha_2 = -\alpha_3$, or only one eigenvalue is purely real and the other two are complex conjugates so that $\alpha_1 = \alpha_{Re} + i\alpha_{Im}$, $\alpha_2 = \alpha_{Re} - i\alpha_{Im}$ and $\alpha_3 = -2\alpha_{Re}$ [17]. Eq. (2.61) shows that small, heavy particles always diverge in regions where the eigenvalues of the rate-of-deformation tensor are complex and $\alpha_{Im}^2 > 3\alpha_{Re}^2$; this is typically the case in regions of high vorticity. In all other regions (typically, strain regions), small heavy particles are concentrated.

The result from Eq. (2.61) is in agreement with the result obtained by Maxey [59]. He found that the particle concentration in an incompressible flow, along the path of a group of small heavy particles which all have approximately the same velocity $\langle \boldsymbol{u}_p \rangle \simeq \boldsymbol{u} - \mathrm{St}\frac{\mathrm{D}\boldsymbol{u}}{\mathrm{D}t}$, develops as:

$$\frac{\mathrm{d}c}{\mathrm{d}t} = -c\nabla \cdot \langle \boldsymbol{u}_p \rangle \simeq c\mathrm{St}\nabla \cdot \left[(\boldsymbol{u} \cdot \nabla)\boldsymbol{u}\right] = c\mathrm{St}\left[e_{ij}e_{ij} - r_{ij}r_{ij}\right], \tag{2.62}$$

where the tensors e_{ij} and r_{ij} are defined as:

$$e_{ij} \equiv \frac{1}{2}\left(\frac{\partial u_i}{\partial x_j} + \frac{\partial u_j}{\partial x_i}\right), \qquad r_{ij} \equiv \frac{1}{2}\left(\frac{\partial u_i}{\partial x_j} - \frac{\partial u_j}{\partial x_i}\right).$$

Again, we see that the concentration of small heavy particles increases in regions of high strain (high $e_{ij}e_{ij}$) and decreases in regions of high vorticity (high $r_{ij}r_{ij}$).

It can be shown that Eq. (2.61) is exactly equivalent to Eq. (2.62). Nevertheless, it is advantageous to use the formulation presented in Eq. (2.60) instead of Eq. (2.62) for two reasons. Firstly, Eq. (2.60) can be easily extended to higher orders in St by taking into account more terms in the Taylor series in Eq. (2.51). Secondly, Eq. (2.60) is equally valid for both incompressible and compressible carrier flows, whereas Eq. (2.62) is valid for incompressible carrier flows only.

2.4 Conclusions

In the present chapter, the equations of motion of small, heavy particles in a non-uniform flow have been presented. Stokes drag and gravity were shown to be the dominant forces.

The particle equations of motion have been solved analytically for flow fields for which the velocity is a linear function of the spatial coordinates. The cases of a linear strain field and of a solid body rotation have been treated explicitly.

Close inspection of the particle equations of motion shows that the motion of heavy particles is described by a dissipative system. This means that the volume in phase space occupied by a group of heavy particles decreases continuously. It has been shown that the contraction of the volume in phase space is non-uniform, i.e. there is no possible flow in which heavy particles are forced towards a certain point from all directions in phase space.

For small Stokes numbers, heavy particles have been shown to always concentrate in strain regions, whereas they diverge in regions where the vorticity is sufficiently high. An explicit criterion for particle accumulation has been derived in terms of the eigenvalues of the local rate-of-deformation tensor $\partial u_i/\partial x_j$, for two-dimensional flows as well as for three-dimensional flows.

Part I

Heavy particles in vortex flows

HEAVY PARTICLES IN BOUNDED ONE-VORTEX FLOW

CHAPTER 3

In the present chapter, the motion of heavy particles in a vortex flow is investigated theoretically and numerically. The configuration of a single vortex in a closed circular domain is considered. Potential flow is assumed and the point vortex follows a circular path inside the domain. It is shown that small heavy particles may accumulate in elliptic regions of the flow, counter-rotating with respect to the vortex. When the Stokes number of a particle exceeds a threshold value that depends on the vortex configuration, however, all particles are expelled from the circular domain. A stability criterion for particle accumulation is derived analytically and verified by numerical results. The influence of gravity on the particle accumulation is discussed as well. Finally, the results of the potential flow model are compared to the results from a numerical solution of the full Navier-Stokes equations for laminar flow in two dimensions.

3.1 Introduction

Gas-particle and gas-condensate separators are widely used in industry [28], [29]. Their purpose is to separate small dust particles or small liquid droplets from gas flows. In general the separators consist of a cylindrical tube containing a region of high vorticity or a solid-body type of rotational flow field. In some applications, such as the gas-liquid separator described in section 1.2.3, the vorticity is concentrated in a slender helical vortex filament, generated upstream by some vortex generator. The goal of the present research is to determine the influence of such a coherent structure of vorticity on the motion of heavy particles.

The configuration of a slender helical vortex filament in a cylindrical tube is sketched in Fig. 3.1. The vortex filament is assumed to be so slender that the contribution due to the three-dimensionality of the filament may be neglected [2]. In this limit, the velocity field reduces to a superposition of a constant axial velocity U and a time-dependent two-dimensional flow in the cross-sectional plane, convected with velocity U, as sketched in Fig. 3.1. The two-dimensional flow is characterized by an eccentri-

cally placed point vortex in a circular domain.

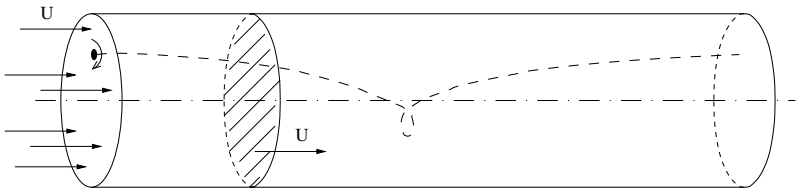

FIGURE 3.1: *Helical vortex filament in a gas-liquid separator. In the cross section indicated, the flow may be approximated by a point vortex placed in a closed circular domain.*

The motion of one point vortex in an inviscid flow in a closed circular domain has been considered already by Lamb [44], §155. The solution makes use of an image vortex placed outside the circular domain in order to satisfy the boundary condition on the wall. Due to the velocity induced by the image vortex, the vortex describes a steady circular motion. In a frame rotating with the vortex, the flow field is steady and the motion of passive tracers follows from a time-independent stream function.

The dynamics of heavy particles in dilute suspensions have received much attention in the past two decades. Various investigations (e.g. [21] and [60]), have reported the behavior of heavy particles in flows around fixed vortices. The general conclusion is that heavy particles are expelled from regions of high vorticity and tend to accumulate in regions of high strain; this conclusion is supported by our analysis in section 2.3. If the centrifugal motion from the vortex centers is balanced by another force such as gravity, a group of heavy particles may be attracted to a single trajectory. This has been shown to happen in a Burgers vortex [56] and in a plane mixing layer [26].

The motion of heavy particles in rotating two-dimensional flows has been investigated in the context of planet formation in the solar nebula (e.g. [15], [6]). The solar nebula is a collection of gas particles situated on a large disk, whose rotation is described by the laws of Kepler. If it is assumed that the turbulent flow in the solar nebula is approximately two-dimensional, large coherent vortex structures are likely to evolve. Bracco *et al.* [15] show that heavy particles tend to accumulate in large anticyclonic vortices, i.e. vortices with sign opposite to the major Keplerian rotation. Chavanis [16] analytically derived an estimate of the time it takes to capture a heavy particle in an anticyclonic vortex, by assuming the flow to be a superposition of a prescribed elliptic patch of uniform vorticity and a steadily rotating Keplerian disk; both the particle inertia and the gravitational influence of the star located in the center of the disk are taken into account. An overview of the motion of heavy particles in two-dimensional flows is provided by Provenzale [79], who pays attention to flows generated by a large number of point vortices on an infinite plane and to the case of

a distribution of finite vorticity on a Keplerian disk.

In the present chapter we investigate the motion of heavy particles in a closed circular domain containing one point vortex. The presence of the boundary results in a rotation of the flow field [68]. The focus is on the accumulation of particles due to their inertia in sufficiently dilute flows. In order to isolate the effect of the particle inertia, the simulations are based on a one-way coupling. A stability criterion for particle accumulation is derived and verified numerically.

This chapter is organized as follows. In section 3.2 we present the dynamical equations governing the motion of a point vortex in a closed circular domain, and we derive the stream function of the flow field induced by the vortex. In addition, the equations of motion for heavy particles are introduced. The numerical results of the motion of heavy particles in a circular domain containing one point vortex are presented in section 3.3 for the case of zero gravity, and in section 3.4 for the case of non-zero gravity. In order to quantify the influence of viscosity, the results for the potential flow model are compared to the solution of the full Navier-Stokes equations describing the viscous (laminar) flow in a circular domain containing a means to generate circulation; the results are presented in section 3.5. Finally, a summary and conclusions are given in section 3.6.

3.2 Physical-mathematical model

3.2.1 Potential flow field

Consider a closed circular domain with radius R, containing a potential flow generated by one point vortex. In the following, all variables are made dimensionless by choosing R as the characteristic length and the strength of the vortex Γ_1 as the characteristic circulation. The position of the vortex is given by its radial position r_1 and angle θ_1. An image vortex with strength -1 is placed on the position (r_1^{-1},θ_1) in order to satisfy the boundary condition of zero normal velocity at $r = 1$. Since the velocity field is divergence-free ($\nabla \cdot \boldsymbol{u} = 0$), in $2D$ the motion of passive tracers is governed by a stream function which plays the role of a Hamiltonian.

The stream function Ψ is conveniently described in polar coordinates:

$$\Psi(r,\theta) \equiv \left[\Psi_V(r,\theta,r_1,\theta_1) - \Psi_I(r,\theta,r_1,\theta_1)\right], \tag{3.1}$$

with:

$$\Psi_V(r,\theta,r_1,\theta_1) \equiv -\frac{1}{4\pi}\ln\left[r^2 + r_1^2 - 2rr_1\cos(\theta-\theta_1)\right], \tag{3.2}$$

and:

$$\Psi_I(r,\theta,r_1,\theta_1) \equiv \Psi_V(r,\theta,r_1^{-1},\theta_1). \tag{3.3}$$

The function $\Psi_V(r, \theta, r_1, \theta_1)$ represents the partial stream function associated with the vortex, whereas $\Psi_I(r, \theta, r_1, \theta_1)$ represents the partial stream function due to the image vortex. The velocity field is obtained from the canonical equations:

$$u_r = \frac{1}{r}\frac{\partial \Psi}{\partial \theta}, \quad u_\theta = -\frac{\partial \Psi}{\partial r}. \tag{3.4}$$

The motion of the point vortex itself is governed by Hamiltonian dynamics. The Hamiltonian H is:

$$H = \frac{1}{4\pi}\ln\left[1 - r_1^2\right]. \tag{3.5}$$

The velocity of the vortex is then obtained from the canonical equations:

$$\dot{r}_1 = \frac{1}{r_1}\frac{\partial H}{\partial \theta_1}, \quad r_1\dot{\theta}_1 = -\frac{\partial H}{\partial r_1}, \tag{3.6}$$

where the dots indicate differentiation with respect to time. As a result, the motion of the vortex is:

$$\dot{r_1} = 0, \quad \dot{\theta}_1 = \frac{1}{2\pi}\frac{1}{1 - r_1^2}, \tag{3.7}$$

which shows that the vortex moves on a circle with constant angular velocity; the period of the vortex motion is denoted by T:

$$T = 2\pi/\dot{\theta}_1 = 4\pi^2(1 - r_1^2). \tag{3.8}$$

We now choose a frame of reference that co-rotates with the vortex. Upon introducing $\phi \equiv \theta - \theta_1$, the stream function becomes:

$$\hat{\Psi}(r, \phi) \equiv \Psi(r, \phi + \theta_1) + \frac{1}{2}r^2\dot{\theta}_1, \tag{3.9}$$

with corresponding velocity components:

$$u_r = \frac{1}{r}\frac{\partial \hat{\Psi}}{\partial \phi}, \quad u_\phi = -\frac{\partial \hat{\Psi}}{\partial r}. \tag{3.10}$$

Inserting Eq. (3.1) and Eq. (3.9) into Eq. (3.10) results in:

$$\begin{aligned} u_r(r, \phi; r_1) &= -\frac{r_1 \sin\phi}{2\pi[r^2 + r_1^2 - 2rr_1\cos\phi]} + \frac{r_1 \sin\phi}{2\pi[1 + r^2r_1^2 - 2rr_1\cos\phi]}, \\ u_\phi(r, \phi; r_1) &= -r\dot{\theta}_1 + \frac{r - r_1\cos\phi}{2\pi[r^2 + r_1^2 - 2rr_1\cos\phi]} - \frac{rr_1^2 - r_1\cos\phi}{2\pi[1 + r^2r_1^2 - 2rr_1\cos\phi]}. \end{aligned} \tag{3.11}$$

Contour lines of the stream function $\hat{\Psi}$ are plotted in Fig. 3.2 for $r_1 = 0.5$ (see also [68], p. 135). Three stagnation points in the co-rotating frame can be distinguished:

E is an elliptic stagnation point, and H_1 and H_2 denote two hyperbolic stagnation points. The character of the stagnation point is determined by the Hessian of the stream function evaluated at the stagnation point, $\mathcal{H}_0$:

$$\begin{array}{lcl} \mathcal{H}_0 < 0 & \Leftrightarrow & \text{saddle point (hyperbolic point),} \\ \mathcal{H}_0 > 0 & \Leftrightarrow & \text{extremum (elliptic point).} \end{array} \tag{3.12}$$

The Hessian $\mathcal{H}$ is defined as

$$\mathcal{H} \equiv \left(\frac{\partial^2 \hat{\Psi}}{\partial \xi^2}\right)\left(\frac{\partial^2 \hat{\Psi}}{\partial \eta^2}\right) - \left(\frac{\partial^2 \hat{\Psi}}{\partial \xi \partial \eta}\right)^2, \quad (r,\theta) \neq (r_1,\theta_1), \tag{3.13}$$

where $\xi \equiv r\cos\phi$ and $\eta \equiv r\sin\phi$. With Eq. (3.9) and $\nabla^2\Psi = 0$, it follows that:

$$\mathcal{H} \equiv -\left(\frac{\partial^2 \Psi}{\partial x^2}\right)^2 - \left(\frac{\partial^2 \Psi}{\partial x \partial y}\right)^2 + \dot{\theta}_1^2, \tag{3.14}$$

where $x = r\cos\theta$ and $y = r\sin\theta$. Thus, in a fixed frame, $\mathcal{H} < 0$ everywhere, so that critical points can only be saddle points [3]. In a rotating frame, however, elliptic stagnation points do exist, provided $\dot{\theta}_1$ is sufficiently large. It can be shown that the rotation of the flow around an elliptic stagnation point is always opposite to the rotation of the frame; this is generally called anticyclonic motion [15], [79].

3.2.2 Equations of motion of heavy particles

The motion of the particles is described by Eq. (2.5). In the present chapter, we define the Stokes number and the Froude number using R as the characteristic length scale and Γ_1 as the characteristic circulation, so that:

$$\mathrm{St} = \frac{\tau_p \Gamma_1}{R^2}, \quad \mathrm{Fr} = \sqrt{\frac{\Gamma_1^2}{R^3|\boldsymbol{g}|}}. \tag{3.15}$$

Particles with $\mathrm{St} = 0$ react instantaneously to changes in the flow and act as passive tracers, whereas particles with $\mathrm{St} \to \infty$ are not affected by the flow field.

We rewrite the equations of motion, Eq. (2.5), in a rotating frame of reference:

$$\begin{aligned} \frac{\mathrm{d}\boldsymbol{\xi}_p}{\mathrm{d}t} &= \boldsymbol{v}_p, \\ \frac{\mathrm{d}\boldsymbol{v}_p}{\mathrm{d}t} &= \frac{1}{\mathrm{St}}(\boldsymbol{v} - \boldsymbol{v}_p) + \frac{1}{\mathrm{Fr}^2}\frac{\boldsymbol{g}(t)}{|\boldsymbol{g}|} + 2\dot{\theta}_1 J \boldsymbol{v}_p + \dot{\theta}_1^2 \boldsymbol{\xi}_p, \end{aligned} \tag{3.16}$$

where $\boldsymbol{\xi}_p$ and $\boldsymbol{v}_p$ denote the position and the velocity of the particle in the rotating frame, respectively; the matrix J is defined as:

$$J \equiv \begin{pmatrix} 0 & 1 \\ -1 & 0 \end{pmatrix}. \tag{3.17}$$

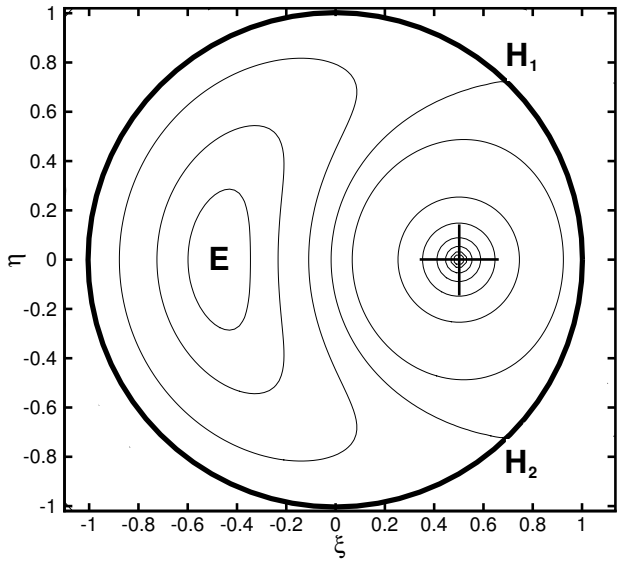

FIGURE 3.2: *Contour lines of stream function in a one-vortex system, plotted in the frame rotating with the vortex;* $r_1 = 0.5$. H_1 *and* H_2 *are hyperbolic stagnation points, and* E *is an elliptic stagnation point. For convenience, the position of the vortex,* $(\xi, \eta) = (0.5, 0)$*, is drawn as well.*

The two additional terms on the right hand side of Eq. (3.16), which both depend on the rotation rate $\dot{\theta}_1$, denote the Coriolis force and the centrifugal force, respectively.

We consider the trajectories of two particles in close proximity. The differences in position and velocity are denoted by $\delta\boldsymbol{\xi}_p$ and $\delta\boldsymbol{v}_p$, respectively. When the magnitude of the 4-dimensional separation vector $\boldsymbol{R} \equiv [\delta\boldsymbol{\xi}_p, \delta\boldsymbol{v}_p]^T$ is very small, the separation between the two trajectories can be expressed in the following form:

$$\frac{\mathrm{d}}{\mathrm{d}t}\boldsymbol{R}(t) = M\boldsymbol{R}(t), \tag{3.18}$$

with:

$$M = \begin{pmatrix} 0 & 0 & 1 & 0 \\ 0 & 0 & 0 & 1 \\ \frac{1}{\mathrm{St}}\frac{\partial^2\hat{\Psi}}{\partial\xi\partial\eta} + \dot{\theta}_1^2 & \frac{1}{\mathrm{St}}\frac{\partial^2\hat{\Psi}}{\partial\eta^2} & -\frac{1}{\mathrm{St}} & 2\dot{\theta}_1 \\ -\frac{1}{\mathrm{St}}\frac{\partial^2\hat{\Psi}}{\partial\xi^2} & -\frac{1}{\mathrm{St}}\frac{\partial^2\hat{\Psi}}{\partial\xi\partial\eta} + \dot{\theta}_1^2 & -2\dot{\theta}_1 & -\frac{1}{\mathrm{St}} \end{pmatrix}. \tag{3.19}$$

When all eigenvalues of the matrix M have negative real parts, we have $|\boldsymbol{R}(t)| \to 0$ for $t \to \infty$. This means that the trajectories of the two particles converge for sufficiently large times.

3.3 Heavy particles in bounded one-vortex flow with zero gravity

The equations of motion, Eq. (3.16), are solved numerically for each individual particle by using a fourth-order Runge-Kutta method. In the numerical integration we employ a series of decreasing values of the time step, where each next value is half of the previous value. When the difference between two subsequent solutions is below a certain preset level, the last obtained solution is considered sufficiently accurate. At the start of the simulation, the particles have the same velocity as the local gas flow. When a particle reaches the circular boundary, it is absorbed by the boundary. In the present section, we consider the case in which the gravity is neglected, i.e. Fr $\to \infty$; the case of non-zero gravity is discussed in section 3.4.

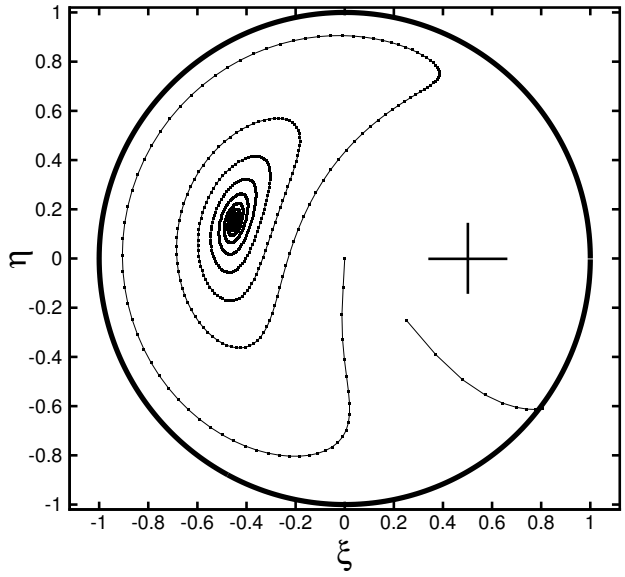

FIGURE 3.3: *Trajectories of two slipping particles in a one-vortex system plotted in the frame rotating with the vortex, for a time* $0 \leq t < 1000$ *(i.e. approximately* 34 *revolutions of the vortex);* $r_1 = 0.5$*,* $St = 0.5$*,* $Fr \to \infty$*. The initial positions of the two particles are:* $(\xi, \eta)\big|_{t=0} = (0, 0)$ *and* $(\xi, \eta)\big|_{t=0} = (0.25, -0.25)$*.*

In Fig. 3.3, two different particle trajectories, in the frame co-rotating with the vortex, are plotted for $r_1 = 0.5$. Two regimes of particle motion can be distinguished in Fig. 3.3: either a particle is quickly expelled from the circular domain and is absorbed by the boundary, or a particle is attracted to a point within the circular domain. Since

we are observing the flow in a frame co-rotating with the vortex, the attraction point in a fixed frame corresponds to a circular trajectory, in phase with the vortex motion.

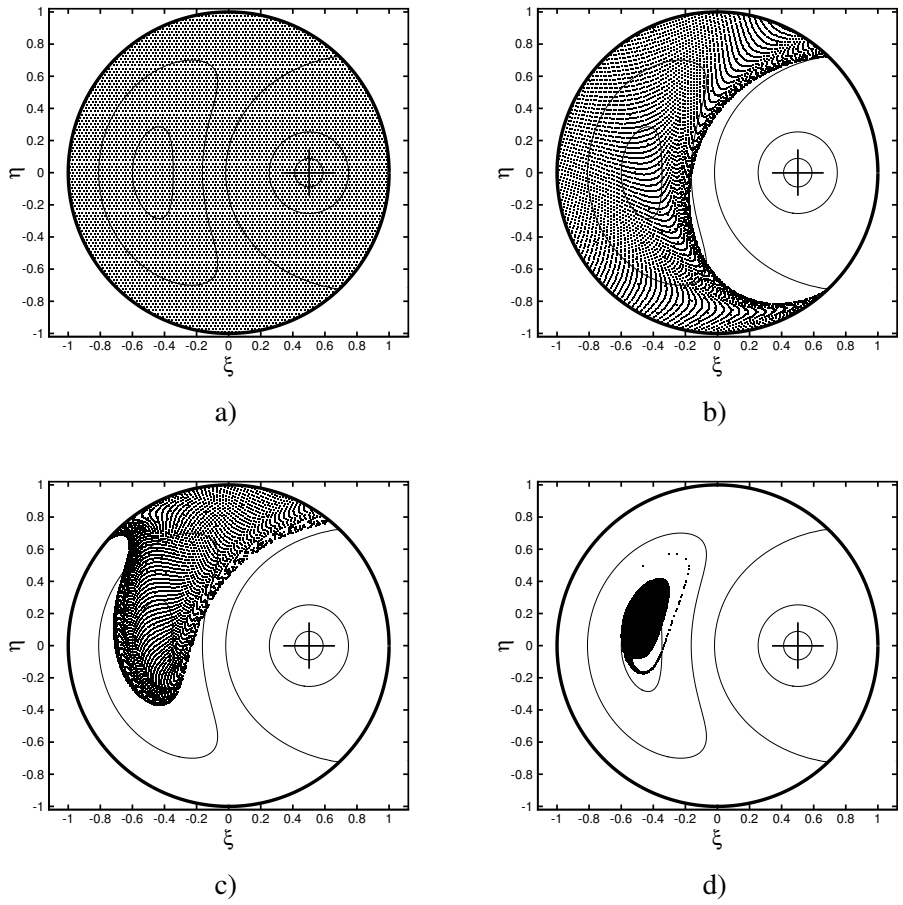

FIGURE 3.4: *Positions of heavy particles in one-vortex system, plotted in the frame rotating with the vortex;* $r_1 = 0.5$*,* $St = 0.5$*,* $Fr \to \infty$*: a)* $t = 0$*, b)* $t = 5$*, c)* $t = 25$*, d)* $t = 100$*. Streamlines of passive tracers are plotted as thin solid lines.*

In Fig. 3.4, the positions of 7495 particles are plotted for four instants in (dimensionless) time: $t = 0$, $t = 5$, $t = 25$, and $t = 100$, for Stokes number $\mathrm{St} = 0.5$. At the start of the simulation ($t = 0$), the particles are uniformly distributed on a mesh of equilateral triangles with sides of length 0.022. For large times, many particles are trapped in a region around the attraction point.

The particle trapping efficiency P_t, defined as:

$$P_t \equiv \frac{\text{(number of particles with } r < 1 \text{ after time } t)}{\text{(total number of initially uniformly distributed particles)}} \times 100\%, \qquad (3.20)$$

is plotted in Fig. 3.5, for $r_1 = 0.5$ and five different values of t which are expressed in terms of the period of the vortex motion T, see Eq. (3.8). Note that the separation efficiency equals $100\% - P_t$. The particle trapping efficiency gradually decreases during the first two revolutions of the vortex. After that a steady state is reached in which more than 70% of the particles are trapped if St $\lesssim 0.5$. If, however, St $\gtrsim 2.0$, no particles are trapped at all and all particles eventually reach te wall.

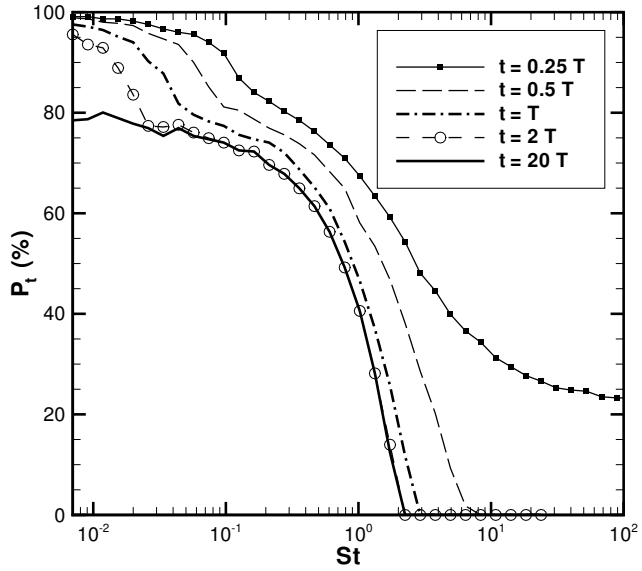

FIGURE 3.5: *Percentage of trapped particles in a one-vortex system P_t as a function of St, after five values of dimensionless time: $t = 0.25T$, $t = 0.5T$, $t = T$, $t = 2T$ and $t = 20T$; $r_1 = 0.5$, $Fr \to \infty$.*

The value of P_t for $t \to \infty$ is shown in Fig. 3.6, for three different configurations of bounded one-vortex flow: $r_1 = 0.3$, $r_1 = 0.5$, and $r_1 = 0.7$. Fig. 3.6 shows that the particle trapping phenomenon becomes more important for larger values of the vortex position r_1 and for smaller values of the Stokes number. For sufficiently large values of the Stokes number $P_\infty = 0$, i.e. trapping does not occur.

For particle accumulation to occur, two conditions must be met:

(i) a fixed point must exist, and

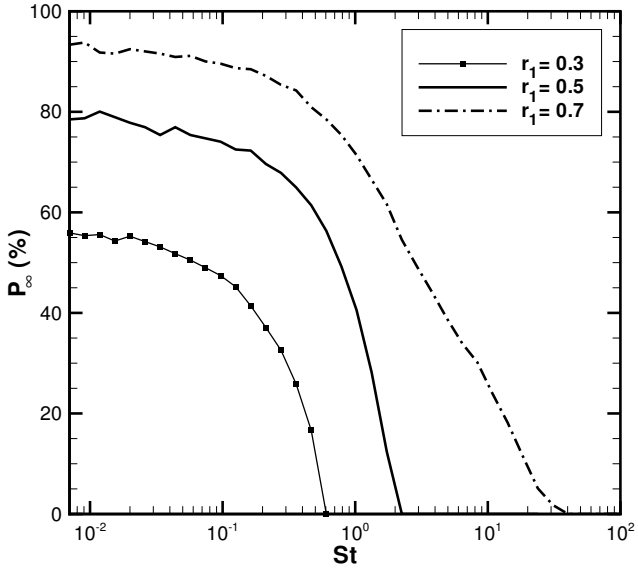

FIGURE 3.6: *Percentage of trapped particles in a one-vortex system for $t \to \infty$ as a function of St, for three different vortex positions: $r_1 = 0.3$, $r_1 = 0.5$ and $r_1 = 0.7$; $Fr \to \infty$.*

(ii) the fixed point must be stable.

In the remainder of this section, these two conditions are investigated.

3.3.1 Location of fixed points

For the case without effects of gravity, Eq. (3.16) becomes:

$$\frac{\mathrm{d}\boldsymbol{\xi}_p}{\mathrm{d}t} = \boldsymbol{v}_p,$$
$$\frac{\mathrm{d}\boldsymbol{v}_p}{\mathrm{d}t} = \frac{1}{\mathrm{St}}(\boldsymbol{v} - \boldsymbol{v}_p) + 2\dot{\theta}_1 J\boldsymbol{v}_p + \dot{\theta}_1^2\boldsymbol{\xi}_p. \tag{3.21}$$

The velocity field of the gas $\boldsymbol{v}$ is time-independent in this co-rotating frame. In a fixed point, say $\boldsymbol{\xi}^*$, we have $\boldsymbol{v}_p = 0$, and the Stokes drag balances the centrifugal acceleration force:

$$\boldsymbol{v}(\boldsymbol{\xi}^*) + \mathrm{St}\,\dot{\theta}_1^2\boldsymbol{\xi}^* = 0. \tag{3.22}$$

Writing $\xi^* = r^*\cos\phi^*$ and $\eta^* = r^*\sin\phi^*$, we have for the velocity components in ϕ and r direction, respectively:

$$u_\phi(r^*, \phi^*; r_1) = 0, \tag{3.23}$$
$$u_r(r^*, \phi^*; r_1) = -\mathrm{St}\,\dot{\theta}_1^2 r^*. \tag{3.24}$$

For given r_1 and St, these two equations can be solved for r^* and ϕ^*.

To facilitate the actual computation of (r^*, ϕ^*) for a given r_1, it is convenient to solve Eq. (3.23) for $\cos\phi^*$ for a range of values of $0 < r^* < 1$, by using Eq. (3.11):

$$\cos\phi^* = \frac{-b \pm \sqrt{b^2 - 4ac}}{2a}, \tag{3.25}$$

where:

$$a = -8\pi\dot{\theta}_1 r_1^2 r^{*3}, \tag{3.26}$$

$$b = 4\pi\dot{\theta}_1(r_1 r^{*4} + r_1^3 r^{*2} + r_1 r^{*2} + r_1^3 r^{*4}) + r_1^3 - r_1 + r_1^3 r^{*2} - r_1 r^{*2}, \tag{3.27}$$

$$c = -2\pi\dot{\theta}_1(r^{*3} + r_1^2 r^* + r_1^2 r^{*5} + r_1^4 r^{*3}) + r^* - r_1^4 r^*. \tag{3.28}$$

Thus, for each r^* we find either zero, one or two solutions for $\cos\phi^*$. The Stokes number corresponding to each combination of (r^*, ϕ^*) is then found from Eq. (3.24). The position of fixed points is presented in Fig. 3.7 for $r_1 = 0.5$, together with data obtained from numerical simulations for St = 0.1, St = 0.3, St = 0.6, and St = 0.9. Excellent agreement is obtained between results from the above analysis and data from the trajectories.

For small Stokes numbers, the distance of the fixed point with respect to the stagnation point can be approximated in closed form. From Eq. (3.22), it follows that:

$$\lim_{\mathrm{St}\downarrow 0} |\boldsymbol{\xi}^* - \boldsymbol{\xi}_0| = 0, \tag{3.29}$$

where $\boldsymbol{\xi}_0$ is a stagnation point of the flow. This must be the elliptic stagnation point situated on the negative ξ-axis (point E in Fig. 3.2), since the hyperbolic stagnation points (i.e. saddle points of the stream function) are unstable which is shown in the next section. Upon using the fact that $\partial^2\hat{\Psi}/\partial\xi\partial\eta\big|_{\boldsymbol{\xi}_0} = 0$, the ξ component of Eq. (3.22) becomes:

$$\left(\frac{\partial^2\hat{\Psi}}{\partial\eta^2}\bigg|_{\boldsymbol{\xi}_0}\right)(\eta^* - \eta_0) + \mathrm{St}\,\dot{\theta}_1^2\xi_0 + O(\mathrm{St}^2) = 0, \tag{3.30}$$

and it follows that:

$$\Delta \equiv |\boldsymbol{\xi}^* - \boldsymbol{\xi}_0| = \mathrm{St}\dot{\theta}_1^2|\boldsymbol{\xi}_0|\left(\frac{\partial^2\hat{\Psi}}{\partial\eta^2}\bigg|_{\boldsymbol{\xi}_0}\right)^{-1} + O(\mathrm{St}^2). \tag{3.31}$$

The physical reason for this is that larger particles (larger Stokes number) will slip more with respect to the carrier flow than smaller particles (smaller Stokes number). In order to balance the larger centrifugal force with the drag force, the fixed point needs to be situated further away from the elliptic point, where the carrier flow velocity is larger.

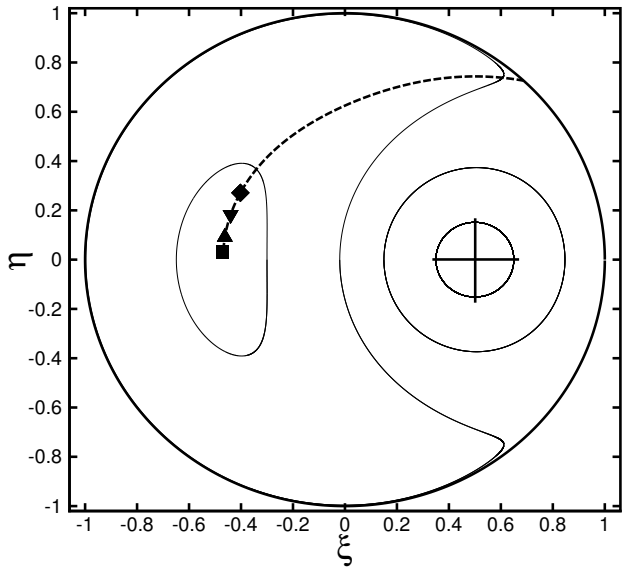

FIGURE 3.7: *Position of fixed points in a one-vortex system plotted in the frame rotating with the vortex, obtained from numerical simulations;* $r_1 = 0.5$, $Fr \to \infty$; ■: $St = 0.1$, ▲: $St = 0.3$, ▼: $St = 0.6$, ♦: $St = 0.9$. *The dashed line depicts the locations of fixed points obtained analytically from Eq. (3.23) and Eq. (3.24). The thin solid lines are streamlines.*

We have compared the values of Δ obtained from the approximation given in Eq. (3.31) with the exact values based on solution of Eq. (3.23) and Eq. (3.24). The deviation between the two solutions is plotted in Fig. 3.8 as a function of St for three different values of r_1. Indeed, for small Stokes numbers the error is relatively small for all three vortex positions considered, so the approximation presented in Eq. (3.31) is accurate. Moreover, the error tends to zero as $\mathrm{St} \downarrow 0$, confirming the consistency of the approximation.

3.3.2 Stability of fixed points

In this section the stability of the fixed point $\boldsymbol{\xi}^*$ is assessed by means of a linear stability analysis. When the particle is sufficiently close to the attraction point, the equation of motion, Eq. (3.16), can be approximated by:

$$\frac{\mathrm{d}}{\mathrm{d}t}\boldsymbol{R}^*(t) = M^*\boldsymbol{R}^*(t), \tag{3.32}$$

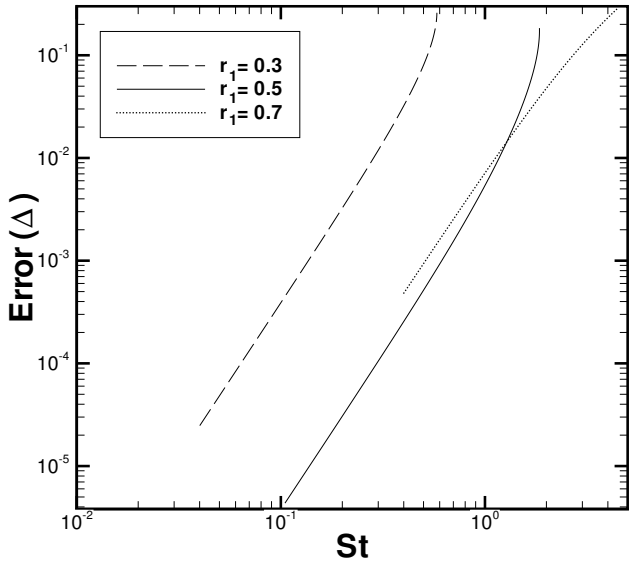

FIGURE 3.8: *Difference between the distance* Δ *obtained from the approximation given in equation Eq. (3.31) and the exact value, as a function of the Stokes number.*

where $\boldsymbol{R}^*$ is a vector in $\mathbb{R}^4$ denoting the separation between the particle and the fixed point in phase space:

$$\boldsymbol{R}^* \equiv [\boldsymbol{\xi}_p - \boldsymbol{\xi}^*, \boldsymbol{v}_p]^T, \tag{3.33}$$

and M^* is the matrix M defined by Eq. (3.19), evaluated at $\boldsymbol{\xi}^*$. In the present case of a steadily rotating vortex, the matrix M^* is independent of time. When the real parts of all eigenvalues $\lambda_1, \ldots, \lambda_4$ of M^* are negative, then $|\boldsymbol{R}^*| \to 0$ for $t \to \infty$, and the fixed point $\boldsymbol{\xi}^*$ is an attraction point. Hence, we define a stable fixed point as a fixed point which satisfies:

$$\max_k Re(\lambda_k) < 0, \quad \text{for } k = 1, \ldots, 4. \tag{3.34}$$

The eigenvalues λ_k are the roots of the characteristic polynomial for the eigenvalues of M^*:

$$\mathrm{St}^2\lambda^4 + 2\mathrm{St}\lambda^3 + (2\mathrm{St}^2\dot{\theta}_1^2 + 1)\lambda^2 + 2\mathrm{St}\dot{\theta}_1^2\lambda + \mathrm{St}^2\dot{\theta}_1^4 + \mathcal{H}^* = 0, \tag{3.35}$$

where $\mathcal{H}^* = \mathcal{H}(r^*, \phi^*; r_1, \mathrm{St})$ is the Hessian defined in Eq. (3.13), evaluated at the fixed point $\boldsymbol{\xi}^*$. In the derivation, it has been used that $\nabla^2\hat{\Psi} = 2\dot{\theta}_1$. The solutions of Eq. (3.35) are:

$$\lambda_{1,2,3,4} = \frac{-1 \pm \sqrt{1 - 4\dot{\theta}_1^2\mathrm{St}^2 \pm 4i\mathrm{St}\sqrt{\mathcal{H}^*}}}{2\mathrm{St}}. \tag{3.36}$$

We start to analyze the eigenvalues in the limit of $\mathrm{St} \downarrow 0$, and expand Eq. (3.36):

$$\lambda_{1,2,3,4} = \frac{-1 \pm 1}{2\mathrm{St}} + \mathrm{St}(\mathcal{H}^* - \dot{\theta}_1^2) \pm i\sqrt{\mathcal{H}^*} + O(\mathrm{St}^2). \tag{3.37}$$

In the previous section we found that $|\boldsymbol{\xi}^* - \boldsymbol{\xi}_0| = O(\mathrm{St})$, hence $\mathcal{H}^* = \mathcal{H}_0 + O(\mathrm{St})$, and:

$$\lambda_{1,2,3,4} = \frac{-1 \pm 1}{2\mathrm{St}} + \mathrm{St}(\mathcal{H}_0 - \dot{\theta}_1^2) \pm i\sqrt{\mathcal{H}_0} + iO(\mathrm{St}) + O(\mathrm{St}^2). \tag{3.38}$$

We assume that the fixed point at hand belongs to a curve of stable fixed points $\boldsymbol{\xi}^*(\mathrm{St}; r_1)$ with $\boldsymbol{\xi}^*(0; r_1) = \boldsymbol{\xi}_0(r_1)$, i.e., when $\mathrm{St} \downarrow 0$ the fixed point tends to a stagnation point. If $\mathcal{H}_0 < 0$ then $i\sqrt{\mathcal{H}_0} \in \mathbb{R}$ and the fixed point cannot be stable for $\mathrm{St} \downarrow 0$. Therefore, we require $\mathcal{H}_0 > 0$ as a necessary condition, i.e., the stagnation point must be elliptic. Furthermore, from Eq. (3.14) we observe that $\left(\mathcal{H}^* - \dot{\theta}_1^2\right) < 0$, and therefore the condition $\mathcal{H}_0 > 0$ is also sufficient for the fixed point to be stable. It is noted that the real parts of the eigenvalues, if all negative, describe the rate at which a particle moves towards the fixed point, which is apparently linear in the Stokes number. Therefore, the particle trapping time is inversely proportional to the Stokes number.

We continue by analyzing the eigenvalues for arbitrary values of the Stokes number. Upon definition of the following two variables:

$$A \equiv 1 - 4\dot{\theta}_1^2\mathrm{St}^2, \quad B \equiv 4\mathrm{St}\sqrt{|\mathcal{H}^*|}, \tag{3.39}$$

we observe that:

$$\max_k Re(\lambda_k) = \begin{cases} \frac{-1+\sqrt{\frac{1}{2}A+\frac{1}{2}\sqrt{A^2+B^2}}}{2\mathrm{St}}, & \mathcal{H}^* > 0, \\ -\frac{1}{2\mathrm{St}}, & \mathcal{H}^* < 0 \quad A+B < 0, \\ \frac{-1+\sqrt{A+B}}{2\mathrm{St}}, & \mathcal{H}^* < 0 \quad A+B > 0. \end{cases} \tag{3.40}$$

From these observations we derive the following sufficient stability conditions:

$$\mathcal{H}^* < 0 \text{ and } A + B < 1 \quad \Rightarrow \quad \max_k Re(\lambda_k) < 0, \tag{3.41}$$

$$\mathcal{H}^* > 0 \text{ and } A + \sqrt{A^2 + B^2} < 2 \quad \Rightarrow \quad \max_k Re(\lambda_k) < 0. \tag{3.42}$$

Finally, we determine $\mathrm{St}_{cr}(r_1)$, the maximum value of St for which a stable fixed point can be found. For given r_1 we identify the set $\mu(r_1)$ of points (r_1, r^*) where fixed points are stable, i.e. where $\max_k Re(\lambda_k(r_1, r^*)) < 0$. Then, we determine the maximum value of the Stokes number over the set $\mu(r_1)$; this is $\mathrm{St}_{cr}(r_1)$. We note that for each (r_1, r^*) one finds two values for $\cos\phi^*$ by Eq. (3.25). Whenever both values

lead to stable fixed points, we take into account the value that results in the largest value of St.

The critical Stokes number can also be determined numerically by repeating the simulation of particles for a wide range of Stokes numbers at a given r_1: the smallest value of the Stokes number for which no trapping takes place is $\mathrm{St}_{cr}(r_1)$.

The numerically obtained data set for St_{cr} is compared to the exact formulation in Fig. 3.9. For $r_1 > 0.6$, the critical Stokes number becomes infinite according to the exact formulation. In the numerical simulations, however, the critical Stokes number remains finite, although it increases very quickly as $r_1 > 0.6$. The reason for the deviation of the numerical results from the exact ones is that, for a finite number of particles in phase space (position *and* velocity), there may be no particles close enough to the attraction point. Still, it is clear from the exact result for St_{cr} that small heavy particles may always accumulate inside the circular domain, and that this phenomenon becomes more important as r_1 increases.

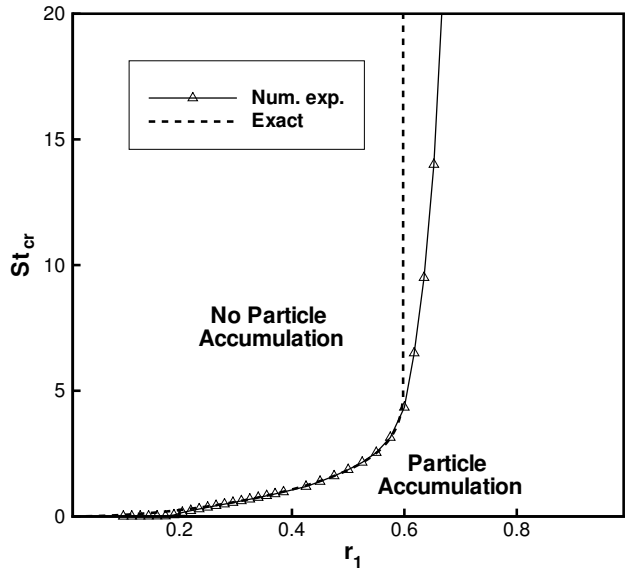

FIGURE 3.9: *Critical Stokes number as a function of the vortex position r_1; the solid line with small triangles is the result of numerical experiments, the dashed line is determined from Eq. (3.36).*

The stability criterion derived in Eq. (3.36) is evidently not restricted to the flow induced by a point vortex in a circular domain. It can be applied to any incompressible flow, as long as it is steady in some steadily rotating frame of reference. Examples

of this comprise the motion of vortices on a regular polygon on an infinite plane, the viscous flow solution in a steadily rotating frame presented in section 3.5, or an approximation of the flow field on a Keplerian disk as given by Chavanis [16]. Chavanis prescribes an anticyclonic vortex region a priori; in our case, the elliptic island is formed naturally just by the presence of a vortex inside a circular boundary.

3.4 Heavy particles in bounded one-vortex flow with non-zero gravity

In the present section, we study the particle motion in a one-vortex flow when gravity is not neglected, i.e. the Froude number is finite. We first investigate whether heavy particles accumulate in that situation, and we determine the influence of the Froude number on particle accumulation quantitatively.

Fig. 3.10a) shows two different particle trajectories in the frame co-rotating with the vortex for $r_1 = 0.5$. The Stokes number is 0.5 and the Froude number is 10. Just like in Fig. 3.3, two regimes of particle motion can be distinguished: either a particle is quickly expelled from the circular domain and is absorbed by the wall, or a particle remains within the circular domain.

There is, however, one important difference with respect to the zero-gravity case: the attraction trajectory is not a fixed point in the rotating frame, but instead it is a point moving periodically with period T of the vortex motion. This becomes clear from Fig. 3.10b) where the position of the particle is only plotted at the moments that the vortex crosses the positive x-axis: the particle approaches one single point.

In Fig. 3.11, the positions of a group of initially uniformly distributed particles are plotted at four instants in time; the Stokes number is 0.5, and the Froude number is 10. At time $t = 0$, the vortex is placed at position $(x, y) = (0.5, 0)$ and the gravity vector is directed in the negative y-direction. It is clear that the result in Fig. 3.11 is very similar to Fig. 3.4, where the same case is treated but with $\mathrm{Fr} \to \infty$ instead of $\mathrm{Fr} = 10$: again a large number of particles accumulate in the region opposite of the vortex.

In the following section, we first determine the position of the attraction point in the course of time. Subsequently, the stability of the moving attraction point is proven for small Stokes number and large Froude number.

3.4.1 Trajectory of moving attraction point

In the present section, we determine the trajectory of the moving attraction point. For the sake of simplicity, we assume the gravity vector to be relatively small in comparison to the other forces acting on a heavy particle. More precisely, we assume that $0 < \mathrm{Fr}^{-2} \ll 1$.

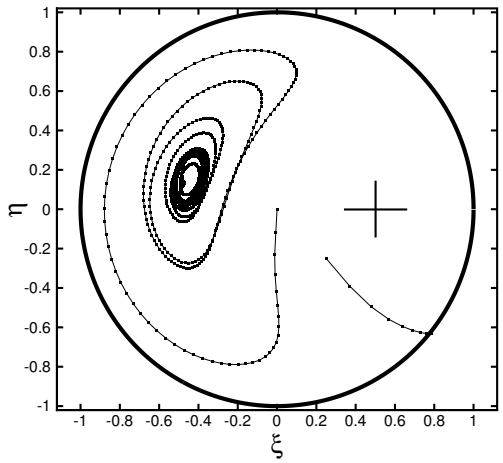

a)

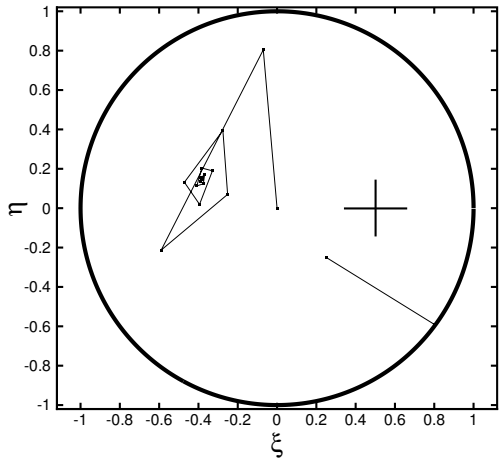

b)

FIGURE 3.10: *Trajectories of two slipping particles in one-vortex system with non-zero gravity, plotted in the frame rotating with the vortex;* $r_1 = 0.5$*;* $St = 0.5$*,* $Fr = 10$*. The initial positions of the two particles are:* $(\xi,\eta)\big|_{t=0} = (0,0)$ *and* $(\xi,\eta)\big|_{t=0} = (0.25,-0.25)$*. a) Positions of the two particles in the course of time. b) Position of the two particles only plotted at the moments that the vortex passes the positive x-axis; thus, these are Poincaré sections with period* T*.*

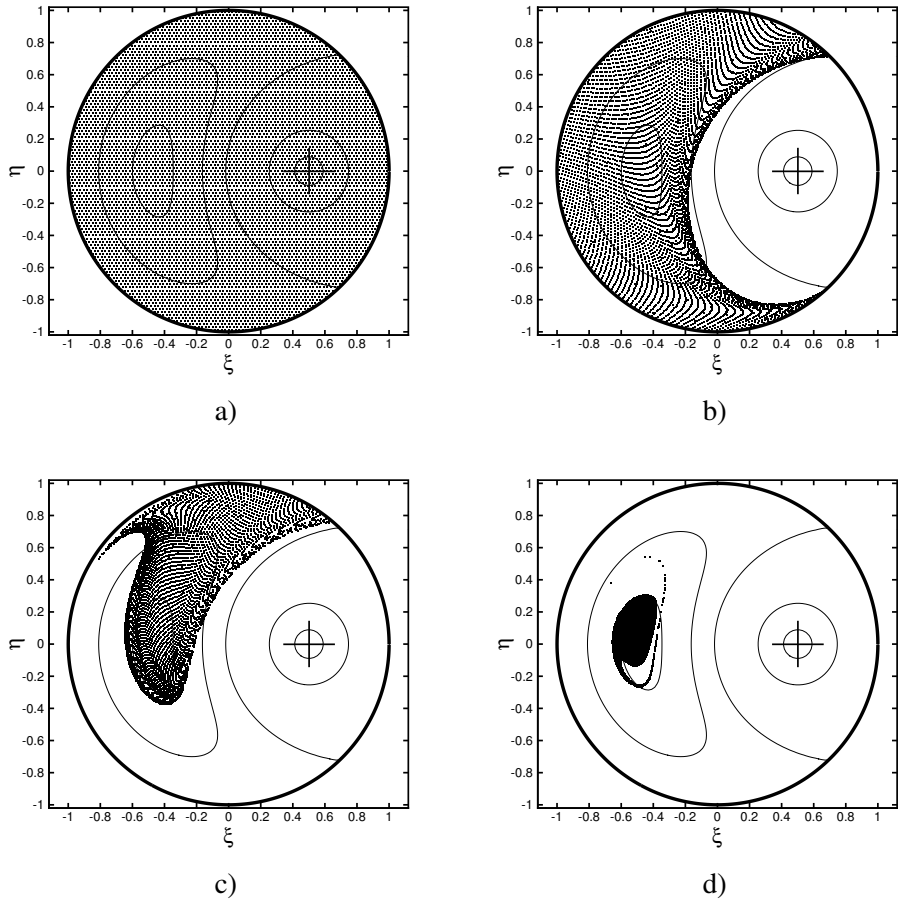

FIGURE 3.11: *Positions of heavy particles in one-vortex system with non-zero gravity, plotted in the frame rotating with the vortex;* $r_1 = 0.5$*,* $St = 0.5$*,* $Fr = 10$*: a)* $t = 0$*, b)* $t = 5$*, c)* $t = 25$*, d)* $t = 100$*. Streamlines are plotted as thin solid lines.*

We start this analysis from the equations of motion, Eq. (3.16), and determine an equilibrium trajectory in the corotating frame. Let the equilibrium trajectory be denoted by $\boldsymbol{\xi}^*(t)$. This can be written as $\boldsymbol{\xi}^*(t) = \boldsymbol{\xi}^*_\infty + \boldsymbol{h}(t)$, where $\boldsymbol{\xi}^*_\infty$ is the fixed point in the corotating frame in the case of zero-gravity ($\mathrm{Fr} \to \infty$), see Eq. (3.22). A Taylor expansion up to first order of the carrier flow field around $\boldsymbol{\xi}^*_\infty$ allows Eq. (3.16) to be rewritten in terms of $\boldsymbol{h}(t)$:

$$\begin{aligned} \frac{\mathrm{d}\boldsymbol{h}}{\mathrm{d}t} &= \boldsymbol{v}_p, \\ \frac{\mathrm{d}\boldsymbol{v}_p}{\mathrm{d}t} &= \frac{1}{\mathrm{St}}(\boldsymbol{h}\cdot\nabla\boldsymbol{v} - \boldsymbol{v}_p) + \frac{1}{\mathrm{Fr}^2}\frac{\boldsymbol{g}(t)}{|\boldsymbol{g}|} + 2\dot{\theta}_1 J\boldsymbol{v}_p + \dot{\theta}_1^2\boldsymbol{h}. \end{aligned} \tag{3.43}$$

In a frame of reference rotating steadily with angular velocity $\dot{\theta}_1$, the gravity vector takes the following form:

$$\frac{1}{\mathrm{Fr}^2}\frac{\boldsymbol{g}(t)}{|\boldsymbol{g}|} = \frac{1}{\mathrm{Fr}^2}\begin{pmatrix} -\sin(\dot{\theta}_1 t) \\ -\cos(\dot{\theta}_1 t) \end{pmatrix}. \tag{3.44}$$

We try the following solution for $\boldsymbol{h}(t)$:

$$\boldsymbol{h}(t) = \boldsymbol{p}\sin(\dot{\theta}_1 t) + \boldsymbol{q}\cos(\dot{\theta}_1 t). \tag{3.45}$$

It is noted that the trajectory of $\boldsymbol{h}(t)$ is an ellipse. Inserting Eq. (3.44) and Eq. (3.45) in Eq. (3.43), and separating the sine and the cosine parts results in:

$$\begin{aligned} \mathrm{St}^{-1}[B]\boldsymbol{p} + \dot{\theta}_1[A]\boldsymbol{q} &= \mathrm{Fr}^{-2}\begin{pmatrix} 1 \\ 0 \end{pmatrix}, \\ \mathrm{St}^{-1}[B]\boldsymbol{q} - \dot{\theta}_1[A]\boldsymbol{p} &= \mathrm{Fr}^{-2}\begin{pmatrix} 0 \\ 1 \end{pmatrix}, \end{aligned} \tag{3.46}$$

where the matrices $[A]$ and $[B]$ are defined as:

$$[A] \equiv \begin{pmatrix} \mathrm{St}^{-1} & -2\dot{\theta}_1 \\ 2\dot{\theta}_1 & \mathrm{St}^{-1} \end{pmatrix}, \qquad [B] \equiv \begin{pmatrix} \frac{\partial^2\hat{\Psi}}{\partial\xi\partial\eta} + 2\dot{\theta}_1^2 & \frac{\partial^2\hat{\Psi}}{\partial\eta^2} \\ -\frac{\partial^2\hat{\Psi}}{\partial\xi^2} & -\frac{\partial^2\hat{\Psi}}{\partial\xi\partial\eta} + 2\dot{\theta}_1^2 \end{pmatrix}. \tag{3.47}$$

Eq. (3.46) can be rewritten, so that the following expressions for $\boldsymbol{p}$ and $\boldsymbol{q}$ are obtained:

$$\begin{aligned} \Big([K] + [K]^{-1}\Big)\boldsymbol{p} &= \frac{1}{\dot{\theta}_1\mathrm{Fr}^2}[A]^{-1}\begin{pmatrix} 1 \\ 0 \end{pmatrix} - \frac{\mathrm{St}}{\mathrm{Fr}^2}[B]^{-1}\begin{pmatrix} 0 \\ 1 \end{pmatrix}, \\ \Big([K] + [K]^{-1}\Big)\boldsymbol{q} &= \frac{1}{\dot{\theta}_1\mathrm{Fr}^2}[A]^{-1}\begin{pmatrix} 0 \\ 1 \end{pmatrix} + \frac{\mathrm{St}}{\mathrm{Fr}^2}[B]^{-1}\begin{pmatrix} 1 \\ 0 \end{pmatrix}, \end{aligned} \tag{3.48}$$

where the matrix $[K] \equiv \mathrm{St}\dot{\theta}_1[B]^{-1}[A]$ is introduced for the sake of brevity. The solution for $\boldsymbol{p}$ and $\boldsymbol{q}$ is then:

$$\begin{aligned} \boldsymbol{p} &= \frac{1}{\dot{\theta}_1\mathrm{Fr}^2}\Big([K] + [K]^{-1}\Big)^{-1}[A]^{-1}\begin{pmatrix} 1 \\ 0 \end{pmatrix} - \frac{\mathrm{St}}{\mathrm{Fr}^2}\Big([K] + [K]^{-1}\Big)^{-1}[B]^{-1}\begin{pmatrix} 0 \\ 1 \end{pmatrix}, \\ \boldsymbol{q} &= \frac{1}{\dot{\theta}_1\mathrm{Fr}^2}\Big([K] + [K]^{-1}\Big)^{-1}[A]^{-1}\begin{pmatrix} 0 \\ 1 \end{pmatrix} + \frac{\mathrm{St}}{\mathrm{Fr}^2}\Big([K] + [K]^{-1}\Big)^{-1}[B]^{-1}\begin{pmatrix} 1 \\ 0 \end{pmatrix}. \end{aligned} \tag{3.49}$$

Since both $[A]$ and $[B]$ have a determinant unequal to zero, $[A]^{-1}$ and $[B]^{-1}$ exist and Eq. (3.49) yields a solution for $\boldsymbol{p}$ and $\boldsymbol{q}$ in closed form. Thus, a trapped particle describes an elliptic trajectory around the point $\boldsymbol{\xi}^*_\infty$, provided $|\boldsymbol{h}(t)|$ is sufficiently small.

Elaboration of Eq. (3.49) shows that the solution for $\boldsymbol{p}$ and $\boldsymbol{q}$ is, up to first order in the Stokes number:

$$\boldsymbol{p} = \frac{\mathrm{St}}{\mathrm{Fr}^2(\dot{\theta}_1^2 - \mathcal{H})} \begin{pmatrix} \frac{\partial^2 \hat{\Psi}}{\partial \xi \partial \eta} \\ -\frac{\partial^2 \hat{\Psi}}{\partial \xi^2} - \dot{\theta}_1 \end{pmatrix} + O(\mathrm{St}^2), \quad \boldsymbol{q} = \frac{\mathrm{St}}{\mathrm{Fr}^2(\dot{\theta}_1^2 - \mathcal{H})} \begin{pmatrix} \frac{\partial^2 \hat{\Psi}}{\partial \eta^2} + \dot{\theta}_1 \\ -\frac{\partial^2 \hat{\Psi}}{\partial \xi \partial \eta} \end{pmatrix} + O(\mathrm{St}^2). \tag{3.50}$$

When $\mathrm{St} \downarrow 0$, $\boldsymbol{\xi}^*_\infty$ is situated close to the ξ-axis, where $\partial^2\hat{\Psi}/\partial\xi\partial\eta = 0$. Therefore, in the limit of sufficiently small Stokes numbers, we may approximate $\boldsymbol{h}(t)$ by:

$$\boldsymbol{h}(t) \simeq \frac{\mathrm{St}}{\mathrm{Fr}^2(\dot{\theta}_1^2 - \mathcal{H})} \begin{pmatrix} \left(\frac{\partial^2 \hat{\Psi}}{\partial \eta^2} + \dot{\theta}_1\right) \cos(\dot{\theta}_1 t) \\ -\left(\frac{\partial^2 \hat{\Psi}}{\partial \xi^2} + \dot{\theta}_1\right) \sin(\dot{\theta}_1 t) \end{pmatrix}. \tag{3.51}$$

The corresponding velocity of the trapped particle is equal to:

$$\boldsymbol{v}_p(t) = \frac{\mathrm{d}\boldsymbol{h}}{\mathrm{d}t} \simeq \frac{\mathrm{St}\dot{\theta}_1}{\mathrm{Fr}^2(\dot{\theta}_1^2 - \mathcal{H})} \begin{pmatrix} -\left(\frac{\partial^2 \hat{\Psi}}{\partial \eta^2} + \dot{\theta}_1\right) \sin(\dot{\theta}_1 t) \\ -\left(\frac{\partial^2 \hat{\Psi}}{\partial \xi^2} + \dot{\theta}_1\right) \cos(\dot{\theta}_1 t) \end{pmatrix}. \tag{3.52}$$

Apparently, a trapped particle describes a counterclockwise trajectory of elliptic shape around the point $\boldsymbol{\xi}^*_\infty$. The mean radius of the elliptic trajectory is proportional to the Stokes number St and to the length of the gravity vector Fr^{-2}. A sketch of this solution is given in Fig. 3.12.

If gravity is relatively important (i.e. Froude number is low) while the Stokes number is small, the approximation that $|\boldsymbol{h}(t)|$ is small is not valid anymore. Then, there is a strong competition between the Stokes drag forcing the particle to closely follow the carrier flow, and gravity causing high accelerations of the particle in different directions. As a consequence, different, leaf-like, attraction trajectories can be observed, which are sometimes present in addition to a 'normal' elliptically shaped attraction trajectory. An example of these different attraction trajectories in one flow is given in Fig. 3.13, where $r_1 = 0.5$, $\mathrm{St} = 0.01$ and $\mathrm{Fr} = \frac{1}{2}\sqrt{2}$. Particles on the elliptically shaped trajectory in Fig. 3.13a) move along the trajectory for a time T before returning to the same position. Particles on the more complex trajectory plotted in Fig. 3.13b) return to the same position after a time $3T$; following the terminology of dynamical system theory [72], this can be regarded as a period-3 trajectory.

In the same flow field, the positions of initially uniformly distributed particles are plotted in Fig. 3.14 for four instants in time. The important role of gravity in this case is reflected by the distribution of particles which is very different from the ones shown in Fig. 3.4 and Fig. 3.11. As $t \to \infty$, some particles are attracted to one of four different moving attraction points, which are highlighted by the numbers 1, 2, 3 and 4 in Fig. 3.14d) for convenience. The particles in group 1 are attracted to the almost elliptically shaped trajectory which is periodic with the vortex motion T, see

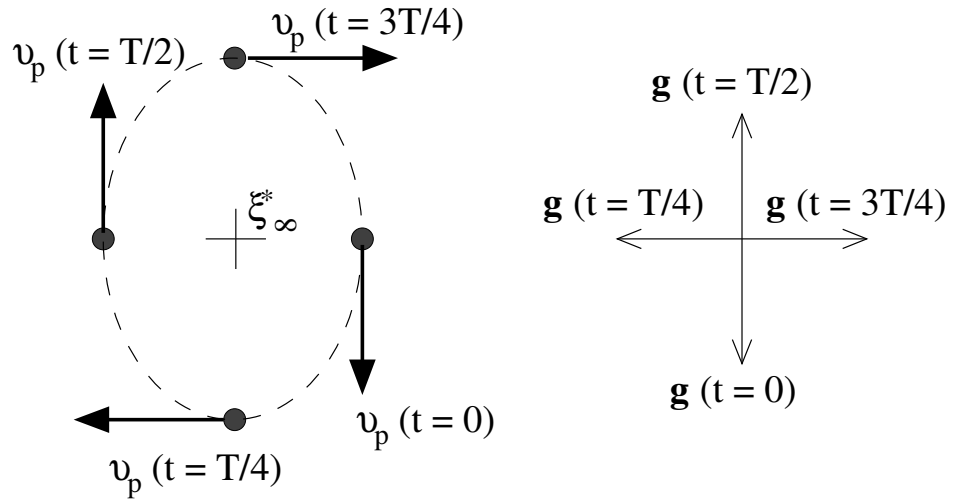

FIGURE 3.12: *Sketch of attraction trajectory of a heavy particle for a small Stokes number in the frame of reference rotating with the vortex, for case of non-zero gravity with* $0 < Fr^{-2} \ll 1$. *Left: position and velocity of a trapped particle at four instants in time, corresponding to Eq. (3.51) and Eq. (3.52). Right: the direction of the gravity vector at the same four instants in time.*

Fig. 3.13a). The particles in groups 2, 3 and 4 on the other hand follow the period-3 trajectory depicted in Fig. 3.13b).

Possibly, even different attraction trajectories may be observed when the Stokes number and the Froude number are decreased further. This has not been done in the present study, because of the large calculation times which are required to observe particle accumulation for very small Stokes numbers; it is noted that the rate of particle accumulation reduces with smaller Stokes numbers: $|\boldsymbol{\xi}(t) - \boldsymbol{\xi}^*| \sim \exp(-t\mathrm{St})$, see Eq. (3.38). In addition, due to the very small values of the Froude number, the results would probably be of little practical interest.

3.4.2 Stability of moving attraction point

In the present section, we show by a stability analysis that heavy particles may accumulate in a moving attraction point in the case of non-zero gravity. The particle equation of motion Eq. (3.16) can be written as follows:

$$\frac{\mathrm{d}}{\mathrm{d}t}\chi_i(t) = F_i(\boldsymbol{\chi}(t)) + G_i(t), \tag{3.53}$$

where $G_i(t)$ is a function taking account of the gravity, which is periodic with period T, see Eq. (3.8). The difference in position and velocity over one period T of a single particle trajectory is given by:

$$\frac{\mathrm{d}}{\mathrm{d}t}\big(\chi_i(t+T) - \chi_i(t)\big) = F_i(\boldsymbol{\chi}(t+T)) - F_i(\boldsymbol{\chi}(t)) + G_i(t+T) - G_i(t). \tag{3.54}$$

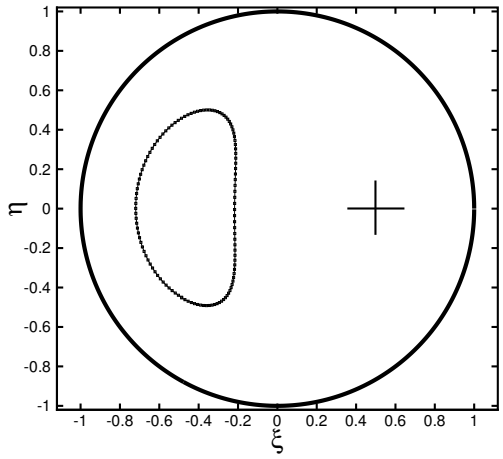

a)

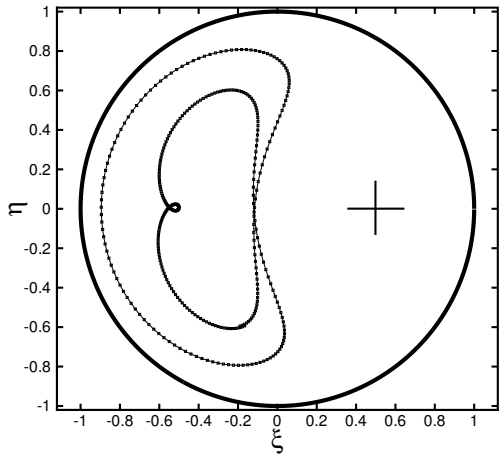

b)

FIGURE 3.13: *Attraction trajectories of particles in one-vortex system with non-zero gravity, plotted in the frame rotating with the vortex; St* $= 0.01$*, Fr* $= \frac{1}{2}\sqrt{2}$*,* $r_1 = 0.5$*. a) Attraction trajectory of a particle released at position* $(x, y) = (-0.275, 0)$*; the particle moves along the trajectory for a time T before returning to the same position. b) Attraction trajectory of a particle released at position* $(x, y) = (-0.3, 0)$*; the particle moves along the trajectory for a time* $3T$ *before returning to the same position.*

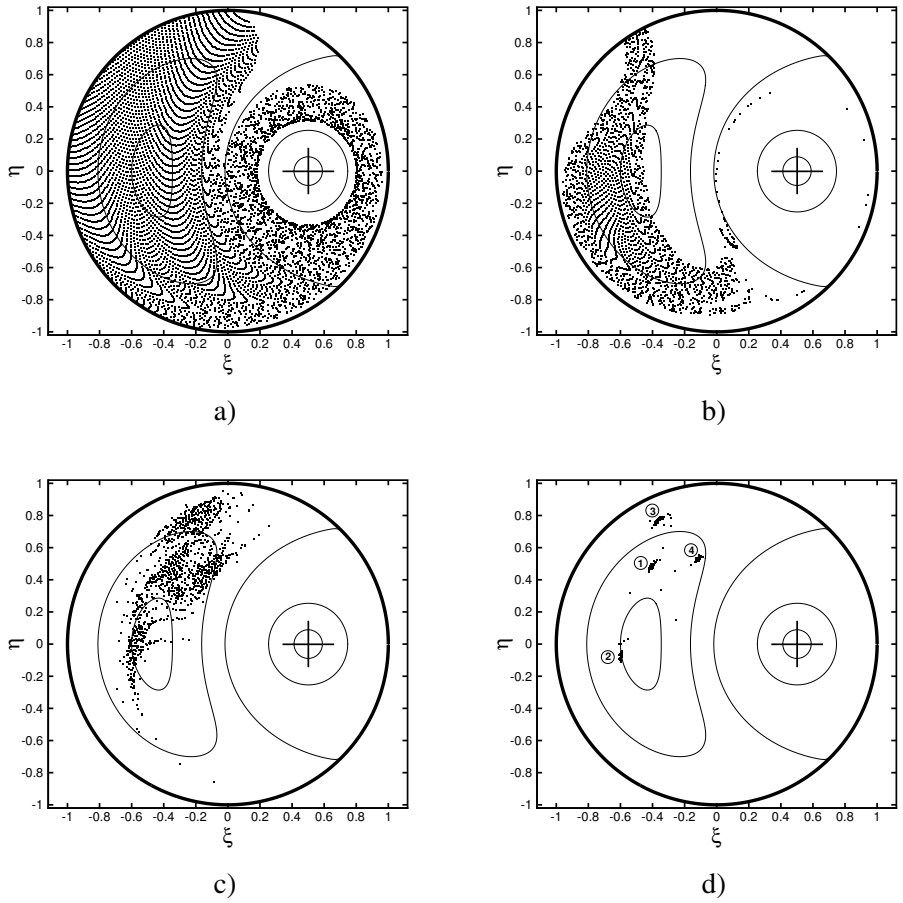

FIGURE 3.14: *Positions of initially uniformly distributed heavy particles in one-vortex system with non-zero gravity, plotted in the frame rotating with the vortex;* $St = 0.01$, $Fr = \frac{1}{2}\sqrt{2}$, $r_1 = 0.5$*: a)* $t = 10$*, b)* $t = 100$*, c)* $t = 1000$*, d)* $t = 10000$*. Streamlines of passive tracers are plotted in the background. The numbers* $1-4$ *in d) denote four groups of particles which accumulate in different moving attraction points.*

Since $G_i(t + nT) = G_i(t), \forall n \in \mathbb{N}$, Eq. (3.54) can be reduced to:

$$\frac{\mathrm{d}}{\mathrm{d}t}(\chi_i(t+T) - \chi_i(t)) = F_i(\boldsymbol{\chi}(t+T)) - F_i(\boldsymbol{\chi}(t)). \tag{3.55}$$

For convenience, we introduce the variable $r_i(t) = \chi_i(t + T) - \chi_i(t)$:

$$\frac{\mathrm{d}}{\mathrm{d}t} r_i(t) = F_i(\mathbf{r}(t) + \boldsymbol{\chi}(t)) - F_i(\boldsymbol{\chi}(t)). \tag{3.56}$$

We now assume $|\mathbf{r}| \ll 1$ to be small, so that $\boldsymbol{\chi}(t)$ is close to the moving fixed point $\boldsymbol{\chi}^*(t)$. Then, a Taylor expansion of Eq. (3.56) results in:

$$\frac{\mathrm{d}}{\mathrm{d}t} r_i(t) = r_j(t) \frac{\partial F_i(\boldsymbol{\chi}^*(t))}{\partial \chi_j} + O(|\mathbf{r}|^2). \tag{3.57}$$

If the real parts of the eigenvalues of the matrix $\partial F_i / \partial \chi_j$ are all smaller than 0 for all time, then $|\mathbf{r}| \to 0$ as $t \to \infty$. Physically, this would mean that the equilibrium trajectory is stable, i.e. it attracts heavy particles.

From section 3.3, we know that the four eigenvalues of $\partial F_i / \partial \chi_j$ are:

$$\lambda_{1,2,3,4} = \frac{-1 \pm \sqrt{1 - 4\dot{\theta}_1^2 \mathrm{St}^2 \pm 4i\mathrm{St}\sqrt{\mathcal{H}^*(t)}}}{2\mathrm{St}}, \tag{3.58}$$

where $\mathcal{H}^*(t)$ denotes the value of the Hessian at the position of an attracted particle. For small Stokes numbers, the values of λ_i can be approximated by:

$$\lambda_{1,2,3,4} = \frac{-1 \pm 1}{2\mathrm{St}} + \mathrm{St}(\mathcal{H}^*(t) - \dot{\theta}_1^2) \pm i\sqrt{\mathcal{H}^*(t)} + iO(\mathrm{St}) + O(\mathrm{St}^2). \tag{3.59}$$

We know from section 3.4.1 that a moving fixed point describes an elliptic trajectory around $\boldsymbol{\xi}^*_\infty$, provided Fr^{-2} is sufficiently small. Therefore $\mathcal{H}(\boldsymbol{\xi}^*(t)) = \mathcal{H}(\boldsymbol{\xi}^*_\infty) + O(\mathrm{Fr}^{-2})$. Since $0 < \mathcal{H}(\boldsymbol{\xi}^*_\infty) < \dot{\theta}_1^2$, we now have proven for sufficiently small values of St and Fr^{-2} that the equilibrium trajectory, periodic with T, exists and is stable.

3.4.3 Particle accumulation in (St, Fr)-space

In order to quantify the influence of gravity, we now determine the region in parameter space for which particle accumulation takes place. This means that we investigate the region in (St, Fr)-space for which the particle trapping efficiency, defined in Eq. (3.20), is larger than zero as time tends to infinity: $P_\infty > 0$.

Given an initially uniform distribution of particles with an initial velocity equal to the local carrier flow velocity, the phenomenon of particle accumulation depends on three parameters: the vortex position r_1, the Stokes number St and the Froude number Fr. For the sake of convenience, we take the vortex radius as $r_1 = 0.5$. While keeping the Stokes number fixed, we determine the minimum value of the Froude number for which $P > 0$ by running a large number of numerical simulations for different values of Fr.

The result for the critical Froude number is shown in Fig. 3.15. A clear distinction can be made between the region in parameter space where $P_\infty > 0$ and the region where $P_\infty = 0$. The separation between the regions is almost linear in St and in Fr^2 as long as $\mathrm{St} \lesssim 0.3$ and $\mathrm{Fr}^2 \lesssim 10$. The curve steepens as St becomes larger; from Fig. 3.9 it follows that, as $\mathrm{Fr} \to \infty$, particle accumulation only takes place if $\mathrm{St} \lesssim 1.85$.

The almost linear part of the (St, Fr)-curve for St and Fr^2 can be explained by the fact that the attraction point in the frame rotating with the vortex describes an almost elliptic trajectory around the point $\boldsymbol{\xi}^*_\infty$. The mean radius of the elliptic trajectory is proportional to St/Fr^2, see Eq. (3.51). Thus when St/Fr^2 increases, the mean radius of the trajectory increases accordingly. If the radius of the trajectory is too large, the particle may hit the wall, and the mechanism of particle accumulation breaks down. Therefore, there exists an upper bound in the value of St/Fr^2 for which accumulation takes place.

The steepening of the curve as St approaches 1 can be explained as follows. As the Stokes number increases, the point $\boldsymbol{\xi}^*_\infty$ is situated further away from the elliptic stagnation point; it is situated closer to the boundary of the circular domain (see Fig. 3.7). Therefore, the approximately elliptic equilibrium trajectory is more likely to intersect with the wall. As a consequence, particle accumulation is restricted to either lower values of the Stokes number, or to higher values of the Froude number.

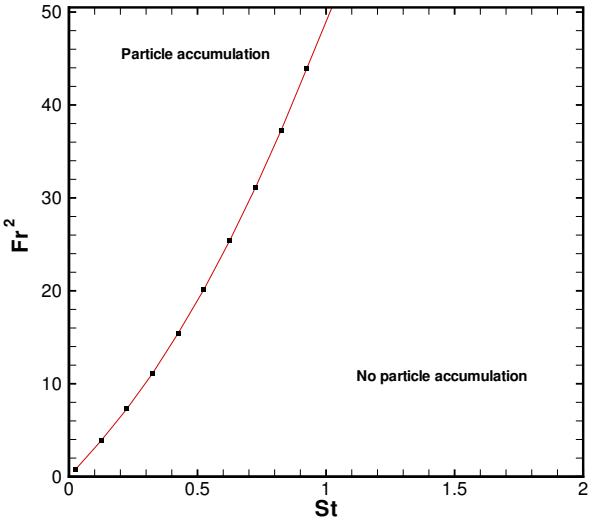

FIGURE 3.15: *The critical Fr^2 as a function of St for $r_1 = 0.5$.*

3.5 Particle clustering in two-dimensional viscous vortex flows

In order to investigate the effect of viscosity in vortex flows, neglected so far, the motion of slipping droplets in a laminar viscous flow field containing a means to gener-

ate circulation is studied numerically. In accordance with the point vortex model, the means to generate circulation (a rotating rod with radius $\tilde{r}_0$) is assumed to rotate not only around its own axis, but also around the center of the circular domain. A sketch of the problem is given in Fig. 3.16. The rotation rate of the rod around its own axis is $\Gamma_0/(2\pi\tilde{r}_0^2)$, thus mimicking a point vortex with circulation Γ_0. The rotation rate of the rod around the center of the circular domain is, dimensional:

$$\tilde{\Omega} = \frac{\Gamma_0}{2\pi}\frac{1}{R^2 - \tilde{r}_1^2}. \tag{3.60}$$

In the rest of this section, we make all variables dimensionless using the vortex strength Γ_0 and the radius of the circular domain R. The dimensionless rotation rate of the rod around its own axis is then $1/(2\pi r_0^2)$, with $r_0 \equiv \tilde{r}_0/R$. The dimensionless rotation rate around the center of the circular domain becomes:

$$\Omega = \frac{1}{2\pi}\frac{1}{1 - r_1^2}, \tag{3.61}$$

where $r_1 \equiv \tilde{r}_1/R$.

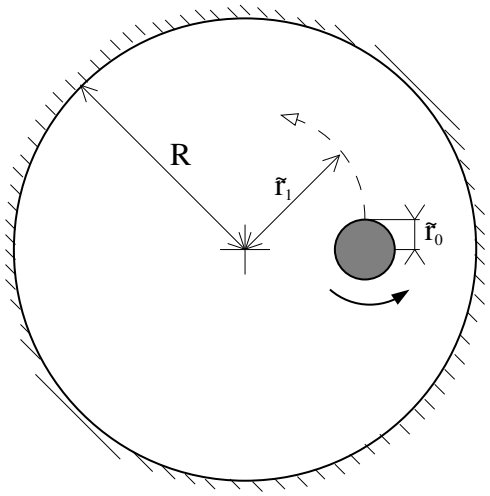

FIGURE 3.16: *Sketch of the configuration of a moving, rotating rod with radius $\tilde{r}_0$ in a cylindrical domain with radius R. The radial position of the rod is constant and denoted by $\tilde{r}_1$.*

3.5.1 Physical model

The Navier-Stokes equations for incompressible viscous flow in a fixed frame of reference, made dimensionless by Γ_0, R and the fluid density ρ, are given by:

$$\nabla \cdot \boldsymbol{u} = 0, \qquad \frac{\partial}{\partial t}\boldsymbol{u} + \boldsymbol{u} \cdot \nabla \boldsymbol{u} = -\nabla p + \frac{1}{\mathrm{Re}}\nabla^2 \boldsymbol{u}. \tag{3.62}$$

We rewrite Eq. (3.62) in a rotating frame, with rotation rate Ω around the center of the domain:

$$\nabla \cdot \boldsymbol{v} = 0, \qquad \frac{\partial}{\partial t}\boldsymbol{v} + \boldsymbol{v} \cdot \nabla \boldsymbol{v} = -\nabla \hat{p} + \frac{1}{\mathrm{Re}}\nabla^2 \boldsymbol{v}, \tag{3.63}$$

where $\boldsymbol{v} \equiv \boldsymbol{u} + \Omega J \boldsymbol{\xi}$ is the relative velocity in the rotating frame, and $\hat{p}$ denotes the modified pressure: $\hat{p} \equiv p + 2\Omega\hat{\Psi} + \frac{1}{2}\Omega^2 \boldsymbol{\xi} \cdot \boldsymbol{\xi}$. The boundary conditions in the rotating frame are:

$$\begin{aligned} \boldsymbol{v} &= \Omega[\eta, -\xi]^T, \quad \text{for } r = \sqrt{\xi^2 + \eta^2} = 1, \\ \boldsymbol{v} &= \frac{1}{2\pi r_0^2}[-\eta, \xi - r_1]^T, \quad \text{for } \sqrt{(\xi - r_1)^2 + \eta^2} = r_0. \end{aligned} \tag{3.64}$$

The only parameter of the problem is the Reynolds number $\mathrm{Re} \equiv \Gamma_0/\nu$, which together with the boundary conditions and the initial conditions uniquely defines the solution of Eq. (3.63) for $\boldsymbol{v}$ and $\hat{p}$.

In this flow field, we investigate the motion of heavy particles. The motion of the particles is assumed to be accurately described by Eq. (3.16), just like in the case of potential flow. The particles are assumed not to influence the carrier flow field; thus, a one-way coupling is employed.

3.5.2 Numerical solution method

Eq. (3.63), subject to the boundary conditions Eq. (3.64), is solved using the finite-volume method in the commercial fluid dynamics software code CFX (version 10). The physical domain is subdivided in grid cells whose node points are situated on isolines of the functions γ_1 and γ_2, which are given by:

$$\gamma_1 = \arctan\!\left(\frac{\eta}{\xi - 1/r_1}\right) - \arctan\!\left(\frac{\eta}{\xi - r_1}\right), \quad \gamma_2 = \ln \frac{(\xi - 1/r_1)^2 + \eta^2}{(\xi - r_1)^2 + \eta^2}, \tag{3.65}$$

which are related to the velocity potential and the streamfunction of the potential flow problem of a point vortex inside a circular domain. Since $\partial\gamma_1/\partial\xi = \partial\gamma_2/\partial\eta$ and $\partial\gamma_1/\partial\eta = -\partial\gamma_2/\partial\xi$, the isolines of γ_1 and γ_2 are always orthogonal. Therefore, each combination of (ξ, η) corresponds to exactly one combination of (γ_1, γ_2).

In the γ_1-direction, the grid points are distributed equidistantly, whereas the grid points in γ_2-direction are distributed as on a Chebyshev grid. The mesh generation is shown schematically in Fig. 3.17.

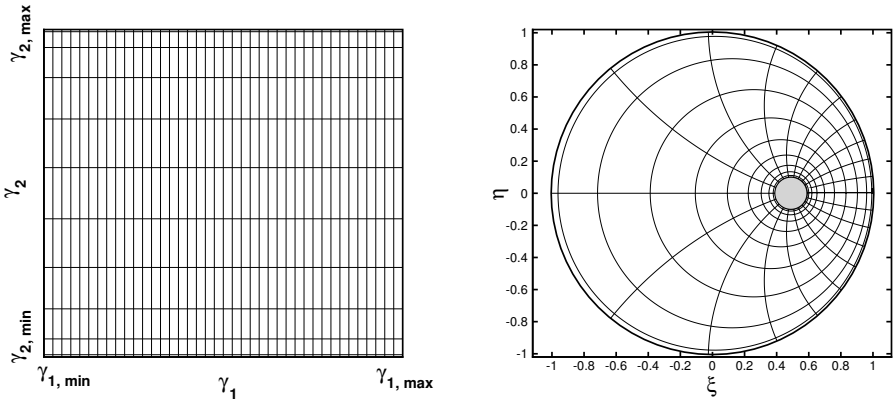

a) b)

FIGURE 3.17: *Schematic view of the generation of the grid. a) Distribution of grid points in γ_1- and γ_2-direction. b) Projection of the (γ_1, γ_2)-grid onto the physical domain. For the sake of clarity, the plots show* 20 *cells in the γ_1-direction, and* 10 *cells in the γ_2-direction only.*

Iterations in time are carried out using an explicit second-order Runge-Kutta scheme, starting from the initial condition that $\boldsymbol{v} = 0, \forall \boldsymbol{\xi}$. The iteration process is continued until a converged steady flow solution is obtained, i.e. $\partial \boldsymbol{v}/\partial t = 0, \forall \boldsymbol{\xi}$.

Subsequently, the particle trajectories are determined by integrating Eq. (3.16) using a 4-th order Runge Kutta scheme. At each time step the velocity of the carrier flow at the position of the particle, which generally does not coincide with a grid point, is obtained using a bilinear interpolation.

3.5.3 Results

The Navier-Stokes equations, Eq. (3.63), have been solved on a grid of 304 cells in the γ_1-direction and 81 cells in the γ_2-direction. In order to check the accuracy of the obtained solution, the solution has been obtained on other grids too, and extensive convergence tests were carried out; for more details on these tests, the reader is referred to [20].

In Fig. 3.18, we show the streamlines of the time-independent laminar flow field satisfying the Navier Stokes equations Eq. (3.63) when Re = 200. The resulting flow field is rather similar to the potential flow presented in Fig. 3.2: the flow around the rotating rod is dominated by a counterclockwise motion, whereas the left half plane is dominated by a large rotating motion in clockwise direction around an elliptic stagnation point. Nevertheless, there are some differences with respect to the potential flow field as well: in the viscous flow only one hyperbolic stagnation point is found (on the positive ξ-axis) instead of two on the wall, and regions of high vorticity are

found in the boundary layer. Besides, it is noted that the viscous flow field is not symmetric: the elliptic stagnation point is situated well below the negative ξ-axis.

The flow field in Fig. 3.18 is also reminiscent of the flow in a journal bearing presented in Figure 7.4.2c) in §7.4 of Ottino's book [73]. Ottino studied the same configuration as the one considered here, but he calculated the flow field only for very low Reynolds numbers so that the convective terms can be neglected (Stokes flow). Comparison of Fig. 3.18 with Ottino's work shows that the inclusion of the convective terms results in a very similar, albeit slightly asymmetric, flow field: the flow field is characterized by a cyclonic motion around the rotating rod and an anticyclonic motion in a large part of the domain.

The flow field for a Reynolds number of 2000 is depicted in Fig. 3.19. Since a higher Reynolds number corresponds to a smaller influence of viscosity, it is expected that the differences with respect to the potential flow model have decreased: indeed the boundary layer is thinner than in the case $\mathrm{Re} = 200$ and the position of the elliptic stagnation point is closer to the negative ξ-axis.

In Fig. 3.18 and Fig. 3.19, the positions of a group of 451 initially uniformly distributed heavy particles are plotted at four instants in time as well. The particles have a Stokes number of $\mathrm{St} = 0.25$; at the beginning of the simulation they have the same velocity as the local carrier flow. The heavy particles accumulate in the region around the elliptic stagnation point inside the physical domain as $t \to \infty$. It is clear that these results are very similar to the ones obtained in the case of a point vortex model, see e.g. Fig. 3.4.

In viscous vortex flows, the fixed point $\boldsymbol{\xi}^*$ is found to be close to an elliptic stagnation point of the flow field in the corotating frame. This is not much of a surprise considering the results presented for the case of inviscid flow. In fact, the analysis presented in section 3.3.1 is equally valid for viscous flows and for inviscid flows. Therefore, also in the viscous flow, a fixed point for the accumulation of heavy particles can be found in the vicinity of the elliptic stagnation point, if the Stokes number is sufficiently small. In the limit of $\mathrm{St} \downarrow 0$, the fixed point corresponds to the elliptic stagnation point of the flow field.

Particle accumulation in $(\mathbf{St}, \mathbf{Fr})$-space

We determine the region in parameter space $(\mathrm{St}, \mathrm{Fr})$ for which the particle accumulation takes place in the viscous vortex flow. This is equivalent to determining the parameter space for which $P_{\infty,\mathrm{visc}}$, defined as:

$$P_{\infty,\mathrm{visc}} \equiv \frac{(\text{number of particles with } r < 0.9 \text{ for } t \to \infty)}{(\text{total number of initially uniformly distributed particles})} \times 100\%, \quad (3.66)$$

is larger than 0. It is noted that this definition is different from the one in Eq. (3.20), since the maximum radial position is taken as 0.9 instead of 1. This modification has

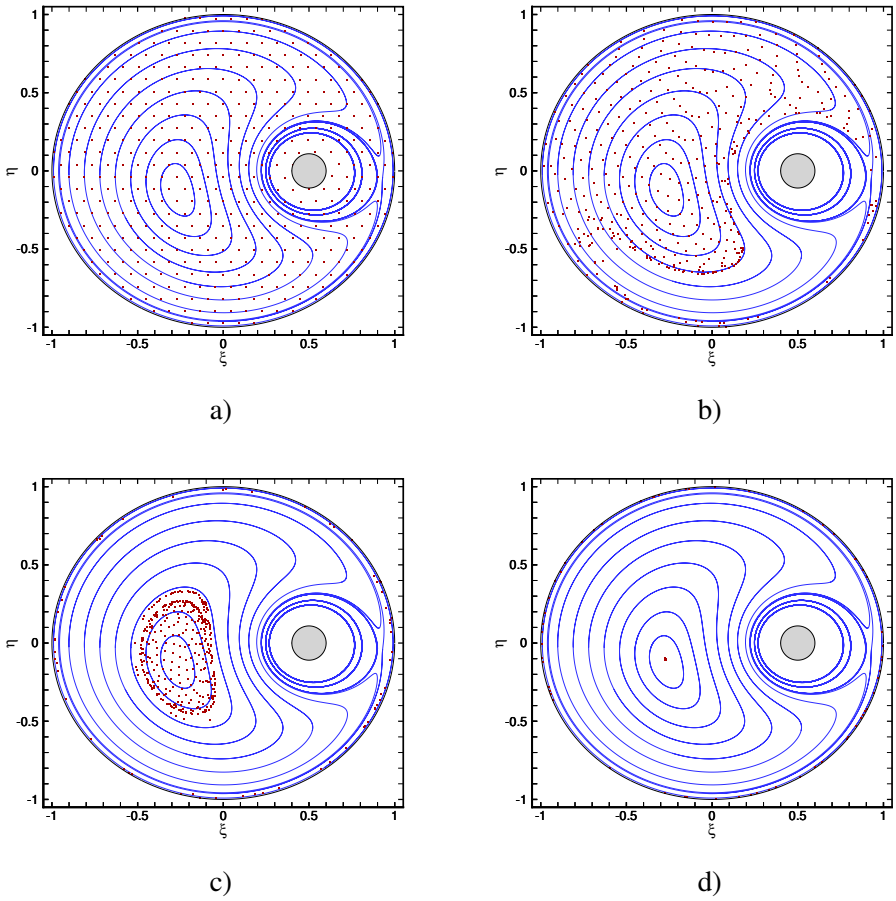

FIGURE 3.18: *Dots: positions of heavy particles in steady viscous vortex flow;* $r_1 = 0.5$*,* $r_0 = 0.1$*,* $St = 0.25$*,* $Fr \to \infty$ *and* $Re = 200$*: a)* $t = 0$*, b)* $t = 10$*, c)* $t = 100$ *and d)* $t = 1000$*. Streamlines of the carrier flow are plotted as thin solid lines.*

been made in order to exclude particles which get trapped in the viscous boundary layer close to the boundary of the domain; especially if the particle Stokes number is small, the particles may become trapped in the boundary layer without ever reaching the wall. The numerically obtained parameter space in which $P_{\infty,\mathrm{visc}} > 0$ is depicted in Fig. 3.20, for Re = 200 and Re = 2000.

For both values of the Reynolds number, the curve separating the two regimes is almost a straight line, i.e. $\mathrm{St}/\mathrm{Fr}^2$ is approximately a constant. Although this result for a viscous is very similar to the result obtained in section 3.4.3 for potential flow, there is one important difference: for small Froude numbers, the maximum Stokes number for which accumulation takes place is lower than in the case of potential flow.

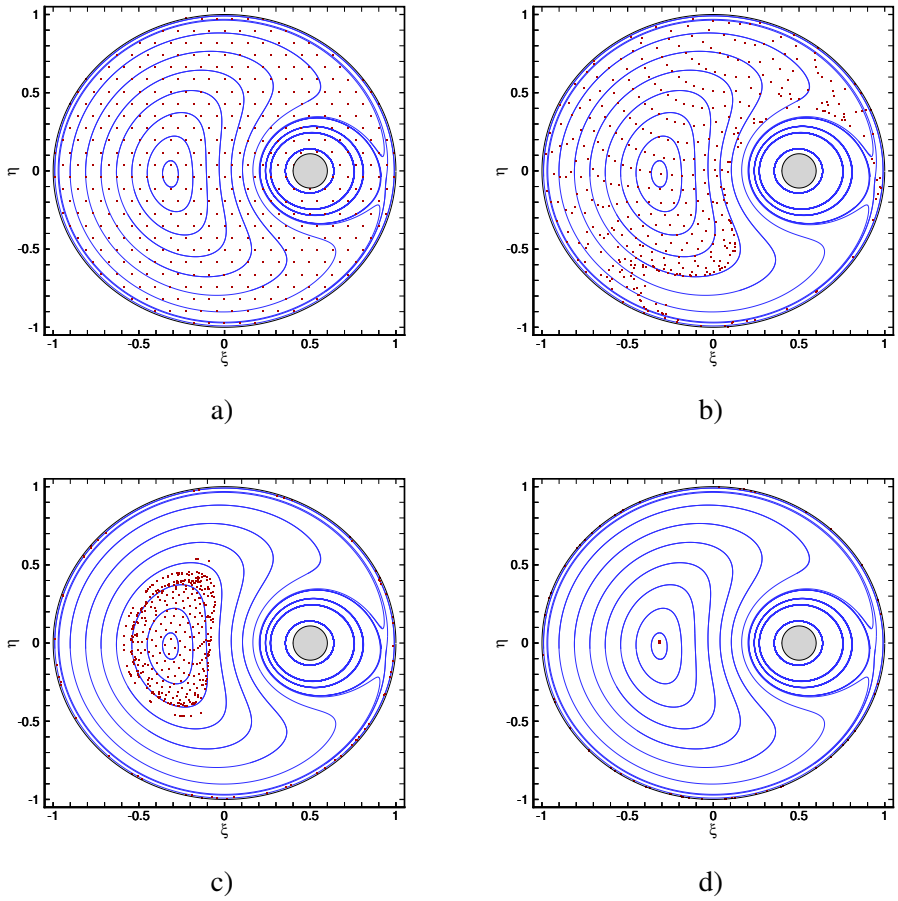

FIGURE 3.19: *Dots: positions of heavy particles in steady vortex flow;* $r_1 = 0.5$, $r_0 = 0.1$, $St = 0.25$, $Fr \to \infty$ *and* $Re = 2000$*: a)* $t = 0$*, b)* $t = 10$*, c)* $t = 100$ *and d)* $t = 1000$*. Streamlines of the carrier flow are plotted as thin solid lines.*

This can be explained by the observation that a small Froude number (i.e. a large length of the gravity vector) results in a long trajectory of the particles around the elliptic stagnation point. When the particle passes through the viscous boundary layer, its velocity is reduced, and the Coriolis force decreases consequently. As a result, the particle relaxes in the boundary layer instead of being attracted to an equilibrium trajectory around the elliptic stagnation point. Therefore, when the Stokes number is small, particle accumulation occurs at larger values of the Froude number in the viscous flow than in the potential flow.

3.6 Conclusions

In this chapter, the motion of heavy particles in a bounded point vortex flow has been investigated both theoretically and numerically. The case of one vortex in a closed circular domain has been studied, which corresponds to the flow induced by a slender helical vortex filament in a pipe. The numerical simulations are based on a one-way coupling. Only the Stokes drag and gravity are taken into account in the equation of motion for the particles. The flow field is modelled by a potential flow field containing a point vortex which is allowed to move freely, i.e. it follows a circular trajectory at fixed radius at constant angular velocity.

The results for the zero-gravity case ($\mathrm{Fr} \to \infty$) reveal that heavy particles may accumulate in regions where the centrifugal and the drag forces acting on the particles balance each other, resulting in an equilibrium trajectory. A linear stability analysis shows that particles are always attracted to a fixed point in an anticyclonic region, as long as the Stokes number is below a critical value. This critical Stokes number is higher when the radial position of the vortex increases. The fixed point is situated further away from the center of the anticyclonic region as the Stokes number increases. The rate at which a particle approaches an attraction point, is approximately linear in the Stokes number.

It is shown that gravity causes the particles to accumulate towards a moving attraction point in the frame of reference moving with the vortex. For small Stokes numbers and large Froude numbers, the moving attraction point describes an elliptically shaped attraction trajectory in the frame of reference rotating with the vortex. The trajectory is periodic with the rotation of the frame of reference. The stability of the moving attraction point has been proven by a linear stability analysis, for small values of the Stokes number and large values of the Froude number. For smaller values of the Froude number, particle accumulation is observed, too, provided the ratio $\mathrm{St}/\mathrm{Fr}^2$ remains below a critical level; then, some particles do not describe an elliptically shaped equilibrium trajectory but rather a leaf-like trajectory.

The results obtained from the inviscid (potential) flow model are compared to the results from a simulation for which the flow field satisfies the Navier-Stokes equations for two-dimensional incompressible viscous flow. Although the viscous flow field is somewhat different from the potential flow field, heavy particles may accumulate close to an elliptic stagnation point in the flow, just like in the case of potential flow. The attraction mechanism of heavy particles in viscous flows is very similar to the one observed in case of potential flow from both a qualitative and a quantitative point of view.

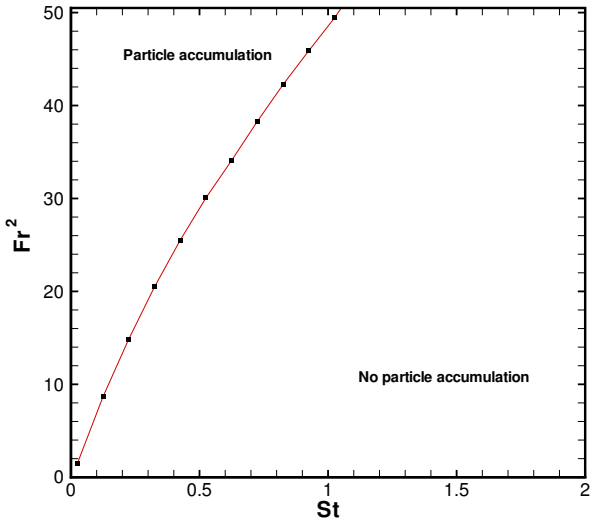

a)

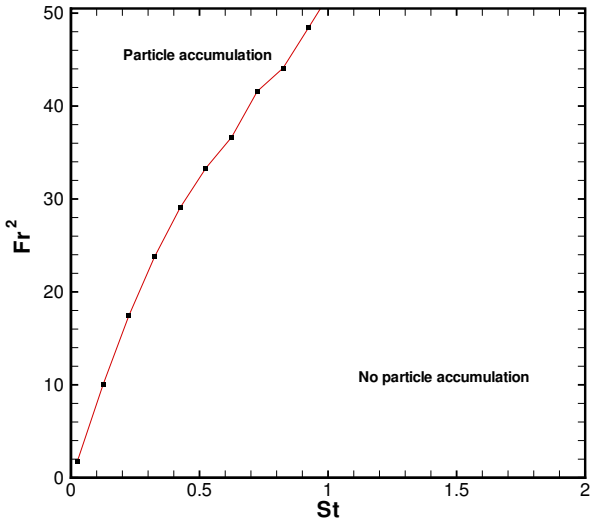

b)

FIGURE 3.20: *The critical value of Fr^2 as a function of St in viscous flow for $r_1 = 0.5$, $r_0 = 0.1$. a) $Re = 200$, b) $Re = 2000$.*

HEAVY PARTICLES IN BOUNDED TWO-VORTEX FLOW

CHAPTER 4

The motion of heavy particles in potential vortex flows on the unit disk is investigated theoretically and numerically. Configurations with two point vortices are considered. Each vortex follows a regular path on the disk. In order to isolate the effect of inertia, in the equation of motion of the heavy particles only Stokes drag is taken into account. Results from numerical simulations show that heavy particles may accumulate inside the closed circular domain. The particle accumulation is shown to be related to the presence of elliptic islands of regular passive tracer motion. The particle accumulation is enhanced for smaller values of the particle Stokes number, and larger values of the angular momentum of the vortices. These results are explained and supported by a stability analysis.

4.1 Introduction

In the present chapter, we study the motion of heavy particles in a potential flow containing two point vortices. This situation can be seen as a model for the flow through a slender tube, in which two compact vortex cores are present. A schematic view of the configuration is presented in Fig. 4.1. In the limit of a very slender tube, the velocity field reduces to a superposition of a constant axial velocity U and a time-dependent two-dimensional flow in the cross-sectional plane, moving at velocity U, as sketched in Fig. 4.1. The two-dimensional flow is characterized by two point vortices in a circular domain. The goal of the present research is to determine the influence of such compact structures of vorticity on the motion of heavy particles.

The motion of two vortices on a disk was studied by Boffetta *et al.* [14]. They showed that the self-induced motion of two free point vortices in a closed circular domain is always regular and integrable. They presented a broad classification of possible orbits of two identical vortices.

The case of two point vortices on a disk is special, since a flow may result that displays chaotic advection of passive tracers despite the regularity of the vortex motion. In this sense, the case of two point vortices on a disk is comparable to the behavior

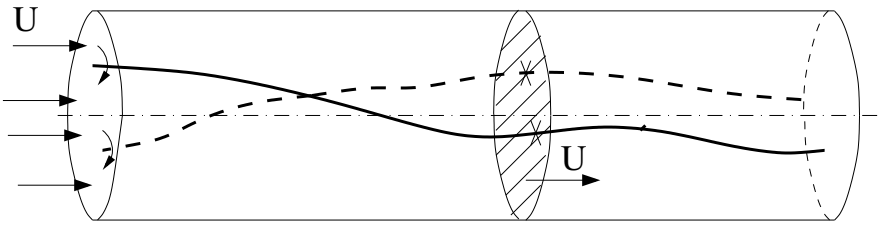

FIGURE 4.1: *Sketch of two vortex filaments in a slender tube, like they may occur in a gas-liquid separator. In the cross section indicated, the flow may be approximated by two point vortices in a closed circular domain.*

of three vortices on an infinite plane [42],[68].

In the present chapter we investigate the motion of heavy particles in a closed circular domain containing two point vortices. It is assumed that the number of particles is such that the flow may be considered as a dilute flow. Just like in Chapter 3, we focus on the accumulation of particles due to their inertia in sufficiently dilute flows. The simulations are based on a one-way coupling. In order to isolate the effect of the particle inertia, gravity is neglected.

The present chapter is organized as follows. In section 4.2 we present the equations governing the motion of point vortices in a closed circular domain, and the equation of motion of passive tracers. In addition, the equations of motion for heavy particles are introduced. The motion of heavy particles in a circular domain containing two vortices is considered in section 4.3. Finally, a summary and conclusions are given in section 4.4.

4.2 Physical-mathematical model

We consider a closed circular domain with radius R, containing a potential flow generated by N point vortices. In this chapter, all variables are made dimensionless by choosing R as the characteristic length and the strength of the first vortex Γ_1 as the characteristic circulation. The position of the j-th vortex is given by its radial position r_j and angle θ_j while its strength is Γ_j. For each vortex j, an image vortex with strength $-\Gamma_j$ is placed at the position (r_j^{-1},θ_j) in order to satisfy the boundary condition of zero normal velocity at $r = 1$. Since the velocity field is divergence-free ($\nabla \cdot \boldsymbol{u} = 0$), the motion of passive tracers is governed by a stream function which plays the role of a Hamiltonian.

The stream function Ψ is conveniently described in polar coordinates:

$$\Psi(r,\theta) \equiv \sum_{j=1}^{N} \Gamma_j \Big[\Psi_V(r,\theta,r_j,\theta_j) - \Psi_I(r,\theta,r_j,\theta_j)\Big], \tag{4.1}$$

with:

$$\Psi_V(r,\theta,r_j,\theta_j) \equiv -\frac{1}{4\pi}\ln\left[r^2 + r_j^2 - 2rr_j\cos(\theta-\theta_j)\right], \tag{4.2}$$

and:

$$\Psi_I(r,\theta,r_j,\theta_j) \equiv \Psi_V(r,\theta,r_j^{-1},\theta_j). \tag{4.3}$$

The function $\Psi_V(r,\theta,r_j,\theta_j)$ represents the partial stream function corresponding to the j-th vortex, whereas $\Psi_I(r,\theta,r_j,\theta_j)$ represents the partial stream function corresponding to the image of the j-th vortex. The velocity field is obtained by the canonical equations:

$$u_r = \frac{1}{r}\frac{\partial\Psi}{\partial\theta}, \quad u_\theta = -\frac{\partial\Psi}{\partial r}. \tag{4.4}$$

The motion of the point vortices itself is governed by Hamiltonian dynamics. The Hamiltonian H is chosen as:

$$\begin{aligned} H &= \sum_{i=1}^{N-1}\sum_{j=i+1}^{N}\Gamma_i\Gamma_j\left[\Psi_V(r_i,\theta_i,r_j,\theta_j) - \Psi_I(r_i,\theta_i,r_j,\theta_j) + \frac{1}{4\pi}\ln r_j^2\right] \\ &- \frac{1}{2}\sum_{i=1}^{N}\Gamma_i^2\left[\Psi_I(r_i,\theta_i,r_i,\theta_i) - \frac{1}{4\pi}\ln r_i^2\right]. \end{aligned} \tag{4.5}$$

The velocities of the vortices are finally obtained from the canonical equations:

$$\Gamma_\alpha\dot{r}_\alpha = \frac{1}{r_\alpha}\frac{\partial H}{\partial\theta_\alpha}, \quad \Gamma_\alpha r_\alpha\dot{\theta}_\alpha = -\frac{\partial H}{\partial r_\alpha}, \tag{4.6}$$

where the dots indicate differentiation with respect to time. In Eq. (4.6) the repeated indices no not imply summation.

During the motion of N point vortices on a disk, two quantities are conserved. The first conserved quantity is the Hamiltonian H defined by Eq. (4.5). The second conserved quantity is the angular momentum L^2, defined as:

$$L^2 \equiv \sum_{i=1}^{N}\Gamma_i r_i^2. \tag{4.7}$$

Its conservation can be demonstrated as follows. The time derivative of L^2 is:

$$\frac{\mathrm{d}L^2}{\mathrm{d}t} = \sum_{i=1}^{N}\frac{\partial L^2}{\partial r_i}\dot{r}_i = \sum_{i=1}^{N}\left(\frac{2\Gamma_i r_i}{\Gamma_i r_i}\frac{\partial H}{\partial\theta_i}\right) = 2\sum_{i=1}^{N}\left(\frac{\partial H}{\partial\theta_i}\right). \tag{4.8}$$

Since Eq. (4.5) does not depend on θ_i and θ_j individually but only on $(\theta_i - \theta_j)$, this results in the sum of the derivatives of H with respect to θ_i, $i = 1,\ldots,N$, to be equal to zero identically. The time derivative of the angular momentum then becomes 0, so that it is indeed a conserved quantity. Physically, the conservation of L^2 follows from the rotational symmetry of the disk [68].

4.2.1 Motion of two point vortices on a disk

The Hamiltonian formulation (Eq. (4.5)) in the case of two vortices is:

$$H = \Gamma_1\Gamma_2\left[\Psi_V(r_1,\theta_1,r_2,\theta_2) - \Psi_I(r_1,\theta_1,r_2,\theta_2) + \frac{1}{4\pi}\ln r_2^2\right] + \frac{1}{4\pi}\sum_{i=1}^{2}\Gamma_i^2\ln\left[1-r_i^2\right]. \tag{4.9}$$

This is a four-degree-of-freedom Hamiltonian, since it depends on r_1, θ_1, r_2 and θ_2. Using the conservation of angular momentum, Eq. (4.9) can be reduced to a system of two degrees of freedom. For this purpose, the angle $\phi \equiv \theta - \theta_1$ is introduced, and r_1 is written in terms of r_2 using the invariant L^2:

$$r_1 = \sqrt{\frac{L^2-\Gamma_2 r_2}{\Gamma_1}}, \quad \frac{\mathrm{d}r_1}{\mathrm{d}r_2} = -\frac{\Gamma_2 r_2}{\Gamma_1 r_1}. \tag{4.10}$$

Then, the Hamiltonian, Eq. (4.9), can be written as follows [14]:

$$H(r_1,\theta_1,r_2,\theta_2) = \hat{H}(r_2,\phi_2), \tag{4.11}$$

with:

$$\begin{aligned}\hat{H}(r_2,\phi_2) \;=\; & \frac{1}{4\pi}\Gamma_1\Gamma_2\ln\Big[\Gamma_1\Gamma_2 + \Gamma_2 r_2^2(L^2-\Gamma_2 r_2^2) - 2\sqrt{\Gamma_1\Gamma_2^2 r_2^2(L^2-\Gamma_2 r_2^2)}\cos\phi_2\Big] \\ & -\frac{1}{4\pi}\Gamma_1\Gamma_2\ln\Big[\Gamma_1\Gamma_2 r_2^2 + \Gamma_2(L^2-\Gamma_2 r_2^2) - 2\sqrt{\Gamma_1\Gamma_2^2 r_2^2(L^2-\Gamma_2 r_2^2)}\cos\phi_2\Big] \\ & +\frac{1}{4\pi}\Gamma_1^2\ln\Big[1-\frac{L^2}{\Gamma_1}+\frac{\Gamma_2 r_2^2}{\Gamma_1}\Big] + \frac{1}{4\pi}\Gamma_2^2\ln[1-r_2^2].\end{aligned} \tag{4.12}$$

The time development of r_2 and ϕ_2 can be obtained from the canonical equations:

$$\Gamma_2\dot{r}_2 = \frac{1}{r_2}\frac{\partial\hat{H}}{\partial\phi_2}, \quad \Gamma_2 r_2\dot{\phi}_2 = -\frac{\partial\hat{H}}{\partial r_2}. \tag{4.13}$$

The radial position of the first vortex, r_1, then follows directly from Eq. (4.10).

The contour lines of the Hamiltonian (Eq. (4.12)) in the case of two equally strong vortices ($\Gamma_1 = \Gamma_2 = 1$) are plotted in Fig. 4.2, for $L^2 = 0.18$, $L^2 = 0.37$, $L^2 = 0.72$ and $L^2 = 0.82$. In all figures, the contour lines correspond to trajectories of the second vortex in the frame rotating with the first vortex, which is placed on the positive ξ-axis ($\phi_1 \equiv 0$). The period of the trajectory, denoted by T_v, depends on the initial position of the vortices and their strengths.

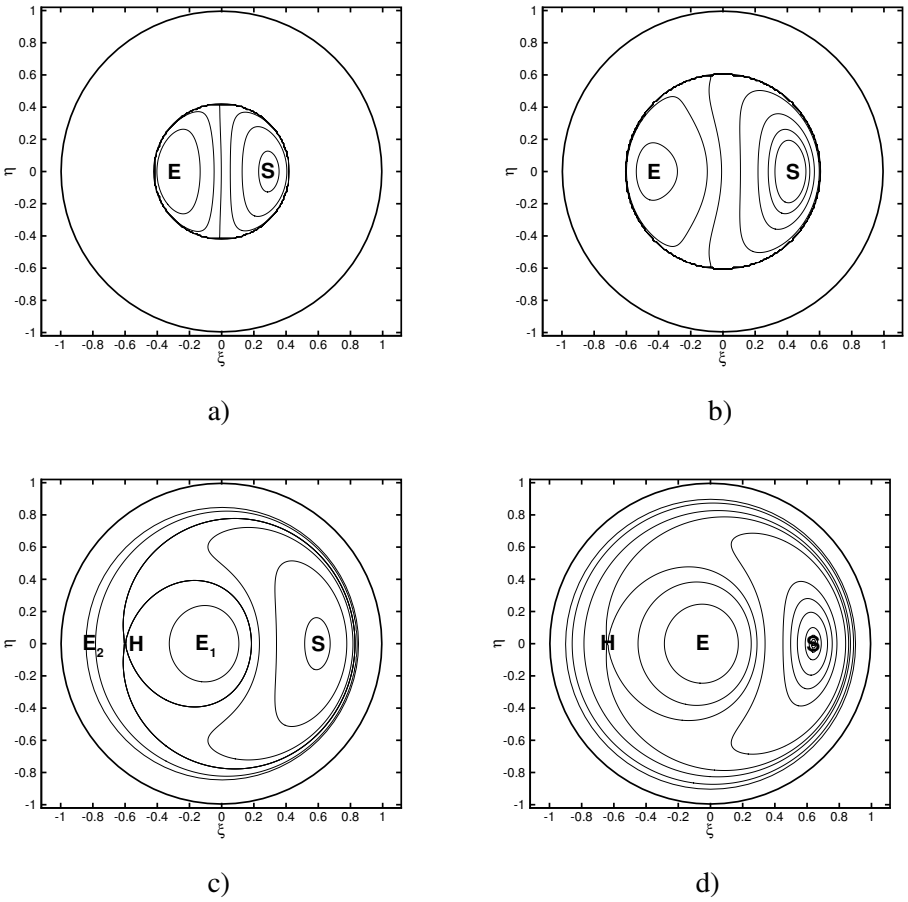

FIGURE 4.2: *Contour lines of Hamiltonian (Eq. (4.12)) describing the motion of vortex* 2 *in the frame rotating with vortex* 1*;* $\xi \equiv r\cos\phi$*,* $\eta \equiv r\sin\phi$*. Both vortices have the same strength. E denotes a stable (elliptic) equilibrium configuration of the vortices, H is an unstable (hyperbolic) equilibrium configuration, and S is the singular configuration of two coinciding vortices: a)* $L^2 = 0.18$*, b)* $L^2 = 0.37$*, c)* $L^2 = 0.72$*, d)* $L^2 = 0.82$*.*

4.2.2 Flow field induced by two point vortices on a disk

The motion of passive tracers in the case of two vortices on a disk is described by the following stream function:

$$\Psi(r,\theta) = \sum_{j=1}^{2} \Gamma_j \left[\Psi_V(r,\theta,r_j,\theta_j) - \Psi_I(r,\theta,r_j,\theta_j) \right], \tag{4.14}$$

which depends on both the passive tracer position (r,θ) and the vortex positions (r_1,θ_1) and (r_2,θ_2). In the co-rotating frame the vortices have one degree of freedom less than in the fixed frame. Still, the remaining number of degrees of freedom makes the stream function not-integrable [68]. Thus the advection of passive tracers in a 2-vortex system on a disk is chaotic, except for a number of special cases [14].

Besides chaotically moving passive tracers, some patches of regularly moving passive tracers can be found. These patches are called islands of regular motion, which can be either hyperbolic or elliptic. On the one hand, hyperbolic islands are situated around the point vortex centers. They persist even when the vortex motion itself is chaotic [4]. On the other hand, elliptic islands may arise in regions far away from vortex cores. Since these islands do not contain a singular vortex core, the relative velocity of passive tracers tends to zero in the center of the island; therefore they are called elliptic islands [42].

4.2.3 Equations of motion of heavy particles

The motion of heavy particles is assumed to be described by Eq. (2.5). In order to isolate the phenomenon of heavy particles influenced by the vortices, gravity is neglected (i.e. $\mathrm{Fr} \to \infty$). The Stokes number St is defined as the particle relaxation time τ_p divided by the characteristic time scale of the flow, R^2/Γ_1:

$$\mathrm{St} = \frac{\tau_p \Gamma_1}{R^2}. \tag{4.15}$$

We rewrite the equations of motion in a rotating reference frame:

$$\begin{aligned} \frac{\mathrm{d}\boldsymbol{\xi}_p}{\mathrm{d}t} &= \boldsymbol{v}_p, \\ \frac{\mathrm{d}\boldsymbol{v}_p}{\mathrm{d}t} &= \frac{1}{\mathrm{St}}(\boldsymbol{v} - \boldsymbol{v}_p) + 2\Omega J \boldsymbol{v}_p + \Omega^2 \boldsymbol{\xi}_p + \dot{\Omega} J \boldsymbol{\xi}_p, \end{aligned} \tag{4.16}$$

where $\boldsymbol{\xi}$ and $\boldsymbol{v}$ denote the position and the velocity in the rotating frame, respectively; the tensor J is defined in Eq. (3.17). The additional terms on the right hand side, which all depend on the rotation rate Ω and its time derivative $\dot{\Omega}$, denote the Coriolis force, the centrifugal force, and an additional force due to the acceleration of the

reference frame*, respectively. The specific choice of Ω depends on the situation at hand.

Just like in Chapter 3, we consider the trajectories of two nearby particles. The differences in position and velocity are denoted by $\delta\boldsymbol{\xi}_p$ and $\delta\boldsymbol{v}_p$, respectively. When the magnitude of the 4-dimensional separation vector $\boldsymbol{R} \equiv [\delta\boldsymbol{\xi}_p, \delta\boldsymbol{v}_p]^T$ is very small, the separation between the two trajectories can be expressed in the following form:

$$\frac{\mathrm{d}}{\mathrm{d}t}\boldsymbol{R}(t) = M\boldsymbol{R}(t), \tag{4.17}$$

with:

$$M = \begin{pmatrix} 0 & 0 & 1 & 0 \\ 0 & 0 & 0 & 1 \\ \frac{1}{\mathrm{St}}\frac{\partial v}{\partial \xi} + \Omega^2 & \frac{1}{\mathrm{St}}\frac{\partial v}{\partial \eta} + \dot{\Omega} & -\frac{1}{\mathrm{St}} & 2\Omega \\ \frac{1}{\mathrm{St}}\frac{\partial v}{\partial \xi} - \dot{\Omega} & \frac{1}{\mathrm{St}}\frac{\partial v}{\partial \eta} + \Omega^2 & -2\Omega & -\frac{1}{\mathrm{St}} \end{pmatrix}. \tag{4.18}$$

When all eigenvalues of the matrix M have a real part smaller than zero, we have $|\boldsymbol{R}(t)| \to 0$ for $t \to \infty$. This means that the two particles converge for sufficiently large times.

4.3 Heavy particles in bounded two-vortex flow

In this section we consider the motion of heavy particles in a system with two vortices of equal strength. We conduct a numerical simulation in which each particle is traced individually by using a fourth-order Runge-Kutta scheme. The equations of motion are solved for a series of decreasing values of the time step, where each next value is half of the previous value. When the differences between two subsequent solutions are smaller than a certain preset level, the last obtained solution is considered sufficiently accurate. At the start of the simulation, the particles have the same velocity as the local gas flow. When a particle reaches the circular boundary, it is absorbed by the wall.

In order to visualize the results for heavy particles, four vortex configurations have been investigated in particular. The first configuration, with $L^2 = 0.18$, is the same as was treated by Boffetta *et al.*; the vortex positions are initially:

$$(r_1, \theta_1) = (\frac{\sqrt{2}}{10}, 0), \quad \text{at } t = 0,$$
$$(r_2, \theta_2) = (\frac{2}{5}, \pi) \quad \text{at } t = 0.$$

*This force is sometimes referred to as 'Euler force'.

The case with $L^2 = 0.37$ corresponds to the following initial vortex positions:

$$(r_1, \theta_1) = (\frac{1}{10}, 0), \quad \text{at } t = 0,$$
$$(r_2, \theta_2) = (\frac{6}{10}, 0), \quad \text{at } t = 0.$$

In the configuration with $L^2 = 0.72$, the initial vortex positions are chosen to be:

$$(r_1, \theta_1) = (\frac{\sqrt{2}}{5}, 0), \quad \text{at } t = 0,$$
$$(r_2, \theta_2) = (\frac{4}{5}, 0), \quad \text{at } t = 0.$$

Finally, a configuration is treated with $L^2 = 0.82$, where the initial vortex positions are:

$$(r_1, \theta_1) = (\frac{1}{10}, 0), \quad \text{at } t = 0,$$
$$(r_2, \theta_2) = (\frac{9}{10}, 0), \quad \text{at } t = 0.$$

First, we consider the motion of passive tracers in the four configurations. Poincaré sections of passive tracer positions with interval T_v are plotted in Fig. 4.3; passive tracers are represented by small dots. The passive tracers can be classified into three groups: hyperbolic islands, elliptic islands and chaotic regions. In all configurations two hyperbolic islands can be recognized on the ξ-axis, around the point vortex centers; the chaotic regions can be recognized by the random distribution of passive tracers. In addition, some elliptic islands occur. In Fig. 4.3a), the two most important elliptic islands are situated around $(\xi, \eta) \simeq (-0.1, \pm 0.5)$. Three elliptic islands can be identified in Fig. 4.3b), at $(\xi, \eta) \simeq (0.2, \pm 0.5)$ and at $(\xi, \eta) \simeq (-0.6, 0.0)$. In Fig. 4.3c), only one elliptic island is visible, at $(\xi, \eta) \simeq (-0.4, 0)$. Finally, in Fig. 4.3d), an almost circular anticyclonic region of regular motion is found between the two vortices. There is, however, not one particular point in this region where the relative velocity of passive tracers tends to zero.

In Fig. 4.3, the positions of heavy particles are presented too. The 1791 initially uniformly distributed particles, with St = 0.1, are plotted after $t = nT_v \simeq 100$, $n \in \mathbb{N}$. Thus, the heavy particles are plotted at the moment that the two vortices have zero relative angle, i.e. the vortices have the same relative positions as on $t = 0$. In the configuration with $L^2 = 0.18$, a large number of particles have accumulated in two single points near the elliptic islands; all other particles have been expelled from the domain. The case of $L^2 = 0.37$ is similar, since many particles have either accumulated close to the small elliptic islands or in the big elliptic island in the left half-plane. In the case $L^2 = 0.72$, some particles are trapped close to the elliptic island in the left

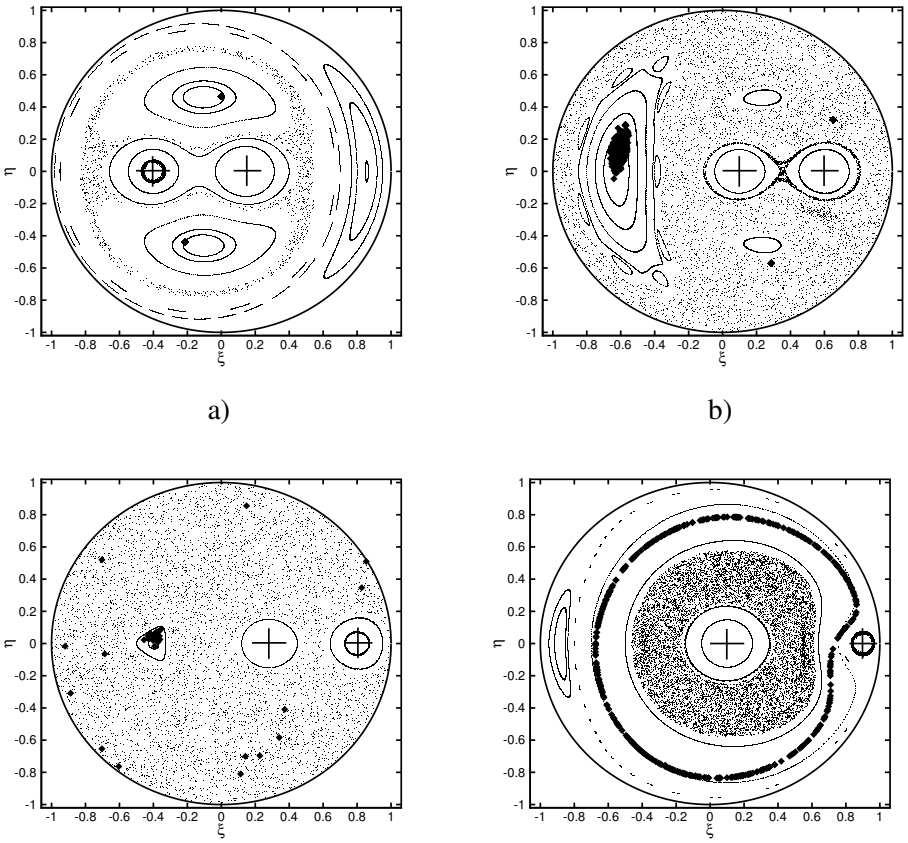

FIGURE 4.3: *Positions of heavy particles (diamonds) in two-vortex system after time* $t = nT_v \simeq 100$, $n \in \mathbb{N}$; $St = 0.1$*: a)* $L^2 = 0.18$*, b)* $L^2 = 0.37$*, c)* $L^2 = 0.72$*, d)* $L^2 = 0.82$*. For comparison, Poincaré sections of passive tracers (small dots) are plotted, too.*

half-plane, a few others are still in the chaotic region. In longer simulations it is observed that the dispersed particles eventually reach the wall, whereas the trapped particles accumulate in the elliptic island. The trapped particles in all these examples are attracted towards a regular trajectory which is in phase with the vortex motion. In the 2-vortex system, the attraction point is not a fixed point like in the 1-vortex system with zero gravity, see section 3.3; it is better to speak of a moving fixed point instead.

In the case of $L^2 = 0.82$, an elliptic island does not exist where the heavy particles can be attracted to. The anticyclonic region of regular passive tracer motion, however, does attract particles that are expelled from the regions around the vortices; as $t \to \infty$ heavy particles can be found on a closed line (see Fig. 4.3d)).

4.3.1 Location of moving fixed point

For the particle accumulation to occur in the two-vortex system, a force-balanced periodically moving fixed point has to exist. First of all, this requires the existence of a regular motion of the heavy particles with respect to the vortices. This regular motion is not straightforward to find, because of the unsteadiness of the flow field. Still, in the limit of $\mathrm{St} \downarrow 0$, the motion of heavy particles corresponds to the motion of passive tracers. So, the moving fixed point of heavy particles should go to a point of regular motion of passive tracers as their Stokes number vanishes. Hence, the particle accumulation takes place around the centers of elliptic islands.

The shape of the elliptic islands is in phase with the vortex motion. The same holds for the trajectory of trapped heavy particles. Therefore, both a trapped particle and the center of the elliptic island are on the same position after every vortex period. Poincaré sections with time T_v can then visualize the influence of the Stokes number on the position of the moving attraction point. The results are presented in Fig. 4.4, for the cases of $L^2 = 0.18$ and $L^2 = 0.72$. In both cases, the center of the elliptic island is plotted too. Clearly, the location of the moving attraction point is increasingly far away from the center of the elliptic island for higher Stokes numbers.

Some particles with higher Stokes numbers even have a fixed point in a region outside of the elliptic islands, as can be observed for three particles in Fig. 4.4b). This means that these heavy particles describe a regular motion, in period with the vortex motion, although they are surrounded by chaotically moving passive tracers. This seems rather contradictory but this phenomenon can be explained from the dissipative nature of the governing equations of motion, Eq. (4.16): whereas passive tracer motion is governed by a Hamiltonian that conserves the phase space volume, the phase space volume of heavy particles tends to 0 for $t \to \infty$ (see also section 2.3, or [73]).

In Fig. 4.5, the distance Δ' is shown as a function of the Stokes number. Here, Δ'

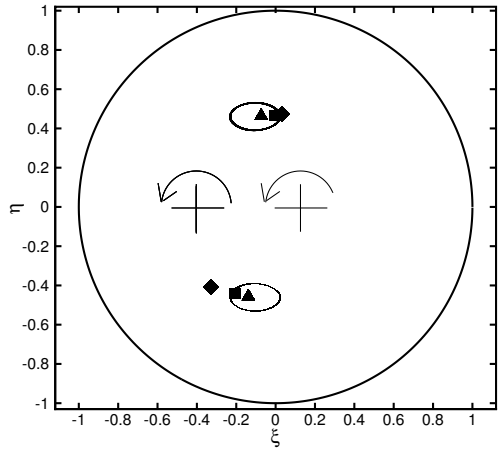

a)

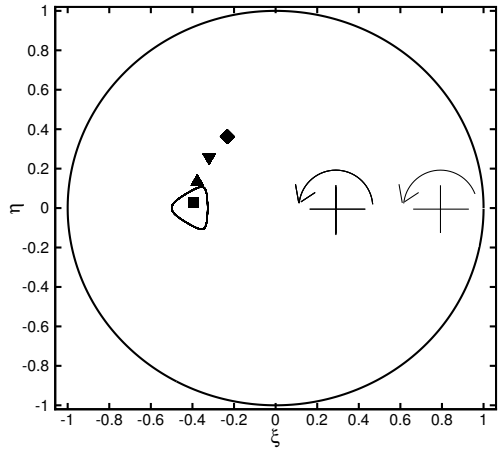

b)

FIGURE 4.4: *Poincaré sections with period T_v of particles trapped in the moving attraction points: a) $L^2 = 0.18$; ▲: $St = 0.03$, ■: $St = 0.09$, ♦: $St = 0.15$, b) $L^2 = 0.72$; ■: $St = 0.1$, ▲: $St = 0.3$, ▼: $St = 0.6$, ♦: $St = 0.9$.*

is defined as:

$$\Delta' \equiv \left(|\boldsymbol{\xi_p}^*(t) - \boldsymbol{\xi}_0(t)|\right)_{t=nT_v}, \quad n \in \mathbb{N}, \tag{4.19}$$

which is the distance between the moving attraction point and the center of the elliptic island, on the moment that the two vortices have zero relative angle. The distance Δ' grows approximately linearly in the Stokes number, as long as the Stokes number is small enough. These results are very similar to the results of the one-vortex case, presented in Fig. 3.8.

4.3.2 Stability of moving fixed point

The stability of the moving fixed point can be investigated by using the separation vector from Eq. (4.17), where the time dependent matrix M is given by Eq. (4.18) and evaluated at the moving fixed point. In Fig. 4.5 we found that $\Delta' \propto \mathrm{St}$, indicating that the moving fixed point is located close to the center of an elliptic island for small values of the Stokes number. Therefore, it is convenient to take the reference frame co-rotating with the center of the elliptic island, whose angular velocity is denoted by Ω_0 and its angular acceleration by $\dot{\Omega}_0$. The eigenvalues of M then follow from the (time-dependent) characteristic polynomial:

$$\mathrm{St}^2\lambda^4 + 2\mathrm{St}\lambda^3 + (2\mathrm{St}^2\Omega_0^2 + 1)\lambda^2 + (2\mathrm{St}\Omega_0^2 + 4\mathrm{St}^2\Omega_0\dot{\Omega}_0)\lambda + \mathrm{St}^2\Omega_0^4 + \mathrm{St}^2\dot{\Omega}_0^2 + \mathcal{H}^* = 0, \tag{4.20}$$

In the limit of small relative acceleration compared to the inverse of the Stokes number, i.e.,

$$|\frac{\dot{\Omega}_0}{\Omega_0}| \ll \frac{1}{\mathrm{St}}, \forall t, \tag{4.21}$$

the eigenvalues become:

$$\lambda_{1,2,3,4} \approx \frac{-1 \pm \sqrt{1 - 4\Omega_0^2\mathrm{St}^2 \pm 4\mathrm{St}\sqrt{-\mathcal{H}^*(t) - 2\mathrm{St}\Omega_0\dot{\Omega}_0 - \mathrm{St}^2\dot{\Omega}_0^2}}}{2\mathrm{St}}. \tag{4.22}$$

The Hessian $\mathcal{H}^*$ is strictly positive in the elliptic island for all time. Linearizing Eq. (4.22) with respect to St and using Eq. (4.21) then gives:

$$\lambda_{1,2,3,4} \approx \frac{-1 \pm 1}{2\mathrm{St}} + \mathrm{St}(\mathcal{H}^* - \Omega_0^2) \pm i\sqrt{\mathcal{H}^*} + O(\mathrm{St}^2). \tag{4.23}$$

In Fig. 4.5 it was shown that approximately $\mathcal{H}^* = \mathcal{H}_0 + O(\mathrm{St})$, such that:

$$\lambda_{1,2,3,4} \approx \frac{-1 \pm 1}{2\mathrm{St}} + \mathrm{St}(\mathcal{H}_0 - \Omega_0^2) \pm i\sqrt{\mathcal{H}_0} + iO(\mathrm{St}) + O(\mathrm{St}^2). \tag{4.24}$$

A completely similar reasoning as is conducted in section 3.3, based on the observation that $\left(\mathcal{H}_0 - \Omega_0^2\right) < 0$, leads to the conclusion that the condition $\mathcal{H}_0 > 0$ is both

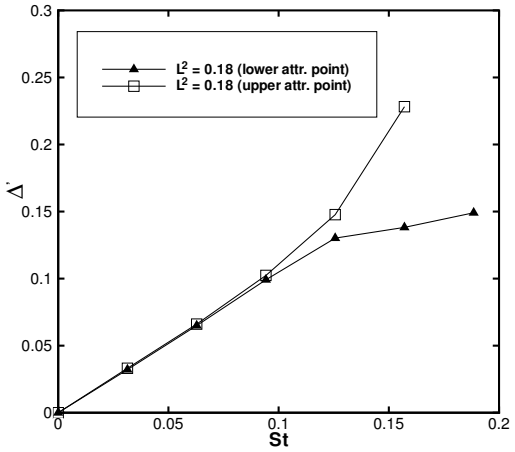

a)

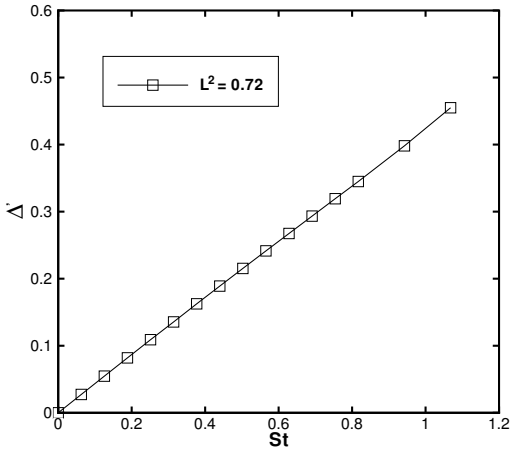

b)

FIGURE 4.5: *Distance between a trapped particle and the center of the elliptic island Δ' as a function of the Stokes number, on the moment that the two vortices have zero relative angle: a) $L^2 = 0.18$, b) $L^2 = 0.72$.*

necessary and sufficient for the fixed point to be stable for small Stokes numbers. It is noted that the real parts of the eigenvalues are approximately linear in the Stokes number, so that the particle trapping time is inversely proportional to the Stokes number, just like in the one-vortex case.

The region of attraction consists predominantly of heavy particles which are released in the regular elliptic islands. Also from other regions of the flow, a large number of particles may eventually be forced towards the moving attraction point.

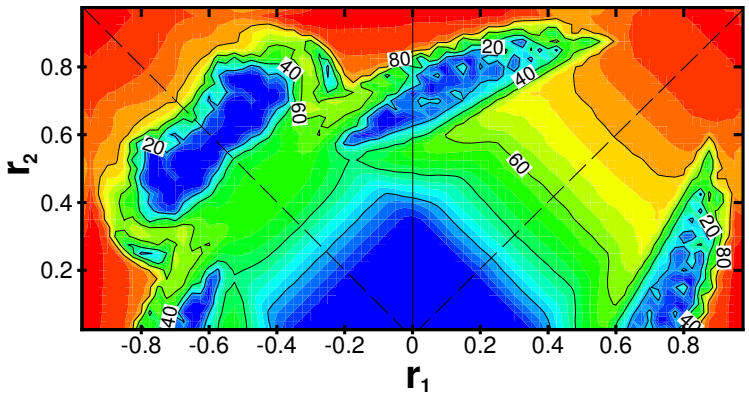

a)

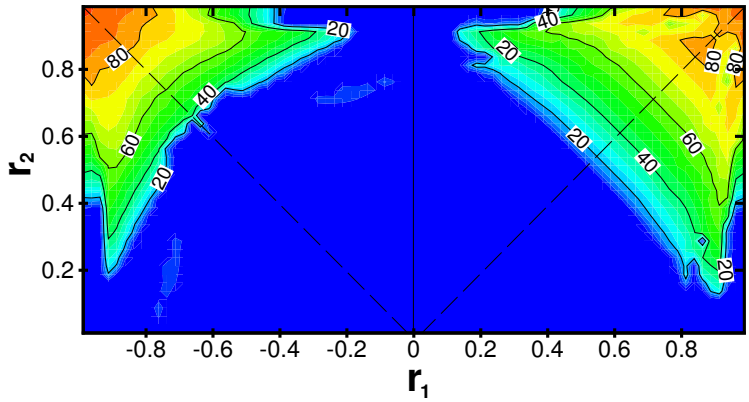

b)

FIGURE 4.6: *Percentage P_∞ of accumulated heavy particles as a function of the initial condition (r_1, r_2) of the* 2*-vortex configuration; a) $St = 0.1$, b) $St = 1$.*

In order to quantify the particle accumulation, numerical simulations were carried

for a large variety of configurations with two identical vortices. For a range of 40×80 initial vortex positions (r_1, r_2), the positions of heavy particles are calculated at t = 500, for two different Stokes numbers: St = 0.1 and St = 1. After such a long time, generally only the accumulated particles are present in the domain, whereas all other particles have reached the wall. On the basis of these simulations, the parameter P_∞, defined in Eq. (3.20), is determined. The results are presented in Fig. 4.6, as a function of the vortex configuration parameters r_1 and r_2, where a negative value of r_1 indicates an initial position of vortex 1 on the negative x-axis. Since r_1 and r_2 may be interchanged without any consequence for the flow, the figures are symmetric around the lines $r_2 = \pm r_1$, which are drawn for convenience.

Generally, the accumulation of heavy particles is enhanced with higher angular momentum and lower Stokes numbers. The low percentage of particle accumulation in the left half-plane of Fig. 4.6a) (especially around $(r_1, r_2) = (-0.7, 0.4)$, or $(r_1, r_2) = (-0.4, 0.7)$) can be explained by the fact that the motion of passive tracers is highly chaotic; no elliptic islands exist in these configurations. This supports the hypothesis that heavy particle accumulation in bounded 2-vortex flows takes place in elliptic islands of regular passive tracer motion.

4.4 Conclusions

In this chapter, the motion of heavy particles in a bounded potential flow generated by two point vortices in a circular domain is investigated both theoretically and numerically. Due to the limited number of degrees of freedom, the two vortices display a regular periodic motion inside the circular domain.

The numerical simulations are based on a one-way coupling. In order to isolate the effect of inertia, in the equations of motion only the Stokes drag is taken into account.

The results reveal that heavy particles may accumulate at a moving attraction point within the circular domain. This means that all forces on the particle (the Stokes drag plus fictitious forces due to the formulation of the equations of motion in a rotating frame of reference) are such that a particle is trapped on an equilibrium trajectory as time tends to infinity.

The moving attraction point is situated near the center of an elliptic island, i.e. a region of regular anticyclonic motion of passive tracers. The distance between the moving attraction point and the center of the elliptic island increases for larger Stokes numbers.

A linear stability analysis shows that the attraction trajectory is stable for particles with small Stokes numbers, i.e. particles in the neighborhood are always attracted to the center of an elliptic island of regular motion. The rate at which a particle approaches the moving attraction point is approximately proportional to the Stokes number.

In order to quantify the effect of particle accumulation, the particle trapping efficiency has been calculated for a wide range of initial vortex positions. From the results of these simulations, two main conclusions can be drawn: (i) the accumulation of heavy particles is closely related to the presence and the size of elliptic islands of regular passive tracer motion, and (ii) the percentage of accumulated heavy particles is enhanced by increasing the angular momentum and lowering the Stokes numbers.

HEAVY PARTICLES NEAR A HELICAL VORTEX FILAMENT

5 CHAPTER

The motion of small heavy particles near a helical vortex filament in incompressible flow is investigated. Both the configurations of a helical vortex filament in free space and a helical vortex filament concentrically positioned in a pipe are considered, and the corresponding helically symmetric velocity fields are expressed in terms of stream functions. Particle motion is assumed to be driven by Stokes drag, and the flow fields are assumed to be independent from the motion of particles. Numerical results show that heavy particles may be attracted to helical trajectories. The stability of these attraction trajectories is demonstrated by linear stability analysis. In addition, the correlation between the attraction trajectories and the streamline topologies is investigated.

5.1 Introduction

Helical vortex filaments are observed in many natural and industrial applications [28]. They can be found in wakes downstream of propellors and wind turbines [97], in combusting flows containing a precessing vortex core [2], and in industrial gas conditioners used for the separation of heavy particles and droplets, see section 1.2.3. In addition, a recent numerical study has shown that the advection of fluid particles in turbulence is largely influenced by the presence of small-scale helical vortices [11]. Helical vortex structures are also interesting from a theoretical point of view, because a helical vortex filament is the simplest three-dimensional vortex structure having non-zero curvature and non-zero torsion [10], [49], [66], [85]. Although the flow field induced by a helical vortex filament has been widely studied, the motion of heavy particles in such flows has received little attention. In the present chapter, we present particle trajectories and attraction trajectories generated by helical vortex flow, both in free space and in a pipe.

The velocity field induced by a vortex filament in an incompressible, inviscid fluid in free space is described by the Biot-Savart law. Hardin [30] evaluated the Biot-Savart law for the case of an infinite helical vortex filament in terms of an infinite

series of modified Bessel functions. The same series had already been found by Lamb [43] when he calculated the magnetic field induced by a spool. The velocity field derived by Hardin is invariant along helical curves and may therefore be formulated in terms of a two-dimensional stream function in helical coordinates. Mezić *et al.* [62] showed that the resulting flow field can have three different topologies, depending on the values of the helix curvature, the helix pitch (the length of one revolution) and the thickness of the vortex core.

The flow field induced by a helical vortex filament concentrically positioned in a pipe is different from the free space configuration, since the radial velocity on the pipe wall is required to be zero. To approximately accommodate this boundary condition, Sarasúa *et al.* [88] employ a single image vortex of helical shape exterior to the pipe, which leads to an exact formulation in the limit of infinite pitch of the helix. Okulov [69] produces an exact formulation by rigorous solution of the governing partial differential equation. As an alternative, we derive the stream function by employing a vortex distribution on the pipe wall, which efficiently reproduces the result of Okulov.

From experiments and numerical studies [2], it is known that a free helical vortex filament in a pipe can have a stationary shape, although the helix may propagate in itself. The self-induced velocity of a helical vortex filament can be calculated directly from the Biot-Savart law (see e.g. §7.1 of Batchelor's book [7]), leading to a singular logarithmic term. In case of a finite-core vortex the self-induced velocity is finite, and several models have been developed in order to overcome the singularity in the velocity induced by a vortex filament, see [13] and [84] for reviews. In the present work, the self-induced and wall-induced velocities are compensated by a uniform axial velocity field, to obtain a stationary helix.

In the present chapter, we investigate the motion of small heavy particles in the three-dimensional flow field around an infinite helical vortex filament, with the particle motion driven by Stokes drag. Gravity is neglected since it typically is a minor effect in many industrial applications. Both the configuration of a helical vortex filament in a pipe and in free space are studied. It is shown that heavy particles are attracted to a helical trajectory. The attraction is shown to take place for a wide range of Stokes numbers, and to be closely related to the streamline topology of the carrier flow.

In section 5.2, we derive the stream functions for the free space configuration as well as for the pipe configuration. In addition, the equations for particle motion are presented and transformed to a helical frame of reference. Finally, the numerical integration method is outlined. In section 5.3, the streamline topologies encountered are identified, and section 5.4 presents the results for the particle motion. Attraction trajectories are identified, and their stability is demonstrated by linear stability analysis. Finally, conclusions are formulated in section 5.5.

5.2 Physical-mathematical model

5.2.1 Flow field

We consider an infinitely long helical vortex filament with strength Γ, winding radius a, and pitch $h = 2\pi l$, located within a cylindrical pipe with radius R. A uniform flow U_∞ in axial direction is superimposed onto the flow field in order to fix the helix in space. All variables are made dimensionless by Γ and a, such that the problem is completely defined by the dimensionless parameters l/a, $U_\infty a/\Gamma$, and R/a. A sketch of the helix configuration is given in Fig. 5.1. It is noted that the case of a helical vortex filament in free space corresponds to the limit $R/a \to \infty$.

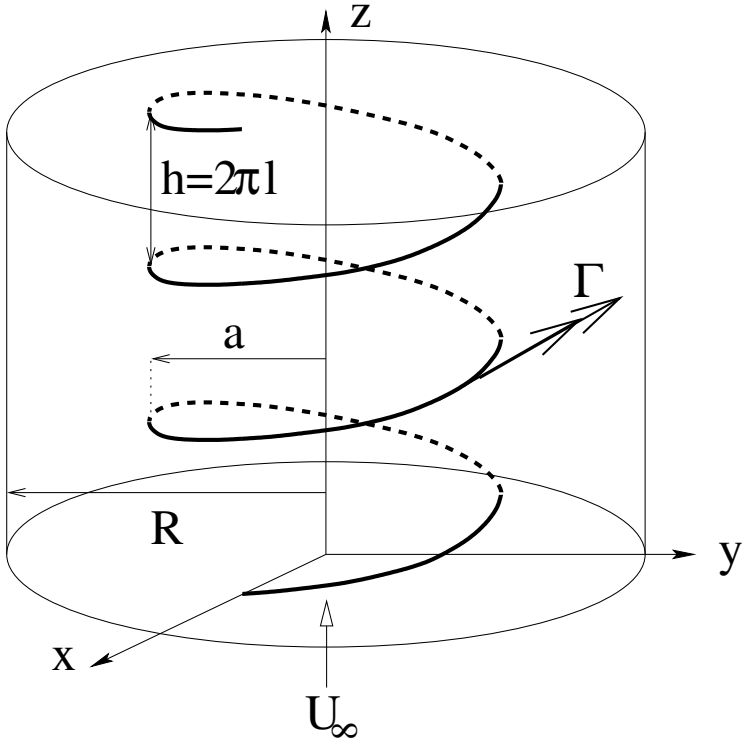

FIGURE 5.1: *Configuration of a helical vortex filament concentrically positioned in a pipe.*

We define a helical curve, or helix, with pitch $2\pi l/a$, and dimensionless winding radius r as:

$$\boldsymbol{h}(\alpha; \frac{l}{a}, r, \alpha_0) = \left(r\cos\alpha, r\sin\alpha, (\alpha - \alpha_0)\frac{l}{a} \right)^T , \tag{5.1}$$

where α is the coordinate along the helix, and α_0 is the value of α for which the z coordinate is zero. Without loss of generality we choose the helical vortex filament

as $\boldsymbol{h}(\alpha; \frac{l}{a}, 1, 0)$. The local tangent, normal, and binormal unit vectors (Frenet vectors) on helical curves are defined as:

$$\boldsymbol{t} \equiv \frac{\mathrm{d}\boldsymbol{h}}{\mathrm{d}\alpha}\left\|\frac{\mathrm{d}\boldsymbol{h}}{\mathrm{d}\alpha}\right\|^{-1}, \quad \boldsymbol{n} \equiv \frac{\mathrm{d}^2\boldsymbol{h}}{\mathrm{d}\alpha^2}\left\|\frac{\mathrm{d}^2\boldsymbol{h}}{\mathrm{d}\alpha^2}\right\|^{-1}, \quad \boldsymbol{b} \equiv \boldsymbol{t} \times \boldsymbol{n}. \tag{5.2}$$

In terms of the unit basis vectors in cylindrical coordinates, $\boldsymbol{e}_r$, $\boldsymbol{e}_\theta$ and $\boldsymbol{e}_z$, and introduction of:

$$\beta \equiv \left(1 + \left(\frac{ar}{l}\right)^2\right)^{-1/2}, \tag{5.3}$$

these expressions can be written as:

$$\boldsymbol{t} = \beta\left(\boldsymbol{e}_z + \frac{ar}{l}\boldsymbol{e}_\theta\right), \quad \boldsymbol{n} = -\boldsymbol{e}_r, \quad \boldsymbol{b} = \beta\left(\frac{ar}{l}\boldsymbol{e}_z - \boldsymbol{e}_\theta\right). \tag{5.4}$$

To introduce the concept of helical symmetry, we use an orthogonal map $\boldsymbol{\xi}(\boldsymbol{x})$, which defines helical coordinates $\boldsymbol{\xi} = (\xi, \eta, \zeta)^T$:

$$\boldsymbol{\xi}(\boldsymbol{x}) = R\left(\frac{az}{l}\right)\boldsymbol{x}, \quad R\left(\frac{az}{l}\right) = \begin{pmatrix} \cos\left(\frac{az}{l}\right) & \sin\left(\frac{az}{l}\right) & 0 \\ -\sin\left(\frac{az}{l}\right) & \cos\left(\frac{az}{l}\right) & 0 \\ 0 & 0 & 1 \end{pmatrix}. \tag{5.5}$$

The map $\boldsymbol{\xi}(\boldsymbol{x})$ is illustrated in Fig. 5.2. Helical curves in the $\boldsymbol{x}$-frame reduce to straight lines parallel to the ζ-axis in the $\boldsymbol{\xi}$-frame. As a consequence, the helical vortex filament, which is projected onto the (x, y)-plane as the unit circle, is projected onto the (ξ, η)-plane as a single point. A function $f(\boldsymbol{x})$ is called helical symmetric if it is independent of ζ:

$$\frac{\partial f}{\partial \zeta} = 0. \tag{5.6}$$

Let the velocity field in the $\boldsymbol{x}$-frame be denoted by $\boldsymbol{u}$. In terms of cylindrical coordinates related to the $\boldsymbol{x}$-frame, $(r, \theta, z)^T$, the velocity components are u_r, u_θ, and u_z, respectively. Furthermore, let the velocity field in the $\boldsymbol{\xi}$-frame be denoted by $\boldsymbol{v}$. In terms of cylindrical coordinates related to the $\boldsymbol{\xi}$-frame, $(r, \phi, \zeta)^T$, with $\phi = \theta - za/l$, the velocity components are v_r, v_ϕ, and v_ζ, respectively. The following relations are valid [30]:

$$v_r = u_r, \quad v_\phi = u_\theta - \frac{ar}{l}u_z, \quad v_\zeta = u_z. \tag{5.7}$$

For a helical vortex filament in free space, as well as for a helical vortex filament enclosed by a concentric circular pipe, we have:

$$\frac{\partial \boldsymbol{v}}{\partial \zeta} = 0, \tag{5.8}$$

i.e., the velocity field $\boldsymbol{v}$ is helically symmetric [2], [46].

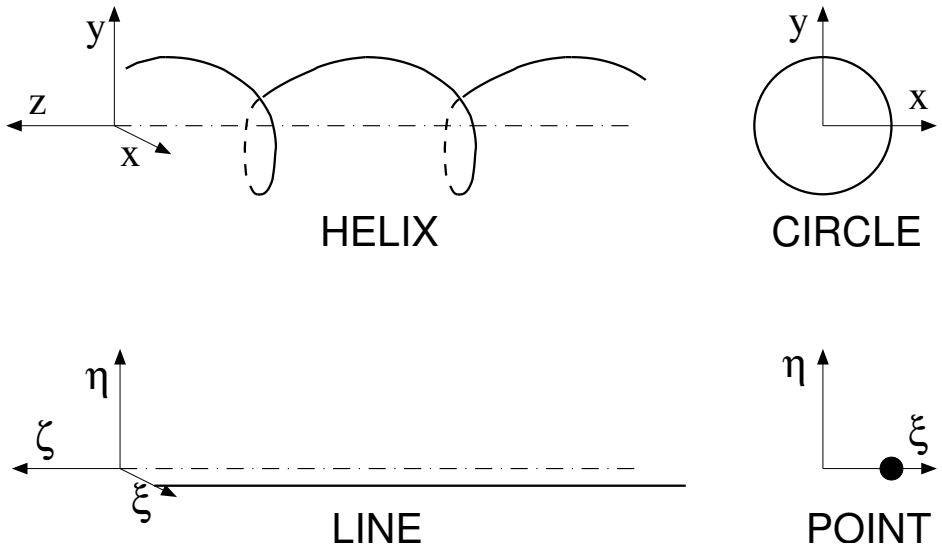

FIGURE 5.2: *Helical vortex filament in the $\boldsymbol{x}$-frame and in the $\boldsymbol{\xi}$-frame.*

Because of helical symmetry, the flow field can be described by a stream function $\Psi(r, \phi)$, and the velocities follow from the canonical equations:

$$v_r = \frac{1}{r}\frac{\partial \Psi}{\partial \phi}, \quad v_\phi = -\frac{\partial \Psi}{\partial r}. \tag{5.9}$$

The stream function can be decomposed into three terms:

$$\Psi = \Psi_u + \Psi_w + \Psi_\infty, \tag{5.10}$$

where Ψ_u accounts for the flow induced by a stationary helical vortex filament in free space, Ψ_w accommodates a correction due to the presence of the pipe wall, and Ψ_∞ accounts for the uniform axial flow.

The stream function Ψ_u can be obtained from the Biot-Savart law [30]:

$$\Psi_u = \begin{cases} \dfrac{1}{4\pi}\left(r^2\dfrac{a^2}{l^2}\right) - \dfrac{ra^2}{\pi l^2}\displaystyle\sum_{m=1}^{\infty} I'_m\left(\frac{ma}{l}r\right)K'_m\left(\frac{ma}{l}\right)\cos m\phi, & r < 1, \\ \dfrac{1}{4\pi}\left(\dfrac{a^2}{l^2} - \ln r^2\right) - \dfrac{ra^2}{\pi l^2}\displaystyle\sum_{m=1}^{\infty} I'_m\left(\frac{ma}{l}\right)K'_m\left(\frac{ma}{l}r\right)\cos m\phi, & r > 1. \end{cases} \tag{5.11}$$

Here, I_m and K_m, denote modified Bessel functions of the first and second kind, respectively, and the prime represents differentiation with respect to the argument.

The stream function Ψ_w satisfies the boundary condition

$$\frac{1}{r}\frac{\partial \Psi_w}{\partial \phi} = -\frac{1}{r}\frac{\partial \Psi_u}{\partial \phi} \text{ for } r = R/a. \tag{5.12}$$

Although an expression for Ψ_w was obtained by Okulov [69] by formally solving a partial differential equation in r and ϕ subject to the condition (5.12), we present a different approach based on the observation that Ψ_w corresponds to a continuous vortex disribution Γ'_w on the pipe wall. Because of helical symmetry, Γ'_w is a periodic function of ϕ, independent of ζ, which can be expressed as a Fourier series:

$$\Gamma'_w(\phi') = \sum_{k=1}^{\infty} [a_k \cos(k\phi') + b_k \sin(k\phi')]. \tag{5.13}$$

The term a_0 has been omitted, since it only generates a uniform axial flow inside the circular pipe. The flow field induced follows from the Biot-Savart law, and can be calculated using Hardin's solution method (for $r < 1$):

$$\Psi_w = \int_0^{2\pi} r^2 \Gamma'_w(\phi') \frac{a^2}{4\pi l^2} d\phi' - \tag{5.14}$$

$$- \int_0^{2\pi} r \Gamma'_w(\phi') \frac{aR}{\pi l^2} \sum_{m=1}^{\infty} I'_m(mra/l) K'_m(mR/l) \cos(m(\phi - \phi')) d\phi'. \tag{5.15}$$

With

$$\cos(m(\phi - \phi')) = \cos(m\phi)\cos(m\phi') + \sin(m\phi)\sin(m\phi'),$$

and the standard integrals

$$\int_0^{2\pi} \cos(k\phi')\cos(m\phi') d\phi' = \delta_{km}\pi, \quad k, m \geq 1,$$

$$\int_0^{2\pi} \sin(k\phi')\sin(m\phi') d\phi' = \delta_{km}\pi, \quad k, m \geq 1,$$

the following expression is obtained:

$$\Psi_w = \frac{a_0 r^2}{4} \frac{a^2}{l^2}$$

$$- \frac{raR}{l^2} \sum_{m=1}^{\infty} a_m I'_m(mra/l) K'_m(mR/l) \cos(m\phi)$$

$$- \frac{raR}{l^2} \sum_{m=1}^{\infty} b_m I'_m(mra/l) K'_m(mR/l) \sin(m\phi). \tag{5.16}$$

Substitution of Eq. (5.16) and Eq. (5.11) into Eq. (5.12) yields:

$$\begin{aligned} a_m &= -\frac{a}{\pi R}\frac{I'_m(ma/l)}{I'_m(mR/l)}, \quad m \geq 1, \\ b_m &= 0, \quad \forall \quad m. \end{aligned}$$

and the resulting expression for Ψ_w is:

$$\Psi_w = \frac{ra^2}{\pi l^2}\sum_{m=1}^{\infty} I'_m(mar/l)I'_m(ma/l)\frac{K'_m(mR/l)}{I'_m(mR/l)}\cos(m\phi). \tag{5.17}$$

The stream function Ψ_∞ is computed by requiring that the helical vortex filament be stationary. Due to its curvature, the helical vortex filament induces a velocity onto itself in the binormal direction. It is well-known that the magnitude of this velocity is infinite for an infinitely thin vortex filament [7], [49], [66], [84]. For a vortex with a finite core radius ϵ, however, an approximation for the self-induced velocity $\boldsymbol{U}_{s,u}$ has been derived by Da Rios [85] for a helical vortex with pitch l:

$$\boldsymbol{U}_{s,u} = \frac{1}{4\pi(1 + a^2/l^2)}\ln\Big(\frac{1 + l^2/a^2}{\epsilon/a}\Big)\boldsymbol{b}, \tag{5.18}$$

which is valid for small core radii, i.e. $\epsilon/a \ll (1 + (l/a)^2)$. In addition to the self-induced motion, the vortex filament moves under the influence of the wall vorticity:

$$\boldsymbol{U}_{s,w} = \beta\Big(\frac{\partial\Psi_w}{\partial r}\Big)\boldsymbol{b}. \tag{5.19}$$

Substitution of Eq. (5.17) into Eq. (5.19) yields

$$\boldsymbol{U}_{s,w} = \frac{a\sqrt{1 + a^2/l^2}}{\pi l}\sum_{m=1}^{\infty} mI_m(ma/l)I'_m(ma/l)\frac{K'_m(mR/l)}{I'_m(mR/l)}\boldsymbol{b}. \tag{5.20}$$

Since the product $I_m(ma/l)I'_m(ma/l) < 0$, the wall-induced velocity is directed opposite to the self-induced velocity of the helical vortex filament. To obtain a stationary filament, the sum of the wall-induced velocity and the self-induced velocity must be compensated for by a uniform axial velocity U_∞, such that:

$$\Big(\frac{U_\infty a}{\Gamma}\boldsymbol{e}_z + \boldsymbol{U}_{s,u} + \boldsymbol{U}_{s,w}\Big)\cdot\boldsymbol{b} = 0. \tag{5.21}$$

Therefore,

$$\begin{aligned} \frac{U_\infty a}{\Gamma} &= -\frac{1}{\pi}\frac{a}{l}\left(1 + \frac{a^2}{l^2}\right)\left[\frac{1}{4}\left(1 + \frac{a^2}{l^2}\right)^{-3/2}\ln\left(\frac{1 + l^2/a^2}{\epsilon/a}\right)\right. \\ &+ \left.\frac{l}{a}\sum_{m=1}^{\infty} mI_m\left(\frac{ma}{l}\right)\frac{K'_m\left(\frac{mR}{l}\right)}{I'_m\left(\frac{mR}{l}\right)}I'_m\left(\frac{ma}{l}\right)\right], \end{aligned} \tag{5.22}$$

which defines a relation between the dimensionless parameters $U_\infty a/\Gamma$, l/a, R/a and ϵ/a. It is noted that when $U_\infty a/\Gamma > 0$, wall-induced velocity dominates over self-induced velocity, and when $U_\infty a/\Gamma < 0$, self-induced velocity dominates over wall-induced velocity.

Finally, the corresponding stream function Ψ_∞ is:

$$\Psi_\infty = \frac{r^2}{2}\Big(\frac{a}{l}\Big)\Big(\frac{U_\infty a}{\Gamma}\Big), \tag{5.23}$$

and the composite stream function Ψ becomes:

$$\Psi = \begin{cases} \dfrac{r^2a^2}{4\pi l^2} + \dfrac{r^2 a}{2l}\Big(\dfrac{U_\infty a}{\Gamma}\Big) - \dfrac{ra^2}{\pi l^2}\displaystyle\sum_{m=1}^{\infty} I'_m(mra/l)Z'_m(ma/l)\cos m\phi, & r < 1, \\ \dfrac{a^2}{4\pi l^2} - \dfrac{1}{4\pi}\ln r^2 + \dfrac{r^2 a}{2l}\Big(\dfrac{U_\infty a}{\Gamma}\Big) - \dfrac{ra^2}{\pi l^2}\displaystyle\sum_{m=1}^{\infty} I'_m(ma/l)Z'_m(mra/l)\cos m\phi, & r > 1, \end{cases}$$

with Z_m defined as:

$$Z_m(mx/l) \equiv K_m(mx/l) - \frac{K'_m(mR/l)}{I'_m(mR/l)} I_m(mx/l). \tag{5.24}$$

It is noted that, in the limit of $R/a \to \infty$, the function Z_m reduces to K_m, so that the free space formulation Eq. (5.11) is retrieved.

The velocity components $(u_r, u_\theta, u_z)^T$ can be retrieved from Eq. (5.24) by using the expressions for the vorticity $\boldsymbol{\omega} = \nabla \times \boldsymbol{u}$. Since $\boldsymbol{\omega} \cdot \boldsymbol{n} = 0$ and $\boldsymbol{\omega} \cdot \boldsymbol{b} = 0$ everywhere in the flow, it can be shown that:

$$u_z + r\frac{a}{l}u_\theta = u_0, \tag{5.25}$$

where u_0 is a constant. By means of Eq. (5.7) and Eq. (5.25), we can express the three components of $\boldsymbol{u}$ in terms of v_r, v_ϕ and u_0:

$$u_r = v_r, \quad u_\theta = \beta^2\Big(v_\phi + r\frac{a}{l}u_0\Big), \quad u_z = \beta^2\Big(u_0 - r\frac{a}{l}v_\phi\Big). \tag{5.26}$$

The value of u_0 can be determined by noting that $\boldsymbol{\omega} \cdot \boldsymbol{t} = 0$ everywhere except on the vortex filament:

$$\boldsymbol{\omega} \cdot \boldsymbol{t} = \frac{2\beta^5 u_0 a}{l} - \beta\Big[\frac{1}{r^2}\frac{\partial^2\Psi}{\partial\phi^2} + \frac{1}{r}\frac{\partial}{\partial r}\Big(r\beta^2\frac{\partial\Psi}{\partial r}\Big)\Big] = 0, \quad \forall \quad (r,\phi) \neq (1,0), \tag{5.27}$$

which leads to:

$$u_0 = \frac{a}{2\pi l} + \frac{U_\infty a}{\Gamma}. \tag{5.28}$$

As a result, the velocity components $(u_r, u_\theta, u_z)^T$ become:

$$u_r = \begin{cases} \dfrac{a^2}{\pi l^2} \displaystyle\sum_{m=1}^{\infty} m I'_m\left(\frac{ma}{l}r\right) Z'_m\left(\frac{ma}{l}\right) \sin m\phi, & r < 1, \\ \dfrac{a^2}{\pi l^2} \displaystyle\sum_{m=1}^{\infty} m I'_m\left(\frac{ma}{l}\right) Z'_m\left(\frac{ma}{l}r\right) \sin m\phi, & 1 < r < \dfrac{R}{a}, \end{cases} \tag{5.29}$$

$$u_\theta = \begin{cases} \dfrac{a}{\pi r l} \displaystyle\sum_{m=1}^{\infty} m I_m\left(\frac{ma}{l}r\right) Z'_m\left(\frac{ma}{l}\right) \cos m\phi, & r < 1, \\ \dfrac{1}{2\pi r} + \dfrac{a}{\pi r l} \displaystyle\sum_{m=1}^{\infty} m I'_m\left(\frac{ma}{l}\right) Z_m\left(\frac{ma}{l}r\right) \cos m\phi, & 1 < r < \dfrac{R}{a}, \end{cases} \tag{5.30}$$

$$u_z = \begin{cases} \dfrac{U_\infty a}{\Gamma} + \dfrac{a}{2\pi l} - \dfrac{a^2}{\pi l^2} \displaystyle\sum_{m=1}^{\infty} m I_m\left(\frac{ma}{l}r\right) Z'_m\left(\frac{ma}{l}\right) \cos m\phi, & r < 1, \\ \dfrac{U_\infty a}{\Gamma} - \dfrac{a^2}{\pi l^2} \displaystyle\sum_{m=1}^{\infty} m I'_m\left(\frac{ma}{l}\right) Z_m\left(\frac{ma}{l}r\right) \cos m\phi, & 1 < r < \dfrac{R}{a}. \end{cases} \tag{5.31}$$

Eq. (5.29)-Eq. (5.31) are identical to the results obtained by Alekseenko *et al.* [2].

5.2.2 Particle motion

In many applications, such as gas-liquid separators, the particle-laden flow is dilute, and one-way coupling is an adequate approximation. The particles are assumed to be small, spherical, and to have a much higher mass density than the carrier fluid. In the present chapter, gravity is neglected in order to isolate the effect of particle inertia, i.e. Fr $\to \infty$, so that the dimensionless equations of motion for the particles, Eq. (2.5), reduce to:

$$\frac{\mathrm{d}\boldsymbol{x}_p}{\mathrm{d}t} = \boldsymbol{u}_p, \quad \frac{\mathrm{d}\boldsymbol{u}_p}{\mathrm{d}t} = \frac{1}{\mathrm{St}}(\boldsymbol{u} - \boldsymbol{u}_p), \tag{5.32}$$

where $\boldsymbol{x}_p$ and $\boldsymbol{u}_p$ denote the position and the velocity of the particle, respectively. The Stokes number St is the ratio between the particle relaxation time τ_p and a typical timescale of the flow. In the present chapter, we define the Stokes number as:

$$\mathrm{St} \equiv \frac{\tau_p \Gamma}{a^2}. \tag{5.33}$$

Transormation of Eq. (5.32) to the $\boldsymbol{\xi}$-frame gives

$$\frac{\mathrm{d}\boldsymbol{\xi}_p}{\mathrm{d}t} = \boldsymbol{v}_p, \quad \frac{\mathrm{d}\boldsymbol{v}_p}{\mathrm{d}t} = \frac{1}{\mathrm{St}}(\boldsymbol{v} - \boldsymbol{v}_p) - \boldsymbol{\Omega}_p \times (\boldsymbol{\Omega}_p \times \boldsymbol{\xi}_p) - 2\boldsymbol{\Omega}_p \times \boldsymbol{v}_p - \dot{\boldsymbol{\Omega}}_p \times \boldsymbol{\xi}_p, \tag{5.34}$$

where $\boldsymbol{\Omega}_p$ is defined as the rotation rate due to the translation of the particle along the z-axis:

$$\boldsymbol{\Omega}_p = (0, 0, \Omega_p)^T, \quad \Omega_p = \frac{a}{l} v_{\zeta,p}. \tag{5.35}$$

The three additional terms on the right-hand side of Eq. (5.34) represent acceleration terms due to the coordinate transformation: the centrifugal acceleration, the Coriolis acceleration, and the time-change of the rotation rate.

5.2.3 Numerical approach

The equations of motion for heavy particles, Eqs. (5.32), are solved numerically by using a 4-th order Runge-Kutta scheme. A particle trajectory is calculated for a series of decreasing values of the time step, where each next value is half of the previous value. When the differences between two subsequent trajectories are below a certain preset level, the last obtained solution is considered sufficiently accurate. For each particle, both its initial position and its initial velocity are required. The initial velociy of a particle is taken equal to the local velocity of the carrier flow at the initial position of the particle. The pipe wall is modelled as an absorbing wall; particles that reach the wall stay there.

The velocity components of the carrier flow, which need to be calculated during each time step in the Runge-Kutta scheme, are obtained from Eq. (5.29)-Eq. (5.31). In the calculation procedure, the modified Bessel functions are evaluated using a routine from Press *et al.* [78]. This routine is based on a system of four equations for the unknown functions $I_n(\hat{z})$, $I_n'(\hat{z})$, $K_n(\hat{z})$, and $K_n'(\hat{z})$, for fixed n and $\hat{z}$. The algorithm is not universally applicable: for $|\hat{z}| \ll 1$, for $|\hat{z}| > 10^6$ and for $n > 100$, different algorithms have to be used.

Firstly, the argument $\hat{z}$ in the modified Bessel functions becomes very small when $r \downarrow 0$, causing a problem in evaluating the term $\frac{1}{r} I_m(mra/l)$ which appears in Eq. (5.30). In order to avoid this, the following asymptotic expansion is used [1], [100]:

$$I_n(\hat{z}) \simeq \frac{(\frac{1}{2}\hat{z})^n}{n!}, \qquad \text{for } z \ll 1. \tag{5.36}$$

In this way, the tangential velocity component on the z-axis becomes

$$\lim_{r\downarrow 0} u_\theta = \frac{1}{2\pi} Z_1'(\frac{a}{l}) \cos\phi. \tag{5.37}$$

For large orders ($n \gg 1$), the modified Bessel functions of the first kind and their derivatives approach zero. On the other hand, the modified Bessel functions of the second kind and their derivatives approach infinity. Their products, however, remain finite. These products have been calculated using an asymptotic expansion, derived from theory of differential equations with a large parameter [70].

Finally, for large arguments ($|\hat{z}| \to \infty$), an asymptotic expansion has been implemented, based on theory for differential equations with an irregular singularity [70].

As was stated by Hardin [30], the series in Eq. (5.29) to Eq. (5.31) converge for all ϕ and $r \neq 1$. For $r = 1$, the series do not converge, and for $r \simeq 1$ the convergence

is very slow. Therefore, the series cannot be used if a particle is within a cylindrical shell with inner radius $r^- = 1 - \delta$ and outer radius $r^+ = 1 + \delta$, with δ a small number, here taken equal to 0.005. Inside this shell, a linear interpolation is applied:

$$f(r,\phi) = \frac{(r^+ - r)f(r^-,\phi) + (r - r^-)f(r^+,\phi)}{r^+ - r^-}, \tag{5.38}$$

for any function $f(r,\phi)$.

5.3 Flow field topologies

We present a classification of the flow field topologies as determined by the dimensionless groups R/a, l/a and $U_\infty a/\Gamma$. The limiting case of $R/a \to \infty$ has been described by Mezić *et al.* [62]. The flow field topologies are distinguished by the presence, character and location of stagnation points $\boldsymbol{\xi}_0$, i.e., points of zero velocity in the $\boldsymbol{\xi}$-frame:

$$v_r(\boldsymbol{\xi}_0) = \frac{1}{r}\frac{\partial \Psi}{\partial \phi} = 0, \quad v_\phi(\boldsymbol{\xi}_0) = -\frac{\partial \Psi}{\partial r} = 0. \tag{5.39}$$

The character of a stagnation point is fully determined by the local value of the Hessian $\mathcal{H}$, defined as:

$$\begin{aligned} \mathcal{H} &\equiv \left(\frac{\partial^2\Psi}{\partial\xi^2}\right)\left(\frac{\partial^2\Psi}{\partial\eta^2}\right) - \left(\frac{\partial^2\Psi}{\partial\xi\partial\eta}\right)^2 = \\ &= \frac{1}{r^2}\left[\left(\frac{\partial^2\Psi}{\partial r^2}\right)\left(\frac{\partial^2\Psi}{\partial\phi^2}\right) + r\left(\frac{\partial\Psi}{\partial r}\right)\left(\frac{\partial^2\Psi}{\partial r^2}\right) + \frac{\partial}{\partial r}\left(\frac{1}{r}\left(\frac{\partial\Psi}{\partial\phi}\right)^2\right) - \left(\frac{\partial^2\Psi}{\partial r\partial\phi}\right)^2\right]. \end{aligned} \tag{5.40}$$

Let $\mathcal{H}_0 \equiv \mathcal{H}(\boldsymbol{\xi}_0)$, then we have the following classification:

$$\mathcal{H}_0 \begin{cases} > 0 & \to \quad \text{elliptic point, extreme value of } \Psi \\ < 0 & \to \quad \text{hyperbolic point, saddle point of } \Psi \end{cases} \tag{5.41}$$

Due to symmetry, stagnation points only exist on the line $\eta = 0$ and on the circle $r \equiv \sqrt{\xi^2 + \eta^2} = R/a$. On these curves $v_r \equiv 0$, and the existence of stagnation points is completely determined by the condition $v_\phi = 0$. Since $\partial v_r/\partial\phi = 0$ for $r = R/a$, critical points on the pipe wall are hyperbolic points. On the ξ-axis, on the other hand, critical points can be either elliptic, hyperbolic or shear points.

The presence of stagnation points is examined here for a wide range of values for the dimensionless parameters: $-5 \le U_\infty a/\Gamma \le 5$ (step size of 0.05), $0 < l/a \le 5$ (step size of 0.05), and R/a= 1.05, 1.1, 1.25, 1.5, 2.0, 2.5, 3.0, 4.0, 5.0, and ∞, respectively. As a result, seven different topologies have been found, summarized in Table 5.1, and examples of each topology are shown in Fig. 5.3.

When $R/a \to \infty$, there is no wall-induced velocity, so that $U_\infty a/\Gamma$ is negative. In this case, only topologies I, II and III have been found, see Fig. 5.4. In the same

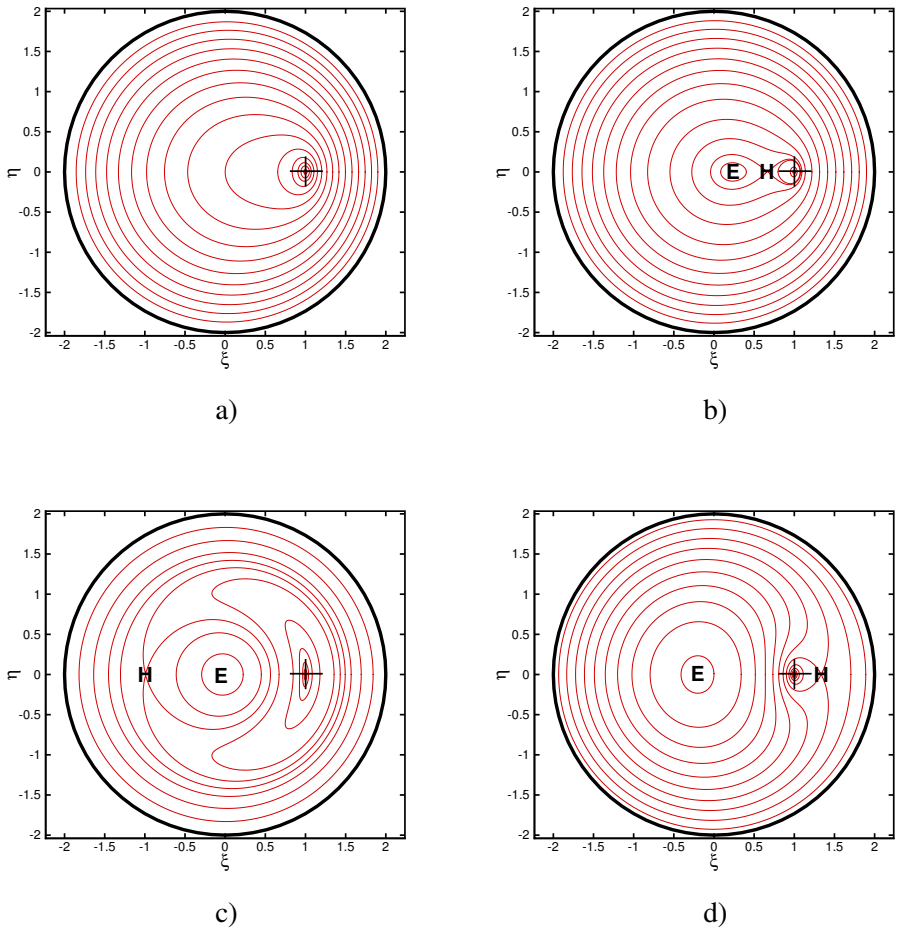

FIGURE 5.3: *Examples of different topologies in a helical vortex flow. a) Topology I;* $R/a = 2.0$; $l/a = 1.0$; $U_\infty a/\Gamma = -0.5$. *b) Topology II;* $R/a = 2.0$; $l/a = 1.0$; $U_\infty a/\Gamma = -1.0$. *c) Topology III;* $R/a = 2.0$; $l/a = 0.25$; $U_\infty a/\Gamma = -0.25$. *d) Topology IV;* $R/a = 2.0$; $l/a = 1.0$; $U_\infty a/\Gamma = 0.5$.

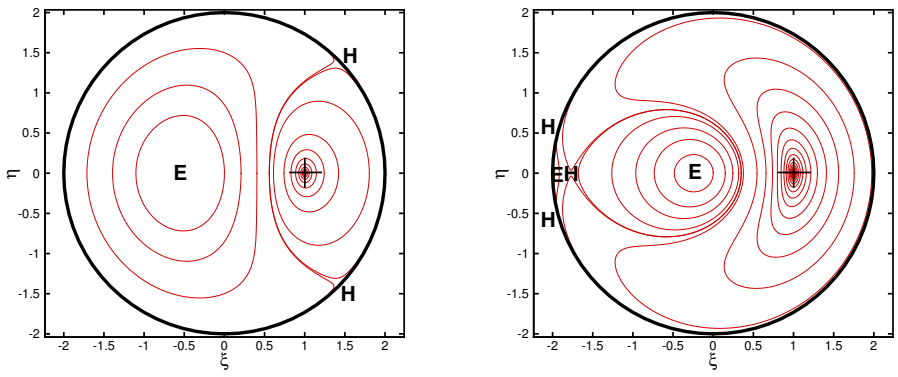

e) f)

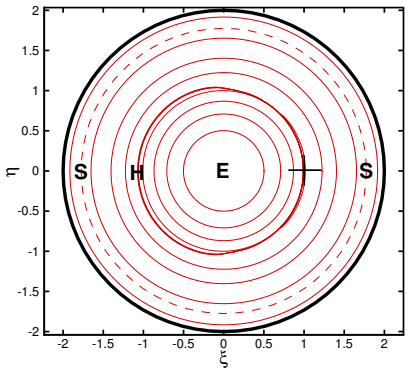

g)

FIGURE 5.3 (CONTINUED): *Examples of different topologies in a helical vortex flow. e) Topology V;* $R/a = 2.0$; $l/a = 1.0$; $U_\infty a/\Gamma = 0.1$. *f) Topology VI;* $R/a = 2.0$; $l/a = 0.5$; $U_\infty a/\Gamma = -0.03$. *g) Topology VII;* $R/a = 2.0$; $l/a = 0.01$; $U_\infty a/\Gamma = 0.0005$.

Topology	# at ξ-axis	Type and location of points at the ξ-axis	# at pipe wall
I	0	-	0
II	2	$0 < \xi_E < \xi_H < 1$	0
III	2	$-R/a < \xi_H < \xi_E < 0$	0
IV	2	$-R/a < \xi_E < 0$; $1 < \xi_H < R/a$	0
V	1	$0 < \xi_E < R/a$	2
VI	3	$-R/a < \xi_{E,1} < \xi_H < \xi_{E,2} < 0$	2
VII	4	$-R/a < \xi_{S,1} < \xi_H < \xi_E < 0$; $1 < \xi_{S,2} < R/a$	0

TABLE 5.1: *Classification of topologies in bounded space; ξ_E is the location of an elliptic point, ξ_H is the location of a hyperbolic point and ξ_S is the location of a shear point.*

figure, we also show iso-lines of the dimensionless vortex core thickness, ϵ/a, which is uniquely determined by the values of $U_\infty a/\Gamma$, l/a and R/a. The result agrees with the work of Mezic *et al.* [62], who used different dimensionless parameters:

$$a/l, \quad \text{and} \quad \gamma \equiv \frac{-a}{\pi l \sqrt{1 + a^2/l^2}} \Big(\frac{U_\infty a}{\Gamma} \Big).$$

Topology I is the dominant topology as the pitch l/a increases, whereas topology II occurs for small pitches and moderate vortex core thicknesses. When $l/a > 1$, topology II still exists, but then it is restricted to extremely small values of the vortex core ϵ/a. Finally, the occurence of topology III is limited by the (l/a)-axis and the line $-U_\infty l/\Gamma$ = constant [62].

In the wall-bounded case, topologies IV, V, VI and VII exist in addition to topologies I, II and III. Topologies IV and V both contain one elliptic stagnation point on the negative ξ-axis, and they occur for a wide range of values for l/a, $U_\infty a/\Gamma$, and R/a. Topology VI exists in a very narrow band in parameter space only and is therefore not visible in Fig. 5.5. It includes two counterrotating elliptic islands on the negative ξ-axis. Finally, topology VII occurs for very small pitches only ($l/a < 0.1$), and is characterized by an almost circular line where the velocity is zero; such a stagnation line corresponds to a shear flow.

The topologies II to VII are characterized by the presence of one or two elliptic stagnation points. In topology II the elliptic stagnation point is always located on the positive ξ-axis, and the flow field around it is corotating with the vortex. In contrast, in topologies III to VII the elliptic stagnation points are all located on the negative ξ-axis, and the flow field around them is counterrotating with the vortex.

In the limiting case of $l/a \to \infty$, topology I occurs in the unbounded case. The resulting flow field is similar to the one induced by a rectilinear vortex filament. For the wall-bounded case, topology V occurs when the helix pitch approaches infinity. This

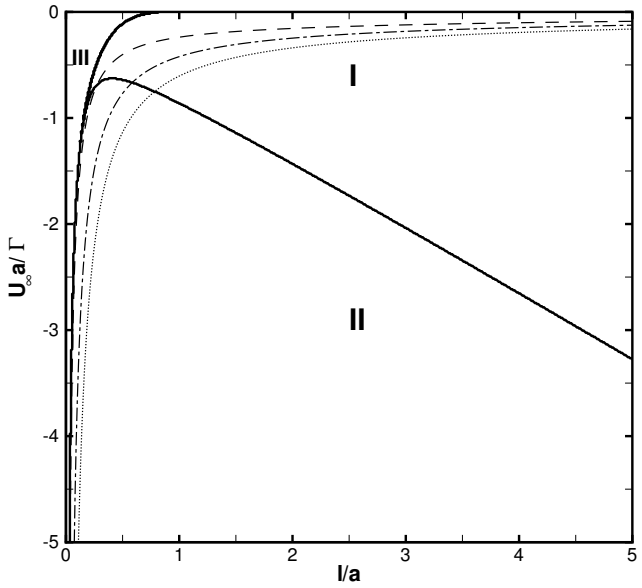

FIGURE 5.4: *Flow field topologies as a function of l/a and $U_\infty a/\Gamma$ in unbounded space ($R/a \to \infty$). Corresponding isolines of the dimensionless core radius ϵ/a are shown, too; dashed: $\epsilon/a = 10^{-1}$, dash-dotted: $\epsilon/a = 10^{-2}$, dotted: $\epsilon/a = 10^{-3}$.*

result is in agreement with the two-dimensional approximation of the helical vortex flow by a point vortex on a disk, as studied in Chapter 3. In the two-dimensional case, the self-induced velocity is defined to be zero, so that $U_\infty a/\Gamma$ is related explicitly to l/a and R/a:

$$\left(\frac{U_\infty a}{\Gamma}\right)_{2D} = \frac{1}{2\pi(R^2/a^2 - 1)}\left(\frac{l}{a}\right). \tag{5.42}$$

The influence of the torsion of the helical vortex filament on the flow field in topology V can be assessed by comparison with the point vortex model presented in Chapter 3. We determine the position of the elliptic stagnation point in the left half-plane and the position of the two hyperbolic stagnation points on the pipe wall, and compare these positions to the $2D$-approximation of the flow field. The calculation is repeated for a wide range of values of the helix pitch l/a, for the case the pipe radius is taken constant at $R/a = 2.0$. The axial velocity $U_\infty a/\Gamma$ is then obtained from Eq. (5.42). We define two errors as:

$$\begin{aligned} \text{Error}_H &= \|\boldsymbol{\xi}_{H,2D} - \boldsymbol{\xi}_{H,3D}\|, \\ \text{Error}_E &= \|\boldsymbol{\xi}_{E,2D} - \boldsymbol{\xi}_{E,3D}\|, \end{aligned}$$

The results are presented in Fig. 5.6, showing that the differences between the full 3D problem and its 2D approximation vanish as $l/a \to \infty$. The difference is only appreciable for $l/a \leq 10$.

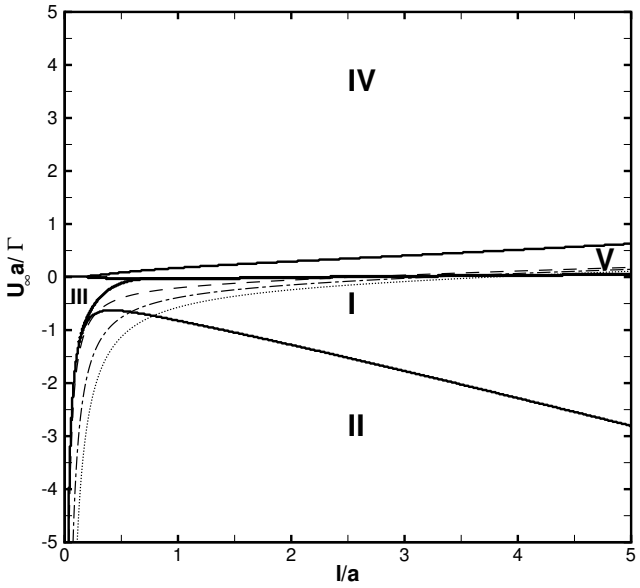

FIGURE 5.5: *Flow field topologies as a function of l/a and $U_\infty a/\Gamma$ in bounded space ($R/a = 2.0$). Corresponding isolines of the dimensionless core radius ϵ/a are shown, too; dashed: $\epsilon/a = 10^{-1}$, dash-dotted: $\epsilon/a = 10^{-2}$, dotted: $\epsilon/a = 10^{-3}$.*

5.4 Attraction trajectories

In this section we consider the motion of heavy particles in the flow fields presented in the previous section. In Fig. 5.7, the positions in the (ξ, η)-frame of 805 particles are plotted in the course of time, for a typical example of topology V; the particles are uniformly distributed at the start of the simulation. Some particles are quickly expelled from the circular domain. Most other particles, however, are approaching an attraction point. The attraction point in the (ξ, η)-frame corresponds to a helical attraction trajectory in the $\boldsymbol{x}$-frame. This is illustrated by Fig. 5.8 where the particle positions in physical space are plotted. Clearly, most particles approach a helical trajectory which is more or less in antiphase with the vortex filament.

In Fig. 5.9, we show the positions of initially uniformly distributed heavy particles after 100 dimensionless time units for topologies I-IV. Accumulation of particles in the center of the domain is observed in all topologies except for topology I.

In the remainder of this section we analyze this accumulation of particles. First, it is noted that a heavy particle can only be trapped in an attraction point if two conditions are met:

- a fixed point must exist, and
- the fixed point must be stable.

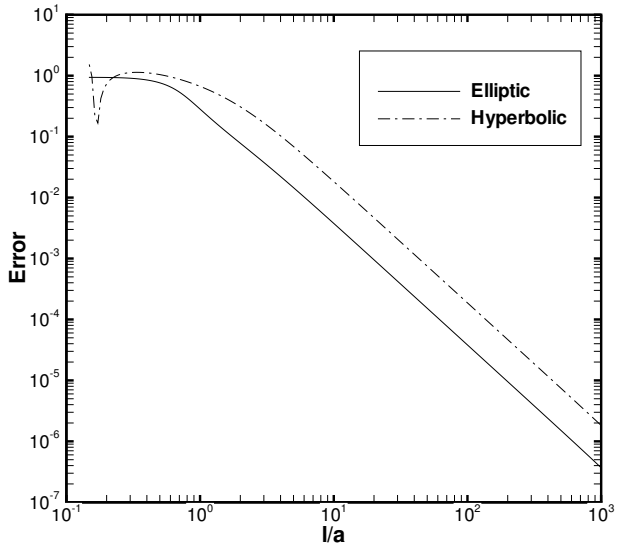

FIGURE 5.6: *Position of stagnation points in helical vortex flow field, compared to the 2D approximation, as a function of the helix pitch l/a; $R/a = 2$.*

These two conditions are investigated separately.

5.4.1 Fixed points

Let (ξ^*, η^*) denote a fixed point in the (ξ, η)-frame. Therefore, for a particle located at the fixed point the following relations hold:

$$\xi_p = \xi^*, \ \eta_p = \eta^*, \ v_{\xi,p} = 0, \ v_{\eta,p} = 0, \ v_{\zeta,p} = v_\zeta^*, \tag{5.43}$$

where (ξ_p, η_p, ζ_p) denotes the position of the particle in the $\boldsymbol{\xi}$-frame, and $(v_{\xi,p}, v_{\eta,p}, v_{\zeta,p})$ denotes its velocity. Substitution of the relations Eq. (5.43) into the equation of motion, viz. Eq. (5.34), gives:

$$\begin{aligned} \frac{\mathrm{d}\xi_p}{\mathrm{d}t} &= 0, \\ \frac{\mathrm{d}\eta_p}{\mathrm{d}t} &= 0, \\ \frac{\mathrm{d}\zeta_p}{\mathrm{d}t} &= v_\zeta(\xi^*, \eta^*), \end{aligned}$$

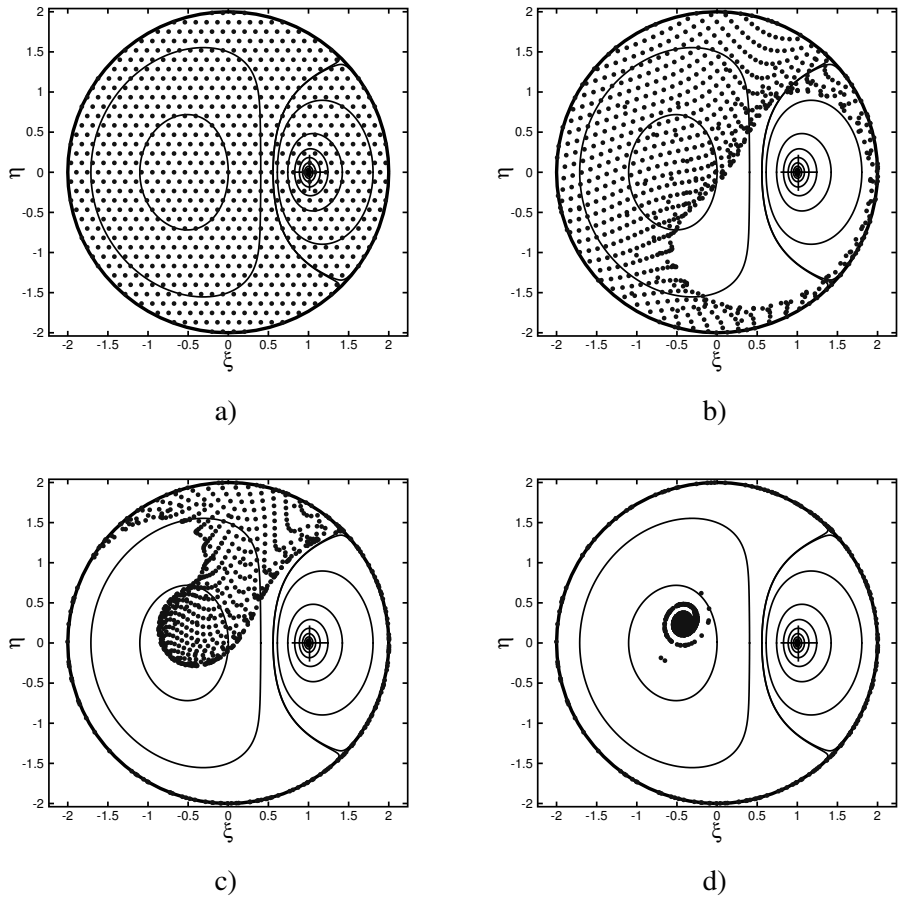

FIGURE 5.7: *Dots: positions of* 805 *heavy particles around helical vortex filament at four instants in time, in the curvilinear frame;* $l/a = 1.0, U_\infty a/\Gamma = 0.1, R/a = 2.0$ *(Topology V);* $St = 2.0$*: a)* $t = 0$*, b)* $t = 5$*, c)* $t = 25$*, d)* $t = 100$*. Streamlines of passive tracers are plotted as thin solid lines.*

$$\begin{aligned} \frac{\mathrm{d}v_{\xi,p}}{\mathrm{d}t} &= \frac{1}{\mathrm{St}}(v_\xi(\xi^*,\eta^*)) + \Omega^{*2}\xi^* = 0, \\ \frac{\mathrm{d}v_{\eta,p}}{\mathrm{d}t} &= \frac{1}{\mathrm{St}}(v_\eta(\xi^*,\eta^*)) + \Omega^{*2}\eta^* = 0, \\ \frac{\mathrm{d}v_{\zeta,p}}{\mathrm{d}t} &= 0, \end{aligned} \tag{5.44}$$

where $\Omega^* \equiv (a/l)v_\zeta(\xi^*,\eta^*)$. This reveals that the attraction trajectory corresponds to a point in velocity space, and to a straight line parallel to the ζ-axis in position space.

Inspection of Eq. (5.44) shows that the centrifugal force and the Stokes drag on a

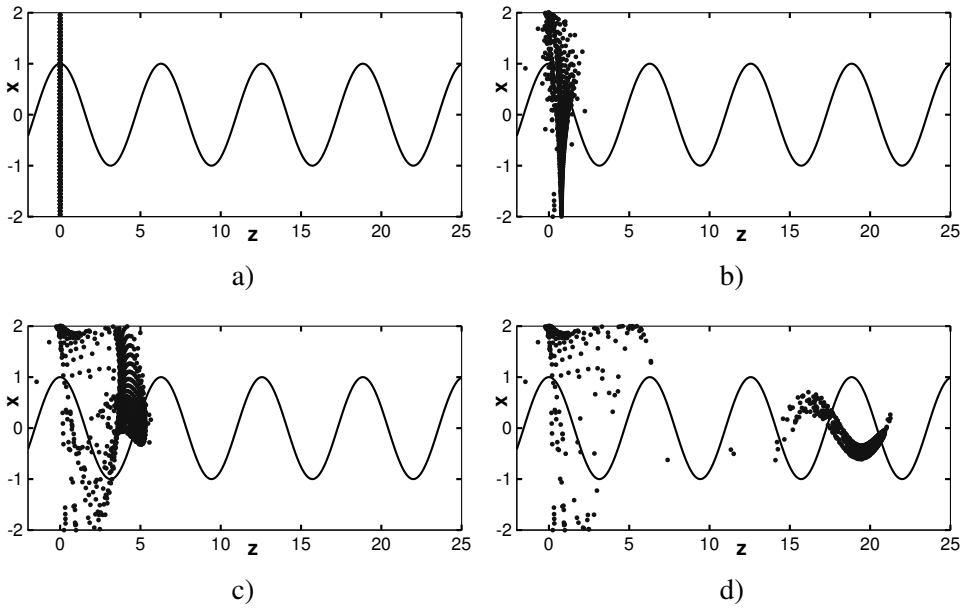

FIGURE 5.8: *Dots: positions in physical space of* 805 *heavy particles around helical vortex filament at four instants in time (top view);* $l/a = 1.0, U_\infty a/\Gamma = 0.1, R/a = 2.0$ *(Topology V);* $St = 2.0$*: a)* $t = 0$*, b)* $t = 5$*, c)* $t = 25$*, d)* $t = 100$*. The solid line denotes the position of the helical vortex filament.*

heavy particle are exactly balanced in a fixed point. Since the centrifugal force is always directed outward (with respect to the origin), we see that the velocity of the carrier flow in the fixed point must be directed in the radial direction. Hence, $v_\phi = 0$ and $v_r < 0$. Since it can be derived from Eq. (5.24) that $v_r = -(1/r)\partial\Psi/\partial\phi < 0$ if and only if $\eta > 0$, fixed points can only occur in the upper half of the (ξ, η)-plane.

After rewriting the fourth and the fifth relation of Eq. (5.44) as:

$$\begin{aligned} v_\xi(\xi^*, \eta^*) &= -\mathrm{St}\Omega^{*2}\xi^*, \\ v_\eta(\xi^*, \eta^*) &= -\mathrm{St}\Omega^{*2}\eta^*, \end{aligned} \tag{5.45}$$

we can conclude that the fixed point for $\mathrm{St} \downarrow 0$ is located near a stagnation point in the carrier flow. A fixed point for $\mathrm{St} \to \infty$, on the other hand, satisfies $|\boldsymbol{\xi}^*| \downarrow 0$. In Fig. 5.10, the location of the fixed points is plotted for a range of different Stokes numbers, for topologies II and III in the unbounded case. Clearly, the fixed point for $\mathrm{St} \downarrow 0$ is the elliptic stagnation point itself, whereas the fixed point for $\mathrm{St} \to \infty$ is the origin.

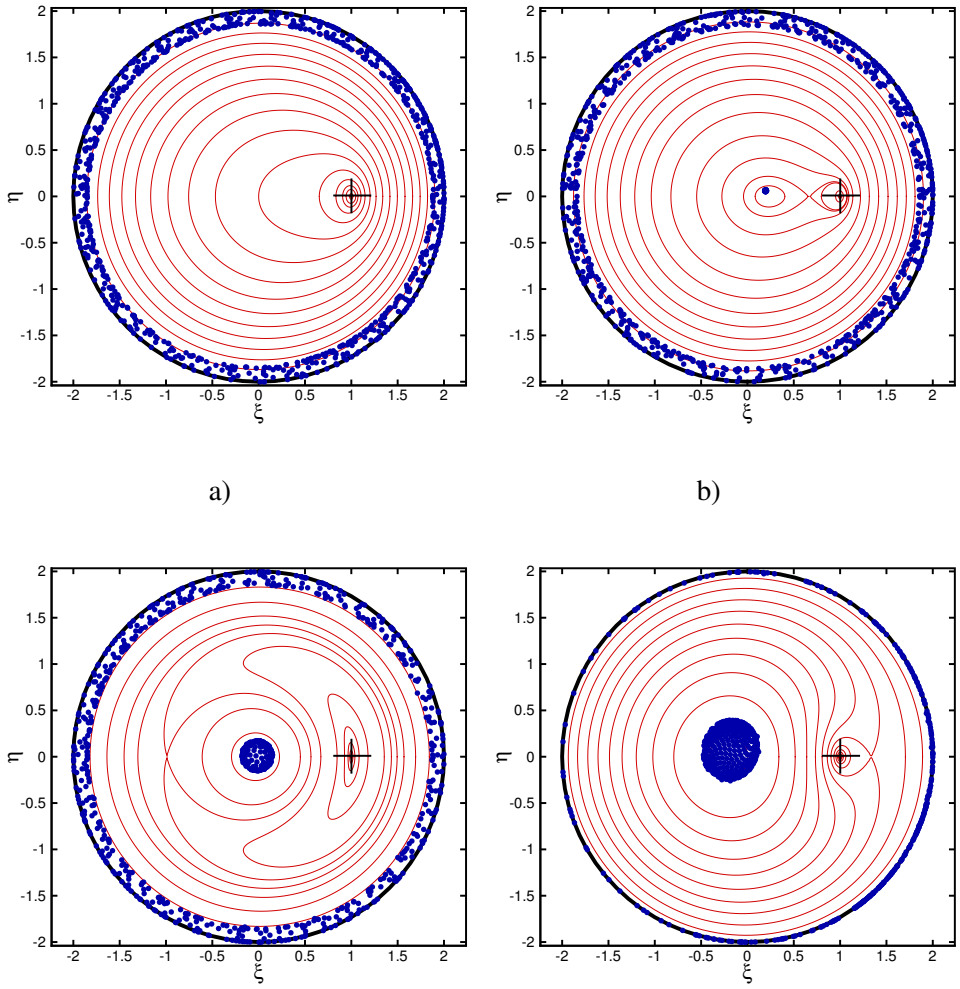

FIGURE 5.9: *Dots: positions of* 805 *initially uniformly distributed particles with St* = 0.5 *after dimensionless time* $t = 100$. *a) Topology I:* $l/a = 1.0; U_\infty a/\Gamma = -0.5; R/a = 2.0$. *b) Topology II:* $l/a = 1.0; U_\infty a/\Gamma = -1.0; R/a = 2.0$. *c) Topology III:* $l/a = 0.25; U_\infty a/\Gamma = -0.25; R/a = 2.0$. *d) Topology IV:* $l/a = 1.0; U_\infty a/\Gamma = 0.5; R/a = 2.0$.

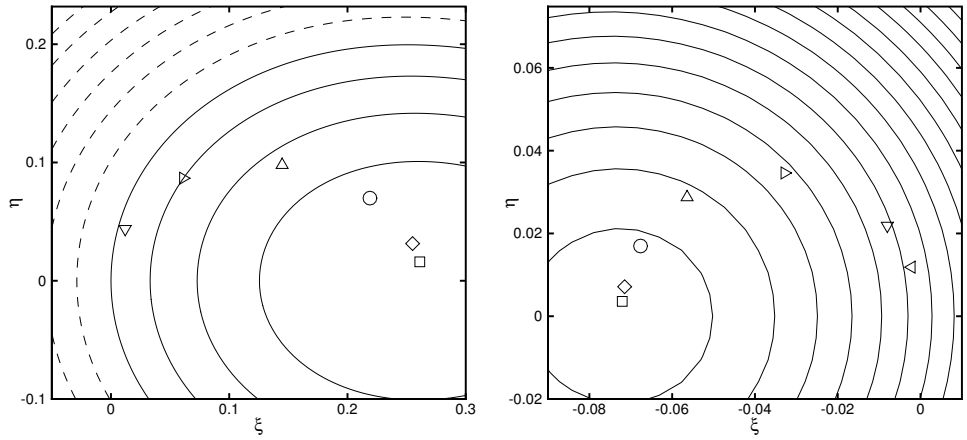

a) b)

FIGURE 5.10: *Position of attraction points for different Stokes numbers;* □ $St = 0.1$; ◇ $St = 0.2$; ◯ $St = 0.5$; △ $St = 1.0$; ▷ $St = 2.0$; ▽ $St = 5.0$; ◁ $St = 10.0$. *a) Example of topology II:* $l/a = 1.0$; $U_\infty a/\Gamma = -1.0$; $R/a \to \infty$. *b) Example of topology III:* $l/a = 0.25$; $U_\infty a/\Gamma = -0.5$; $R/a \to \infty$.

5.4.2 Stability of fixed points

In the present section we investigate the stability of the fixed-point trajectories in order to determine whether they are attraction trajectories. The physical reason for particle attraction is the Coriolis force, which in the $\boldsymbol{\xi}$-frame is directed perpendicularly to the particle trajectory. In the case when $\xi_E < 0$, the flow around the elliptic stagnation point is counterrotating with respect to the vortex, and $\Omega = (a/l)v_\zeta(\xi_E, 0) > 0$. As a result, the Coriolis force is directed to the center of the elliptic island. On the other hand, when $\xi_E > 0$, the flow around the elliptic stagnation point is corotating with the vortex. The velocity component v_ζ, however, is negative for $\xi_E > 0$, so that $\Omega < 0$. Hence, also in this case the Coriolis force is directed to the center of an elliptic island. Therefore there is no qualitative distinction in particle attraction for $\xi_E > 0$ (such as in topology II), compared to situations for which $\xi_E < 0$ (such as in topology III-VIII).

We carry out a linear stability analysis in order to investigate the stability of the attraction points. The five equations for ξ_p, η_p, $v_{\xi,p}$, $v_{\eta,p}$ and $v_{\zeta,p}$ in Eq. (5.34) are of the form:

$$\frac{\mathrm{d}\boldsymbol{\chi}}{\mathrm{d}t} = \boldsymbol{f}(\boldsymbol{\chi}), \tag{5.46}$$

with $\boldsymbol{\chi} \equiv [\xi_p, \eta_p, v_{\xi,p}, v_{\eta,p}, v_{\zeta,p}]^T$. Linearization of these equations around a fixed

point $\boldsymbol{\chi}^*$ leads to:

$$\frac{\mathrm{d}\chi_i}{\mathrm{d}t} = f_i(\boldsymbol{\chi}^*) + (\chi_j - \chi_j^*)\frac{\partial f_i}{\partial \chi_j}\bigg|_{\boldsymbol{\chi}^*} + O(|\boldsymbol{\chi} - \boldsymbol{\chi}^*|^2). \tag{5.47}$$

In the fixed point, $\boldsymbol{f}(\boldsymbol{\chi}^*) = 0$, which reduces Eq. (5.47) to:

$$\frac{\mathrm{d}\chi_i}{\mathrm{d}t} = \frac{\mathrm{d}(\chi_i - \chi_i^*)}{\mathrm{d}t} = (\chi_j - \chi_j^*)\frac{\partial f_i}{\partial \chi_j}\bigg|_{\boldsymbol{\chi}^*} + O(|\boldsymbol{\chi} - \boldsymbol{\chi}^*|^2). \tag{5.48}$$

If the real parts of all of the eigenvalues of the matrix $\partial f_i/\partial \chi_j$ are smaller than zero, any sufficiently small perturbation in $\boldsymbol{\chi}$ with respect to $\boldsymbol{\chi}^*$ will be damped, so that $|\boldsymbol{\chi} - \boldsymbol{\chi}^*| \to 0$ as $t \to \infty$. Based on Eq. (5.34), the matrix $M_{ij} \equiv \partial f_i/\partial \chi_j$ is:

$$M = \begin{pmatrix} 0 & 0 & \mathrm{St}^{-1}\frac{\partial v_\xi}{\partial \xi} + {\Omega_p}^2 + \eta_p\frac{\partial \dot{\Omega}_p}{\partial \xi} & \mathrm{St}^{-1}\frac{\partial v_\eta}{\partial \xi} - \dot{\Omega}_p - \xi_p\frac{\partial \dot{\Omega}_p}{\partial \xi} & \mathrm{St}^{-1}\frac{\partial v_\zeta}{\partial \xi} \\ 0 & 0 & \mathrm{St}^{-1}\frac{\partial v_\xi}{\partial \eta} + \dot{\Omega}_p + \eta_p\frac{\partial \dot{\Omega}_p}{\partial \eta} & \mathrm{St}^{-1}\frac{\partial v_\eta}{\partial \eta} + {\Omega_p}^2 + \xi_p\frac{\partial \dot{\Omega}_p}{\partial \eta} & \mathrm{St}^{-1}\frac{\partial v_\zeta}{\partial \eta} \\ 1 & 0 & -\mathrm{St}^{-1} & -2\Omega_p & 0 \\ 0 & 1 & 2\Omega_p & -\mathrm{St}^{-1} & 0 \\ 0 & 0 & \eta_p\frac{\partial \dot{\Omega}_p}{\partial v_{\zeta,p}} + 2(\Omega_p\xi_p + v_{\eta,p})\frac{\partial \Omega_p}{\partial v_{\zeta,p}} & -\xi_p\frac{\partial \dot{\Omega}_p}{\partial v_{\zeta,p}} + 2(\Omega_p\eta_p - v_{\xi,p})\frac{\partial \Omega_p}{\partial v_{\zeta,p}} & -\mathrm{St}^{-1} \end{pmatrix}^T. \tag{5.49}$$

Expressing Ω_p and $\dot{\Omega}_p$ in terms of the independent variables, and evaluating the matrix at $\boldsymbol{\chi}^*$ leads to:

$$M = \begin{pmatrix} 0 & 0 & \Omega^{*2} + \mathrm{St}^{-1}\Psi_{\xi\eta} + (\eta^*/\mathrm{St})(a/l)\frac{\partial v_\zeta}{\partial \xi} & -\mathrm{St}^{-1}\Psi_{\xi\xi} - (\xi^*/\mathrm{St})(a/l)\frac{\partial v_\zeta}{\partial \xi} & \mathrm{St}^{-1}\frac{\partial v_\zeta}{\partial \xi} \\ 0 & 0 & \mathrm{St}^{-1}\Psi_{\eta\eta} + (\eta^*/\mathrm{St})(a/l)\frac{\partial v_\zeta}{\partial \eta} & \Omega^{*2} - \mathrm{St}^{-1}\Psi_{\xi\eta} - (\xi^*/\mathrm{St})(a/l)\frac{\partial v_\zeta}{\partial \eta} & \mathrm{St}^{-1}\frac{\partial v_\zeta}{\partial \eta} \\ 1 & 0 & -\mathrm{St}^{-1} & -2(a/l)v_\zeta^* & 0 \\ 0 & 1 & 2(a/l)v_\zeta^* & -\mathrm{St}^{-1} & 0 \\ 0 & 0 & -(\eta^*/\mathrm{St})(a/l) + 2\xi^*(a^2/l^2)v_\zeta^* & (\xi^*/\mathrm{St})(a/l) + 2\eta^*(a^2/l^2)v_\zeta^* & -\mathrm{St}^{-1} \end{pmatrix}^T, \tag{5.50}$$

where $v_\zeta^* \equiv v_\zeta(\xi^*, \eta^*)$.

Limit of infinite pitch

In the limit of $l/a \to \infty$, $\Omega^* \equiv (a/l)v_\zeta^*$ remains finite, and the matrix given by Eq. (5.50) reduces to:

$$M\Big|_{l/a \gg 1} = \begin{pmatrix} 0 & 0 & 1 & 0 & 0 \\ 0 & 0 & 0 & 1 & 0 \\ \mathrm{St}^{-1}\Psi_{\xi\eta} + \Omega^{*2} & \mathrm{St}^{-1}\Psi_{\eta\eta} & -\mathrm{St}^{-1} & 2\Omega^* & 0 \\ -\mathrm{St}^{-1}\Psi_{\xi\xi} & -\mathrm{St}^{-1}\Psi_{\xi\eta} + \Omega^{*2} & -2\Omega^* & -\mathrm{St}^{-1} & 0 \\ 0 & 0 & 0 & 0 & -\mathrm{St}^{-1} \end{pmatrix}. \tag{5.51}$$

The characteristic polynomial for the eigenvalues λ is:

$$\begin{aligned}\lambda^5 + 4\lambda^4 + (3 + 2\mathrm{St}^2\Omega^{*2})\lambda^3 + (1 + 4\mathrm{St}^2\Omega^{*2})\lambda^2 + \\ +(\mathrm{St}^4\Omega^{*4} + 2\mathrm{St}^2\Omega^{*2} + \mathrm{St}^2\mathcal{H}^*)\lambda + \mathrm{St}^4\Omega^{*4} + \mathrm{St}^2\mathcal{H}^* &= 0, \qquad (5.52)\end{aligned}$$

where $\mathcal{H}^*$ is the Hessian defined in Eq. (5.40), evaluated in the fixed point. The solution for λ is:

$$\begin{aligned}\lambda_{1,2} &= \frac{-1}{2\mathrm{St}} + \frac{1}{2\mathrm{St}}\sqrt{1 - 4\mathrm{St}^2\Omega^{*2} \pm i4\mathrm{St}\sqrt{\mathcal{H}^*}}, \\ \lambda_{3,4} &= \frac{-1}{2\mathrm{St}} - \frac{1}{2\mathrm{St}}\sqrt{1 - 4\mathrm{St}^2\Omega^{*2} \pm i4\mathrm{St}\sqrt{\mathcal{H}^*}}, \\ \lambda_5 &= \frac{-1}{\mathrm{St}}.\end{aligned}$$

For small Stokes numbers, the fixed point is located close to the elliptic stagnation point in the $\boldsymbol{\xi}$-frame, where the Hessian satisfies $0 < \mathcal{H}^* < \Omega^{*2}$. The eigenvalues can then be approximated by:

$$\begin{aligned}\lambda_{1,2} &\simeq -\mathrm{St}(\Omega^{*2} - \mathcal{H}^*) \pm i\sqrt{\mathcal{H}^*} + O(\mathrm{St}^2), \\ \lambda_{3,4} &\simeq -\frac{1}{\mathrm{St}} + \mathrm{St}(\Omega^{*2} - \mathcal{H}^*) \pm i\sqrt{\mathcal{H}^*} + O(\mathrm{St}^2), \\ \lambda_5 &= -\frac{1}{\mathrm{St}}.\end{aligned}$$

It is observed that the real parts of all eigenvalues are negative, provided the Stokes number is sufficiently small. Hence, the fixed point is stable and it is an attraction point. The real parts of the largest eigenvalues, λ_1 and λ_2, give an indication of the attraction rate. Since they are linear in St, particle trapping occurs on a larger time scale when the Stokes number is smaller.

The above analysis is especially relevant for the wall-bounded case ($R/a < \infty$), because topology V, containing one elliptic stagnation point in the $\boldsymbol{\xi}$-frame, arises naturally. In the unbounded case ($R/a \to \infty$), however, the flow field for infinite pitch corresponds to topology I. In this topology, there are no elliptic stagnation points in the $\boldsymbol{\xi}$-frame, and therefore a stable attraction trajectory of heavy particles does not exist.

Limit of zero pitch

For very small pitches ($l/a \downarrow 0$), we can approximate the velocity component $v_\zeta = u_z$ by Eq. (5.31). We note that elliptic points can not exist for $r > 1$ when $l/a \downarrow 0$. The product $I_m(mra/l)Z'_m(ma/l)$ reduces to:

$$I_m(mra/l)Z'_m(ma/l) \simeq \frac{\exp[mra/l]}{\sqrt{2\pi mra/l}}\left[\frac{\pi\exp[-mra/l]}{\sqrt{2\pi ma/l}} - \frac{\pi^2\exp[mra/l - 2mR/l]}{\sqrt{2\pi ma/l}}\right], \qquad (5.53)$$

in which expansions for large arguments have been used [1]. When $l/a \downarrow 0$, the right hand side of Eq. (5.53) vanishes, leading to

$$v_\zeta = \frac{U_\infty a}{\Gamma} + O(l/a)^k, \qquad \text{with } k \geq 1. \tag{5.54}$$

In addition, we know that in the limit $l/a \downarrow 0$, the velocity components in the ξ- and η-directions tend to zero inside the helix. Thus, the only possible fixed point in the rotating frame is the origin, where $\Psi_{\xi\xi} = \Psi_{\eta\eta} = \Omega$ and $\Psi_{\xi\eta} = 0$. Hence, the Hessian $\mathcal{H} \to \Omega^2$. The matrix for the separation vector reduces again to the one in Eq. (5.51). The real parts of the eigenvalues of this matrix are $-\mathrm{St}^{-1}$ (with multiplicity 3) and 0 (with multiplicity 2), respectively, indicating that the fixed point is not an attraction point. This result is perfectly in agreement with the physical intuition that particles do not accumulate in a uniform axial jet induced by a helical vortex filament with $l/a \ll 1$, which is similar to the magnetic field induced by a spool. In conclusion, when $l/a \downarrow 0$, particle accumulation does not occur; nevertheless, heavy particles located inside the helix, do not leave this region. In this sense, a helical vortex filament can transport heavy particles.

Finite pitch

For finite values of l/a, our numerical results show that the helical attraction trajectory of heavy particles exists in all of the topologies II-VII. Particles are attracted when the Stokes number is below a critical value, which in turn depends on the values of l/a, R/a and $U_\infty a/\Gamma$.

The attraction rate can be quantified by the first Lyapunov exponent Λ_1, defined as:

$$\Lambda_1 \equiv \lim_{t\to\infty} \frac{1}{t} \ln \frac{\|\boldsymbol{\xi}_1(t) - \boldsymbol{\xi}_2(t)\|}{\|\boldsymbol{\xi}_1(0) - \boldsymbol{\xi}_2(0)\|}, \tag{5.55}$$

where $\boldsymbol{\xi}_1(t)$ and $\boldsymbol{\xi}_2(t)$ denote the positions of two particles, respectively, which are approaching the attraction point. When the Lyapunov exponent has a negative value, the particle trajectories converge. The convergence rate is proportional to the absolute value of the Lyapunov exponent, which depends on the dimensionless parameters.

In order to determine the dependency on the pitch, the Lyapunov exponent is calculated for a wide range of values of l/a. The result is plotted in Fig. 5.11, for two different values of $U_\infty a/\Gamma$ with $R/a = 2.0$ and $\mathrm{St} = 1.0$. Apparently, the Lyapunov exponent is approximately linear in $(l/a)^{-1}$. Furthermore, the Lyapunov exponent is proportional to the value of $U_\infty a/\Gamma$.

This result can be explained by the observation that, when the spatial variation in v_ζ is moderate, the angular velocity of the particle in the $\boldsymbol{\xi}$-frame, Ω, is approximately proportional to a/l and to $U_\infty a/\Gamma$. Therefore, if either a/l or $U_\infty a/\Gamma$ increases, the Coriolis force increases, and particle accumulation is enhanced.

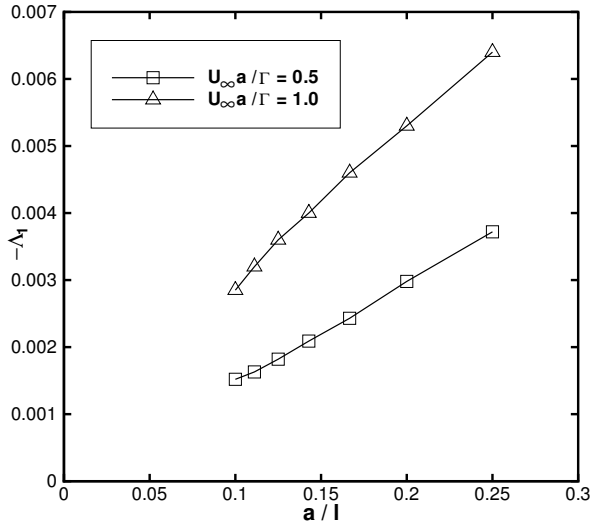

FIGURE 5.11: *The Lyapunov exponent* Λ_1 *as a function of the pitch* l/a*, for two different values of* $U_\infty a/\Gamma$*;* $R/a = 2.0$ *and St* $= 1.0$*.*

An interpretation in terms of the vortex core thickness ϵ/a can be given as well. From Fig. 5.5, it is clear that a lower value of ϵ/a corresponds to a lower value of $U_\infty a/\Gamma$ at equal l/a, or to a higher value of l/a at equal $U_\infty a/\Gamma$. Fig. 5.11 then shows that a lower value of ϵ/a results in a lower particle accumulation rate.

To address the dependency of the Lyapunov exponent on the particle Stokes number, we calculate Λ_1 for for a range of Stokes numbers varying between 0.1 and 1.1, with $l/a = 5.0$, $U_\infty a/\Gamma = 0.2$ and $R/a = 2.0$ (Topology V). The result is given in Fig. 5.12. It is observed that the Lyapunov exponent is approximately linear in the Stokes number in this case. This is in accordance with Eq. (5.52), valid for $l/a \gg 1$, which reveals that the real part of the largest eigenvalues is approximately linear in the Stokes number, as long as the Stokes number is small. In the limit of St $\downarrow 0$ (passive tracer limit) there can be no accumulation due to continuity, so Λ_1 approaches zero. Hence, the attraction rate is proportional to the Stokes number.

It should be noted that in the limit St $\to \infty$, the particle becomes insensitive to the carrier flow. Then the Lyapunov exponent should go to zero. The Stokes numbers in Fig. 5.12, however, are not large enough to visualize this.

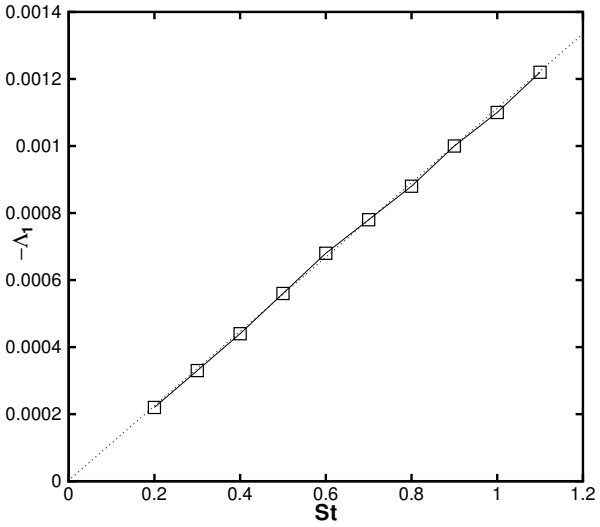

FIGURE 5.12: *The Lyapunov exponent* Λ_1 *as a function of the Stokes number St;* $l/a = 5.0$*,* $U_\infty a/\Gamma = 0.2$ *and* $R/a = 2.0$*.*

5.4.3 Particle trapping efficiency

The amount of particle accumulation, as function of time, can be quantified by the particle trapping efficiency P, defined as:

$$P \equiv \frac{\text{number of particles with } r < R/a \text{ for } t \to \infty}{\text{total number of initially uniformly distributed particles}}. \tag{5.56}$$

The particle trapping efficiency at $t = 1000$ is plotted in Fig. 5.13 as a function of the Stokes number, for typical examples of topology II, III, IV and V.

Topology I is left out of Fig. 5.13, because in this topology there is no particle accumulation at all. In topology II, P has a maximum around $\mathrm{St} = O(1)$. For topologies III, IV an V, P is close to one when the Stokes number is small, and close to zero when the Stokes number is large. This reflects the decreasing influence of the carrier flow on particles for increasing Stokes number.

Finally, we investigate the correlation between the particle trapping efficiency and the size of the area around an elliptic stagnation point in the (ξ, η)-plane, circumscribed by a separatrix of the stream function. The (normalized) elliptic area size is defined as:

$$A_E \equiv \frac{1}{\pi(R/a)^2} \int_0^{R/a} \int_0^{2\pi} H(\Psi_{sep} - \Psi(r,\phi)) r \mathrm{d}\phi \mathrm{d}r \tag{5.57}$$

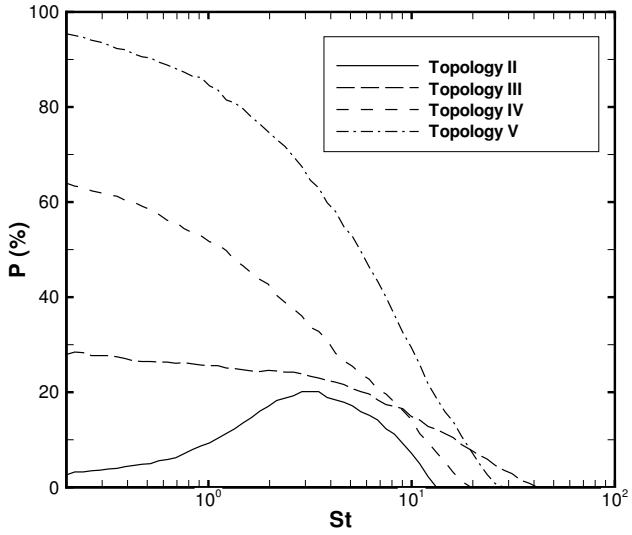

FIGURE 5.13: *Particle trapping efficiency P as a function of St for topology II* (R/a = 2.0; l/a = 1.0; $U_\infty a/\Gamma = -1.0$)*, topology III* (R/a = 2.0; l/a = 0.25; $U_\infty a/\Gamma = -0.25$)*, topology IV* ($R/a$ = 2.0; l/a = 1.0; $U_\infty a/\Gamma$ = 0.50) *and topology V* (R/a = 2.0; l/a = 1.0; $U_\infty a/\Gamma$ = 0.10)*.*

where $H(\ldots)$ is the Heaviside function and Ψ_{sep} denotes the value of Ψ at the separatrix, which is equal to the value of Ψ in the hyperbolic point on the separatrix. The correlation between A_E and P can be expressed by Error $_P$, defined as:

$$\text{Error}_P \equiv |P - A_E| \times 100\%. \tag{5.58}$$

The value of Error $_P$ is plotted as a function of the helix pitch and the axial flow velocity in Fig. 5.14, for particles with St = 1.0, in bounded space with R/a = 2.0. Clearly, the correlation between A_E and P is very good over a wide range of flow parameters. This indicates that the particle accumulation is closely related to the flow field topology in a helical vortex flow.

5.5 Conclusions

In the present chapter, the motion of heavy particles near a helical vortex filament is investigated both numerically and analytically. The numerical simulations are based on a one-way coupling between the potential flow field and the particle equations of motion. Only Stokes drag is taken into account in order to isolate the effect of inertia of heavy particles on their distribution.

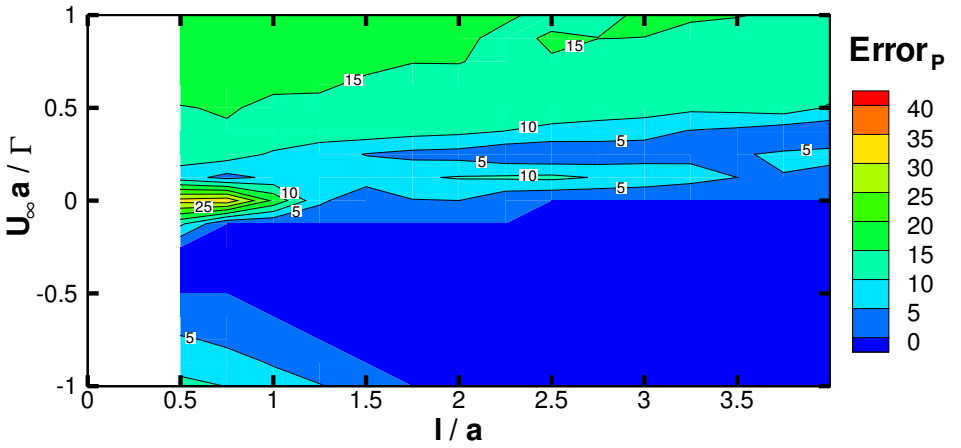

FIGURE 5.14: *Difference between particle trapping efficiency P and the elliptic area size A_E as a function of l/a and $U_\infty a/\Gamma$; $St = 1.0$ and $R/a = 2.0$.*

The numerical results reveal that heavy particles may be attracted to a helicly shaped attraction trajectory. In a $\boldsymbol{\xi}$-frame, this trajectory corresponds to an attraction point. The physical reason for the particle trapping is that the Coriolis force drives inertial particles to the center of an elliptic region of the stream function, where the particles are trapped by a balance between the Stokes drag and the centrifugal force.

The stability of the attraction points is proven analytically for helices with large pitch $l/a \gg 1$ in bounded space. Further analysis shows that heavy particles are captured inside the helical vortex structure when the helix pitch is small, i.e. $l/a \ll 1$. For intermediate values of the helix pitch, the particle trapping phenomenon is enhanced by the curvature and the torsion of the helical vortex, as is illustrated by the numerically determined Lyapunov exponent.

The particle accumulation is closely related to the area of an elliptic region in the stream function. These elliptic regions occur in six out of seven possible flow field topologies of a flow induced by a helical vortex inside a circular pipe.

Part II

Heavy particles in turbulent boundary layers

STOCHASTIC DIFFERENTIAL EQUATIONS

CHAPTER 6

The second part of this thesis is dedicated to the motion of heavy particles in turbulent boundary layers. The flow over a flat plate is treated in Chapter 7, and the swirling flow in a cylindrical pipe is considered in Chapter 8. In both configurations, the turbulent flow field is modelled using a stochastic differential equation.

By means of an introduction to the subject, we present some general properties of Stochastic Differential Equations (SDEs) in the present chapter. First, we describe how probability density functions of stochastic processes can be determined. Then, we introduce the SDE as a mathematical description of a Markov processes. Finally, after having presented the generalized form of a multivariate SDE, we show a few relevant and instructive examples of SDE applications.

6.1 Markov processes

A Stochastic Differential Equation is the result of a description for a Markov process. A Markov process is a stochastic process which is only defined on discrete moments in time; each next step depends on the previous step only. Consider the Markov process $q(t)$; the change of the process over a time interval h is called the increment $\Delta_h q(t)$ and obeys by definition the following equality [77]:

$$\Delta_h q(t) \equiv q(t+h) - q(t). \tag{6.1}$$

It is important to note that h is positive and that the increment is defined forward in time. A process can be considered as a sum of its increments, e.g. at time t_N we have:

$$q(t_N) = q(t_0) + \Delta_{t_1-t_0} q(t_0) + \Delta_{t_2-t_1} q(t_1) + \ldots + \Delta_{t_N-t_{N-1}} q(t_{N-1}). \tag{6.2}$$

Just like any stochastic variable, the Markov process $q(t)$ is defined by (i) a set of possible values, and (ii) a probability distribution over this set [39]. Therefore, a stochastic process is intrinsically related to probability density functions (PDFs).

6.2 Probability density functions

Let the probability that a stochastic process $q(t)$ has a value Q_1 at time t_1 be denoted by $f(Q_1; t_1)$. Similarly, the probability of the process having a value Q_2 at time t_2 *and* a value Q_1 at time t_1 is $f(Q_2, t_2; Q_1, t_1)$. The conditional probability density function $f_1(Q_2; t_2 \big| Q_1, t_1)$ is defined as the probability that the process $q(t)$ has a value Q_2 at time t_2, *given* the condition that its value at t_1 is Q_1. It is equal to:

$$f_1(Q_2; t_2 \big| Q_1, t_1) = f(Q_2, t_2; Q_1, t_1)/f(Q_1; t_1). \tag{6.3}$$

By definition, if $q(t)$ is a Markov process then the conditional PDFs are:

$$f_{N-1}(Q_N; t_N \big| Q_{N-1}, t_{N-1}, Q_{N-2}, t_{N-2}, \ldots, Q_1, t_1) = f_1(Q_N; t_N \big| Q_{N-1}, t_{N-1}). \tag{6.4}$$

This means that the value of $q(t_N)$ does only depend on $q(t_{N-1})$.

The probability of any process, Markovian or not, satisfies the following equation:

$$f_1(Q_3; t_3 \big| Q_1, t_1) = \int_{-\infty}^{\infty} f_2(Q_3; t_3 \big| Q_2, t_2, Q_1, t_1) f_1(Q_2; t_2 \big| Q_1, t_1) \mathrm{d}Q_2. \tag{6.5}$$

For a Markov process, f_2 can be replaced by f_1 using Eq. (6.4):

$$f_1(Q_3; t_3 \big| Q_1; t_1) = \int_{-\infty}^{\infty} f_1(Q_3; t_3 \big| Q_2, t_2) f_1(Q_2; t_2 \big| Q_1, t_1) \mathrm{d}Q_2. \tag{6.6}$$

This equation is called the Chapman-Kolmogorov equation [77].

Multiplying Eq. (6.6) by the PDF of the initial conditions $f(Q_1; t_1)$ and integrating over all Q_1 results in an expression for $f(Q_3; t_3)$, i.e. the probability that the stochastic process has value Q_3 at time t_3:

$$f(Q_3; t_3) = \int_{-\infty}^{\infty} f_1(Q_3; t_3 \big| Q_2, t_2) f(Q_2; t_2) \mathrm{d}Q_2. \tag{6.7}$$

Without loss of generality, we may replace t_3 by t, t_2 by $t - h$ (with $h > 0$), Q_3 by Q, and Q_2 by $Q - \Delta_h Q$ in order to obtain:

$$f(Q; t) = \int_{-\infty}^{\infty} f_1(Q; t \big| Q - \Delta_h Q, t - h) f(Q - \Delta_h Q; t - h) \mathrm{d}\Delta_h Q. \tag{6.8}$$

By employing a Taylor expansion around Q, one obtains:

$$f(Q; t) = \int_{-\infty}^{\infty} \sum_{n=0}^{\infty} \frac{(-\Delta_h Q)^n}{n!} \frac{\partial^n}{\partial Q^n} (f_1(Q + \Delta_h Q; t \big| Q, t - h) f(Q; t - h)) \mathrm{d}\Delta_h Q, \tag{6.9}$$

which is equal to:

$$f(Q;t) = f(Q;t-h) + \int_{-\infty}^{\infty} \sum_{n=1}^{\infty} \frac{(-\Delta_h Q)^n}{n!} \frac{\partial^n}{\partial Q^n} (f_1(Q + \Delta_h Q; t \big| Q, t-h) f(Q;t-h)) \mathrm{d}\Delta_h Q. \tag{6.10}$$

Dividing by h and taking the limit $h \downarrow 0$ results in an equation for the time development of $f(Q;t)$, known as the Kramers-Moyal expansion [77]:

$$\frac{\partial f(Q;t)}{\partial t} = \sum_{n=1}^{\infty} \frac{(-1)^n}{n!} \frac{\partial^n}{\partial Q^n} \Big(B_n(Q,t) f(Q;t) \Big), \tag{6.11}$$

where B_n denote the infinitesimal parameters of the stochastic process, defined as:

$$B_n(Q,t) \equiv \lim_{h \downarrow 0} \frac{1}{h} \int_{-\infty}^{\infty} (\Delta_h Q)^n f_1(Q + \Delta_h Q; t \big| Q, t-h) \mathrm{d}\Delta_h Q = \lim_{h \downarrow 0} \frac{1}{h} \langle [\Delta_h q(t)]^n \big| q(t) = Q \rangle. \tag{6.12}$$

It is observed that B_n stands for the n-th moment of the increment $\Delta_h Q$, divided by h, in the limit that $h \downarrow 0$.

6.3 Diffusion processes

There are qualitatively different kinds of Markov processes, which are distinguished from each other by different B_n, thus by the behavior of their increments $\Delta_h q(t)$ in the limit that h tends to zero. A defining property of a diffusion process is that both the drift coefficient,

$$a(Q,t) \equiv B_1(Q,t), \tag{6.13}$$

and the diffusion coefficient,

$$b^2(Q,t) \equiv B_2(Q,t), \tag{6.14}$$

exist, and that the remaining infinitesimal parameters are zero:

$$B_n(Q,t) = 0, \quad \text{for } n \geq 3. \tag{6.15}$$

If we insert the values of B_n for a diffusion process into Eq. (6.11), we obtain the so-called Fokker-Planck equation:

$$\frac{\partial f(Q;t)}{\partial t} = -\frac{\partial}{\partial Q} \Big(a(Q,t) f(Q;t) \Big) + \frac{1}{2} \frac{\partial^2}{\partial Q^2} \Big(b^2(Q,t) f(Q;t) \Big). \tag{6.16}$$

Clearly, the PDF $f(Q;t)$ changes due to advection by the drift term $a(Q,t)$ and due to diffusion by the term $b^2(Q,t)$.

As an example, we now consider the Wiener process, denoted by $W(t)$. This is the most fundamental diffusion process from which all others can be derived [77]. $W(t)$ is defined for $t \geq 0$ by the initial condition $W(0) = 0$ and by the specification of the drift and diffusion coefficients,

$$a(Q,t) = 0, \quad b^2(Q,t) = 1.$$

We insert this into Eq. (6.16) in order to obtain the development in time of the PDF of the Wiener process $f_W(Q;t)$:

$$\frac{\partial f_W(Q;t)}{\partial t} = \frac{1}{2}\frac{\partial^2}{\partial Q^2}\Big(f_W(Q;t)\Big). \tag{6.17}$$

Apparently, the PDF of the Wiener process satisfies the heat equation. From the initial distribution $f_W(Q;0) = \delta(Q)$, with $\delta(\ldots)$ the Dirac delta function, it follows that $f_W(Q;t)$ is a normal distribution, with a mean of zero and a variance equal to t.

6.4 Formulation of stochastic differential equations

Since diffusion processes are not differentiable with respect to time, they can not be described by ordinary differential equations. Instead, diffusion processes are described by stochastic differential equations [39], [77]. It is common to formulate a stochastic differential equation by using the infinitesimal increment of the process $q(t)$, defined as:

$$\mathrm{d}q(t) \equiv q(t + \mathrm{d}t) - q(t), \tag{6.18}$$

where $\mathrm{d}t$ is a positive time interval. For the Wiener process, the infinitesimal increment is:

$$\mathrm{d}W(t) \equiv W(t + \mathrm{d}t) - W(t), \tag{6.19}$$

Note that the probability of $\mathrm{d}W$ is normally distributed with mean zero and variance $\mathrm{d}t$.

Any diffusion process with parameters $a[q(t),t]$ and $b[q(t),t]$ can be described by the following stochastic differential equation:

$$\mathrm{d}q(t) = a[q(t),t]\mathrm{d}t + b[q(t),t]\mathrm{d}W(t). \tag{6.20}$$

The stochastic differential equation Eq. (6.20) shows that the infinitesimal increment of a diffusion process is Gaussian: i.e. the increment $\mathrm{d}q(t)$ has a normally distributed probability with mean $a[q(t),t]\mathrm{d}t$ and variance $\{b[q(t),t]\}^2\mathrm{d}t$ [77].

6.5 Multi-variate stochastic differential equations

The theory presented for scalar-valued diffusion processes can be extended to vector-valued processes as well. The multi-variate stochastic diffusion process $\boldsymbol{q}(t)$ satisfies the following equation:

$$\mathrm{d}q_i = a_i(\boldsymbol{q}, t)\mathrm{d}t + b_{ij}(\boldsymbol{q}, t)\mathrm{d}W_j, \tag{6.21}$$

where a_i and b_{ij} are defined by:

$$a_i(\boldsymbol{Q}, t) = \lim_{h\downarrow 0} \frac{1}{h}\langle[\Delta_h q_i(t)]|\boldsymbol{q}(t) = \boldsymbol{Q}\rangle, \tag{6.22}$$

$$B_{ij}(\boldsymbol{Q}, t) = b_{ik}b_{jk} = \lim_{h\downarrow 0} \frac{1}{h}\langle[\Delta_h q_i(t)\Delta_h q_j(t)]|\boldsymbol{q}(t) = \boldsymbol{Q}\rangle. \tag{6.23}$$

The vector $\boldsymbol{W}$ denotes a vector-valued Wiener process; the increment $\mathrm{d}\boldsymbol{W}$ is a joint normal with zero mean and variance $\langle \mathrm{d}W_i \mathrm{d}W_j\rangle = \delta_{ij}\mathrm{d}t$.

The Fokker-Planck equation for the multivariate case is [39], [77]:

$$\frac{\partial f(\boldsymbol{Q};t)}{\partial t} = -\frac{\partial}{\partial Q_i}(a_i(\boldsymbol{Q},t)f(\boldsymbol{Q};t)) + \frac{1}{2}\frac{\partial^2}{\partial Q_i \partial Q_j}(B_{ij}(\boldsymbol{Q},t)f(\boldsymbol{Q};t)). \tag{6.24}$$

6.6 Diffusion processes in turbulent flow

The stochastic differential equation, Eq. (6.21), can be used to calculate the position and the velocity of passive tracers in a turbulent flow. Of course, the success of the stochastic method depends on the definition of the random variables $\boldsymbol{q}(t)$, and on the drift and diffusion coefficients. In the present section, we present a method to calculate these drift and diffusion coefficients in such a way that the PDF corresponding to the SDE, whose development is given by the Fokker-Planck equation, Eq. (6.24), corresponds to the Eulerian PDF of the flow field. The Eulerian PDF of the flow field denotes the probability of finding a passive tracer with a certain velocity on a certain position, and should be known a priori. The link between the SDE and the Eulerian PDF is generally referred to as the 'well-mixedness condition' [96].

In the previous section, it was shown that the development of the PDF of a stochastic process is described by the Fokker-Planck equation Eq. (6.24), which can be determined directly when the drift and diffusion coefficients, a_i and b_{ij}, in Eq. (6.21) are known. In the present section, we study the inverse problem: when the development of the PDF is given, what should be the values of the drift and diffusion coefficients in the SDE?

The remainder of this section is devoted to the choice of the random variables q_i and the drift and diffusion coefficients a_i and b_{ij} in view of relevant applications.

6.6.1 One-dimensional dispersion in homogeneous turbulence

We study the horizontal dispersion of passive tracers in a stationary homogeneous turbulent flow of an incompressible fluid. The position of a passive tracer is denoted by x, and its velocity by u.

Let the Eulerian PDF of the velocity field be denoted by $p_E(u; x, t)$, i.e. the probability of finding a passive tracer with velocity u, given the position x and the time t. If the turbulence is assumed to be Gaussian, $p_E(u; x, t)$ is given by:

$$p_E(u; x, t) = p_E(u) = \frac{1}{\sqrt{2\pi\sigma^2}} \exp\Big[-\frac{u^2}{2\sigma^2}\Big]. \tag{6.25}$$

This implies that the mean velocity of passive tracers is 0, and the mean r.m.s. velocity fluctuations are equal to σ.

The probability of finding a passive tracer at a position x with velocity u, given the time t, $f(u, x; t)$, can be obtained by multiplying p_E with the number density of passive tracers $n(x; t)$:

$$f(u, x; t) = n(x; t)p_E(u; x, t) \tag{6.26}$$

It is noted that the number density of passive tracers is proportional to the mass density of the fluid: $n(x; t) \propto \rho(x, t)$. In the present research, we focus on incompressible flows only, so that $n(x; t)$ is a constant: $n(x; t) = n_0$.

When the position x and the velocity u are chosen as random variables, the multivariate SDE Eq. (6.21) with $q_1 = x$ and $q_2 = u$ is formulated as follows:

$$\begin{aligned} \mathrm{d}x &= a_1(u, x, t)\mathrm{d}t + b_{11}(u, x, t)\mathrm{d}W_1 + b_{12}(u, x, t)\mathrm{d}W_2, \\ \mathrm{d}u &= a_2(u, x, t)\mathrm{d}t + b_{21}(u, x, t)\mathrm{d}W_1 + b_{22}(u, x, t)\mathrm{d}W_2, \end{aligned} \tag{6.27}$$

Due to the kinematic condition $\mathrm{d}x = u\mathrm{d}t$, it follows that $a_1 = u$ and $b_{11} = b_{12} = 0$. Since Eq. (6.23) implies that $B_{ij} = b_{ik}b_{jk}$ is symmetric, $b_{ik}b_{jk} = b_{kj}b_{ki}$ and necessarily $b_{21} = 0$ as well. It is common [32],[96] to set $b_{22} = \sqrt{2\sigma^2/\tau}$, where τ denotes some time scale. The coefficient a_2 can be determined by employing the Fokker-Planck equation Eq. (6.24) for the Stochastic Differential Equation, which in this case reduces to:

$$\frac{\partial f(u, x; t)}{\partial t} = -\frac{\partial}{\partial x}(uf(u, x; t)) - \frac{\partial}{\partial u}(a_2 f(u, x; t)) + \frac{\sigma^2}{\tau}\frac{\partial^2}{\partial u^2}(f(u, x; t)). \tag{6.28}$$

In order to satisfy the well-mixedness condition, $f(u, x; t) = n_0 p_E(u; x, t)$, so that we obtain:

$$\frac{\partial p_E(u; x, t)}{\partial t} = -\frac{\partial}{\partial x}(up_E(u; x, t)) - \frac{\partial}{\partial u}(a_2 p_E(u; x, t)) + \frac{\sigma^2}{\tau}\frac{\partial^2}{\partial u^2}(p_E(u; x, t)). \tag{6.29}$$

Inserting Eq. (6.25) into Eq. (6.29) yields:

$$0 = \frac{a_2 p_E u}{\sigma^2} - p_E \frac{\partial a_2}{\partial u} + \frac{p_E}{\tau}\left(\frac{u^2}{\sigma^2} - 1\right). \tag{6.30}$$

The solution for the drift coefficient a_2 is then:

$$a_2 = -\frac{u}{\tau}, \tag{6.31}$$

so that Eqs. (6.27) become:

$$\begin{aligned} \mathrm{d}x &= u\mathrm{d}t, \\ \mathrm{d}u &= -\frac{u}{\tau}\mathrm{d}t + \sqrt{\frac{2\sigma^2}{\tau}}\mathrm{d}W, \end{aligned} \tag{6.32}$$

The process $u(t)$ is called the Ornstein-Uhlenbeck process. It is a stationary, Gaussian and Markovian process. In fact, all other processes which have these three properties can be derived from the Ornstein-Uhlenbeck process, as Doob's theorem states [39].

6.6.2 Three-dimensional dispersion in homogeneous turbulence

We now consider a stationary homogeneous turbulent flow field in which the velocities in x,y and z-direction are given by u, v and w, respectively. The mean (time-averaged) velocities are assumed to be zero everywhere, so that we have:

$$\langle u \rangle = \langle v \rangle = \langle w \rangle = 0, \quad \forall \quad x, y, z. \tag{6.33}$$

The variance of the velocity fluctuations is:

$$\langle u^2 \rangle = \langle v^2 \rangle = \langle w^2 \rangle = \sigma^2, \quad \forall \quad x, y, z. \tag{6.34}$$

If the turbulence is assumed to be Gaussian, the Eulerian PDF of the flow field is given by:

$$p_E(\boldsymbol{u}; \boldsymbol{x}, t) = p_E(\boldsymbol{u}) = \frac{1}{(2\pi\sigma^2)^{3/2}} \exp\left[-\frac{\boldsymbol{u} \cdot \boldsymbol{u}}{2\sigma^2}\right]. \tag{6.35}$$

Now, we look for a Langrangian stochastic model describing the position $\boldsymbol{x}$ and the velocity $\boldsymbol{u}$, which corresponds exactly to Eq. (6.33), Eq. (6.34) and Eq. (6.35). For this purpose, we introduce the following six random variables:

$$\{q_1, q_2, q_3, q_4, q_5, q_6\}^T = \{x, y, z, u, v, w\}^T.$$

In general form, the evolution of $\boldsymbol{q}$ is given by the stochastic differential equations Eq. (6.21). The probability of $\boldsymbol{q}$ having value $\boldsymbol{Q}$ at time t is described by $f(\boldsymbol{Q}; t)$, whose

evolution is given by Eq. (6.24). For $1 \leq i \leq 3$, the drift and diffusion coefficients are determined entirely by the kinematic condition $\mathrm{d}\boldsymbol{x} = \boldsymbol{u}\mathrm{d}t$:

$$a_i = q_{i+3} \quad \text{and} \quad b_{ij} = 0, \quad \forall \quad 1 \leq i \leq 3, \quad \forall j. \tag{6.36}$$

The other coefficients can be determined by requiring that $f(\boldsymbol{u}, \boldsymbol{x}; t) = n_0 p_E(\boldsymbol{u}; \boldsymbol{x}, t)$:

$$\frac{\partial p_E}{\partial t} = -\frac{\partial}{\partial q_i}(a_i p_E) + \frac{1}{2}\frac{\partial^2}{\partial q_i \partial q_j}(B_{ij} p_E). \tag{6.37}$$

Inserting Eq. (6.35), and assuming that the velocity fluctuations in the three directions are independent of each other, i.e. $b_{ij}(\boldsymbol{q}, t) = \delta_{ij} b$, yields:

$$\frac{\partial p_E}{\partial t} = 0 = \sum_{i=4}^{6}\Big(\frac{p_E a_i q_i}{\sigma^2} - p_E \frac{\partial a_i}{\partial q_i} + \frac{b^2}{2}\Big(\frac{q_i^2 - \sigma^2}{\sigma^4}\Big)p_E\Big). \tag{6.38}$$

Dividing by p_E gives the following equation for a_i and b:

$$\sum_{i=4}^{6}\Big(\frac{\partial a_i}{\partial q_i} - \frac{a_i q_i}{\sigma^2}\Big) = \sum_{i=4}^{6}\Big(\frac{b^2}{2}\Big(\frac{q_i^2 - \sigma^2}{\sigma^4}\Big)\Big). \tag{6.39}$$

A solution to this equation is:

$$a_i = -\frac{b^2 q_i}{2\sigma^2}, \tag{6.40}$$

so that the SDE for the dispersion of passive tracers becomes:

$$\begin{aligned} \mathrm{d}x_i &= u_i \mathrm{d}t, \\ \mathrm{d}u_i = -\frac{u_i b^2}{2\sigma^2}\mathrm{d}t + b\mathrm{d}W_i &= -\frac{u_i}{\tau}\mathrm{d}t + \sqrt{\frac{2\sigma^2}{\tau}}\mathrm{d}W_i, \end{aligned} \tag{6.41}$$

where $b^2/2\sigma^2$ has been replaced by the time scale τ. Comparison of Eq. (6.32) and Eq. (6.41) shows that the stochastic differential equation for $\boldsymbol{u}$ corresponds to the Ornstein-Uhlenbeck process in three dimensions.

6.6.3 One-dimensional dispersion in non-homogeneous turbulence

In many practical applications, turbulence is non-homogeneous, i.e. the mean fluctuations σ^2 and the time scale τ may depend on the position. In this section, we determine the drift and diffusion coefficients which should be chosen such that the well-mixedness condition is not violated in a spatially inhomogeneous flow.

We consider the dispersion of passive tracers with position x and velocity u. The (Eulerian) position-dependent r.m.s. velocity is denoted by $\sigma(x)$, so that $\langle u^2 \rangle(x) =$

$\sigma^2(x)$. We assume that the turbulence is stationary and Gaussian, so that the Eulerian PDF has the following form:

$$p_E(u;x,t) = p_E(u;x) = \frac{1}{\sqrt{2\pi\sigma^2(x)}}\exp\Big[-\frac{u^2}{2\sigma^2(x)}\Big]. \tag{6.42}$$

Just like in the case of one-dimensional homogeneous turbulence, the SDE is given by Eq. (6.21) where the random variables are: $q_1 = x$ and $q_2 = u$; the evolution of these variables is given by Eq. (6.27). The condition $\mathrm{d}x = u\mathrm{d}t$ implies that $a_1 = u$ and $b_{11} = b_{12} = b_{21} = 0$ in Eq. (6.21). By setting $b_{22}(x) = \sqrt{2\sigma^2(x)/\tau(x)}$, an exact expression for $a_2(u,x)$ can be derived from the Fokker-Planck equation Eq. (6.24). The result is [96]:

$$a_2 = -\frac{u}{\tau} + \frac{1}{2}\Big(1 + \frac{u^2}{\sigma^2}\Big)\frac{\partial\sigma^2}{\partial x}. \tag{6.43}$$

Thus, the total stochastic differential equation for the motion of passive tracers is:

$$\begin{aligned} \mathrm{d}x &= u\mathrm{d}t, \\ \mathrm{d}u &= -\frac{u}{\tau}\mathrm{d}t + \frac{1}{2}\frac{\partial\sigma^2}{\partial x}\Big[1 + \frac{u^2}{\sigma^2(x)}\Big]\mathrm{d}t + \sqrt{\frac{2\sigma^2(x)}{\tau(x)}}\mathrm{d}W. \end{aligned} \tag{6.44}$$

As an alternative, the Stochastic Differential Equation Eq. (6.21) may be formulated in terms of the random variables $q_1 = x$ and $q_2 = \xi \equiv u/\sigma$. Then, the Eulerian PDF $p_E(\xi;x,t)$ is independent of the position in Gaussian non-homogeneous turbulence; the value of σ may depend on x, but the distribution of ξ remains unaltered:

$$p_E(\xi;x,t) = p_E(\xi) = \frac{1}{\sqrt{2\pi}}\exp\Big[-\frac{\xi^2}{2}\Big]. \tag{6.45}$$

The SDE Eq. (6.21) becomes:

$$\begin{aligned} \mathrm{d}x &= a_1\mathrm{d}t + b_{11}\mathrm{d}W_1 + b_{12}\mathrm{d}W_2, \\ \mathrm{d}\xi &= a_2\mathrm{d}t + b_{21}\mathrm{d}W_1 + b_{22}\mathrm{d}W_2. \end{aligned} \tag{6.46}$$

Upon using the fact that $\mathrm{d}x = u\mathrm{d}t = \sigma\xi\mathrm{d}t$, we see that $a_1 = \sigma\xi$ and $b_{11} = b_{12} = b_{21} = 0$ in Eq. (6.21). The diffusion coefficient b_{22} can be formulated in an analogous way as before:

$$b_{22} = \sqrt{\frac{2}{\tau}}. \tag{6.47}$$

Inserting the values for the drift and diffusion coefficients into Eq. (6.24) gives the time development of the probability density function $f(\xi,x;t)$ of the SDE Eq. (6.46):

$$\frac{\partial f}{\partial t} = -\frac{\partial}{\partial x}(\sigma\xi f) - \frac{\partial}{\partial\xi}(a_2 f) + \frac{1}{\tau}\frac{\partial^2 f}{\partial\xi^2} \tag{6.48}$$

Upon using the well-mixedness condition, i.e. $f(\xi, x; t) = n_0 p_E(\xi; x, t)$, the drift coefficient a_2 is obtained from Eq. (6.45) and Eq. (6.48):

$$a_2 = -\frac{\xi}{\tau} + \frac{\mathrm{d}\sigma}{\mathrm{d}x}. \tag{6.49}$$

Clearly, a_2 only consists of a relaxation term plus a term which compensates the spurious drift from regions of high turbulent fluctuations to regions of low turbulent fluctuations.

Putting all terms together, the equations of motion of a passive tracer in non-homogeneous Gaussian turbulence become:

$$\begin{aligned} \mathrm{d}x &= \sigma\xi \mathrm{d}t, \\ \mathrm{d}\xi &= -\frac{\xi}{\tau}\mathrm{d}t + \frac{\mathrm{d}\sigma}{\mathrm{d}x}\mathrm{d}t + \sqrt{\frac{2}{\tau}}\mathrm{d}W. \end{aligned} \tag{6.50}$$

Apparently, the formulation in x and ξ yields only linear terms in the SDE; this is a considerable simplification with respect to the formulation in terms of x and u given in Eq. (6.44), where a u^2-term appears.

6.6.4 Dispersion in radially non-homogeneous turbulence

Finally, we study the dispersion of passive tracers in a turbulent flow in a pipe, where the average turbulent fluctuations vary with the radial coordinate r only. The turbulence is assumed to be Gaussian and stationary. For the sake of simplicity, we only consider fluctuations in the radial direction.

The Stochastic Differential Equation Eq. (6.21) may be formulated in terms of the random variables $q_1 = r$ and $q_2 = \xi \equiv u_r/\sigma$, where u_r denotes the velocity in radial direction. The Eulerian PDF p_E is again assumed to be independent of the position in the pipe:

$$p_E(\xi; r, t) = p_E(\xi) = \frac{1}{\sqrt{2\pi}} \exp\left[-\frac{\xi^2}{2}\right]. \tag{6.51}$$

The SDE Eq. (6.21) becomes:

$$\begin{aligned} \mathrm{d}r &= a_1\mathrm{d}t + b_{11}\mathrm{d}W_1 + b_{12}\mathrm{d}W_2, \\ \mathrm{d}\xi &= a_2\mathrm{d}t + b_{21}\mathrm{d}W_1 + b_{22}\mathrm{d}W_2. \end{aligned} \tag{6.52}$$

Upon using the fact that $\mathrm{d}r = u_r\mathrm{d}t = \sigma\xi\mathrm{d}t$, we see that $a_1 = \sigma\xi$ and $b_{11} = b_{12} = b_{21} = 0$ in Eq. (6.21). The diffusion coefficient b_{22} is again taken as:

$$b_{22} = \sqrt{\frac{2}{\tau}}. \tag{6.53}$$

Inserting the values for the drift and diffusion coefficients into Eq. (6.24), formulated in cylindrical coordinates, gives the time development of the probability density function $f(\xi, r; t)$ of the SDE Eq. (6.52):

$$\frac{\partial f}{\partial t} = -\frac{1}{r}\frac{\partial}{\partial r}(\sigma r \xi f) - \frac{\partial}{\partial \xi}(a_2 f) + \frac{1}{\tau}\frac{\partial^2 f}{\partial \xi^2} \tag{6.54}$$

Upon using the well-mixedness condition, i.e. $f(\xi, r; t) = n_0 p_E(\xi; r, t)$, the drift coefficient a_2 is obtained from Eq. (6.51) and Eq. (6.54):

$$a_2 = -\frac{\xi}{\tau} + \frac{\mathrm{d}\sigma}{\mathrm{d}r} + \frac{\sigma}{r}. \tag{6.55}$$

Hence, the equations of motion of a passive tracer in non-homogeneous Gaussian turbulence in an axisymmetric flow become:

$$\begin{aligned} \mathrm{d}r &= \sigma\xi \mathrm{d}t, \\ \mathrm{d}\xi &= -\frac{\xi}{\tau}\mathrm{d}t + \frac{\mathrm{d}\sigma}{\mathrm{d}r}\mathrm{d}t + \frac{\sigma}{r}\mathrm{d}t + \sqrt{\frac{2}{\tau}}\mathrm{d}W. \end{aligned} \tag{6.56}$$

Obviously, in the limit that $r \to \infty$, Eq. (6.56) reduces to Eq. (6.50).

6.7 Conclusions

In this chapter, an introduction is given to the concept of stochastic differential equations, aimed at modelling dispersion of passive tracers in turbulent flows. The coefficients in the stochastic differential equations can to be tuned in order to model the physical situation at hand. In the present thesis, the coefficients are determined on the basis of two criteria: (i) the passive tracers must satisfy the well-mixedness condition, and (ii) the r.m.s. velocity fluctuations of a large group of passive tracers must correspond to the local r.m.s. velocity fluctuations of the flow field.

Examples show that the dispersion in stationary homogeneous Gaussian turbulence may be modelled by an Ornstein-Uhlenbeck process. In non-homogeneous turbulence (where the r.m.s. velocity fluctuations depend on the position), a drift term must be added to the Ornstein-Uhlenbeck process in order to prevent passive tracers to accumulate in regions of low turbulence intensity. It has been shown that the simplest drift term is obtained when the position of the passive tracer and the parameter $\xi \equiv u/\sigma$ are used as the stochastic variables, rather than the position and the velocity of the passive tracer.

Heavy particles in turbulent flow over a flat plate

Chapter 7

The motion of small heavy particles in the turbulent boundary layer over a flat plate is investigated numerically. Lagrangian tracking is used for the calculation of the particle trajectories. The Stokes drag force is taken into account in the equation of motion of the particles. The turbulent carrier flow field along the particle trajectory is modelled by a stochastic method. In order to isolate the effect of turbophoresis, only velocity fluctuations in the wall-normal direction are taken into account. We present numerical results for the non-uniform concentration of heavy particles in this two-dimensional flow. In addition we calculate the deposition velocity of particles on the wall, and we show probability density functions for the wall-hitting velocity. Finally, the influence of inter-particle collisions and coalescence is discussed.

7.1 Introduction

The motion of heavy particles in fully developed turbulent pipe flows is particularly interesting for two important phenomena, observed in experiments: preferential concentration of particles close to the wall and the deposition of particles on the wall. Both phenomena depend non-trivially on the particle Stokes number, i.e. the dimensionless particle relaxation time.

The term 'preferential concentration' was introduced by Squires & Eaton [91] in order to describe the elevated concentration of particles close to the wall in fully developed turbulent channel flow. Both experiments [23] and Direct Numerical Simulations [54],[91] have revealed that particles tend to concentrate in low-speed streaks. As a parameter study shows [76], the maximum concentration is found for particles which have a Stokes number of $\mathrm{St} \simeq 25$, where the Stokes number St is defined as the particle relaxation time τ_p made dimensionless by the wall friction velocity u_τ and the kinematic viscosity of the carrier flow ν: $\mathrm{St} \equiv \tau_p u_\tau^2/\nu$.

The phenomenon of particle deposition can be characterized by the dimensionless

deposition velocity K^+_{dep}, defined as [103]:

$$K^+_{dep} = \frac{j_{wall}}{\rho_p \bar{c} u_\tau} \tag{7.1}$$

where j_{wall} is equal to the mean flux of mass depositing on the wall per unit of area per unit of time, ρ_p is the density of particles and $\bar{c}$ denotes the mean concentration of particles in the flow. Experimental results show that the value of K^+_{dep} is strongly dependent on the particle Stokes number St. For instance, small particles ($\mathrm{St} \lesssim 0.2$) deposit only due to Brownian diffusion in the near-wall region so that the deposition velocity is rather low. Large particles on the other hand ($\mathrm{St} \gtrsim 22.9$) may coast through the viscous sublayer close to the wall, and deposit due to their intertia. For particles of moderate size ($0.2 \lesssim \mathrm{St} \lesssim 22.9$), a transition region exists in which both diffusion and intertia are important. McCoy & Hanratty [61] made the following fit through available experimental data, reflecting the three regimes (see also Fig. 7.1):

$$\begin{aligned} K^+_{dep} &\simeq 10^{-5}, \text{for St} < 0.2; && \text{diffusional deposition regime,} \\ K^+_{dep} &\simeq 3.25 \times 10^{-4}\mathrm{St}^2, \text{for } 0.2 < \mathrm{St} < 22.9; && \text{diffusion-impaction regime,} \\ K^+_{dep} &\simeq 0.17, \text{for St} > 22.9; && \text{inertia-moderated regime.} \end{aligned} \tag{7.2}$$

Apparently, the deposition velocity increases dramatically with the particle Stokes number in the 'diffusion-impaction regime'; the deposition velocity for $\mathrm{St} = 22.9$ is approximately 4 orders of magnitude higher than for $\mathrm{St} = 0.2$. Because the particle relaxation time is quadratic in the (dimensionless) particle radius a^+_p (see Eq. (2.3)), $K^+_{dep} \propto a^{+4}_p$ for $0.2 < \mathrm{St} < 22.9$. This shows that particle deposition is strongly dependent on the size of the particles.

In recent years, much progress has been made in understanding particle dispersion and deposition by studying the bahavior of heavy particles in a Direct Numerical Simulation (DNS) of turbulent flow. Despite the many advantages of a DNS approach, it has the limitation that it is impractical to use in studying large Reynolds number flows. Moreover, asymptotic behavior of quantities at large times is difficult to assess for a wide range of parameters due to long computing times. Finally, a Direct Numerical Simulation can be very time-consuming when the geometry of the boundaries is not an elementary shape such as a flat plate or a horizontal channel, even when the Reynolds number of the flow is relatively low. Since the present research is aimed at studying particle deposition not only in a flow over a flat plate but also in a swirling flow in a pipe (see Chapter 8), we choose to employ a stochastic method based on a modified Langevin equation in order to model the fluid turbulence.

The application of stochastic models for the dispersion of fluid elements has a long tradition. Already in 1921, G.I. Taylor [94] made an estimate of the diffusion of contaminants originating from a point source in a stationary homogeneous isotropic

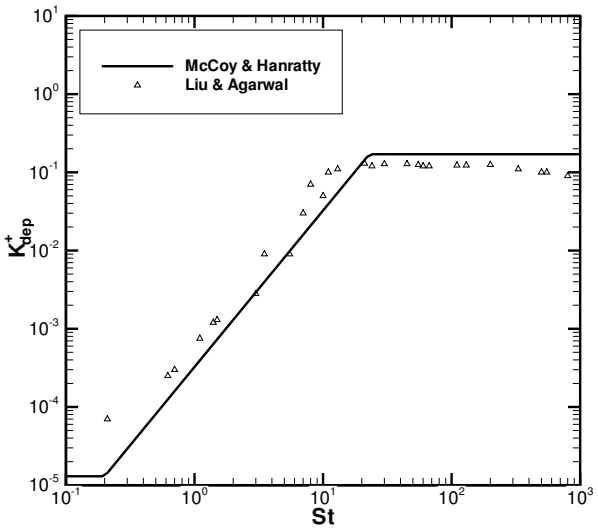

FIGURE 7.1: *Triangles: experimental results for the deposition velocity as a function of the Stokes number for particles in a boundary layer on a flat plate, obtained by Liu & Agarwal [51]. Solid line: a fit through experimental data by McCoy & Hanratty [61] given in Eq. (7.2).*

turbulent flow. Subsequently, stochastic methods have been widely used for the modelling of contaminant dispersion in the atmospheric boundary layer, which is an example of inhomogeneous turbulence [22], [101]. In these studies, contaminants and particles are assumed to be sufficiently small to be modelled as passive tracers, and their trajectories are calculated from a generalized Langevin equation. It was shown that the traced particles tend to accumulate in regions of low turbulence intensity. This is of course non-physical since passive tracers in an incompressible flow should be distributed uniformly over the domain at sufficiently large times. Therefore, much effort has been put in finding a modified Langevin Equation which would not violate the so-called well-mixedness condition. After first attempts by Wilson *et al.* [101] and Van Dop *et al.* [19], the question was finally addressed by Thomson, who proposed a rigorous condition for well-mixedness [96]: in order to guarantee well-mixedness in inhomogeneous turbulent flows, an additional drift term needs to be added to the Langevin equation, which has been shown in Chapter 6 as well. A study by MacInnes & Bracco [53] illustrates that most generic stochastic models (Discontinuous Random Walk models, Continuous Random Walk models and generalized Langevin-based models) indeed fail to satisfy the well-mixedness even in relatively simple flows such as a plane mixing layer and an axial turbulent jet.

Lagrangian stochastic methods have not only been used in order to describe the motion of passive tracers, but they have been applied to model the dispersion of heavy particles as well. Kallio & Reeks [38] employed a discrete eddy model in order to obtain statistics for the deposition of heavy particles on the wall in a fully-developed turbulent flow in a channel. They modelled the wall-normal velocity of the fluid at the position of the particle as a random fluctuation; after a randomly sampled eddy-turnover time, a new fluctuation was obtained from a non-homogeneous Gaussian distribution. The mean velocity profile in streamwise direction and the r.m.s. wall-normal velocity fluctuations were taken from experimental results in a turbulent channel flow. Although their model does not provide correct results in the limit of infinitesimally small particles since the well-mixedness condition was not satisfied, Kallio & Reeks did obtain results for the deposition velocity which are in good agreement with available experimental data. In addition, their model gave a physical explication for the observed phenomenon of turbophoresis, i.e. the accumulation of heavy particles near the wall.

As an alternative, Iliopoulos *et al.* employed a modified Langevin equation for the modelling of the deposition and dispersion of heavy particles in a turbulent channel flow [36]. The modified Langevin equation was modelled such that it satisfied the well-mixedness condition. In order to adjust the constants in the modified Langevin equation, Iliopoulos *et al.* used data from a DNS solution of a turbulent channel flow. They focussed on the dispersion of heavy particles from a point source rather than on the deposition velocity of particles on the wall. They obtained a good agreement between the results from their stochastic model and the results from the DNS, showing the potential of modelling a non-homogeneous turbulent flow by means of a modified Langevin equation. In a recent paper, Mito & Hanratty [64] used the same method to calculate the deposition velocity of particles in an annular flow.

In the present chapter, we investigate the motion of heavy particles in a fully developed turbulent boundary layer over a flat plate. The turbulence of the carrier flow along the trajectory of a heavy particle is modelled by a stochastic differential equation, which guarantees well-mixedness for infinitesimally small particles. We investigate both the preferential concentration of heavy particles and the particle deposition on the wall. In addition, we study the effect of fully elastic particle collisions and of fully inelastic particle collisions both on the deposition of particles and on the concentration profiles. The interactions are expected to change the dispersion of particles significantly, especially when the particle concentration near the wall is elevated due to turbophoresis.

The present chapter is organized as follows. In section 7.2, we introduce the equations of motion for the heavy particles. In addition, we present the stochastic equations describing the turbulent gas velocity along the trajectory of a heavy particle. In section 7.3, the numerical solution method is elucidated. The first part of section 7.4

is devoted to the results for the dispersion and the deposition of individual particles. In the second part of section 7.4, we present the results for simulations where particle interactions are taken into account. The inter-particle collisions are modelled either as fully elastic collisions, or as fully inelastic collisions (i.e. coalescence). The conclusions are formulated in section 7.5.

7.2 Physical-mathematical model

In the present section, we introduce the equations of motion for the particles and the stochastic equation describing the carrier flow velocity at the position of the particle. In addition, we present two methods for modelling particle interactions: both fully elastic and fully inelastic collisions are considered.

7.2.1 Equations of motion of heavy particles

The equations of motion of a particle in a turbulent boundary layer are assumed to be accurately described by Eq. (2.4). Thus, we assume that the flow around the particle is a Stokes flow, which is a reasonable approximation for small heavy particles in turbulent boundary layers; the inclusion of modifications to the equation of motion in order to extend its validity to larger particle Reynolds numbers, such as the Saffman lift force or a modified drag term, does not necessarily give a better result compared to experiments, as Wang *et al.* show [99]. In order to isolate the effect of inertia, we neglect the effect of gravity, i.e. we take $\mathrm{Fr} \to \infty$. Under these assumptions, Eq. (2.4) reduces to:

$$\frac{d\boldsymbol{x}_p^+}{dt^+} = \boldsymbol{u}_p^+, \qquad \frac{d\boldsymbol{u}_p^+}{dt^+} = \frac{1}{\mathrm{St}}(\boldsymbol{u}^+(\boldsymbol{x}_p^+, t^+) - \boldsymbol{u}_p^+), \tag{7.3}$$

where $\boldsymbol{x}_p^+$ and $\boldsymbol{u}_p^+$ denote the position and the velocity of the particle, respectively, and $\boldsymbol{u}^+$ is the carrier flow velocity at the position of the particle. This equation has been made dimensionless by the kinematic viscosity of the carrier flow ν and the friction velocity u_τ. The dimensionless variables are commonly provided with a superscript $^+$. The Stokes number is here defined as: $\mathrm{St} \equiv \tau_p u_\tau^2/\nu$, where τ_p is the particle relaxation time, given by Eq. (2.3).

The velocity of the carrier flow at the location of the particle, $\boldsymbol{u}^+$, is assumed to be given by:

$$\boldsymbol{u}^+ = \langle u_x^+ \rangle \boldsymbol{e}_x + \sigma^+ \xi \boldsymbol{e}_y, \tag{7.4}$$

where x^+ is the coordinate in streamwise direction, y^+ is the wall-normal coordinate, and $\xi \equiv u_y^+/\sigma^+(y^+)$ denotes the fluid velocity in wall-normal direction divided by σ^+, the root-mean-square of the velocity fluctuations in wall-normal direction. The random variable ξ is determined from the following stochastic differential equation:

$$\mathrm{d}\xi = -\frac{\xi}{\tau^+}\mathrm{d}t^+ + \left(\frac{\mathrm{d}\sigma^+}{\mathrm{d}y^+}\right)\mathrm{d}t^+ + \sqrt{\frac{2}{\tau^+}}\mathrm{d}W, \tag{7.5}$$

where W denotes the Wiener process. The term $(\mathrm{d}\sigma^+/\mathrm{d}y^+)$ is introduced in order to satisfy the well-mixedness condition, see section 6.6.3.

In order to solve Eq. (7.5), the values for $\langle u_x^+ \rangle(y^+)$, $\sigma^+(y^+)$ and $\tau^+(y^+)$ have to be known. In the present research, we take these quantities in accordance with experimental results reported in the literature; these results are presented in the following section.

It is noted that the coupled equations described in Eqs. (7.3)-(7.5) can be seen as a system of stochastic diffential equations as given by Eq. (6.21). In this case, the five-dimensional stochastic variable reads $\boldsymbol{q} = (\boldsymbol{x}_p^+, \boldsymbol{u}_p^+, \xi)^T$, and the drift and diffusion coefficients are:

$$\boldsymbol{a} = \left(\boldsymbol{u}_p^+, \mathrm{St}^{-1}(\langle u_x^+ \rangle \boldsymbol{e}_x + \sigma^+ \xi \boldsymbol{e}_y - \boldsymbol{u}_p^+), -\frac{\xi}{\tau^+} + \left(\frac{\mathrm{d}\sigma^+}{\mathrm{d}y^+} \right) \right)^T ,$$

$$b_{55} = \sqrt{\frac{2}{\tau^+}}; \quad b_{ij} = 0, \quad \forall \quad (i,j) \neq (5,5).$$

The corresponding Fokker-Planck equation, which is given in Eq. (6.24), describes the development in time of the probability $f(\boldsymbol{x}_p^+, \boldsymbol{u}_p^+, \xi; t)$, i.e. the probability of finding a particle at position $\boldsymbol{x}_p^+$ having a velocity $\boldsymbol{u}_p^+$ while the local fluid velocity is $\langle u_x^+ \rangle \boldsymbol{e}_x + \sigma^+ \xi \boldsymbol{e}_y$. In principle, solving the Fokker-Planck equation for the probability $f(\boldsymbol{x}_p^+, \boldsymbol{u}_p^+, \xi; t)$ is equivalent to solving Eqs. (7.3)-(7.5) for an infinite number of heavy particles. Direct solution of the Fokker-Planck equation is generally referred to as the PDF-approach [63],[83]; in the present research, however, we solve Eqs. (7.3)-(7.5) by Langrangian tracking of a large number of individual particles.

Average quantities in turbulent boundary layer on flat plate

The mean velocity profile in the streamwise direction is based on the law-of-the-wall relations. The turbulent r.m.s. velocity and time scale profiles are obtained from experimental data. This approach is basically the same as was used by Kallio & Reeks [38] for the calculation of particle deposition in a turbulent boundary layer in a fully developed channel flow.

The mean velocity parallel to the wall, $\langle u_x^+ \rangle$, can be expressed in terms of the distance to the wall y^+ as follows [38],[77]:

$$\begin{aligned} \langle u_x^+ \rangle &= y^+, \qquad \text{for } y^+ \leq 5, \\ \langle u_x^+ \rangle &= 2.5 \ln y^+ + 5.5, \qquad \text{for } y^+ \geq 30. \end{aligned} \tag{7.6}$$

In the buffer region, $5 < y^+ < 30$, the velocity is obtained from a cubic spline interpolation, yielding [38]:

$$\langle u_x^+ \rangle = a_0 + a_1 y^+ + a_2 {y^+}^2 + a_3 {y^+}^3, \tag{7.7}$$

where $a_0 = -1.076$, $a_1 = 1.445$, $a_2 = -0.04885$ and $a_3 = 0.0005813$. The mean velocity component in streamwise direction is plotted in figure Fig. 7.2.

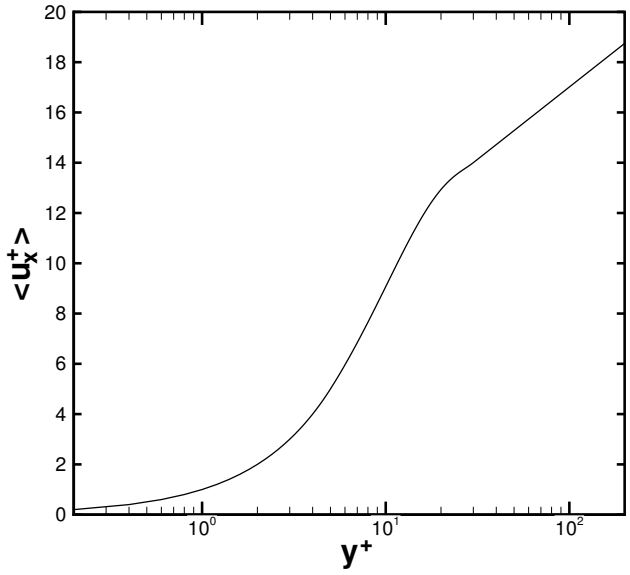

FIGURE 7.2: *The mean velocity profile $\langle u_x^+ \rangle$ as a function of the distance from the wall y^+.*

The mean velocity in the wall-normal direction is equal to zero in case of fully developed turbulence, as considered here. Hence, we have: $\langle u_y^+ \rangle = 0$. The r.m.s. velocity fluctuations in wall-normal direction are [38]:

$$\sigma^+ = \sqrt{\langle u_y^{+2} \rangle} = \frac{k_1 y^{+2}}{1 + k_2 y^{+k_3}}, \tag{7.8}$$

where $k_1 = 0.005$, $k_2 = 0.002923$ and $k_3 = 2.128$.

Finally, a relation for the Lagrangian decorrelation time τ is required. In homogeneous turbulence, the Lagrangian decorrelation time is defined as:

$$\tau \equiv \int_0^\infty R_L \mathrm{d}t, \tag{7.9}$$

where R_L is the Lagrangian correlation coefficient: $R_L = \langle u(0)u(t) \rangle / \langle u(t)u(t) \rangle$. In inhomogeneous turbulence, however, the Lagrangian decorrelation is not rigourously

defined, as Iliopoulos & Hanratty point out in [37]; for inhomogeneous turbulence the integral in Eq. (7.9) may not converge.

Therefore, the Lagrangian time scale in inhomogeneous turbulence needs to be modelled. Since we consider a fully developed turbulent flow over a flat plate, it is logical to suppose that the Lagrangian time scale is a function of the wall-normal distance alone: $\tau = \tau^+(y^+)\nu/u_\tau^2$. The functional relationship between τ^+ and y^+ has been subject to many studies in recent years, e.g. [37] and [55]. Despite the numerous investigations, an unambiguous result seems to be unavailable. For want of anything better, we employ the Lagrangian decorrelation time in accordance with [38], which is based on experimental results:

$$\begin{aligned} \tau^+ &= 10, \qquad \text{for } y^+ < 5, \\ \tau^+ &= C_0 + C_1 y^+ + C_2 y^{+2}, \qquad \text{for } y^+ \geq 5, \end{aligned} \tag{7.10}$$

where $C_0 = 7.122$, $C_1 = 0.5731$ and $C_2 = -0.001290$. Thus, the Lagrangian decorrelation time is assumed to be a constant in the immediate vicinity of the wall ($y^+ < 5$), after which it gradually increases further away from the wall. Both the r.m.s. fluctuations σ^+ and the Lagrangian decorrelation time τ^+ are plotted in Fig. 7.3.

7.2.2 Particle interactions

If two particles touch, their trajectories are altered. In the present research we employ two different particle interactions: either the particles collide fully elastically, or they collide fully inelastically (i.e. coalescence).

Modelling of fully elastic collisions

In fully elastic collisions between two particles, both momentum and kinetic energy are conserved. Momentum is exchanged between the two particles along the line of collision, whereas the momentum of each particle in the two directions perpendicular to the line of collision remains unaltered.

Let the velocities of two particles before a collision be denoted by $\boldsymbol{u}_1^+$ and $\boldsymbol{u}_2^+$, respectively. The separation between the particle centers is $\boldsymbol{R}$ (see Fig. 7.4); when the particles hit each other, of course $|\boldsymbol{R}| = a_{p,1} + a_{p,2}$. The velocities after the collision, $\boldsymbol{u}_1^{+\prime}$ and $\boldsymbol{u}_2^{+\prime}$, can be calculated from:

$$\begin{aligned} \boldsymbol{u}_1^{+\prime} &= \frac{\{m_1 - m_2\}(\boldsymbol{R}\cdot\boldsymbol{u}_1^+)\boldsymbol{R} + 2m_2(\boldsymbol{R}\cdot\boldsymbol{u}_2^+)\boldsymbol{R}}{\{m_1+m_2\}|\boldsymbol{R}|^2} + \frac{(\boldsymbol{R}\times\boldsymbol{u}_1^+)\times\boldsymbol{R}}{|\boldsymbol{R}|^2}, \\ \boldsymbol{u}_2^{+\prime} &= \frac{\{m_2 - m_1\}(\boldsymbol{R}\cdot\boldsymbol{u}_2^+)\boldsymbol{R} + 2m_1(\boldsymbol{R}\cdot\boldsymbol{u}_1^+)\boldsymbol{R}}{\{m_1+m_2\}|\boldsymbol{R}|^2} + \frac{(\boldsymbol{R}\times\boldsymbol{u}_2^+)\times\boldsymbol{R}}{|\boldsymbol{R}|^2}, \end{aligned} \tag{7.11}$$

where m_1 and m_2 stand for the masses of the two particles.

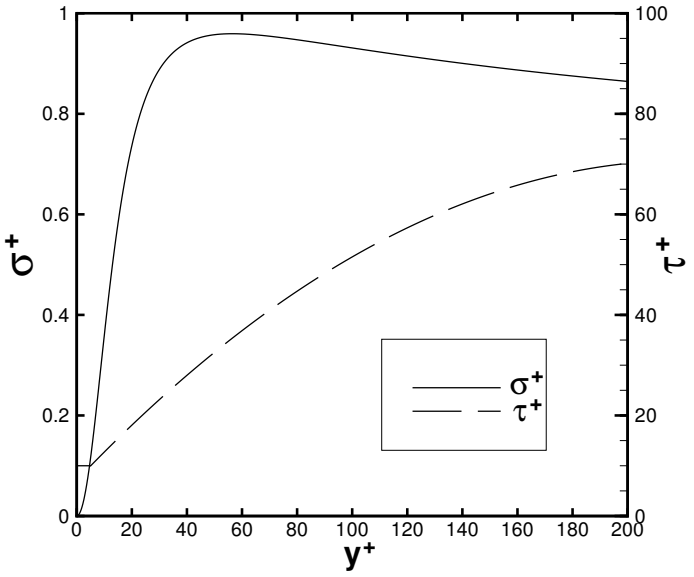

FIGURE 7.3: *The root-mean-square velocity fluctuations* $\sigma^+ = \sqrt{\langle u_y^{+2} \rangle}$ *and the Lagrangian decorrelation time* τ^+*, as a function of the distance from the wall* y^+.

If the particles are identical, then Eq. (7.11) reduces to:

$$\begin{aligned} \boldsymbol{u}_1^{+\prime} &= \frac{(\boldsymbol{R} \cdot \boldsymbol{u}_2^+)\boldsymbol{R}}{|\boldsymbol{R}|^2} + \frac{(\boldsymbol{R} \times \boldsymbol{u}_1^+) \times \boldsymbol{R}}{|\boldsymbol{R}|^2}, \\ \boldsymbol{u}_2^{+\prime} &= \frac{(\boldsymbol{R} \cdot \boldsymbol{u}_1^+)\boldsymbol{R}}{|\boldsymbol{R}|^2} + \frac{(\boldsymbol{R} \times \boldsymbol{u}_2^+) \times \boldsymbol{R}}{|\boldsymbol{R}|^2}. \end{aligned} \tag{7.12}$$

Modelling of fully inelastic collisions

If two particles collide in a fully inelastic way, they travel on attached to each other. This concept is used in the present research in order to model the coalescence process between droplets.

During a fully inelastic collision momentum is conserved, but kinetic energy is partly dissipated. The deficit of kinetic energy is transformed into internal energy of the colliding particles or droplets.

The velocity of the new particle, which is made up out of particle 1 and 2, can be calculated directly from the conservation of momentum:

$$\boldsymbol{u}_{12}^{+\prime} = \frac{m_1 \boldsymbol{u}_1^+ + m_2 \boldsymbol{u}_2^+}{m_1 + m_2}. \tag{7.13}$$

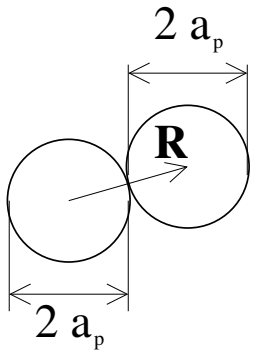

FIGURE 7.4: *A sketch of two identical particles with radius a_p, separated by a distance* ***R****, on the moment of a collision.*

We suppose that the newly formed particle assumes a spherical shape immediately; the radius of the new sphere $a'_{p,12}$ is:

$$a'_{p,12} = (a^3_{p,1} + a^3_{p,2})^{\frac{1}{3}}. \tag{7.14}$$

Since the particle relaxation time τ_p scales by the square of the particle radius (see Eq. (2.3)), the Stokes number of the new particle St'_{12} can be calculated directly from the former Stokes numbers St_1 and St_2 as follows:

$$\mathrm{St}'_{12} = (\mathrm{St}_1^{\frac{3}{2}} + \mathrm{St}_2^{\frac{3}{2}})^{\frac{2}{3}}. \tag{7.15}$$

7.3 Numerical methods

In the numerical simulations, a large number of particles are released in the boundary layer. At the beginning of the simulation, all particles are uniformly distributed in the domain of length L^+ and height h^+. The initial streamwise velocity of a particle is equal to the local mean carrier flow velocity, whereas the initial wall-normal velocity is randomly sampled from a normal distribution with variance $\sigma^+(y_p^+(0))$.

The positions of the particles in the course of time are determined by integrating the equations of motion of heavy particles, Eq. (7.3), combined with the stochastic equation for the turbulent flow field seen by the particle, Eq. (7.5). The time integration is done by a fourth-order Runge-Kutta scheme with numerical time step $\Delta t^+ = 0.05$. Other values for the time step were tested, such as $\Delta t^+ = 0.01$, $\Delta t^+ = 0.002$ and $\Delta t^+ = 0.001$, but these choices did not significantly alter the results.

When a particle hits the wall (i.e. $y_p^+ < a_p^+$), it is absorbed by the wall and thus eliminated from the simulation. Also when a particle leaves the domain at $x^+ = L^+$, it is eliminated. For each eliminated particle, a new particle is injected into the

boundary layer at a randomly chosen injection position on the line $x^+ = 0$. The wall-normal coordinates of the 20 injection positions are chosen such that, on average, the particles enter the turbulent boundary layer in a uniform concentration.

On the other hand, when a particle leaves the domain on the upper side of the turbulent boundary layer ($y_p^+ > h^+$), an identical particle is reinjected into the boundary layer on the same position but with an opposite wall-normal velocity; this corresponds to imposing a Von Neumann boundary condition for the concentration on the upper edge of the boundary layer.

These boundary conditions ensure that a constant number of particles is maintained in the entire domain. By doing so, the numerical solution for the distribution of particles approaches a statistically stationary solution as the time of integration goes to infinity.

7.3.1 Measuring particle concentration profiles

Statistically stationary concentration profiles of particles $c(x^+, y^+)$ in a turbulent boundary layer are determined as follows. First, the particle equations of motion are integrated for a time of $t_1^+ = 5,000$. After such a long time, the effects of the initial distribution of particles are largely dissipated so that a statistically stationary solution is obtained. Subsequently, we continue the integration for another $5,000$ units of time in order to collect statistical information.

A concentration profile is obtained by dividing the domain in identical boxes and by counting the number of particles in each box. In the present simulations we use $N_x = 25$ boxes in the streamwise direction and $N_y = 200$ boxes in the wall-normal direction. Let the center of box i, j be located at (x_i^+, y_j^+). The concentration in the box i, j at one particular instant in time t^+, $\hat{c}(x_i^+, y_j^+; t^+)$, can then be calculated from:

$$\hat{c}(x_i^+, y_j^+; t^+) = N_x N_y \frac{n(x_i^+, y_j^+; t^+)}{N_p}, \tag{7.16}$$

where $n(x_i^+, y_j^+; t^+)$ denotes the number of particles located in the box i, j at instant t^+, and N_p stands for the total number of particles in the entire domain. It is noted that if one measured the particle concentration at only one instant in time on an infinitely fine mesh, Eq. (7.16) would yield a concentration of zero everywhere, except on the positions of the particles where the concentration would be infinity.

In order to obtain a statistically stationary solution for the concentration $c(x^+, y^+)$, we calculate $\hat{c}(x_i^+, y_j^+; t^+)$ at different instants in time and take the average of the results:

$$c(x_i^+, y_j^+) = \frac{1}{T^+/\delta t^+} \sum_{k=1}^{T/\delta t} \hat{c}(x_i^+, y_j^+; t_1^+ + k\delta t^+). \tag{7.17}$$

In the present research we take $T^+ = 5,000$ and $\delta t^+ = 2$, i.e. after every 2 units of time the concentration $\hat{c}(x_i^+, y_j^+; t^+)$ is determined, for all times $5,000 < t^+ \leq 10,000$.

Now, we define the *mean* concentration as a function of the streamwise coordinate as:

$$\bar{c}(x_i^+) \equiv \frac{1}{N_y} \sum_{j=1}^{N_y} c(x_i^+, y_j^+) \tag{7.18}$$

Due to the deposition of particles onto the wall, the flow is continuously being depleted from particles as it goes downstream. As a consequence, the value of $\bar{c}(x^+)$ decreases with x^+ for all finite values of the particle Stokes number. Nevertheless, it is expected that $c(x^+, y^+)/\bar{c}(x^+)$ will go to a converged concentration profile for large enough values of x^+ [38], [36]:

$$\lim_{x^+ \to \infty} \frac{c(x^+, y^+)}{\bar{c}(x^+)} = f(y^+). \tag{7.19}$$

Thus, by measuring both $c(x^+, y^+)$ and $\bar{c}(x^+)$, one can determine the quantity $c/\bar{c}$, for a given value of the particle Stokes number.

In the present research, we determine $c/\bar{c}$ on the basis of the last 5 of the 25 segments in the streamwise direction, i.e. we consider the time-averaged concentration in the range $0.8L^+ < x^+ \leq L^+$.

7.3.2 Measuring the deposition velocity of heavy particles

The dimensionless deposition velocity K_{dep}^+ is defined as the ratio of flux density of particles at a surface to the mean concentration of particles in the boundary layer, see Eq. (7.1). The flux density of particles j_{wall} can be approximated by the number of particles which have left the domain in the infinitesimal segment $\mathrm{d}x^+$:

$$j_{wall} = \rho_p h^+ \bar{U}^+ \frac{\mathrm{d}\bar{c}}{\mathrm{d}x^+}, \tag{7.20}$$

where $\bar{U}^+$ is the mean streamwise velocity over the boundary layer, given by:

$$\bar{U}^+ = \frac{1}{h^+} \int_0^{h^+} \langle u_x^+ \rangle (y^+) \mathrm{d}y^+ \tag{7.21}$$

Since the boundary layer height h^+ and the mean velocity $\bar{U}^+$ are constants, combination of Eq. (7.1) and Eq. (7.20) shows that the deposition velocity is equal to:

$$K_{dep}^+ = \frac{h^+ \bar{U}^+}{(x_2^+ - x_1^+)} \ln \frac{\bar{c}(x_1^+)}{\bar{c}(x_2^+)}. \tag{7.22}$$

Over a large time interval (typically $5,000 < t^+ \leq 10,000$), a converged solution for the depostion velocity is obtained, provided x_2^+ and x_1^+ are sufficiently large; the

effects of the initial conditions and of the conditions at $x^+ = 0$ are then negligible. In the present simulations, we determine the deposition velocity in each of 25 identical segments along the length of the turbulent boundary layer of $L^+ = 20,000$. Good convergence for the deposition velocity is found in all simulations presented in this chapter.

7.3.3 Detection of interparticle collisions

During each time step, inter-particle collisions are detected. In principle, this could be done by comparing the position of each particle with respect to all other particles; if two particles overlap, a collision is registered. The computational cost of this procedure is of order N_p^2, where N_p is the total number of particles in the simulation.

In order to reduce the computational effort of collision detection, we divide the physical domain into a large number of identical boxes. A requirement to the box size is that a particle is not able not pass through an entire box within one single time step. In the simulations presented in the present chapter and in Chapter 8, we use 200 boxes in the streamwise direction, and 100 boxes in the wall-normal direction.

First, we label every particle by a particle number during each numerical time step. Then, the amount of particles inside each of the 200×100 boxes is determined from the particle positions. Subsequently, the particle numbers are rearranged in an array of length N_p on the basis of the number of the box where they are in: the numbers of the particles in the first box are the first entries in the array, the numbers of the particles in the second box are the following entries in the array, etc. Because each box is associated to a limited number of entries in the array, the numbers of all the particles in a certain box can efficiently be found. Finally, we compare the position of each particle to the positions of all the other particles in the same box and of all the particles in neighboring boxes; when a collision is detected, either a fully elastic collision or a fully inlastic collision is executed.

The computational cost of this procedure is of order N_p, and it is thus very beneficial if the total number of particles in the domain is large.

7.4 Results

7.4.1 Verification tests

In this section, we show that passive tracers through the turbulent boundary layer under consideration spread uniformly over the domain. In addition, the collision detection algorithm is tested for the case of heavy particles in a stochastic model for homogeneous turbulence.

Motion of passive tracers in a turbulent boundary layer

We investigate the motion of passive tracers in a turbulent boundary layer. Passive tracers correspond to heavy particles with an infinitesimally small Stokes number. Thus, the position of a passive tracer $\boldsymbol{x}_{pt}^{+}$ in the course of time is described by the following equation of motion:

$$\frac{\mathrm{d}\boldsymbol{x}_{pt}^{+}}{\mathrm{d}t^{+}} = \boldsymbol{u}^{+}(\boldsymbol{x}_{pt}^{+}(t^{+}), t^{+}), \tag{7.23}$$

where the carrier flow velocity $\boldsymbol{u}^{+}$ can be determined by Eq. (7.4) and Eq. (7.5).

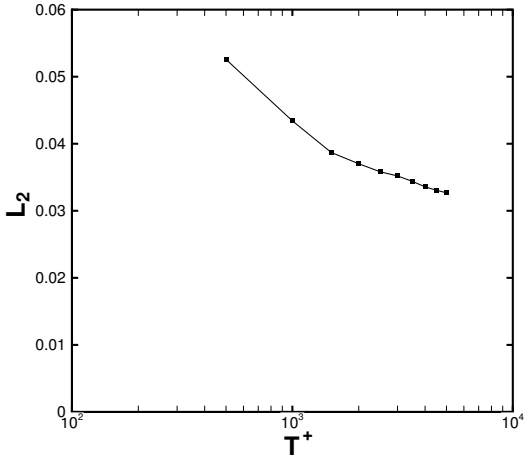

FIGURE 7.5: *L_2-norm of the deviation from uniform concentration, $c(x_i^+, y_j^+) - 1$, of passive tracers ($St = 0$), for different values of the time of integration T^+.*

A simulation is carried out in which 40,000 passive tracers are traced in time. The concentration is then calculated from Eq. (7.17), for different values of the time of integration T^+. On the basis of this result, we calculate the L_2-norm of the deviations from a uniform concentration, $c = 1$, over all $N_x \times N_y$ boxes; the result is shown in Fig. 7.5, as a function of T^+. As expected, as $T^+ \to \infty$, the deviation tends to zero, meaning that passive tracers are uniformly distributed over the domain. This shows that the well-mixedness condition is indeed satisfied.

Testing collision detection in homogeneous flow

In order to test the collision detection algorithm, we carry out a numerical experiment in two-dimensional stationary Gaussian turbulence. The stochastic model describing

the motion of passive tracers is the two-dimensional Ornstein Uhlenbeck process (see Chapter 6).

A group of N_p particels is released in a domain of size $200 \times 200.$; periodic boundary conditions are imposed. The particle equations of motion are given by Eq. (7.4) and Eq. (7.5), where we take $\langle u_x^+ \rangle = \langle u_y^+ \rangle = 0$, $\langle u_x^{+2} \rangle^{1/2} = \langle u_y^{+2} \rangle^{1/2} = \sigma^+ = \sqrt{20}$, and $\tau^+ = 10$. Due to the homogeneity of the carrier flow, the collisions occur statistically uniformly over the domain.

It is known [93] that the collision rate $\dot{\mathcal{N}}_c$ (i.e. the number of collisions per unit of time per unit of volume) is approximately quadratic in the mean particle number density n_0:

$$\dot{\mathcal{N}}_c \simeq \Gamma \frac{n_0^2}{2} = \Gamma \frac{N_p^2}{2\Omega^2}, \tag{7.24}$$

where Ω is the volume of the domain (or surface, in this two-dimensional case). The parameter Γ is called the collision kernel.

We carry out numerical simulations for different values of N_p, and determine the number of collisions per unit of time per unit of volume. This information was used to calculate the collision kernel Γ by Eq. (7.24); the result is shown in Fig. 7.6a), for a particle diameter $d_p = 1$ and $\mathrm{St} = 10$. As expected, Γ goes to a constant value as the number of particles increases.

In Fig. 7.6b) we show the results for a simulation in which the particle diameter d_p was varied; the particle Stokes number St was kept constant. The collision kernel apparently grows linearly with the particle diameter, which corresponds to the theoretical expectation [93]. This shows that the collision detection algorithm is consistent with the theoretical result in [93].

7.4.2 Heavy particles in a turbulent boundary layer; no particle interactions

First, we investigate the motion of heavy particles without taking into account collisions and coalescence. A group of $40,000$ particles is released in a boundary layer of length $L^+ = 20,000$ and height $h^+ = 200$. In order to facilitate comparison to results from Liu and Agarwal who carried out experiments with olive oil droplets in air [51], the mass density ratio is taken as $\rho_p/\rho = 770$.

First, we show the concentration of the particles after time $t^+ = 10,000$ in Fig. 7.7a), for the case $\mathrm{St} = 5$. There is a relatively high concentration of particles close to the wall. On the one hand, these particles have enough inertia to arrive in the viscous sublayer, where the velocity fluctuations are low. On the other hand, most these particles do not have enough inertia to directly reach the wall by 'free flight' through the boundary layer. As a result, they do not deposit onto the wall, nor are they reentrained into the flow. Eventually, an equilibrium concentration exists, in which the concentration close to the wall is larger than the concentration in the rest of the boundary layer.

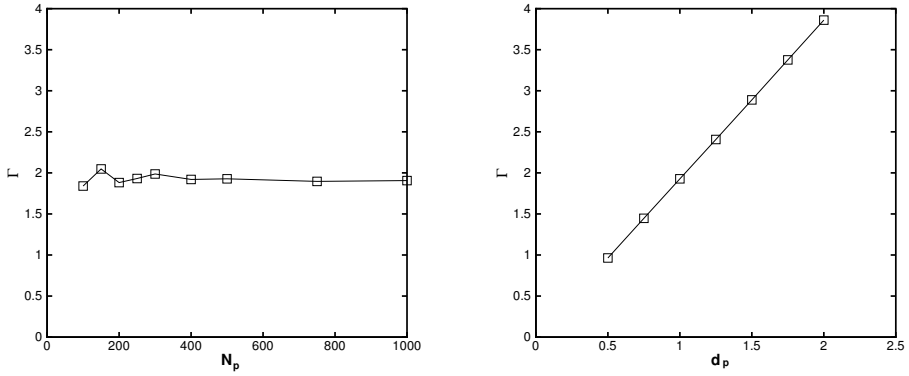

a) $\Gamma(N_p)$, $d_p = 1$. b) $\Gamma(d_p)$, $N_p = 500$.

FIGURE 7.6: *Numerical solution for collision kernel* Γ *in two-dimensional stationary Gaussian turbulence containing* N_p *heavy particles of diameter* d_p*; St* $= 10$*,* $\tau^+ = 10$*,* $\sigma^+ = \sqrt{20}$*.*

The concentration distribution changes considerably when the Stokes number is increased. This can be seen in Fig. 7.7b), where the result for St = 50 is presented. Particles with higher Stokes numbers are less susceptible to small-scale fluctuations of the carrier flow. Therefore, particles with Stokes number St = 50 can pass through the viscous sublayer and reach the wall directly. Due to the deposition of particles on the wall, the concentration of particles gradually decreases downstream. As a consequence, the highest value of the particle concentration is found near the inlet.

The quantity $c/\bar{c}$, with $\bar{c}$ the mean concentration as defined by Eq. (7.18), is presented in Fig. 7.8, for five different Stokes numbers. Apparently, the concentration of particles with St = 1 is almost uniform; there is only a slightly elevated concentration near the wall. The phenomenon of particle accumulation near the wall is much more pronounced in the case of St = 5 and St = 10: the concentration of particles in the viscous sublayer is more than 40 times higher than the mean concentration. For high Stokes numbers such as St = 100, no significant increase in the particle concentration near the wall is visible.

The results are qualitatively very much in agreement with well-known experimental and numerical results obtained in recent years (e.g. [76], [91]) showing that particles of St = $O(10)$ may accumulate in the near-wall region in turbulent boundary layers. Evidently, the relatively simple model applied in the present research is able to predict the concentration profiles and the Stokes numbers for which they occur quite correctly.

Fig. 7.9 shows the PDF of wall-normal impact velocities of particles onto the wall. As becomes clear from this figure, larger particles (St = 100) hit the wall with, on average, a larger wall-normal velocity than smaller particles (St = 10). This once

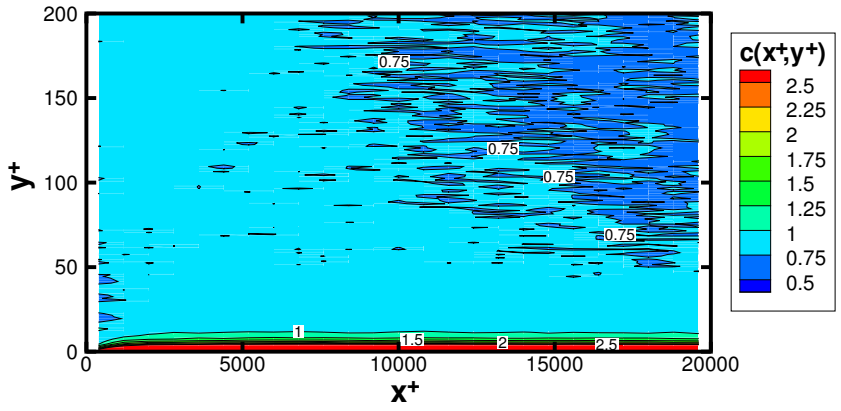

a)

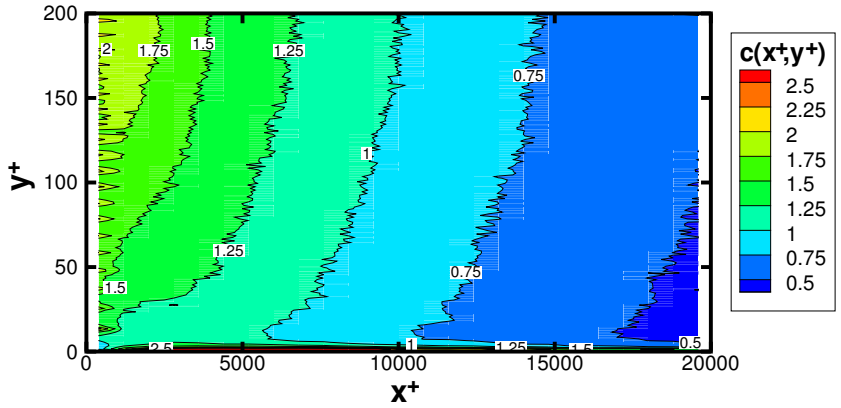

b)

FIGURE 7.7: *Concentration* $c(x^+, y^+)$ *after time* $t^+ = 10,000$*, with particle interactions neglected. a)* $St = 5$*, b)* $St = 50$*.*

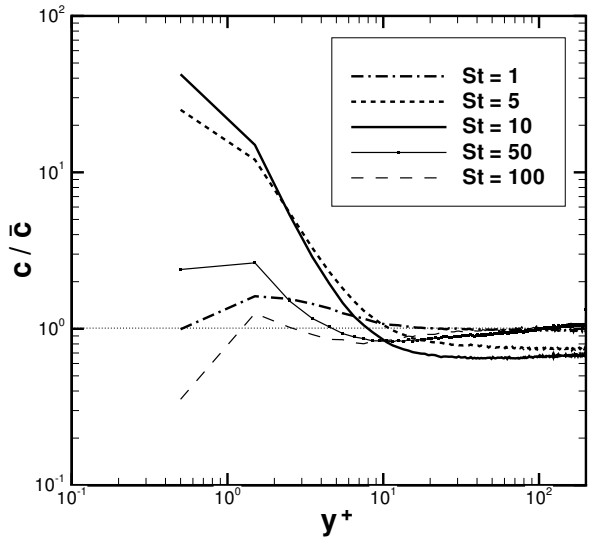

FIGURE 7.8: *Concentration profile $c(x^+, y^+)/\bar{c}(x^+)$ as a function of the wall-normal coordinate, for five different Stokes numbers. Particle interactions have been neglected.*

again supports the hypothesis that large particles may cross the viscous wall-layer directly without being decelerated by the flow, whereas smaller particles reach the wall only through interactions with the small-scale flow structures near the wall.

By repeating the numerical simulations for a wide range of Stokes numbers, the deposition velocity of particles on the wall as a function of St has been calculated. The result is presented in Fig. 7.10, which also shows the experimental results from Liu & Agarwal [51], the fit through experimental data by McCoy & Hanratty [61] and the recent numerical results by Mito & Hanratty [64].

First of all, we see that our result is very similar to the result presented by Mito & Hanratty [64]. It is noted that Mito & Hanratty [64] employed a stochastic method (with Gaussian distribution) in three dimensions, which was tuned using data from a DNS of a turbulent channel flow. Evidently, our one-dimensional method produces very similar results. Both methods are able to capture the general shape of the deposition velocity curve: the deposition velocity increases very fast with St as long as St < 30, whereas it becomes almost independent of the Stokes number as St > 30.

Compared to the experimental results, though, the deposition velocity for smaller particles (St $\lesssim 10$) is underestimated. This can be explained by three main reasons. Firstly, the particle equation of motion employed in the present study involves only Stokes drag, but the Saffman lift force [86] may play a non-negligible role in wall-bounded flows as well. The influence of the Saffman lift force on the motion of

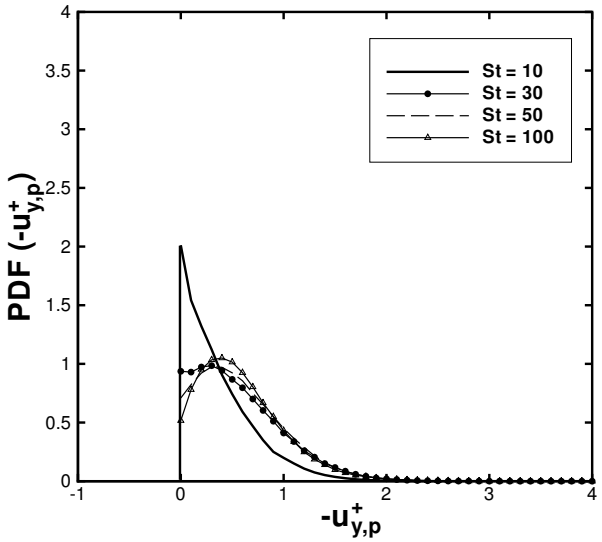

FIGURE 7.9: *Probability density function of the (dimensionless) wall-normal velocity of particles on the moment that they hit the wall, for four different Stokes numbers. Particle interactions have been neglected.*

particles can be described as follows: if a particle is close to a wall and its streamwise velocity is higher than the local carrier flow velocity, then the Saffman lift force gives a particle an acceleration towards the wall. If, on the other hand, the particle lags the local carrier fluid velocity, it is forced away from the wall. Since inertia causes heavy particles to enter the near-wall region with a higher streamwise velocity than passive tracers, the lift force is expected to enhance the deposition of particles on the wall. The studies by Kallio & Reeks [38] and by Wang *et al.* [99] show that the inclusion of this term indeed has a quantitative influence on the deposition velocity curve, especially for small Stokes numbers; the qualitative picture, however, is not altered much.

Secondly, the intermittency of the turbulence is underestimated in the Gaussian stochastic models employed [77]. Intermittency is associated to sudden sweeps of fluid towards the wall, and it is probable that some particles deposit onto the wall due to this effect. Possibly, a more realistic result for the deposition velocity for $\mathrm{St} \lesssim 10$ could be obtained by employing a non-Gaussian stochastic differential equation, which models the intermittent fluctuations of the carrier flow more realistically. Although non-Gaussian stochastic differential equations have been employed in other studies [36], [96], it has the drawback that a good modelling of the non-Gaussianity requires much more statistical information on the flow than just the r.m.s. of the

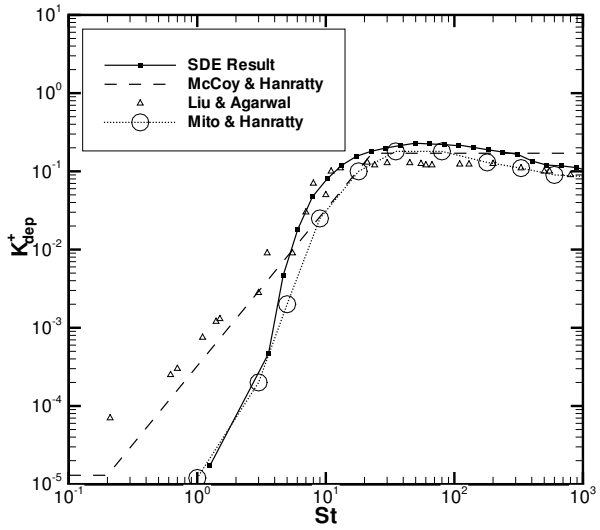

FIGURE 7.10: *Deposition velocity as a function of the Stokes number for particles in a boundary layer on a flat plate, with particle interactions neglected. The results from the SDE model are compared to experimental data from Liu & Agarwal [51], and to the fit through experimental data by McCoy & Hanratty [61] given in Eq. (7.2). In addition, the numerical result from Mito & Hanratty [64] is presented.*

velocity fluctuations. Although this information can be found for the flow over a flat plate either from ample experimental results or from DNS simulations, it is very difficult to obtain it for the more complex flows in industrial gas-liquid separators we would like to study in Chapter 8.

The third reason for the deviations in Fig. 7.10 is related to the neglection of particle interactions. It is possible that particles with small Stokes numbers accumulate in the near-wall region, where they may collide or coalesce. Due to these interactions, some particles may reach the wall eventually. In order to investigate the effect of particle interactions on the dispersion and deposition of particle qualitatively and quantitatively, we carry out simulations in which collisions of particles are taken into account. The results from these simulations are presented in the following sections.

7.4.3 The effect of fully elastic collisions

Now, we investigate the effect of fully elastic collisions on the motion of heavy particles in a turbulent boundary layer. In order to compare results for different Stokes numbers, the mean volumetric concentration of particles in the domain, Φ, is kept constant. This is done by extending the computational domain to three dimensions.

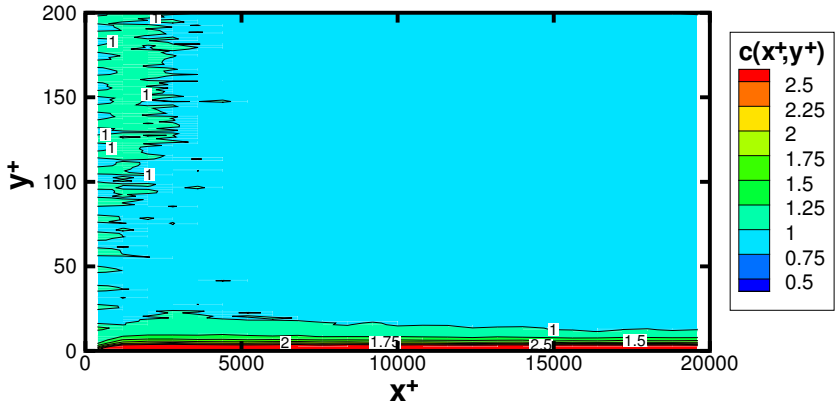

a)

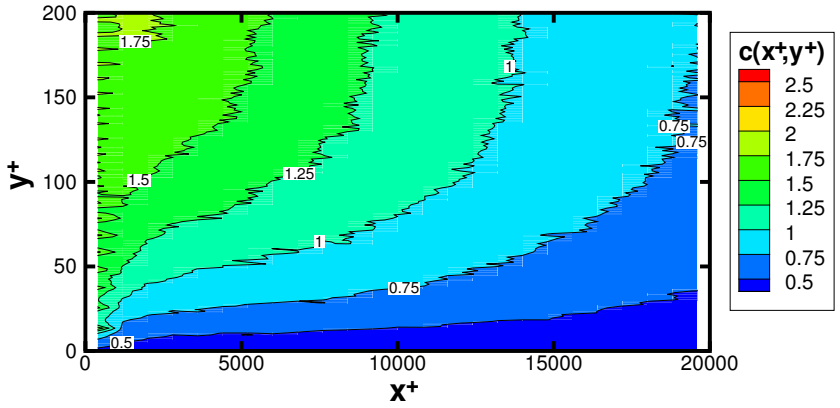

b)

FIGURE 7.11: *Concentration $c(x^+, y^+)$ after time $t^+ = 10,000$. Particle interactions are modelled as fully elastic collisions; the mean volumetric concentration is $\Phi = 10^{-5}$. a) $St = 5$, b) $St = 50$.*

The size of the domain in spanwise direction, z^+_{max}, can be adjusted in order to control the mean volumetric concentration of particles in the domain while keeping the total number of particles in the domain fixed. The particles are initially uniformly distributed in the spanwise direction. The velocity of the carrier flow field is assumed to be zero in the spanwise direction.

The result for the time-averaged particle concentration in the boundary layer is presented in Fig. 7.11a), for the case of fully elastically colliding particles with Stokes number St = 5. The plot is rather similar to Fig. 7.7a), but the region of elevated concentration of particles close to the wall is not as narrow as in Fig. 7.7a). The reason for this is that particles which are forced towards the wall by turbulent fluctuations, collide with other particles which are already close to the wall. As a consequence, these particles are prevented from entering the viscous sublayer, and the concentration in the viscous sublayer is not much larger than in the rest of the flow.

In Fig. 7.11b), which shows the time-averaged concentration of particles with St = 50, the elevated concentration near the wall is not visible anymore. Apparently, these larger particles do not accumulate near the wall if they 'feel' each others presence.

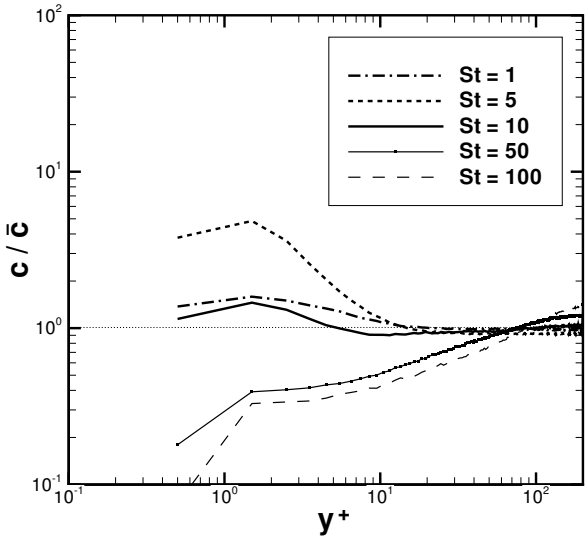

FIGURE 7.12: *Concentration profiles $c(x,y)/\bar{c}(x)$ as a function of the wall-normal coordinate y^+, for five different Stokes numbers. Particle interactions are modelled as fully elastic collisions; the mean volumetric concentration of particles is $\Phi = 10^{-5}$.*

This result is supported by Fig. 7.12, in which the concentration $c/\bar{c}$ is plotted as a function of the wall-normal coordinate, for five different Stokes numbers. It shows

that the concentration of particles with St = 10 near the wall has decreased dramatically; in Fig. 7.8, the concentration near the wall was more than 40 times higher. This significant reduction of particle concentration near the wall can be attributed to the fact that particles are not able to enter the viscous sublayer when this relatively thin layer is already filled with other particles.

The result for the deposition velocity is presented in Fig. 7.13. Apparently, the deposition velocity is not altered much when fully elastic collisions are taken into account. Only relatively small particles with St $\simeq$ 5 benefit from the collisions: they may reach the wall due to the particle interactions, whereas they have too little inertia to cross the boundary layer on their own.

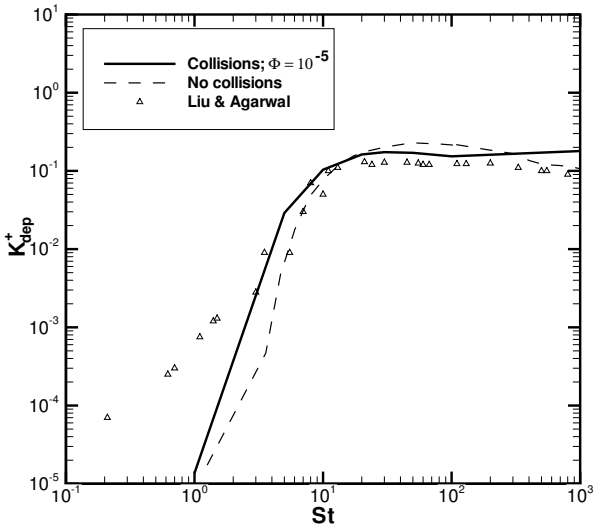

FIGURE 7.13: *Deposition velocity as a function of the Stokes number for particles in a boundary layer on a flat plate, with fully elastic collisions taken into account; the mean particle concentration is* $\Phi = 10^{-5}$. *The deposition velocity curves are compared to the result presented in Fig. 7.10, where no particle interactions have been taken into account, and to the experimental data from Liu & Agarwal [51].*

Finally, we show the PDF of wall-normal impact velocities of particles onto the wall in Fig. 7.14. Comparison of Fig. 7.14 with Fig. 7.9 shows that the PDF of impact velocities of particles with St = 10 is broader when collisions are taken into account. It suggests that the particles do not only reach the wall due to a gradual motion through the viscous sublayer, but also by collisions with other particles close to the wall. Fully elastic collisions imply a redistribution of the velocities of the

involved particles; even two horizontally moving particles may have considerable vertical velocities after having collided with each other.

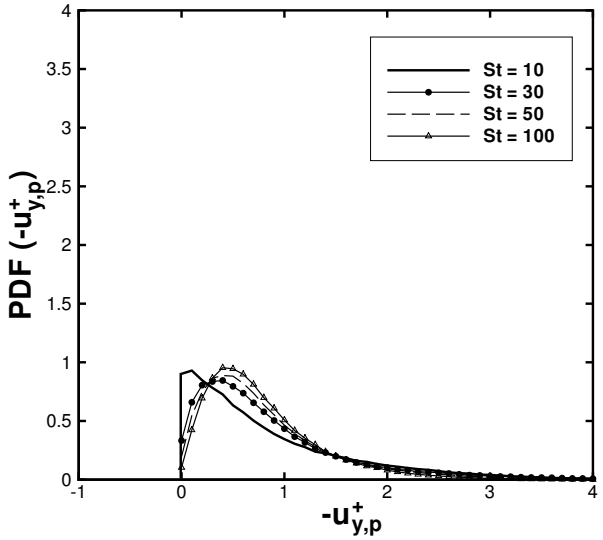

FIGURE 7.14: *Probability density function of the (dimensionless) wall-normal velocity of particles on the moment that they hit the wall, for four different Stokes numbers. Particle interactions are modelled as fully elastic collisions; the mean volumetric concentration of particles is* $\Phi = 10^{-5}$.

In conclusion, in this section we have shown that the incorporation of fully elastic collisions appears to decrease the elevated particle concentration close to the wall for $\mathrm{St} = O(10)$, i.e. to decrease the effect of turbophoresis (i.e. the gradual motion of particles towards the wall). Moreover, we find that the impaction of particles onto the wall results both from the redistribution of particle velocities after a collision and from free-flight of particles close to the wall. Nevertheless, the resulting particle deposition velocity is not altered very much with respect to the situation that particle interactions are neglected.

7.4.4 The effect of coalescence

Now, we study the effect of coalescence on the dispersion and deposition of particles in a turbulent boundary layer. In order to do this, $40,000$ particles are traced in the turbulent boundary layer for a large time. During the simulation, the particles collide and merge to become larger particles. When such a 'composed' particle (consisting of $\tilde{n}$ original particles, say) leaves the domain either by hitting the wall or by passing

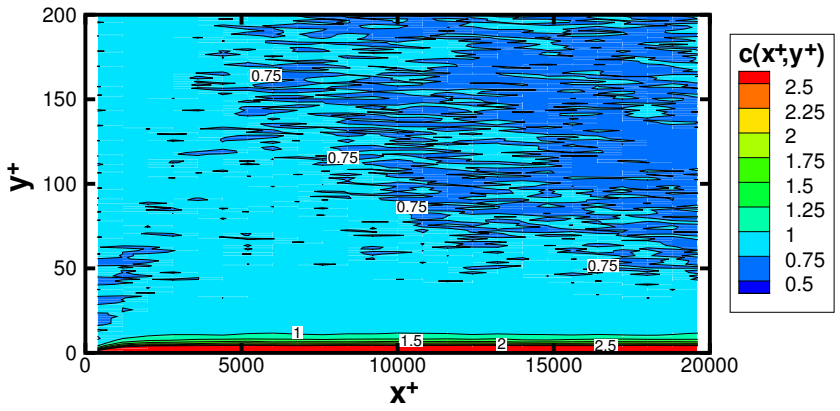

a)

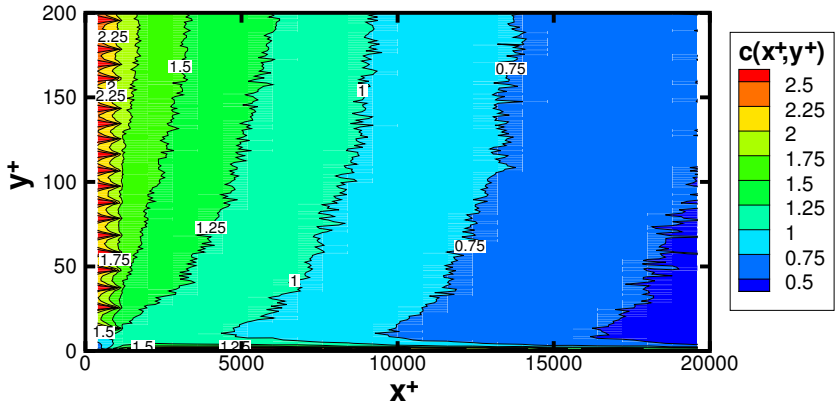

b)

FIGURE 7.15: *Concentration $c(x^+, y^+)$ after time $t^+ = 10,000$. Particle interactions are modelled as fully inelastic collisions (coalescence); the mean volumetric concentration is $\Phi = 10^{-5}$. a) $St = 5$, b) $St = 50$.*

the line $x^+ = L^+$, $\tilde{n}$ new particles of the original size are injected into the boundary layer at $x^+ = 0$, so that the total mass loading of particles in the entire domain remains unaltered.

The time-averaged concentration of 40,000 particles is plotted in Fig. 7.15a), after time $t^+ = 10,000$. The initial Stokes number of the particles is St = 5, and mean the volumetric concentration is $\Phi = 10^{-5}$. Although the result is similar to Fig. 7.7a), the particle concentration decreases more quickly in the downstream direction. This result, which is an indication of a higher deposition velocity, can be explained as follows. In the first part of the channel, the particles accumulate in the viscous sublayer, just like in the case where no particle interactions were taken into account, or the case where the particle interactions were modelled as fully elastic collisions. In the case of coalescence modelled, however, the particles do not only accumulate in the near-wall region, they coalesce to larger particles. When the coalesced particles are sufficiently large, they may even cross the viscous sublayer, either due to fluctuations in the carrier flow field or due to collisions with other particles.

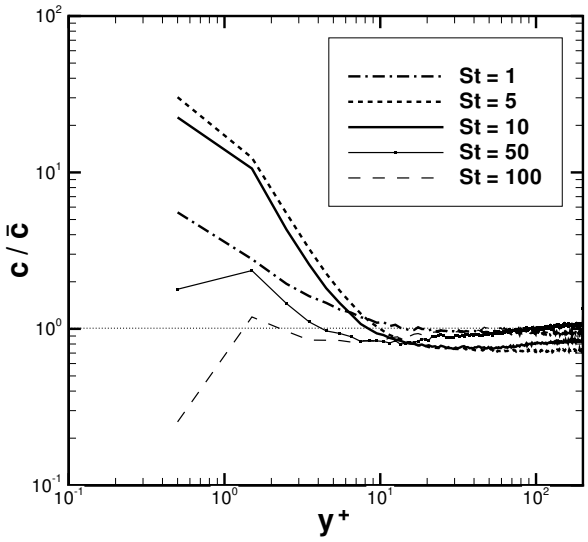

FIGURE 7.16: *Concentration profiles $c(x, y)/\bar{c}(x)$ as a function of the wall-normal coordinate y^+, for five different Stokes numbers. Particle interactions are modelled as fully inelastic collisions (coalescence); the mean volumetric concentration of particles is $\Phi = 10^{-5}$.*

The concentration profiles of a group of particles with an initial particle Stokes number of St = 50 is plotted in Fig. 7.15b). The result is very similar to Fig. 7.7b),

indicating that coalescence does not have much effect on the distribution of large particles.

In Fig. 7.16, the time-averaged value of $c/\bar{c}$ is plotted as a function of the wall-normal coordinate, for five different Stokes numbers. It is noted that the Stokes number here corresponds to the Stokes number of newly injected particles; of course, the Stokes number of a particle may increase due to coalescence. The results for St = 10 and St = 100 are rather similar to the results presented in Fig. 7.8. For particles with small Stokes numbers such as St = 1, however, we see a considerable increase in the particle concentration near the wall. Also, the near-wall concentration of particles with St = 5 is higher than the concentration of particles with St = 10. Evidently, these initially small particles first grow on to larger particles and then accumulate near the wall.

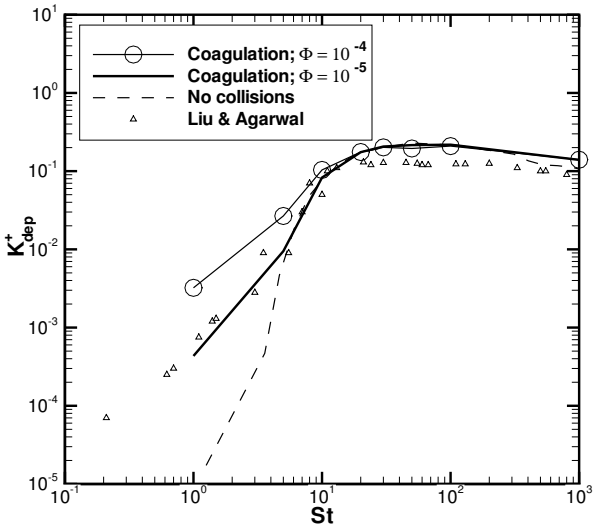

FIGURE 7.17: *Deposition velocity as a function of the Stokes number for particles in a boundary layer on a flat plate, with fully inelastic collisions taken into account. Two different values of the mean particle concentration have been used:* $\Phi = 10^{-5}$ *and* $\Phi = 10^{-4}$. *The deposition velocity curves are compared to the result presented in Fig. 7.10, where no particle interactions have been taken into account, and to the experimental data from Liu & Agarwal [51].*

The deposition velocity has been calculated for a wide range of Stokes numbers, for two values of the mean particle concentration: $\Phi = 10^{-5}$ and $\Phi = 10^{-4}$. The result is plotted in Fig. 7.17. Apparently, the deposition of particles with initially

small Stokes numbers is enhanced considerably by taking into account coalescence effects. Remarkably enough, this effect takes place already for relatively small values of the mean particle concentration. The deposition velocity of particles with a higher initial Stokes number is hardly altered.

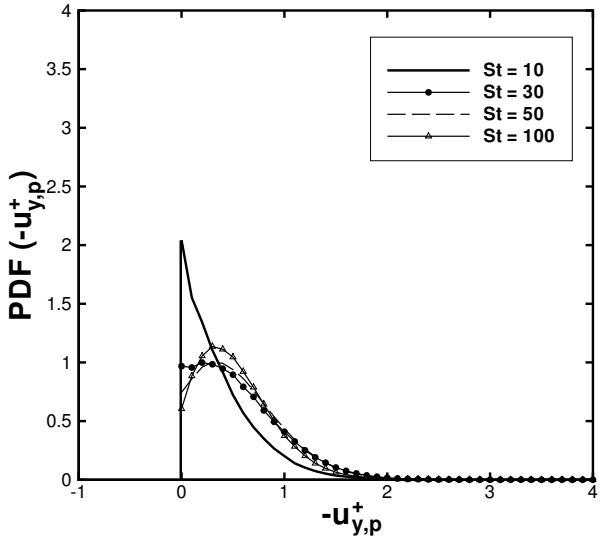

FIGURE 7.18: *Probability density function of the (dimensionless) wall-normal velocity of particles on the moment that they hit the wall, for four different Stokes numbers. Particle interactions are modelled as fully inelastic collisions (coalescence); the mean volumetric concentration of particles is* $\Phi = 10^{-5}$.

Finally, we show the PDF of the wall impact velocities in Fig. 7.18. For the relatively large Stokes numbers considered, between St = 10 and St = 100, the result is very similar to Fig. 7.9. This supports the hypothesis that coalescence does not significantly change the motion of large particles, but it is mainly important for small particles.

7.5 Conclusions

The motion of heavy particles in a turbulent boundary layer flow over a flat plate has been investigated by a Lagrangian numerical simulation. The carrier flow velocity along the trajectory of the particle is modelled by a stochastic method. The stochastic model is selected to satisfy the well-mixedness condition in the limit of

infinitesimally small particles.

The results in the flow over the flat plate indicate that the droplet concentration has a maximum value close to the wall if the particle Stokes number St is $O(10)$. The particle deposition velocity, defined as the particle flux towards the wall divided by the mean concentration of particles, is shown to increase rapidly with the particle Stokes number for $10 < \mathrm{St} < 30$. For $\mathrm{St} \geq 30$, the particle deposition velocity is almost independent of the Stokes number. A comparison with experimental data from literature shows that the SDE model underestimates the particle deposition for small Stokes numbers $\mathrm{St} < 10$. Nevertheless, the general features of the deposition velocity curve as a function of the Stokes number are well captured: the deposition velocity increases rapidly as $\mathrm{St} < 30$ and then becomes almost independent of the Stokes number.

The influence of fully elastic and fully inelastic collisions has been investigated, too. An efficient collision detection algorithm has been developed and implemented in the Lagrangian particle tracking code. Numerical results show that fully elastic collisions do not enhance the particle deposition rate significantly, but rather change the mechanism of particle deposition: particles move to the wall due to collisions rather than due to free-flight diffusion. Fully inelastic collisions on the other hand result in an increase of the mean particle Stokes number. This enhances the particle deposition for small Stokes numbers. These results suggest that droplets (i.e. coalescing particles) with a small Stokes number have a higher probability of depositing on the wall than rigid particles of the same density and of the same size.

HEAVY PARTICLES IN TURBULENT SWIRLING FLOW IN A PIPE

CHAPTER 8

The motion of small heavy particles in the turbulent boundary layer in a swirling flow in a pipe is investigated numerically. The trajectories of the particles are calculated using Lagrangian tracking. The Stokes drag force is the only force acting on the particles. The turbulent carrier flow field at the position of the particle consists of an axial velocity, an azimuthal velocity and random fluctuations in the wall-normal direction. We present numerical results for the concentration of heavy particles in this three-dimensional flow and we calculate the deposition velocity of particles on the wall, and we show probability density functions for the wall-hitting velocity. In addition, fully elastic collisions and fully inelastic collisions between the particles have been implemented. We study the effect of these particle interactions on the concentration profiles and on the deposition velocity.

8.1 Introduction

We study the configuration of a gas-liquid separator presented in section 1.2.3 in which a region of high vorticity is generated in the center of the pipe. Contaminant particles and droplets are expelled towards the wall due to the swirl in the center of the pipe. Close to the wall, the dispersion of particles is expected to be affected by two phenomena: the non-zero flow velocity in tangential direction in the boundary layer and turbulent fluctuations in the flow, which are present in high Reynolds number flows. In Chapter 3, Chapter 4 and Chapter 5, it has been shown that vortex filaments can cause a largely non-uniform concentration of particles. The results of Chapter 7 on the other hand demonstrate that the motion of particles in the turbulent flow over a flat plate is governed by particle-turbulence interactions, which cause the deposition velocity of particles to be a strongly dependent on the particle Stokes number. In a turbulent swirling flow in a pipe, both the mean swirl and the turbulent fluctuations are expected to affect the deposition of heavy particles onto the wall. In the present research, the goal is to determine the dispersion and deposition of heavy particles and droplets in the turbulent boundary layer of a swirling flow in a pipe.

Turbulent swirling flows through a straight pipe are highly complex. From an experimental study, Kitoh [41] obtained a good qualitative and quantitative description of fully developed turbulent swirling flows in a straight circular pipe for Reynolds numbers ranging from 40,000 to 80,000. His results suggest that three different regions can be distinguished inside a pipe with radius R: a core region ($0 < r/R < 0.5$), an annular region ($0.5 \leq r/R \leq 0.9$) and a boundary layer close to the pipe wall ($0.9 < r/R < 1.0$). The core region is characterized by a strong swirl, which causes the velocity field to be similar to a Rankine type of vortex. In the annular region, the turbulent flow is affected by streamline curvature and skewness of the mean velocity vector. This is illustrated by the fact that the direction of the flow*, the direction of the shear stress† and the direction of the velocity gradient‡ do not coincide [41]. The boundary layer region, on the other hand, is hardly affected by the swirl in the sense that the flow direction, the shear direction and the velocity gradient direction do coincide. Close to the wall, the profile of the total mean velocity, defined as the length of the combined mean velocities in axial and in tangential direction $\langle U_{tot} \rangle \equiv \sqrt{\langle u_x \rangle^2 + \langle u_\theta \rangle^2}$, follows the well-known law-of-the-wall for turbulent boundary layers, i.e. $\langle U_{tot} \rangle \sim (1/\kappa) \ln \eta^+ + B$ when the wall-normal coordinate η^+ is between 30 and 1000. Although Kitoh states that the values κ and B are modified as the swirl number increases, for $\eta^+ \lesssim 200$ the classical values $\kappa = 0.41$ and $B = 5.5$ apply. A plot of the total velocity in the near-wall region is given in Fig. 14 in Kitoh's paper [41], for a large number of experiments with three different swirl intensities.

Due to the complexity of the problem, numerical simulations of swirling flows have been a challenge to turbulence modellers in past few decades. Due to the presence of secondary strains, a classical $k - \epsilon$ model is expected to perform poorly [92]. Modifications to this model, investigated by e.g. [74] and [92], do not result in a significantly improved predictions of swirl decay. Therefore, in order to circumvent the computational difficulties associated to swirling pipe flows at high Reynolds number, we concentrate on the wall region only. In this region, the mean velocity profiles in axial and azimuthal direction are a function of the wall-normal distance alone.

To the best of our knowledge, the motion of heavy particles through a turbulent boundary layer in a swirling flow in a pipe has not yet been investigated. We study the influence of the friction Reynolds number Re_τ, which can be seen as a measure of the turbulence intensity, and the swirl angle θ_S, which can be seen as a measure of the swirl. In addition, the effect of particle interactions are investigated.

In section 8.2, we present the equations of motion for the particles, and the velocity of the carrier flow at the position of the particle. In section 8.3 the numerical

*The direction of the flow is characterized by the swirl angle $\theta_S = \arctan(\langle u_\theta \rangle / \langle u_x \rangle)$.

†The direction of the shear stress is characterized by the angle $\theta_{ss} = \arctan(\langle u_\theta u_r \rangle / \langle u_x u_r \rangle)$.

‡The direction of the velocity gradient is characterized by the angle $\theta_g = \arctan\left(r \frac{\partial}{\partial r}\left(\frac{\langle u_\theta \rangle}{r}\right) \Big/ \frac{\partial \langle u_\theta \rangle}{\partial r}\right)$.

methods are explained. Section 8.4 summarizes the results for heavy particles in the turbulent boundary layer of a swirling flow in a pipe. First, the results are presented for the case that particle interactions are neglected. Subsequently, the results for fully elastically and of fully inelastically colliding particles are presented. Conclusions are formulated in section 8.5.

8.2 Physical-mathematical model

8.2.1 Equations of motion of heavy particles

A Lagrangian approach is used for the calculation of the particle trajectories. The particles are assumed to be small, and to good approximation spherical. The mass loading of particles is assumed to be small enough so that the influence of the particles on the flow may be neglected, i.e. one-way coupling is used. Since gravity is typically a minor effect in high-speed gas-liquid separators, it is neglected, as well as added mass effects and Basset history forces. Although the Saffman lift force may have some effect on the motion of heavy particles in turbulent boundary layers [38], we neglect it here in order to concentrate on the effect of the particle inertia. The equations of motion of a particle, in dimensionless form, are then:

$$\frac{d\boldsymbol{x}_p^+}{dt^+} = \boldsymbol{u}_p^+, \qquad \frac{d\boldsymbol{u}_p^+}{dt^+} = \frac{1}{\mathrm{St}}(\boldsymbol{u}^+(\boldsymbol{x}_p^+, t^+) - \boldsymbol{u}_p^+), \tag{8.1}$$

where $\boldsymbol{x}_p^+$ and $\boldsymbol{u}_p^+$ denote the position and the velocity of the particle, respectively, and $\boldsymbol{u}^+$ is the carrier flow velocity at the position of the particle. This equation has been made dimensionless by the kinematic viscosity of the carrier flow ν and the friction velocity u_τ, just like in Chapter 7.

The velocity of the carrier flow at the position of the particle, $\boldsymbol{u}^+$, is assumed to be given by:

$$\boldsymbol{u}^+ = \langle u_x^+ \rangle \boldsymbol{e}_x + \langle u_\theta^+ \rangle \boldsymbol{e}_\theta + \sigma^+ \xi \boldsymbol{e}_r, \tag{8.2}$$

where x is the coordinate in streamwise direction, r is the radial coordinate, and θ is the tangential coordinate. The parameter $\xi \equiv u_r^+/\sigma^+(r^+)$ denotes the fluid velocity in wall-normal direction divided by the root-mean-square of the velocity fluctuations in wall-normal direction. The random variable ξ is determined from the following stochastic differential equation:

$$\mathrm{d}\xi = -\frac{\xi}{\tau^+}\mathrm{d}t^+ + \left(\frac{\mathrm{d}\sigma^+}{\mathrm{d}r^+} + \frac{\sigma^+}{r^+}\right)\mathrm{d}t^+ + \sqrt{\frac{2}{\tau^+}}\mathrm{d}W, \tag{8.3}$$

where W denotes the Wiener process. The term $(\mathrm{d}\sigma^+/\mathrm{d}r^+ + \sigma^+/r^+)$ is introduced in order to satisfy the well-mixedness condition, see section 6.6.4.

In terms of the wall-normal distance $\eta^+ \equiv (R^+ - r^+)$, Eq. (8.3) becomes:

$$\mathrm{d}\xi = -\frac{\xi}{\tau^+}\mathrm{d}t - \left(\frac{\mathrm{d}\sigma^+}{\mathrm{d}\eta^+} - \frac{\sigma^+}{R^+ - \eta^+}\right)\mathrm{d}t + \sqrt{\frac{2}{\tau^+}}\mathrm{d}W. \tag{8.4}$$

The flow over a flat plate corresponds to the case where $R \to \infty$, so that the term $(\sigma^+/(R^+ - \eta^+))$ is zero. Thus, in this limit Eq. (7.5) is retrieved.

In order to solve Eq. (8.1), Eq. (8.2) and Eq. (8.3), the values for $\langle u_x^+\rangle(\eta^+)$, $\langle u_\theta^+\rangle(\eta^+)$, $\sigma^+(\eta^+)$ and $\tau^+(\eta^+)$ have to be known. In the present research, we take the mean velocity profile in accordance with experimental results reported by Kitoh [41], which are presented in the next section.

8.2.2 Averaged quantities in turbulent swirling flow in a pipe

A fully developed turbulent swirling flow in a straight pipe was investigated experimentally by Kitoh [41]. In his experiments, the Reynolds number, based on the average bulk velocity U_m and the pipe diameter $d = 2R$, is varied from $40,000$ to $80,000$.

Kitoh defines the swirl intensity Ω, i.e. the non-dimensional angular momentum flux, as:

$$\Omega \equiv \frac{2\int_0^R \langle u_x\rangle\langle u_\theta\rangle r^2 dr}{R^3 {U_m}^2}. \tag{8.5}$$

If the swirl number is sufficiently high, i.e. $\Omega \gtrsim 0.1$, three different regions can be distinguished in the velocity field in the pipe: a core region which is dominated by a vortex flow, an annular region and a wall region. Although the flow in the annular region is strongly skewed (i.e. the flow angle θ_S, the velocity gradient angle θ_g and the shear stress angle θ_{ss} do not coincide), the flow in the wall region ($\eta^+ < 1000$) is only slightly affected by the swirl. In particular, the velocity magnitude at the wall, defined as $\langle U_{tot}^+\rangle \equiv \sqrt{\langle u_x^+\rangle^2 + \langle u_\theta^+\rangle^2}$, follows the log-law of the wall quite well, especially for $\eta^+ < 200$. This result is almost independent of the swirl intensity Ω [41].

Thus, in the present research, where the motion of droplets in the near-wall region is investigated, it is justified to employ the law-of-the-wall. Only two additional parameters need to be introduced compared to the turbulent flow in a boundary layer over a flat plate, namely (i) R^+, the pipe radius compared to the boundary layer thickness, which is by definition equal to the friction Reynolds number Re_τ [77], and (ii) the angle between the mean velocity vector and the axial direction $\theta_S \equiv \arctan(\langle u_\theta^+\rangle/\langle u_x^+\rangle)$. It is noted that in the boundary layer near the pipe wall, θ_S is virtually independent of the distance to the wall η^+.

The total mean velocity $\langle U^+_{tot}\rangle(\eta^+)$ is assumed to follow the law-of-the-wall:

$$\begin{aligned}\langle U^+_{tot}\rangle(\eta^+) &= \eta^+, \quad \text{for } \eta^+ \le 5,\\ \langle U^+_{tot}\rangle(\eta^+) &= a_0 + a_1\eta^+ + a_2{\eta^+}^2 + a_3{\eta^+}^3, \quad \text{for } 5 < \eta^+ < 30,\\ \langle U^+_{tot}\rangle(\eta^+) &= 2.5\ln\eta^+ + 5.5, \quad \text{for } \eta^+ \ge 30,\end{aligned} \tag{8.6}$$

where the values of the constants a_0, a_1, a_2 and a_3 are given in Eq. (7.7). As a consequence, $\langle u^+_x\rangle(\eta^+)$ and $\langle u^+_\theta\rangle(\eta^+)$ are:

$$\langle u^+_x\rangle(\eta^+) = \langle U^+_{tot}(\eta^+)\rangle\cos\theta_S\,, \quad \langle u^+_\theta\rangle(\eta^+) = \langle U^+_{tot}(\eta^+)\rangle\sin\theta_S\,. \tag{8.7}$$

The mean velocity fluctuations in wall-normal direction and the Lagrangian decorrelation time are taken in accordance with the flow over a flat plate, discussed in Chapter 7. Thus, we have for $\sigma^+ = \sqrt{\langle {u_r^+}^2\rangle}$:

$$\sigma^+ = \sqrt{\langle {u_r^+}^2\rangle} = \frac{k_1{\eta^+}^2}{1 + k_2{\eta^+}^{k_3}}, \tag{8.8}$$

where the constants k_1, k_2 and k_3 are given in Eq. (7.8). Similarly, on the basis of Eq. (7.10) we have for $\tau^+(\eta^+)$:

$$\begin{aligned}\tau^+ &= 10, \quad \text{for } \eta^+ < 5,\\ \tau^+ &= C_0 + C_1\eta^+ + C_2{\eta^+}^2, \quad \text{for } \eta^+ \ge 5,\end{aligned} \tag{8.9}$$

where the values of C_0, C_1 and C_2 are given in Eq. (7.10).

8.3 Numerical methods

In the numerical simulations, a large number of particles are released in the boundary layer. At the beginning of the simulation, all particles are uniformly distributed in the domain. The physical domain is spanned by the following cylindrical coordinates (x^+, r^+, θ): $x^+ \in [0, L^+]$, $r^+ \in [(R^+ - h^+), R^+]$, and $\theta \in [0, \theta_{max}]$; a sketch of the domain is given in Fig. 8.1. The initial velocity of a particle in streamwise and in tangential direction is equal to the local mean carrier flow velocity, whereas the initial velocity in radial direction is randomly sampled from a normal distribution with variance $\sigma^+(\eta^+_p(0))$.

The positions of the particles in the course of time are determined by integrating the equations of motion of heavy particles, Eq. (8.1), combined with the stochastic differential equation for the turbulent flow field seen by the particle, Eq. (8.3). The time integration is done by a fourth-order Runge-Kutta scheme with numerical time step $\Delta t^+ = 0.05$.

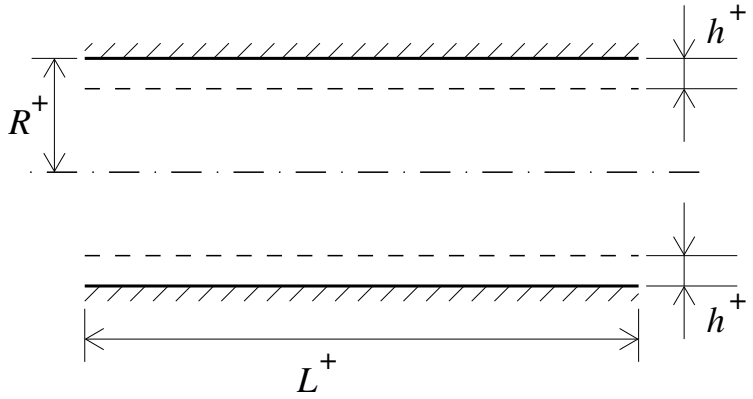

FIGURE 8.1: *Cross-sectional view of the physical domain considered, for the turbulent boundary layer of a swirling flow in a pipe.*

When the wall-normal coordinate of the particle η_p^+ is smaller than the particle radius a_p^+, the particle hits the wall. When this happens, the particle is absorbed by the wall and eliminated from the simulation. Also when a particle leaves the domain at $x^+ = L^+$, it is eliminated. Each eliminated particle is replaced by a new particle injected into the boundary layer at a randomly chosen position on the line $x^+ = 0$. The coordinates of the injection positions are chosen such that, on average, the particles enter the turbulent boundary layer in a uniform concentration.

On the other hand, when a particle leaves the domain on the upper side of the turbulent boundary layer ($\eta^+ > h^+ = 200$), an identical particle is reinjected into the boundary layer on the same position but with an opposite wall-normal velocity.

Periodic boundary conditions are imposed in the θ-direction. Thus, when a particle has a coordinate $\theta_p = \arctan(z_p^+/y_p^+) > \theta_{max}$, an identical particle is injected at $\theta = \theta_p - \theta_{max}$, at the same axial and radial position, with the same axial, radial and tangential velocity. Vice versa, if a particle has a coordinate $\theta_p < 0$, an identical particle is injected at $\theta = \theta_p + \theta_{max}$, again at the same axial and radial position, with the same axial, radial and tangential velocity.

These boundary conditions ensure that a constant number of particles is maintained in the entire domain. By doing so, the numerical solution for the distribution of particles approaches a statistically stationary solution as the time of integration tends to infinity.

8.3.1 Modelling of interparticle collisions

During each time step, inter-particle collisions are detected. The detection algorithm is basically the same as was used in Chapter 7. For the collision detection, 200 boxes are used in the x^+-direction, and 100 boxes in the r^+-direction; the domain is not subdivided into boxes in the θ-direction. When a particle collision is detected, either

a fully elastic collision is calculated using Eq. (7.12) or a fully inelastic collision is determined from Eq. (7.13).

The effects of coalescence and of collisions are studied for a wide range of Stokes numbers. In order to facilitate a meaningful comparison between the results for different Stokes numbers, it is necessary that the mean volumetric concentration of particles in the domain, Φ, remains constant.

If Φ is constant, the number density $\bar{n}$ (i.e. the mean number of particles per unit of volume) scales with the Stokes number as:

$$\bar{n} \sim \mathrm{St}^{-3/2}, \tag{8.10}$$

where it has been used that the Stokes number is quadratic in the particle radius a_p^+ and the total volume occupied by a certain number of particles scales as a_p^{+3}. Therefore, we adapt the value of θ_{max} for each value of the Stokes number as follows:

$$\theta_{max} \sim \mathrm{St}^{3/2}, \tag{8.11}$$

so that the total number of particles in the domain N_p given by:

$$N_p = \bar{n}\left(\frac{\theta_{max}}{2\pi}\right) L^+(\pi R^{+2} - \pi(R^+ - h^+)^2), \tag{8.12}$$

is independent of the Stokes number. This is pracitcal, because too small a value of N_p yields unaccurate results, and too large a value of N_p is computationally expensive.

In the present research, we choose N_p to be approximately $40,000$ for all Stokes numbers tested, except one: for $\mathrm{St} = 1000$ we are restricted to a lower value of N_p because of the maximum size of the physical domain. The length and the height of the domain are chosen to be $h^+ = 200$ and $L^+ = 20,000$, respectively. We use a particle-to-fluid density ratio $\rho_p/\rho = 770$ in order to allow a good comparison to the results presented in Chapter 7. The mean volumetric concentration of particles is $\Phi = 10^{-5}$. Using these parameters, the desired value for θ_{max} can be calculated for a given Stokes number; the results are presented in Table 8.1.

8.4 Results

First, results are presented for the case that particle interactions are neglected. Subsequently, results are given for the case where the particle interactions are modelled as fully elastic collisions, or as fully inelastic collisions.

8.4.1 Heavy particles in turbulent swirling flow in a pipe

In this section, we present the numerical results for the motion of heavy particles in the swirling flow in a pipe. The motion of the particles is modelled by the SDE model

St	N_p	θ_{max} (radials)
0.5	38,677	0.1693×10^{-3}
1	39,839	0.4790×10^{-3}
5	40,107	0.5355×10^{-2}
10	40,005	0.1515×10^{-1}
20	40,306	0.4282×10^{-1}
30	40,151	0.7867×10^{-1}
50	40,021	0.1693
100	39,811	0.4790
1000	4,058	1.5147

TABLE 8.1: *Domain size in tangential direction θ_{max} for nine different values of the Stokes number St. For the sake of completeness, the total number of particles in the domain N_p is presented as well.*

as described by equations Eq. (8.1) and Eq. (8.3). Particle interactions are ignored for the moment.

The concentration of particles with St = 5 after $t^+ = 10,000$ is presented as a function of the coordinates (x^+, η^+) in Fig. 8.2a). The friction Reynolds number in these simulations has been taken as $\mathrm{Re}_\tau = 4000$ and the swirl angle as $\theta_S = \pi/6$. As can be seen, the particle concentration is generally higher in the lower half of the domain. This can be explained by the fact that the heavy particles are expelled from the regions far away from the wall due to the swirl. It is noted that the centrifugal acceleration acting on the heavy particles is approximately equal to $\langle u_\theta^+ \rangle^2 / r^+$, which attains its maximum value in the domain considered at $\eta^+ = h^+$. On the other hand, the particles with St = 5 do not have enough inertia to cross the viscous sublayer directly. As a consequence of these two effects, the particle concentration is slightly elevated in the region $\eta^+ \lesssim 100$, but the particle concentration near the wall is not particularly high. The particle concentration in the near-wall region is comparable to the case that no swirl is present, see Fig. 7.7a).

The concentration of heavy particles with St = 50, again as a function of (x^+, η^+), is shown in Fig. 8.2b). Apparently, the effect of the swirl on the trajectories of these heavy particles is very important. It is clear that the particle concentration quickly decreases in the downstream direction. Because virtually all particles with St = 50 quickly deposit onto the wall, no particles can be found in the region $x^+ \gtrsim 7000$. This result can be fully explained by the high inertia of these particles; the particles are forced towards the wall due to the tangential component of the carrier flow velocity, and deposit onto the wall before they are decelerated by the lower velocities in the carrier flow close to the wall. On the basis of this result, we can draw the conclusion is that the effect of swirl is qualitatively more pronounced in the concentration profiles of particles with large Stokes numbers than with small Stokes numbers.

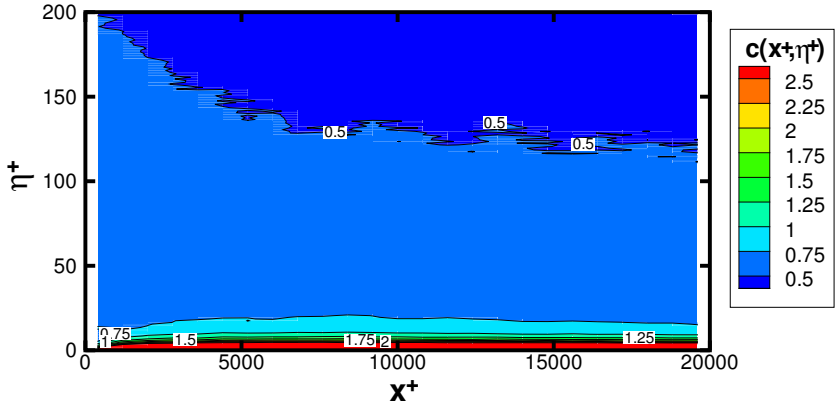

a)

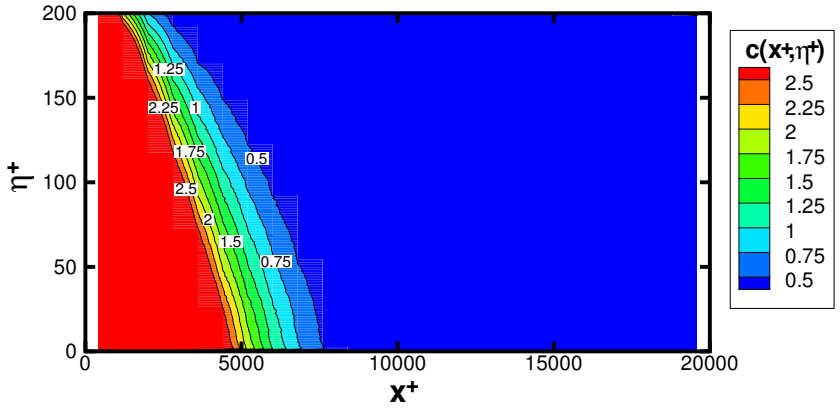

b)

FIGURE 8.2: *Concentration $c(x^+, \eta^+)$ after time $t^+ = 10,000$ in a swirling flow in a pipe, with particle interactions neglected; $Re_\tau = 4000$, $\theta_S = \pi/6$. a) $St = 5$, b) $St = 50$.*

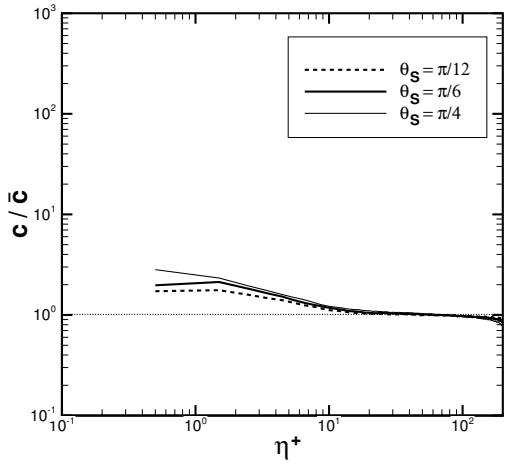

a)

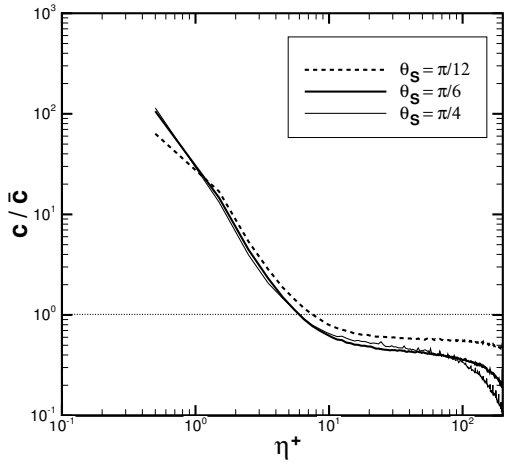

b)

FIGURE 8.3: *Concentration profile $c(x^+, \eta^+)/\bar{c}(x^+)$ of particles as a function of the wall-normal coordinate in a swirling flow in a pipe, for three different values of the swirl angle θ_S; $Re_\tau = 4000$. Particle interactions are not taken into account. a) $St = 1$, b) $St = 10$.*

In order to quantify the effect of swirl, we compare the concentration profiles for $c/\bar{c}$ for three different values of the swirl angle θ_S, in Fig. 8.3. Here, the value of $c/\bar{c}$ has been calculated using Eq. (7.19) in the region $0.8L^+ < x^+ < L^+$. Evidently,

the particle concentration is elevated close to the wall, especially in the case where St = 10. Both for particles with St = 1 and for particles with St = 10, we see that the particle accumulation becomes more important with an increasing value of θ_S. The reason for this is that both the tangential velocity component of the carrier flow and turbulent fluctuations force the particles to go to the wall. When they arrive close to the wall, however, they are stopped by the low velocities of the carrier flow. As a consequence, they relax in the viscous sublayer. Since the centrifugal force on the particles increases with increasing values of θ_S, it is logical that the particle accumulation increases with a higher swirl angle.

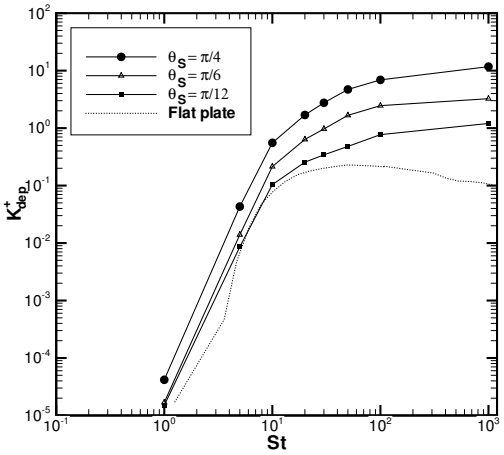

FIGURE 8.4: *Deposition velocity as a function of the Stokes number for particles in a boundary layer in a swirling flow in a pipe, for three different values of θ_S; Re_τ = 4000. Particle interactions are not taken into account.*

We now consider the deposition velocity in the turbulent boundary layer as a function of the Stokes number. The deposition velocity of particle Stokes numbers is plotted in Fig. 8.4, for three values of θ_S, for $\mathrm{Re}_\tau = 4000$. For the sake of convenience, the result for the flow over a flat plate is plotted, too.

First of all, it is clear that the deposition velocity is higher in the swirling flow than in the flow over a flat plate, for all Stokes numbers. The general shape of the deposition velocity curve, however, has not altered very much in a swirling flow compared to the flow over a flat plate: the deposition increases rapidly if St < 30, but then increases only gradually as the Stokes number becomes larger.

It is noted that the value of the deposition velocity increases significantly with increasing values of the swirl angle θ_S, especially for St > 30. This supports the

hypothesis that the swirl has a large effect on the motion of large heavy particles, but does not alter the motion of small heavy particles significantly.

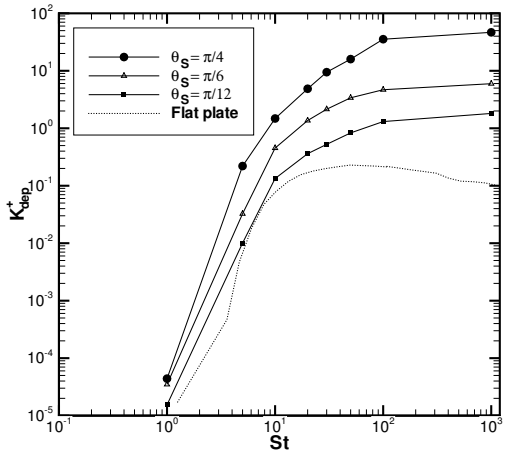

FIGURE 8.5: *Deposition velocity as a function of the Stokes number for particles in a boundary layer in a swirling flow in a pipe, for three different values of θ_S; Re_τ = 2000. Particle interactions are not taken into account.*

In order to study the influence of Re_τ, the deposition velocity for $\mathrm{Re}_\tau = 2000$ is presented in Fig. 8.5, for the same Stokes numbers as in Fig. 8.4. Comparison of Fig. 8.5 with Fig. 8.4 shows that the deposition velocity is considerably larger when Re_τ = 2000. This can be explained from the fact that a lower value of Re_τ corresponds to a smaller radius of the pipe in wall units R^+, i.e. a smaller radius of curvature of the pipe. As a consequence, the heavy particles reach the wall more quickly and the deposition velocity is enhanced.

The PDF of the wall-hitting velocity of the particles is presented in Fig. 8.6 for $\mathrm{Re}_\tau = 4000$, and in Fig. 8.7 for $\mathrm{Re}_\tau = 2000$. It is clear that the particles with large Stokes numbers have, on average, a larger impact velocity than particles with small Stokes numbers. This is in agreement with the results presented above, which indicates that the particles with large Stokes numbers cross the turbulent boundary layer more easily than particles with small Stokes numbers. Besides, we see that the wall-hitting velocity is higher when swirl angle θ_S is larger, and when the friction Reynolds number Re_τ is lower. Thus, there is a positive correlation between the deposition velocity of particles and the mean wall-hitting velocity: if the number of particles reaching the wall increases, so does their (average) radial velocity at the moment they hit the wall.

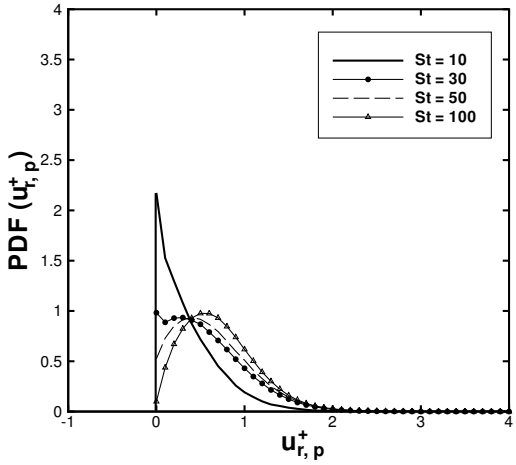

a)

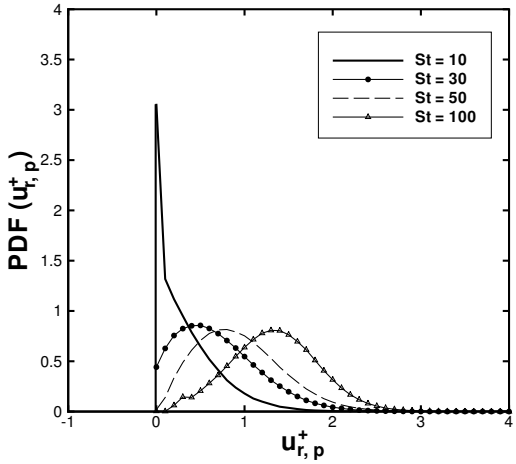

b)

FIGURE 8.6: *Probability density function of the (dimensionless) wall-normal velocity of particles on the moment that they hit the wall, for four different values of the Stokes number;* $Re_\tau = 4000$. *a)* $\theta_S = \pi/12$, *b)* $\theta_S = \pi/6$.

In summary, we have presented results for the concentration and the deposition velocity of heavy particles in a swirling flow in a pipe. We have shown that particles with a Stokes number of $O(10)$ accumulate in the near-wall region, leading to an elevated concentration by two orders of magnitude. Small particles with St $\simeq$ 1 do

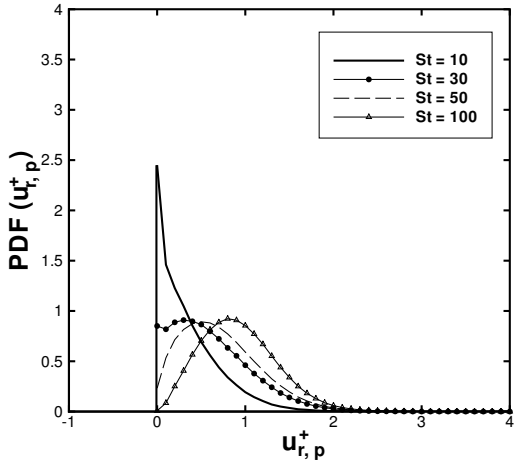

a)

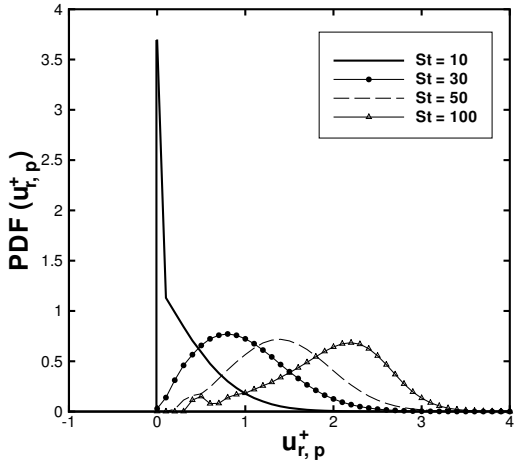

b)

FIGURE 8.7: *Probability density function of the (dimensionless) wall-normal velocity of particles on the moment that they hit the wall, for four different values of the Stokes number;* $Re_\tau = 2000$. *a)* $\theta_S = \pi/12$, *b)* $\theta_S = \pi/6$.

hardly ever reach the wall, whereas large particles with St > 30 move quickly towards the wall. This result is supported by the curve for the deposition velocity: it increases sharply between St = 1 and St = 30, and it increases much more moderately when St > 30. A parameter study shows that the deposition velocity of particles on the wall

is highest for a large value of the swirl angle θ_S, and for a low value of the friction Reynolds number Re_τ.

This result suggests that the particle separation in a swirling pipe flow, such as presented in section 1.2.3, is probably most effective if the flow velocity in tangential direction is relatively high, if the friction Reynolds number is relatively low, and if the particles are relatively large compared to the viscous length scale.

8.4.2 The effect of fully elastic collisions

In order to determine the effect of fully elastic collisions, we study a swirling pipe flow with $\mathrm{Re}_\tau = 4000$ and $\theta_S = \pi/6$ in some detail. The mean volumetric particle concentration in the domain is $\Phi = 10^{-5}$, which corresponds to a relative mass loading of 0.77% in this situation where $\rho_p/\rho = 770$.

The particle concentration as a function of (x^+, η^+) after a time $t^+ = 10,000$ is given in Fig. 8.8a), for a particle Stokes number of $\mathrm{St} = 5$. In comparison with the case in which particle interactions are neglected, see Fig. 8.2a), the colliding particles are distributed more uniformly over the domain. This is in agreement with the results presented in Fig. 7.11: due to collisions, some particles are prevented from entering the viscous sublayer.

Fully elastic collisions have less effect on the distribution of larger particles, as is visible in Fig. 8.8b), where the particle concentration is plotted as a function of (x^+, η^+) after a time $t^+ = 10,000$ for a particle Stokes number of $\mathrm{St} = 50$. These particles go to the wall rapidly due to their inertia, and this behavior is not much altered due to the incorporation of particle collisions. This can be understood by noting that fully elastic collisions redistribute the velocities of individual particles, but do not alter the total kinetic energy of the particles. Thus, the effect of a fully elastic collision is relatively weak if all the particles move in approximately the same direction.

The above results are confirmed by the concentration profiles $c/\bar{c}$, which are plotted in Fig. 8.9 for $\mathrm{St} = 1$, $\mathrm{St} = 5$ and $\mathrm{St} = 10$. Indeed, comparison with Fig. 8.3b) shows that the value of $c/\bar{c}$ near the wall for $\mathrm{St} = 10$ has decreased from approximately 100 to approximately 50. This illustrates that some particles are bounced back into the flow by other particles before entering in the near-wall region.

In Fig. 8.10, the deposition velocity is presented for a range of Stokes numbers, for the case that fully elastic collisions are accounted for. For the sake of comparison, the result for the case that particle interactions are neglected (already presented in Fig. 8.4) is plotted as well. Apparently, the deposition has hardly altered with respect to the no-collisions case.

Finally, the PDF of the wall-hitting velocity is plotted in Fig. 8.11. Comparison with Fig. 8.6b) shows that the particle hitting velocity has not changed much due to the incorporation of collisions. This supports the hypothesis formulated in section

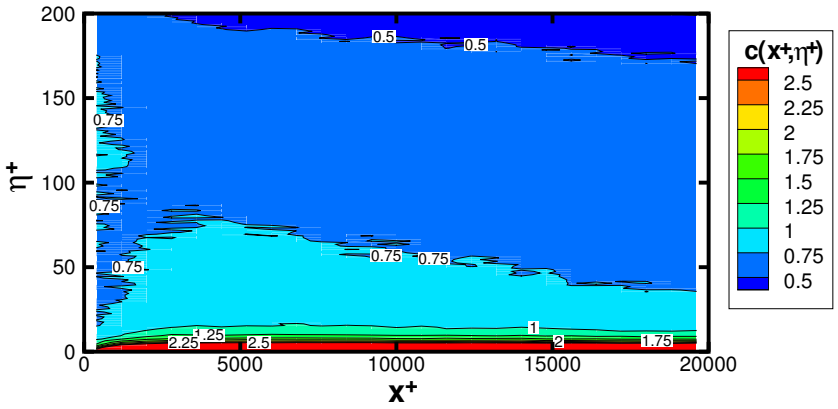

a)

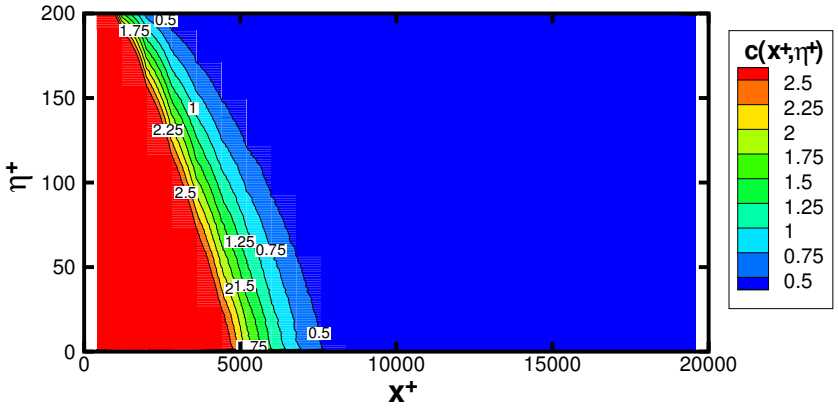

b)

FIGURE 8.8: *Concentration* $c(x^+, \eta^+)$ *after time* $t^+ = 10,000$ *in a swirling flow in a pipe;* $Re_\tau = 4000, \theta_S = \pi/6$. *a)* $St = 5$, *b)* $St = 50$. *Fully elastic collisions are taken into account;* $\Phi = 10^{-5}$.

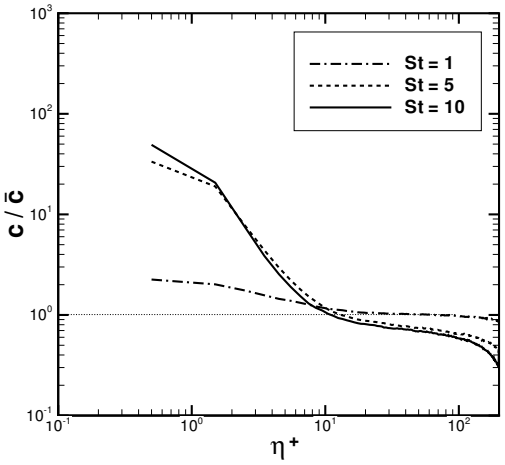

FIGURE 8.9: *Concentration profile $c(x^+, \eta^+)/\bar{c}(x^+)$ of particles as a function of the wall-normal coordinate in a swirling flow in a pipe, for three different values of the Stokes number; $Re_\tau = 4000$, $\theta_S = \pi/6$. Fully elastic collisions are taken into account; $\Phi = 10^{-5}$.*

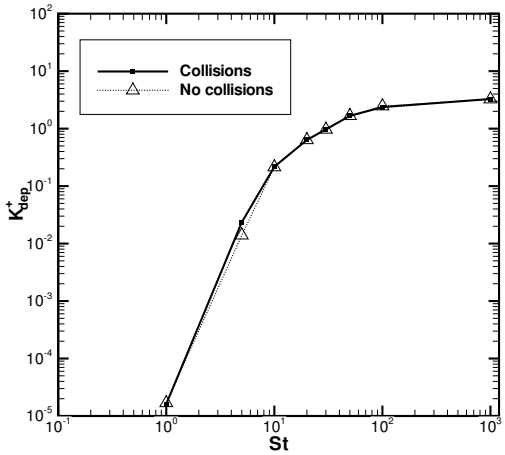

FIGURE 8.10: *Deposition velocity as a function of the Stokes number for particles in a boundary layer in a swirling flow in a pipe; $Re_\tau = 4000$. Fully elastic collisions are taken into account; $\Phi = 10^{-5}$. For the sake of comparison, the result for the case that particle interactions are neglected is shown as well.*

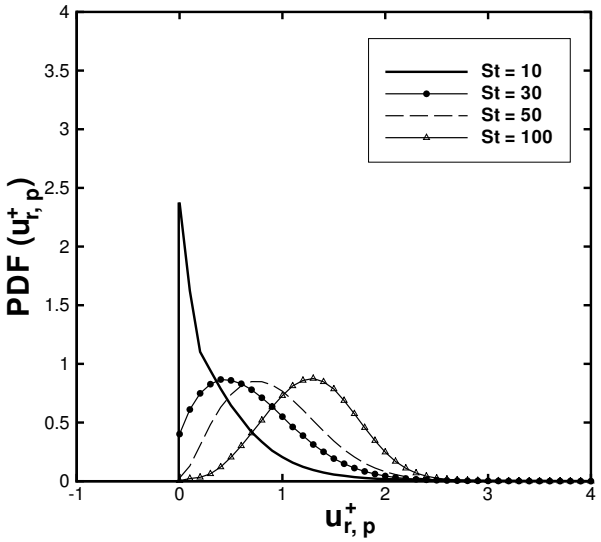

FIGURE 8.11: *Probability density function of the (dimensionless) wall-normal velocity of particles on the moment that they hit the wall, for three different values of the Stokes number;* $Re_\tau = 4000$, $\theta_S = \pi/6$. *Fully elastic collisions are taken into account;* $\Phi = 10^{-5}$.

8.4.1, that the average wall-hitting velocity is in general positively correlated to the deposition velocity.

8.4.3 The effect of coalescence

We now consider the influence of fully inelastic collisions on the concentration and on the deposition of heavy particles in the turbulent boundary layer of a swirling flow in a pipe characterized by $\mathrm{Re}_\tau = 4000$ and $\theta_S = \pi/6$. Just like in the simulations of the fully elastic collisions, we take a mean volumetric particle concentration in the domain $\Phi = 10^{-5}$ and a particle-to-fluid density ratio $\rho_p/\rho = 770$.

Fig. 8.12a) shows the concentration of particles as a function of (x^+, η^+) after a time $t^+ = 10,000$, for particles which have a Stokes number of $\mathrm{St} = 5$ when they are injected. It is noted here that the concentration is defined as the volume occupied by the particles divided by the volume occupied by the carrier flow; hence, in this situation where particles may have different sizes due to coalescence, the normalized concentration does *not* correspond to the normalized particle number density.

The result in Fig. 8.12a) is a bit different from the results in Fig. 8.2a) and Fig. 8.8a) in that it shows a gradually decreasing concentration of particles in the streamwise direction. This can be explained by the fact that the initially small particles may

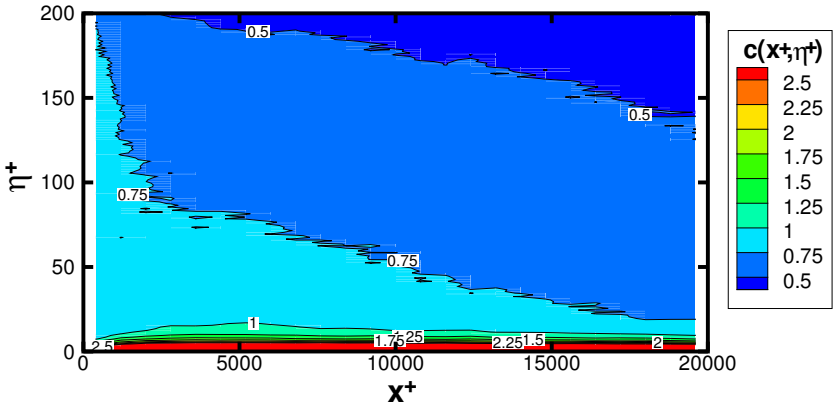

a)

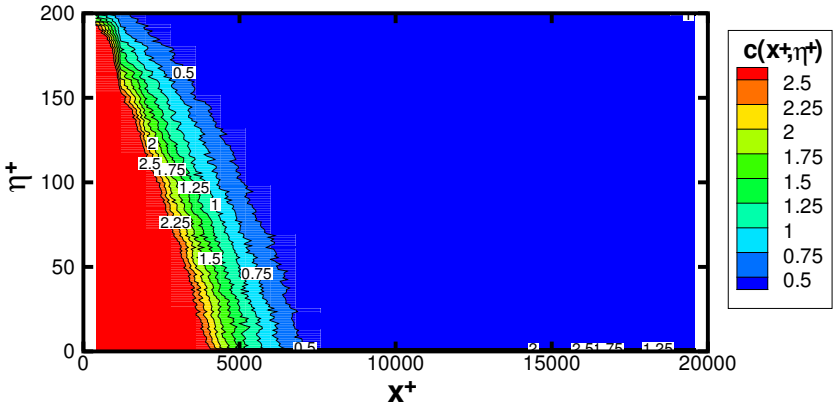

b)

FIGURE 8.12: *Concentration $c(x^+, \eta^+)$ after time $t^+ = 10,000$ in a swirling flow in a pipe; $Re_\tau = 4000$, $\theta_S = \pi/6$. a) $St = 5$, b) $St = 50$. Fully inelastic collisions are taken into account; $\Phi = 10^{-5}$. Note that the Stokes number corresponds to the Stokes number of newly injected particles.*

grow due to collisions. As they grow, they become larger and they have a higher probability of accumulating in the near-wall region. Since the particles require some time to grow due to collisions, the elevated concentration is more pronounced for large values of x^+.

In Fig. 8.12b), the concentration of particles is plotted as a function of (x^+, η^+) after a time $t^+ = 10,000$, for particles which have a Stokes number of St = 50 when they are injected. This result is very similar to previous plots in Fig. 8.2b) and in Fig. 8.8b): these particles quickly deposit onto the wall. It seems that inelastic collisions do not change this phenomenon, i.e. the particles with St = 50 continue their routes towards the wall.

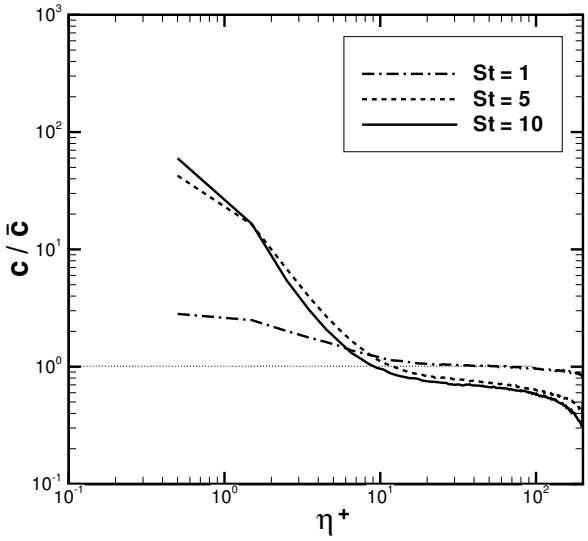

FIGURE 8.13: *Concentration profile $c(x^+, \eta^+)/\bar{c}(x^+)$ of particles as a function of the wall-normal coordinate in a swirling flow in a pipe, for three different values of the Stokes number; $Re_\tau = 4000$, $\theta_S = \pi/6$. Fully inelastic collisions are taken into account (coalescence); $\Phi = 10^{-5}$. Note that the Stokes number corresponds to the Stokes number of newly injected particles.*

In Fig. 8.13, the concentration profile $c/\bar{c}$ is plotted for the case that fully inelastic collisions are implemented. Apparently, small particles with St = 1 accumulate close to the wall due to the collisions. The concentration of larger particles, e.g. with St = 10 is hardly altered. These results are in agreement with Fig. 7.16.

Due to the coalescence of particles, the mean particle diameter may increase in the streamwise direction. As a result, the deposition velocity may vary with the

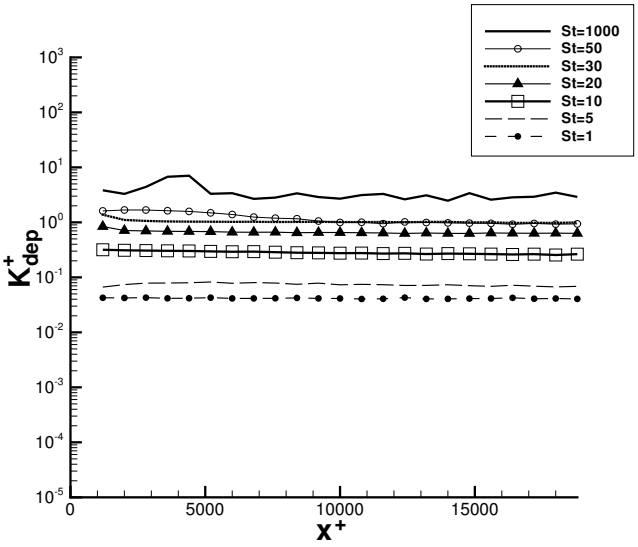

FIGURE 8.14: *Deposition velocity as a function of the axial coordinate x^+ in a turbulent boundary layer of a swirling flow in a pipe, for different values of the Stokes number; $Re_\tau = 4000$, $\theta_S = \pi/6$. Fully inelastic collisions are taken into account; $\Phi = 10^{-5}$. Note that the Stokes number corresponds to the Stokes number of newly injected particles.*

streamwise coordinate x^+. We determine the deposition velocity as a function of x^+ by calcultating the deposition velocity in each of the 25 segments in the streamwise direction. The result is plotted in Fig. 8.14, for seven different Stokes numbers of newly injected particles. Apparently, for large Stokes numbers such as St = 50 and St = 1000 the deposition velocity curve has a maximum at $x^+ \simeq 4000$. Since the particle concentration is relatively high in the region where $x^+ < 4000$, it can be concluded that some of these large particles are forced towards the wall due to interactions with other particles. For most other Stokes numbers, however, the deposition velocity is almost a constant over the length of the boundary layer. This result indicates that there is not much difference between the average size of particles in different segments. Only if we reduced the size of the segments in streamwise direction in which the deposition velocity is calculted, then perhaps some differences in the deposition velocity could be observed in the first few segments for low and moderate Stokes numbers.

On the basis of Fig. 8.14, we determine the deposition velocity for $x^+ \to L^+$, taking into account fully inelastic collisions; the result is given in Fig. 8.15. Comparison to the deposition velocity in the case that particle interactions are neglected shows an important difference: the deposition velocity of particles with St < 10 has increased

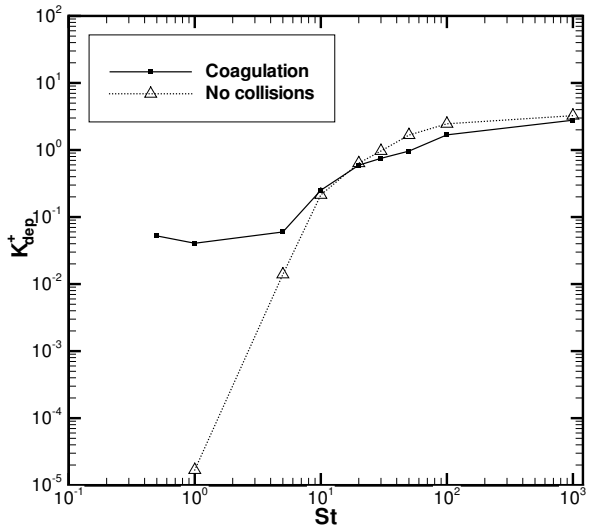

FIGURE 8.15: *Deposition velocity as a function of the Stokes number for particles in a boundary layer in a swirling flow in a pipe;* $Re_\tau = 4000$, $\theta_S = \pi/6$. *Fully inelastic collisions are taken into account;* $\Phi = 10^{-5}$. *Note that the Stokes number corresponds to the Stokes number of newly injected particles.*

by several orders of magnitude. Because the deposition velocity is found to be approximately constant along the length of the pipe, the elevated deposition velocity must be mainly due to collisions in the region far away from the wall. In this region, particles grow on to larger particles which subsequently deposit onto the wall.

Finally, we show the result for the PDF of the wall-hitting velocity in Fig. 8.16. As can be seen, the PDFs are broader than in Fig. 8.6b). Because the impact speed on the wall increases with the size of a particle, the result in Fig. 8.16 indicates that particles with different sizes may reach the wall in the same simulation.

8.5 Conclusions

The motion of heavy particles in a turbulent boundary layer flow of a swirling flow in a pipe has been investigated by a Lagrangian numerical simulation. The carrier flow velocity along the trajectory of the particle is modelled by a stochastic method. The stochastic model is selected to satisfy the well-mixedness condition in the limit of infinitesimally small particles.

The results for non-interacting particles indicate that the particle concentration has a maximum value close to the wall if the particle Stokes number St is $O(10)$. The

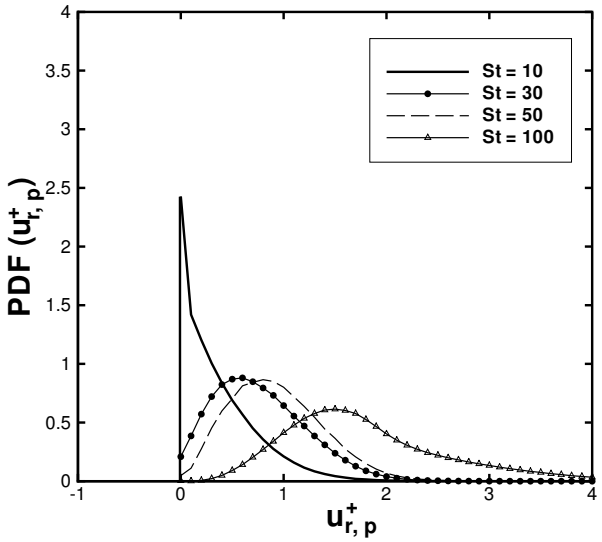

FIGURE 8.16: *Probability density function of the (dimensionless) wall-normal velocity of particles on the moment that they hit the wall, for three different values of the Stokes number;* $Re_\tau = 4000$, $\theta_S = \pi/6$. *Fully inelastic collisions are taken into account;* $\Phi = 10^{-5}$. *Note that the Stokes number corresponds to the Stokes number of newly injected particles.*

deposition velocity, defined as the particle flux towards the wall divided by the mean concentration of particles, is shown to increase rapidly with the particle Stokes number as long as St < 30; if on the other hand St ≥ 30, the particle deposition velocity only increases slowly with the Stokes number. A parameter study shows that the deposition velocity is enhanced by higher values of the swirl angle θ_S and lower values of the friction Reynolds number Re_τ.

The influence of fully elastic and fully inelastic collisions has been investigated, too. Fully elastic collisions do not enhance the particle deposition rate significantly. The particle concentration in the near-wall region decreases when fully elastic collisions are taken into account. Fully inelastic collisions on the other hand result in an increase of the mean particle Stokes number. This enhances the particle deposition by several orders of magnitude if the particles are initially very small, even for a relatively low volumetric particle concentration such as 10^{-5}. These results suggest that droplets (i.e. coalescing particles) with a small Stokes number have a higher probability of depositing on the wall than rigid particles of the same density and of the same size.

CONCLUSIONS AND OUTLOOK

CHAPTER 9

In this chapter, the conclusions of the present research are formulated. These conclusions provide an answer to the research questions posed in section 1.3. In addition, suggestions for further research are presented in section 9.2.

9.1 Summarizing conclusions

Chapter 2 provides a presentation of the equation of motion of heavy particles in a gas flow, in the case of a sufficiently dilute mixture. Stokes drag and gravity are shown to be the dominant forces. At small Stokes numbers, heavy particles ($\rho_p/\rho \gg 1$) have been shown to always concentrate in strain regions, whereas they are expelled from regions of high vorticity. An explicit criterion for particle accumulation is derived in terms of the eigenvalues of the local rate-of-deformation tensor $\partial u_i/\partial x_j$, in two-dimensional flows as well as in three-dimensional flows.

In Chapter 3, we have shown that heavy particles may accumulate in a flow field generated by a single vortex in a closed circular domain, with or without gravity present. The point vortex is allowed to move freely, i.e. it follows a circular trajectory at fixed radius at a constant angular velocity that follows from the configuration. If gravity is not accounted for, the accumulation takes place in regions where the centrifugal and the drag forces acting on the particles balance each other, thus causing an equilibrium trajectory of the particles. A linear stability analysis shows that particles are always attracted to a fixed point in the frame of reference moving with the vortex, as long as the Stokes number is below a critical value. This critical Stokes number is higher as the radial position of the vortex increases. If gravity is accounted for, heavy particles accumulate onto a moving attraction point in the frame of reference moving with the vortex. For small Stokes numbers and large Froude numbers, the moving attraction point describes an elliptically shaped attraction trajectory in the frame of reference rotating with the vortex. The results obtained from the inviscid (potential) flow model are compared to the results from a numerical simulation in which the flow field satisfies the two-dimensional Navier-Stokes equations for vis-

cous flow. Although the viscous flow field is slightly different from the potential flow field, heavy particles may accumulate close to an elliptic stagnation point in the flow as well, just like in the case of potential flow.

In Chapter 4, the motion of heavy particles in a 2-vortex system on a disk has been investigated. The results reveal that heavy particles may accumulate on a moving attraction point within the circular domain. This means that all forces on the particle (the Stokes drag plus fictitious forces due to the formulation of the equations of motion in a rotating frame of reference) are such that a particle is trapped on an equilibrium trajectory as time tends to infinity. In order to quantify the effect of particle accumulation, the percentage of trapped particles has been calculated for a wide range of initial vortex positions. From the results of these simulations, two main conclusions can be drawn: (i) the accumulation of heavy particles is closely related to the presence of elliptic islands of regular passive tracer motion, and (ii) the percentage of accumulated heavy particles is enhanced by more eccentric positions of the vortices and by lower values of the Stokes number.

In Chapter 5, the motion of heavy particles in the three-dimensional flow induced by a helical vortex filament has been considered. The flow field has been expressed in terms of a stream function in helical coordinates. It is shown that heavy particles may accumulate on a helically shaped equilibrium trajectory. The physical reason for the particle accumulation is that the Coriolis force drives inertial particles to the center of an elliptic region of the stream function, where the particles are trapped by a balance between the Stokes drag and the centrifugal force. The level of particle accumulation is closely related to the area of an elliptic region in the stream function. These elliptic regions occur in six out of seven observed flow field topologies in a flow induced by a helical vortex inside a circular pipe. Numerically determined Lyapunov exponents indicate that the accumulation rate is approximately proportional to the particle Stokes number, provided that the Stokes number is sufficiently small.

Recapitulating the results from Chapter 3, Chapter 4 and Chapter 5, we can conclude that if the particle distribution is sufficiently dilute, small heavy particles may be trapped in one single point or on a single line. From the results presented in the present thesis, it may be deduced that particles accumulate in those regions of the flow field that are characterized by the following properties:

- passive tracers remain together for very long times;
- the eigenvalues of the local rate-of-deformation matrix, α_i, satisfy the following inequality: $\sum_i \left(\alpha_i + \mathrm{St}\alpha_i^2\right) > 0$ for all times, indicating that the particle velocity field is compressed continuously.

These properties explain the accumulation of heavy particles in a Burgers vortex [56], the flow in rotating two-dimensional flows such as may be found in protoplanetary systems [15], as well as the flows presented in the present thesis.

After having provided a general introduction to stochastic modelling of diffusion processes employing a stochastic differential equation (SDE) in Chapter 6, in Chapter 7 results are shown for the motion of heavy particles in the turbulent boundary layer over a flat plate. The turbulence is modelled by a modified Langevin equation. The results indicate that if the particle Stokes number St is $O(10)$ the droplet concentration has a maximum value close to the wall. The particle deposition velocity, defined as the particle flux towards the wall divided by the mean concentration of particles, is shown to increase rapidly with the Stokes number for $10 < \mathrm{St} < 30$. For $\mathrm{St} \geq 30$, the particle deposition velocity is almost independent of the Stokes number. A comparison with experimental data from literature shows that the SDE model underestimates the particle deposition for small Stokes numbers $\mathrm{St} < 10$. Nevertheless, the general features of the deposition velocity curve as a function of the Stokes number are well captured: the deposition velocity increases rapidly as $\mathrm{St} < 30$ and then becomes almost independent of the Stokes number for $\mathrm{St} \geq 30$. Numerical results show that fully elastic collisions do not enhance the particle deposition rate significantly, but rather change the mechanism of particle deposition: particles move to the wall due to collisions rather than due to free-flight diffusion. Fully inelastic collisions on the other hand result in an increase of the mean particle Stokes number, which enhances the particle deposition for small Stokes numbers by several orders of magnitude.

The motion of heavy particles in the turbulent boundary layer of a swirling flow in a pipe has been investigated in Chapter 8. It has been demonstrated that the particle concentration close to the wall attains a maximum value if the particle Stokes number St is $O(10)$. The deposition velocity increases rapidly with the particle Stokes number as long as $\mathrm{St} < 30$; if $\mathrm{St} \geq 30$, the particle deposition velocity only increases slowly with the Stokes number. A parameter study shows that the deposition velocity is enhanced by higher values of the swirl angle θ_S and by lower values of the friction Reynolds number Re_τ. The influence of fully elastic and fully inelastic collisions has been investigated, too. Fully elastic collisions do not enhance the particle deposition rate significantly. The particle concentration in the near-wall region decreases when fully elastic collisions are taken into account. Fully inelastic collisions on the other hand result in an increase of the particle deposition for small Stokes numbers by several orders of magnitude, even for a relatively low volumetric particle concentration such as 10^{-5}. These results suggest that droplets (i.e. coalescing particles) with a small Stokes number have a higher probability of depositing on the wall than rigid particles of the same density and of the same size.

9.2 Possible further research

9.2.1 Particles near regions of concentrated vorticity

The accumulation of heavy particles in attraction points is not restricted to the flow fields studied in the present thesis. The flow induced by a steadily rotating vortex soliton [31] is another example in which particle accumulation can probably be observed. The (chaotic) motion of passive tracers around a the vortex soliton, calculated recently by Kimura & Koikari [40], is very reminiscent of the passive tracer plots presented in Chapter 4 for the 2-vortex system in a bounded domain; thus, a group of passive tracers is shown to 'remain together' in a so-called KAM-torus for a long time*. In addition, the flow induced by a vortex solition is potential, since all the vorticity is contained in the singular vortex soliton, and thus $\sum_i \left(\alpha_i + \mathrm{St}\alpha_i^2\right) > 0$. Thus, heavy particle accumulation may be observed in the flow generated by a vortex soliton, and, possibly, near vortex filaments of even more complex shape.

The fact that particles may accumulate in specific points near vortex filaments may have an important impact on the distribution of particles in turbulent flows. Recently, Biferale *et al.* [11] have shown that helically shaped vortex filaments can be found on the smallest scales of a turbulent flow. On the basis of the results obtained in Chapter 5 of the present thesis, in turbulent flows heavy particles are expected to distribute non-uniformly in the vicinity of these vortex filaments. More research is required in order to investigate this further.

9.2.2 Stochastic modelling of particle-laden flows

In part II of the present thesis, particle motion in the turbulent flow field in boundary layers has been investigated. The flow field was modelled by a stochastic differential equation. In this method, the flow field is modelled along the trajectory of one single particle at a time. As a result, at a certain instant in time two particles may be on almost the same position, but with totally different velocities. This is in contrast with the analysis presented in Chapter 2, which shows that the velocity of small heavy particles is closely related to the local properties of the flow field. For the stochastic modelling of mutually interacting heavy particles, these velocity correlations should be taken into account. Thus, it is recommended to develop a stochastic model of turbulent boundary layer flows that accounts for a correlation in the velocities of two particles which are in each other's proximity. Possibly, the separation vector introduced in Chapter 2 can be used for this modelling.

In order to validate existing stochastic models describing the dispersion, deposition and mutual interactions of heavy particles, it would be interesting to study the

*KAM tori, which are named after Kolmogorov, Arnol'd and Moser, denote a group of stable solutions of a non-linear dynamical system; see e.g. the textbook by Ott [72].

deposition and the coalescence processes in a Direct Numerical Simulation of a turbulent channel flow. On the basis of the results reported in Chapter 7 and Chapter 8, it is expected that the deposition velocity of small droplets in a gas flow is vastly enhanced by coalescence.

In the present thesis, in the particle equations of motion only Stokes drag and gravity have been taken into account. Although this approach has the advantage of giving results which are relatively easy to interpret, it is not always an accurate description of the real physical situation. In particular, when the Stokes number becomes of order 1000 in the turbulent boundary layer of a high-speed flow, the assumption that the particle Reynolds number is $O(1)$ or smaller, is not valid anymore; therefore, a correction term to the Stokes drag coefficient should be included. In addition, the Saffman lift force [86] is then expected to affect the motion of particles in flows close to the wall, where the velocity gradients of the carrier flow are very high. The study of particle deposition in a turbulent boundary layer by Kallio & Reeks [38] has shown that the deposition velocity may be altered considerably in case the Saffman lift force is included.

Finally, in the gas-liquid separators produced by Twister B.V., the flow field is not only characterized by slipping droplets; condensation of vapor onto droplets is a major effect, as well as the possible evaporation of droplets in regions of relatively high temperature. The combined effect of condensation/evaporation and turbulence on the size distribution of droplets and on their dispersion could be studied by incorporating a stochastic model for the turbulent fluctuations into a recently developed method which determines the droplet size distribution in a condensing flow [29]. The effect of temperature variations in the turbulent boundary layer could be invesitgated by incorporating a model for the evaporation and growth of droplets in the stochastic method used in Chapter 7 and Chapter 8. As a starting point, a temperature field in the turbulent boundary layer could be prescribed a priori, just like has been done for the velocity field. Models for the evaporation and growth of droplets could be taken from literature, e.g. [52].

REFERENCES

[1] M. Abramovitz and I.A. Stegun, "Handbook of mathematical functions", Dover Publications, New York, 1964.

[2] S.V. Alekseenko, P.A. Kuibin, V.L. Okulov and S.I. Shtork, "Helical vortices in swirl flow", Journal of Fluid Mechanics, **382**, 195, 1999.

[3] H. Aref and M. Brons, "On stagnation points and streamline topology in vortex flows", Journal of Fluid Mechanics, **370**, 1, 1998.

[4] A. Babiano, G. Boffetta, A. Provenzale and A. Vulpiani, "Chaotic advection in point vortex models and two-dimensional turbulence", Physics of Fluids **6**(7), 2465, 1994.

[5] E. Balkovsky, G. Falkovich and A. Fouxon, "Intermittent distribution of inertial particles in turbulent flows", Physical Review Letters, **86**(13), pp. 2790-2793, 2001.

[6] P. Barge and J. Sommeria, "Did planet formation begin inside persistent gaseous vortices?" Astron. Astrophys., **295**, L1, 1995.

[7] G.K. Batchelor, "An introduction to fluid dynamics", Cambridge University Press, 1967.

[8] J. Bec, "Fractal clustering of inertial particles in random flows", Physics of Fluids **15**(11), L81, 2003.

[9] J. Bec, L. Biferale, M. Cencini, A. Lanotte, S. Musacchio and F. Toschi, "Heavy particle concentration in turbulence at dissipative and inertial scales", Physical Review Letters **98**, 084502, 2007.

[10] R. Betchov, "On the curvature and torsion of an isolated vortex filament", Journal of Fluid Mechanics, **22**, pp. 471-479, 1965.

[11] L. Biferale, G. Boffetta, A. Celani, A. Lanotte, F. Toschi, "Particle trapping in three-dimensional fully developed turbulence", Phys. of Fluids, **17**, 021701, 2005.

[12] T.L. Bocksell and E.A. Loth, "Random Walk models for particle diffusion in free shear flows", AIAA Journal, **39**(6), June 2001.

[13] J. Boersma and D.G. Wood, "On the self-induced motion of a helical vortex", Journal of Fluid Mechanics, **384**, pp. 263-280, 1999.

[14] G. Boffetta, A. Celani and P. Franzese, "Trapping of passive tracers in a point vortex system", J. Phys. A: Math. Gen., **29**, 3749, 1996.

[15] A. Bracco, P.H. Chavanis, A. Provenzale and E.A. Spiegel, "Particle aggregation in a turbulent Keplerian flow", Physics of Fluids **11**(8), 2280, 1999.

[16] P.H. Chavanis, "Trapping of dust by coherent vortices in the solar nebula", Astron. Astrophys., **356**, 1089, 2000.

[17] M.S. Chong, A.E. Perry and B.J. Cantwell, "A general classification of three-dimensional flow fields", Physics of Fluids **2**(5), pp. 756-777, 1990.

[18] K. Domelevo and P. Villedieu, "A hierarchy of models for turbulent disperserd two-phase flows derived from a kinetic equation for the joint fluid-particle pdf", Proc. ICMF, Yokohama, Japan, June 2004.

[19] H. van Dop, F.T.M. Nieuwstadt and J.C.R. Hunt, "Random walk models for particle displacements in inhomogeneous unsteady turbulent flows", Physics of Fluids **28**(6), pp. 1639-1653, 1985.

[20] M. Douwes, "Accumulation of heavy particles in viscous vortex flows", MSc Thesis, University of Twente, 2006.

[21] O.A. Druzhinin, "Dynamics of concentration and vorticity modification in a cellular flow laden with solid heavy particles", Physics of Fluids **7**(9), 2132, 1995.

[22] P.A. Durbin, "Stochastic differential equations and turbulent dispersion", NASA Reference Publication 1103, 1983.

[23] J.K. Eaton and J.R. Fessler, "Preferential concentration of particles by turbulence", Int. Journal of Multiphase Flow **20**, pp. 169-209, 1994.

[24] G. Falkovich, A.Fouxon and M.G. Stepanov, "Acceleration of rain initiation by cloud turbulence", Nature **419**, pp.151-154, 2002.

[25] J.R. Fessler, J.D. Kulick, J.K. Eaton, "Preferential concentration of heavy particles in a turbulent channel flow", Physics of Fluids **6**(11), pp. 3742-3749, 1994.

[26] A.M. Gañán-Calvo and J.C. Lasheras, "The dynamics and mixing of small spherical particles in a plane, free shear layer", Phys. of Fluids **3**(5), 1207, 1991.

[27] C.W. Gardiner, "Handbook of stochastic methods", Springer Verlag, 3rd. edition, 2004.

[28] A.K. Gupta, D.G. Lilley and N. Syred, "Swirl flows", Abacus Press, 1984.

[29] R. Hagmeijer, R.H.A. IJzermans and F. Put, "Solution of the General Dynamic Equation along approximate fluid trajectories generated by the Method of Moments", Physics of Fluids, **17**, 056101, 2005.

[30] J.C. Hardin, "The velocity field induced by a helical vortex filament", Physics of Fluids **25**(11), 1949, 1982.

[31] H. Hasimoto, "A soliton on a vortex filament", Journal of Fluid Mechanics, **51**, pp. 477-485, 1972.

[32] D.C. Haworth and S.B. Pope, "A generalized Langevin model for turbulent flows", Physics of Fluids **29**(2), pp. 387-405, 1986.

[33] R.H.A. IJzermans and R. Hagmeijer, "Accumulation of heavy particles in bounded vortex flows", Proc. of the IUTAM Symposium on 'Computational approaches to multiphase flow', Eds. S. Balachandar and A. Prosperetti, Dordrecht, pp. 75-85, 2006.

[34] R.H.A. IJzermans and R. Hagmeijer, "Accumulation of heavy particles in N-vortex flow on a disk", Phys. of Fluids **18**, 063601, 2006.

[35] R.H.A. IJzermans, R. Hagmeijer and P.J. van Langen, "Accumulation of heavy particles near a helical vortex filament", Phys. of Fluids, accepted for publication, 2007.

[36] I. Iliopoulos and T.J. Hanratty, "A stochastic model for solid particle dispersion in a nonhomogeneous turbulent field", Int. Journal of Multiphase Flow **29**, pp. 375-394, 2003.

[37] I. Iliopoulos and T.J. Hanratty, "Turbulent dispersion in a non-homogeneous field", Journal of Fluid Mechanics, **392**, pp. 45-71, 1999.

[38] G.A. Kallio and M.W. Reeks, "A numerical simulation of particle deposition in turbulent boundary layers", Int. Journal of Multiphase Flow **15**(3), pp.433-446, 1989.

[39] N. G. Van Kampen, "Stochastic processes in physics abd chemistry", Elsevier, 1992.

[40] Y. Kimura and S. Koikari, "Particle transport by a vortex soliton", Journal of Fluid Mechanics **510**, pp. 201-218, 2004.

[41] O. Kitoh, "Experimental study of turbulent swirling flow in a straight pipe", Journal of Fluid Mechanics **225**, pp. 445-479, 1991.

[42] L. Kuznetsov and G.M. Zaslavsky, "Regular and chaotic advection in the flow field of a three-vortex system", Physical Review E, vol. **58**(6), 7330, 1998.

[43] H. Lamb, "The magnetic field of a helix", Proceedings of the Cambridge Philosophical Society, **21**, pp. 477-481, 1923.

[44] H. Lamb, "Hydrodynamics", Cambridge University Press, 1932.

[45] L.D. Landau and E.M. Lifshitz, "Fluid Mechanics", Course of Theoretical Physics **6**, Second Edition, Butterworth-Heinemann, Oxford, 1987.

[46] M. J. Landman, "On the generation of helical waves in a circular pipe flow", Phys. of Fluids **2**(5), pp. 738-747, 1990.

[47] P.J. van Langen, "Dynamics of heavy particles near a helical vortex filament", MSc Thesis, University of Twente, 2006.

[48] D.C. Lay, "Linear Algebra and its applications", Addison-Wesley, Boston, 2003.

[49] H. Levy and A.G. Forsdyke, "The steady motion and stability of a helical vortex", Proc. R. Soc. London A, **120**, pp. 670-690, 1928.

[50] J. Lissauer, "Planet formation", Ann. Rev. of Astron. Astrophysics **31**, pp. 129-158, 1993.

[51] B.Y.H. Liu and J.K. Agarwal, "Experimental observations of aerosol deposition in turbulent flow", Journal of Aerosol Science **5**, pp. 145-155, 1974.

[52] X. Luo, "Unsteady flows with phase transition", PhD Thesis, Eindhoven University of Technology, 2004.

[53] J.M. MacInnes and F.V. Bracco, "Stochastic particle dispersion modeling and the tracer-particle limit", Physics of Fluids A **4**(12), pp. 2809-2824, 1992.

[54] C. Marchioli and A. Soldati, "Mechanisms for particle transfer and segregation in a turbulent boundary layer", Journal of Fluid Mechanics, **468**, pp. 283-315, 2002.

[55] C. Marchioli, M. Picciotto and A. Soldati, "Particle dispersion and wall-dependent turbulent flow scales: implications for local equilibrium models", Journal of Turbulence, **7**, no. 60, 2006.

[56] B. Marcu, E. Meiburg and P.K. Newton, "Dynamics of heavy particles in a Burgers vortex", Physics of Fluids **7**(2), pp. 400-410, 1995.

[57] J.E. Martin and E. Meiburg, "The accumulation and dispersion of heavy particles in forced two-dimensional mixing layers. I. The fundamental and subharmonic cases", Physics of Fluids **6**(3), pp. 1116-1132, 1994.

[58] M.R. Maxey and J.J. Riley, "Equation of motion for a small rigid sphere in a nonuniform flow", Physics of Fluids **26**(4), pp. 883-889, 1983.

[59] M.R. Maxey, "The gravitational settling of aerosol particles in homogeneous turbulence and random flow fields", Journal of Fluid Mechanics, **174**, pp. 441-465, 1987.

[60] M.R. Maxey, "On the advection of spherical and non-spherical particles in a non-uniform flow", Phil. Trans. R. Soc. London A **333**, 289, 1990.

[61] D.D. McCoy and T.J. Hanratty, "Deposition of droplets in annular two-phase flow", Int. J. Multiphase Flow **3**, pp. 319-331, 1977.

[62] I. Mezić, S. Wiggins and A. Leonard, "Regular and chaotic particle motion near a helical vortex filament", Physica D **111**, pp. 179-201, 1998.

[63] J.-P. Minier, E. Peirano, "The pdf approach to polydispersed two-phase flows", Physics Reports **352**, Elsevier, 2001.

[64] Y. Mito and T.J. Hanratty, "Use of a stochastic method to describe dispersion and deposition in an idealized annular flow", Proc. of the IUTAM Symposium on 'Computational approaches to multiphase flow', Eds. S. Balachandar and A. Prosperetti, Dordrecht, pp. 31-38, 2006.

[65] A.F. Moene, "Swirling pipe flow with axial strain, experiment and Large Eddy Simulation", PhD Thesis, Eindhoven University of Technology, 2003.

[66] D.W. Moore and P.G. Saffman, "The motion of a vortex filament with axial flow", Philos. Trans. Roy. Soc. London, A 272, pp. 403-422, 1972.

[67] C. Narayanan, D. Lakehal, L. Botto and A. Soldati, "Mechanisms of particle deposition in a fully developed turbulent open channel flow", Physics of Fluids **15**, no. 3, 2003.

[68] P.K. Newton, "The N-vortex problem - Analytical techniques", Springer Verlag, 2001.

[69] V.L. Okulov, "The velocity field induced by helical vortex filaments with cylindrical or conic supporting surface", Russian Journal of Engineering Thermophysics, **5**, pp. 63-75, 1995.

[70] F.W.J. Olver, "Asymptotics and special functions", Academic Press, New York, 1974.

[71] C.T. Oninions (Ed.), "The Oxford Dictionary of English Etymology", Oxford, 1986.

[72] E. Ott, "Chaos in Dynamical Systems", Cambridge University Press, 2002.

[73] J.M. Ottino, "The kinematics of mixing: stretching, chaos and transport", Cambridge University Press, 1989.

[74] R.R. Parchen, "Decay of swirl in turbulent flows", PhD Thesis, Eindhoven University of Technology, 1993.

[75] I. de Pater and J. Lissauer, "Planetary science", Cambridge University Press, 2001.

[76] M. Picciotto, C. Marchioli, M.W. Reeks and A. Soldati, "Statistics of velocity and preferential accumulation of micro-particles in boundary layer turbulence", Nuclear Engineering and Design **235**, pp. 1239-1249, 2005.

[77] S.B. Pope, "Turbulent flows", Cambridge University Press, 2000.

[78] W.C. Press, B.P. Flannery, S.A. Teukolsky and W.T. Vetterling, "Numerical recipes in Fortran 77", Cambridge University Press, 1992.

[79] A. Provenzale, "Transport by coherent barotropic vortices", Ann. Rev. Fluid Mech. **31**, 55, 1999.

[80] H.R. Pruppacher and J.D. Klett, "Microphysics of clouds and precipitation", Kluwer, Dordrecht, 1997.

[81] W.C. Reade and L.R. Collins, "Effect of preferential concentration on turbulent collision rates", Physics of Fluids, **12**(10). pp. 2530-2540, 2000.

[82] M.W. Reeks, "On model equations for particle dispersion in inhmogeneous turbulence", Int. J. of Multiphase Flow, **31**, pp. 93-114, 2004.

[83] M.W. Reeks, "On probability denisty function equations for particle dispersion in a uniform shear flow", J. Fluid Mechanics, **522**, pp. 263-302, 2005.

[84] R. Ricca, "The effect of torsion on the motion of a helical vortex filament", Journal of Fluid Mechanics, **273**, pp. 241-259, 1990.

[85] L. da Rios, "Sul moto d'un liquido indefinito con un filetto vorticoso di forma qualunque", Rendiconti del Circolo Matematico di Palermo **22**, pp. 117-135, 1906.

[86] P.G. Saffman, "The lift force on a small sphere in a slow shear flow", J. Fluid Mechanics, **22**, pp. 385-400, 1965.

[87] P.G. Saffman and J.S. Turner, "On the collision of drops in turbulent clouds", J. Fluid Mechanics, **1**, pp. 16-30, 1956.

[88] L.G. Sarasúa, A.C. Sicardi Schifino and R. González, "The development of helical vortex filaments in a tube", Physics of Fluids **17**, 044104, 2005.

[89] R. Shaw, "Particle-turbulence interactions in atmospheric clouds", Ann. Rev. Fluid Mechanics, **35**, pp. 183-227, 2003.

[90] O. Simonin, E. Deutsch and J.-P. Minier, "Eulerian prediction of the fluid/particle correlated motion in turbulent two-phase flows", Appl. Sci. Res., **51**, pp. 275-283, 1993.

[91] K.D. Squires and J.D. Eaton, "Preferential concentration of particles by turbulence", Phys. of Fliuds **3**(5), pp. 1169-1178, 1990.

[92] W. Steenbergen, "Turbulent pipe flow with swirl", PhD Thesis, Eindhoven University of Technology, 1995.

[93] S. Sundaram, L.R. Collins, "Collision statistics in an isotropic particle-laden turbulent suspension. I. Direct numerical simulations", J. Fluid Mechanics, **335**, pp. 75-109, 1997.

[94] G.I. Taylor, "Diffusion by continuous movements", Proc. Roy. Soc. **20**, pp. 196-212, 1921.

[95] P.J. Thomas, "On the influence of the Basset history force on the motion of a particle through a fluid", Physics of Fluids **4**(9), pp. 2090-2093, 1992.

[96] D.J. Thomson, "Criteria for the selection of stochastic models of particle trajectories in turbulent flows", Journal of Fluid Mechanics, **180**, pp. 529-556, 1987.

[97] A.J.J. Verhoeff, "Aerodynamics of wind turbine rotors", PhD Thesis, University of Twente, The Netherlands, 2005.

[98] L.-P. Wang and M.R. Maxey, "Settling velocity and concentration distribution of heavy particles in homogeneous, isotropic turbulence", Journal of Fluid Mechanics **277**, pp. 347-379, 1993.

[99] Q. Wang, K.D. Squires, M. Chen and J.B. McLaughlin, "On the role of the lift force in turbulence simulations of particle deposition", Int. Journal of Multiphase Flow **23**(4), pp. 749-763, 1997.

[100] G.N. Watson, "A treatise on the theory of Bessel functions", Cambridge University Press, 1966.

[101] J.D. Wilson, B.J. Legg and D.J. Thomson, "Calculation of particle trajectories in the presence of a gradient in turbulent velocity variance", Boundary Layer Meteorology **27**, pp. 163-169, 1983.

[102] J.D. Wilson and B. L. Sawford, "Review of Lagrangian stochastic models for trajectories in the turbulent atmosphere", Boundary Layer Meteorology **78**, pp. 191-210, 1996.

[103] J.B. Young and A. Leeming, "A theory of particle deposition in turbulent pipe flow", Journal of Fluid Mechanics **340**, pp. 129-159, 1997.

SUMMARY

This thesis is devoted to the dynamics of dispersed small heavy particles ($\rho_p/\rho \gg 1$) in swirling flows. Stokes drag and gravity are the dominant forces in the equation of motion of heavy particles in a gas flow, in the case of a sufficiently dilute mixture. At sufficiently small Stokes numbers, i.e. the dimensionless particle relaxation time, heavy particles are concentrated in strain regions, whereas they are expelled from regions of high vorticity. An explicit criterion for particle accumulation has been derived in terms of the eigenvalues of the local rate-of-deformation tensor $\partial u_i/\partial x_j$, in two-dimensional flows as well as in three-dimensional flows.

The motion of heavy particles in a flow field generated by a single vortex in a closed circular domain has been considered. This point vortex is allowed to move freely, i.e. it follows a circular trajectory at fixed radius at constant angular velocity. If gravity is neglected, heavy particles accumulate in one point inside the closed circular domain in the frame of reference moving with the vortex, provided the Stokes number is below a critical value. This critical Stokes number is higher as the radial position of the vortex increases, i.e. the vortex is located closer to the wall. If gravity is accounted for, heavy particles accumulate in a moving attraction point in the frame of reference moving with the vortex. For small Stokes numbers and large Froude numbers, the moving attraction point describes an elliptically shaped attraction trajectory in the frame of reference rotating with the vortex. The results obtained from the inviscid (potential) flow model are in qualitative and quantitative agreement with the results from a simulation in which the flow field satisfies the Navier-Stokes equations for two-dimensional viscous flow.

Also in a 2-vortex system in a closed circular domain, heavy particles accumulate on a moving attraction point within the circular domain in this configuration. This accumulation of heavy particles is closely related to the presence of elliptic islands of regular passive tracer motion. The percentage of accumulated heavy particles, which is related to the size of the elliptic islands, is enhanced by more eccentric positions of the vortices and by lower values of the Stokes number.

The dynamics of heavy particles in the three-dimensional flow induced by a helical vortex filament have been studied, too. The flow field has been expressed in terms of

a stream function in helical coordinates. It has been shown that heavy particles may accumulate on a helically shaped equilibrium trajectory. The particle accumulation is closely related to the area of an elliptic region in the stream function. These elliptic regions occur in six out of seven found flow field topologies in the flow induced by a helical vortex inside a circular pipe. Numerically determined Lyapunov exponents indicate that the accumulation rate is approximately proportional to the Stokes number, provided that the Stokes number is sufficiently small.

Subsequently, the motion of heavy particles in the turbulent boundary layer over a flat plate has been investigated. The turbulent velocity fluctuations along the trajectory of heavy particles are modelled by a modified Langevin equation, which is chosen such that the well-mixedness condition is satisfied in the limit of infinitesimally small heavy particles. The results indicate that the concentration of particles close to the wall has a maximum value if the Stokes number St is $O(10)$. The particle deposition velocity, defined as the particle flux towards the wall divided by the mean concentration of particles, is shown to increase rapidly with the Stokes number for $10 \lesssim \mathrm{St} \lesssim 30$. For $\mathrm{St} \gtrsim 30$, the particle deposition velocity is only weakly dependent on the Stokes number. In general, these results are in agreement with experimental data found in the literature, although the deposition velocity of particles is somewhat underestimated for small Stokes numbers, i.e. $\mathrm{St} \lesssim 10$. It has been shown that fully elastic collisions do not enhance the particle deposition rate significantly, but rather change the mechanism of particle deposition: particles move to the wall due to collisions rather than due to free-flight diffusion. Fully inelastic collisions on the other hand result in an increase of the deposition velocity of particles, at least for initially small Stokes numbers, by several orders of magnitude.

Finally, the dynamics of heavy particles in the turbulent boundary layer of a swirling flow in a pipe have been studied. In this flow, the particle concentration close to the wall is increased if the Stokes number St is $O(10)$; the maximum value of the concentration is higher than in the case of the flow over a flat plate. The deposition velocity increases rapidly with the Stokes number if $\mathrm{St} \lesssim 30$; if $\mathrm{St} \gtrsim 30$, the particle deposition velocity increases only slowly with the Stokes number. A parameter study shows that the deposition velocity is enhanced by higher values of the swirl angle θ_S and the friction Reynolds number Re_τ. The influence of fully elastic and fully inelastic collisions has been investigated, too. Fully elastic collisions do not enhance the particle deposition rate significantly. The particle concentration in the near-wall region decreases when fully elastic collisions are taken into account. Fully inelastic collisions on the other hand enhance the deposition velocity of particles for small Stokes numbers by several orders of magnitude, even if the volumetric particle concentration is as low as 10^{-5}. These results suggest that coalescing droplets with initially a small Stokes number have a higher probability of depositing on the wall than rigid particles of the same density and of the same size.

SAMENVATTING

Dit proefschrift is gewijd aan de beweging van gedispergeerde zware deeltjes ($\rho_p/\rho \gg 1$) in roterende stromingen. De Stokes weerstandskracht en de zwaartekracht zijn de dominante krachten in de bewegingsvergelijkingen voor zware deeltjes in een gasstroming, mits de deeltjesconcentratie voldoende laag is. Bij voldoende kleine Stokes getallen, dat wil zeggen de dimensieloze relaxatietijd van een deeltje, worden zware deeltjes weggeslingerd uit stromingsgebieden met hoge vorticiteit, en concentreren zij zich in stromingsgebieden waar de schuifspanningen hoog zijn. Een expliciet criterium is afgeleid voor de concentratie van zware deeltjes in termen van de locale deformatiesnelheidstensor $\partial u_i/\partial x_j$, zowel in twee-dimensionale als drie-dimensionale stromingen.

De beweging van zware deeltjes in een stromingsveld gegenereerd door één wervel in een gesloten cirkelvorming domein is bestudeerd. De puntwervel is vrij, en volgt derhalve een cirkelvormige baan met een constante straal en met constante hoeksnelheid. Als de invloed van de zwaartekracht wordt verwaarloosd, dan verzamelen zware deeltjes zich in één punt binnen het cirkelvormige domein in het assenstelsel dat meeroteert met de wervel, indien het Stokesgetal beneden een zekere kritische waarde ligt. Dit kritische Stokesgetal is hoger naarmate de radiale positie van de wervel groter is, dus wanneer de wervel dichter bij de wand ligt. Als de zwaartekracht niet wordt verwaarloosd, dan klonteren zware deeltjes samen in een bewegend attractiepunt in het assenstelsel dat meeroteert met de wervel. Voor kleine Stokesgetallen en grote Froudegetallen beschrijft het bewegende attractiepunt een elliptische baan in het assenstelsel dat meeroteert met de wervel. De resultaten van het niet-visceuze (potentiaal) stromingsmodel zijn in kwalitatieve en kwantitatieve overeenstemming met de resultaten van een simulatie waarin het stromingsveld voldoet aan de Navier-Stokesvergelijkingen voor een twee-dimensionale visceuze stroming.

Ook in een 2-wervelsysteem in een gesloten cirkelvorming domein hopen zware deeltjes zich op in een bewegend attractiepunt binnen het cirkelvormige domain. Deze opeenhoping van zware deeltjes is sterk gerelateerd aan de aanwezigheid en de grootte van elliptische eilanden waar gasdeeltjes een regelmatige beweging laten zien. Het percentage van de deeltjes dat samenkomt wordt hoger naarmate de posities

van wervels excentrischer worder, en naarmate het Stokesgetal lager wordt.

De dynamica van zware deeltjes in een drie-dimensionale stroming geïnduceerd door een helische (spiraalvormige) werveldraad is eveneens bestudeerd. Het stromingsveld voor dit geval is uitgedrukt in termen van een stroomfunctie in helische coördinaten. Het blijkt dat er een spiraalvormige evenwichtsbaan is waarop zware deeltjes zich kunnen concentreren. De opeenhoping van deeltjes hangt sterk samen met het oppervlak van een elliptisch gebied in de stroomfunctie. Deze elliptische gebieden zijn zichtbaar in zes van de zeven gevonden verschillende topologieën van het stromingsveld dat geïnduceerd wordt door een helische werveldraad binnen een cylindervormige pijp. Numeriek bepaalde Lyapunov-exponenten laten zien dat de snelheid bij benadering waarmee deeltjes zich concentreren evenredig is aan het Stokesgetal, mits het Stokesgetal voldoende klein is.

Vervolgens is de beweging van zware deeltjes in de turbulente grenslaag over een vlakke plaat onderzocht. De turbulente snelheidsfluctuaties langs de baan van zware deeltjes zijn gemodelleerd door middel van een gemodificeerde Langevin-vergelijking, die zodanig is gekozen dat er voldaan wordt aan de zogenaamde 'goede-mengingsvoorwaarde' in de limiet van oneindig kleine zware deeltjes. De resultaten laten zien dat de concentratie van deeltjes dichtbij de wand een maximale waarde heeft als het Stokesgetal $\mathrm{St} = O(10)$. De depositiesnelheid van deeltjes, die gedefinieerd is als de deeltjesstroom naar de wand toe gedeeld door de gemiddelde concentratie van deeltjes in de stroming, blijkt sterk toe te nemen met het Stokesgetal wanneer $10 \lesssim \mathrm{St} \lesssim 30$. Als $\mathrm{St} \gtrsim 30$, dan is de depositiesnelheid van deeltjes vrijwel onafhankelijk van het Stokesgetal. In algemene zin komen deze resultaten overeen met experimentele data in de literatuur, hoewel de depositiesnelheid van deeltjes enigszins te laag wordt voorspeld voor kleine Stokesgetallen ($\mathrm{St} \lesssim 10$). Volledig elastische botsingen blijken de depositiesnelheid van deeltjes op de wand niet significant te veranderen, hoewel er wel een effect zichtbaar is op de snelheid waarmee deeltjes de wand raken: deeltjes komen dikwijls op de wand terecht ten gevolge van een botsing in plaats van ten gevolge van turbulente diffusie. Volledig inelastische botsingen daarentegen resulteren in een verhoging van de depositiesnelheid van deeltjes voor initieel kleine Stokesgetallen met enkele ordes van grootte.

Ten slotte is de dynamica van zware deeltjes in de turbulente grenslaag van een roterende stroming in een pijp bestudeerd. In deze stroming neemt de deeltjesconcentratie dichtbij de wand toe indien het Stokesgetal St is $O(10)$; de maximale waarde van de concentratie is hoger dan in het geval van een stroming over een vlakke plaat. De depositiesnelheid stijgt snel met het Stokesgetal indien $\mathrm{St} \lesssim 30$; indien $\mathrm{St} \gtrsim 30$ neemt de depositiesnelheid van deeltjes slechts langzaam toe met het Stokesgetal. Een parameterstudie laat zien dat de depositiesnelheid hoger is bij hogere waarden van de rotatiehoek θ_S en het Reynoldsgetal gebaseerd op de wrijving met de wand Re_τ. De invloed van volledig elastische en van volledig inelastische botsingen is ook

onderzocht. Volledig elastische botsingen verhogen de depositiesnelheid van deeltjes niet significant. Wel daalt de deeltjesconcentratie in gebieden dichtbij de wand wanneer de botsingen volledig elastisch zijn. Volledig inelastische botsingen verhogen daarentegen de depositiesnelheid van deeltjes voor kleine Stokes getallen met enkele enkele ordes van grootte, zelfs als de volumetrische deeltjesconcentratie laag is, bijvoorbeeld 10^{-5}. Deze resultaten suggereren dat coalescerende druppels met kleine Stokesgetallen een grotere waarschijnlijkheid hebben om op de wand te komen dan onvervormbare deeltjes met dezelfde afmeting als de initiële afmeting van de druppels en met dezelfde dichtheid.

ACKNOWLEDGMENT

Although only my name is written on the cover of this thesis, many other people have contributed significantly. I would like to mention the following persons in particular.

First of all I would like to express my sincere gratitude to my promotor Harry Hoeijmakers. I am grateful for your support, guidance and advice for all the time that I have been involved in the group of Engineering Fluid Dynamics, both as a MSc student and as a PhD student. Especially, I thank you very much for the careful reading of the manuscript of this thesis.

I am very grateful to my daily supervisor and assistant-promotor Rob Hagmeijer. Rob, thank you very much for the long, fruitful and highly enjoyable collaboration, both during my MSc project and during my PhD project. I thank you for for all the useful suggestions, for showing me the importance of mathematically correct reasoning, and for giving me the freedom to carry out the research largely according to my own ideas. Finally, I am happy that you gave me ample possibilities to practice my teaching skills in working classes and by supervising MSc projects.

During the past four years, I have had the pleasure of supervising the graduation projects of two Mechanical Engineering students. Firstly, Pieter van Langen studied the motion of heavy particles near a helical vortex filament. Pieter, I thank you for the large amount of work that you have carried out, and for its quality. Although I am the first to admit that my opinion may be a bit biased, I think you fully deserve the Unilever Research Prize that you have won! Secondly, Martijn Douwes studied the motion of heavy particles in two-dimensional viscous vortex flows. Martijn, I thank you for your (typically Frisian?) persistence in obtaining accurate results from the CFD software CFX, and for your enthusiasm during the entire project.

The results presented in this thesis could not have been achieved without the support by Technologiestichting STW, through project TSF.6104 “Formation of dense wall-layer in high-speed swirling dispersed multiphase flow”. The financial contribution in the budget of this project by Twister B.V. is gratefully acknowledged. In addition, I am thankful for the interesting and motivating discussions with STW’s ‘user’s committee’ consisting of Stefan Belfroid (TNO), Rini van Dongen (TU/e), Leo Korstanje (STW), Bart Lammers (Twister), Chris Marcelis (STW), Corine Meuleman

(STW), Bart Prast (Twister), Johan Romate (Shell) and Paul Verbeek (Shell).

During my PhD work, it happened once every now and then that my computer suddenly stopped doing what I wanted it to do. Sometimes the computer reverted to its task automatically after having recognized its disobedience, but most of the times I had to invoke the help of Wouter den Breeijen to get it going again. Wouter, thank you for your great willingness to solve (computer) problems quickly and adequately! I would like to thank Yvonne Weber and Anjenet Mettivier-Meyer for taking some of the administrative burden out of my hands. I am thankful to the rest of the Engineering Fluid Dynamics staff, fellow PhD students and MSc students for the entertaining discussions over the past five years, not necessarily related to fluid dynamics. Special thanks go to Ryan Sidin, Marc van de Zande and Hüseyin Özdemir, who have shared the office with me in the past few years and have given me a pleasant working environment. On his own request, I hereby praise Dennis van Putten for the excellent printing of the concept of my thesis.

I would like to express my gratitude to my friends and family for the support and friendship over the years. In particular, I am grateful to Joris van den Berg and Arjen Koop for their willingness to be the paranymphs during my PhD defence. I thank my brother Wouter for designing the cover of this thesis, which looks really nice. Finally, I am thankful to my parents for their unconditional love and understanding during all my life.

Enschede, 11 June 2007,

Rutger IJzermans

ABOUT THE AUTHOR

Rutger IJzermans was born on May 31, 1980, in Zevenaar, The Netherlands, and raised in the nearby village 't Loo. After graduating from high school at "Liemers College" in Zevenaar in 1997, he started to study Mechanical Engineering at the University of Twente in Enschede. In 2001 he did a traineeship at the Dipartimento di Ingegneria Meccanica e Aeronautica of the University "La Sapienza" in Rome under the supervision of prof. R. Piva, investigating turbulence modulation by polymer additives. In January 2003 he obtained his master degree (with honors) with prof. dr. ir. H.W.M. Hoeijmakers and dr. ir. R. Hagmeijer. His graduation thesis "Droplet size distribution in condensing flow" was awarded the KIvI Prize for "Best MSc thesis of the year 2003 in Mechanical Engineering at the University of Twente".

In May 2003, he started to work as a PhD student on the research project "Formation of dense wall-layer in high-speed swirling dispersed multiphase flow", under the supervision of prof. dr. ir. H.W.M. Hoeijmakers and dr. ir. R. Hagmeijer. The project was financed by the Dutch Technology Foundation STW and by Twister B.V.. Results from this research are described in the present thesis. Parts of the work were presented at the IUTAM symposium on "Computational approaches to multiphase flow" in Chicago in October 2004, at the EUROMECH Conference in Stockholm in June 2006, at the ASME FEDSM06 Conference in Miami in July 2006 and at the Lorentz Centre Workshop "Environmental dispersion processes" in September 2006.

During his study in Mechanical Engineering, Rutger IJzermans was a member of several committees of the study association W.S.G. Isaac Newton. In addition, he was involved in the organization Twente Summer Campus, which arranges summer camps for secondary school students. From September 2004 to August 2006, he was a representative in the University Council of the University of Twente.